An atomistic investigation on the nanometric cutting mechanism of hard, brittle materials

Saurav Goel

A dissertation submitted for the degree of Doctor of Philosophy in Mechanical Engineering

Heriot-Watt University

School of Engineering and Physical Sciences

May 2013

Abstract

The demand for ultra precision machined devices and components is growing at a rapid pace in various areas such as the aerospace, energy, optical, electronics and bio-medical industries. Because of their outstanding engineering properties such as high refractive index, wide energy bandgap and low mass density, there is a continuing requirement for developments in manufacturing methods for hard, brittle materials. Accordingly, an assessment of the nanometric cutting of the optical materials silicon and silicon carbide (SiC), which are ostensibly hard and brittle, has been undertaken.

Using an approach of parallel molecular dynamics simulations with a three-body potential energy function combined with experimental characterization, this thesis provides a quantitative understanding of the ductile-regime machining of silicon and SiC (polytypes: 3C, 4H and 6H SiC), and the mechanism by which a diamond tool wears during the process. The distinctive MD algorithm developed in this work provides a comprehensive analysis of thermal effects, high pressure phase transformation, tool wear (both chemical and abrasive), influence of crystal anisotropy, cutting forces and machining stresses (hydrostatic and von Mises), hitherto not done so far.

The calculated stress state in the cutting zone during nanometric cutting of single crystal silicon indicated Herzfeld–Mott transition (metallization) due to high pressure phase transformation (HPPT) of silicon under the influence of deviatoric stress conditions. Consequently, the transformation of pristine silicon to β-silicon (Si-II) was found to be the likely reason for the observed ductility of bulk silicon during its nanoscale cutting. Tribochemical formation of silicon carbide through a solid state single phase reaction between the diamond tool and silicon workpiece in tandem with sp^3-sp^2 disorder of carbon atoms from the diamond tool up to a cutting temperature of 959 K has been suggested as the most likely mechanism through which a diamond cutting tool wears while cutting silicon.

The recently developed dislocation extraction algorithm (DXA) was employed to detect the nucleation of dislocations in the MD simulations of varying cutting orientation and cutting direction. Interestingly, despite of being a compound of silicon and carbon, silicon carbide (SiC) exhibited characteristics more like diamond, e.g. both SiC

workpiece and diamond cutting tool were found to undergo sp^3-sp^2 transition during the nanometric cutting of single crystal SiC. Also, cleavage was found to be the dominant mechanism of material removal on the (111) crystal orientation. Based on the overall analysis, it was found that 3C-SiC offers ease of deformation on either (111) <-110>, (110) <001> or (100) <100> setups. The simulated orthogonal components of thrust force in 3C-SiC showed a variation of up to 45% while the resultant cutting forces showed a variation of 37% suggesting that 3C-SiC is anisotropic in its ease of deformation. The simulation results for three major polytypes of SiC and for silicon indicated that 4H-SiC would produce the best sub-surface integrity followed by 3C-SiC, silicon and 6H-SiC.

While, silicon and SiC were found to undergo HPPT which governs the ductility in these hard, brittle materials, corresponding evidence of HPPT during the SPDT of polycrystalline reaction bonded SiC (RB-SiC) was not observed. It was found that, since the grain orientation changes from one crystal to another in polycrystalline SiC, the cutting tool experiences work material with different crystallographic orientations and directions of cutting. Thus, some of the grain boundaries cause the individual grains to slide along the easy cleavage direction. Consequently, the cutting chips in RB-SiC are not deformed by plastic mechanisms alone, but rather a combination of phase transformation at the grain boundaries and cleavage of the grains both proceed in tandem. Also, the specific-cutting energy required to machine polycrystalline SiC was found to be lower than that required to machine single crystal SiC. Correspondingly, a relatively inferior machined surface finish is expected with a polycrystalline SiC.

Based on the simulation model developed, a novel method has been proposed for the quantitative assessment of tool wear from the MD simulations. This model can be utilized for the comparison of tool wear for various simulation studies concerning graphitization of diamond tools. Finally, based on the theoretical simulation results, a novel method of machining is proposed to suppress tool wear and to obtain a better quality of the machined surface during machining of difficult-to-machine materials.

Acknowledgements

If the completion of a PhD study is all about persistence than it was a major challenge to complete this study without the inspirational guidance and support of many individuals. Although the list of people, whom I wish to express my deepest gratitude, far exceeds the words, there are certain individuals who deserve special mention for their care, motivation, guidance, support, and encouragement.

At the outset, I would like to express my deepest gratitude to Prof. Xichun Luo, my primary supervisor, who has extended his support beyond being an academic supervisor. His ingenuity and resourcefulness is phenomenal which has propelled and fostered my intellectual maturity that I will benefit from, for a long time to come. I also wish to express my immense appreciation to my co-supervisor Prof. Robert L. Reuben who has played a key role in my work and has made countless suggestions at each step of my work. I am indebted to them more than they know.

I would also like to thank Heriot-Watt University, UK for providing me the generous financial support in the form of a highly prestigious award of Scottish Overseas Research Scholarship Award Scheme (SORSAS). I would also like to acknowledge the use of Queensgate Grid at University of Huddersfield and STFC Hartree Centre resources in this work.

I also extend my sincere thanks to Dr. Alexander Stukowski (Darmstadt University of Technology, Germany), Prof. Ekkard Brinksmeier (University of Bremen, Germany), Prof. James Ritchie (Heriot-Watt University, UK), Mr. Alan Heaume (Cranfield University, UK), Mr. Andrew Cox (Contour Fine Tooling Limited, UK) and Prof. V.K. Jain (IIT Kanpur, India) for their generous support. Helpful suggestions of Dr. John Patten (Western Michigan University, USA), Prof. Jiwang Yan (Kieo University, Japan) and Mr. Gaurav Goel (Sharda University, India) are also sincerely appreciated. My keen appreciation also goes to Mrs. Marian Miller and Mrs. Crawford Rebecca for providing me the departmental and allied facilities at Heriot-Watt University.

While every individual mentioned above has helped me in the systematic learning to write this thesis, its credit is theirs; the errors (if any) are solely mine.

I am also thankful to Dr. Anupam Agrawal (UIUC, USA), Mr. Sachindra Mahato (NERIST, India) and Mr. Michael Marshal (Larsen and Toubro Limited, India) for providing their valuable recommendations which were needed as a prerequisite to enter to the PhD Programme at Heriot-Watt University. I thank to all my colleagues, especially Mr. Waleed Bin Rashid (soon to be Dr.), Dr. Hongmin Pen and Dr. Jining Sun and for their kind hospitality and support.

Words would be few to describe my gratitude towards my beloved parents, Mrs. Shashi Bala Goel and Mr. Shri Krishan Goel for their endless patience, support and encouragement to whom this thesis is dedicated.

ACADEMIC REGISTRY
Research Thesis Submission

Name*:*	Saurav Goel		
School/PGI:	Engineering and Physical Sciences (EPS)		
Version: *(i.e. First, Resubmission, Final)*	Final	Degree Sought (Award **and** Subject area)	PhD, Mechanical Engineering

Declaration

In accordance with the appropriate regulations I hereby submit my thesis and I declare that:

1) the thesis embodies the results of my own work and has been composed by myself
2) where appropriate, I have made acknowledgement of the work of others and have made reference to the work carried out in collaboration with other persons
3) the thesis is the correct version of the thesis for submission and is the same version as any electronic versions submitted*.
4) my thesis for the award referred to, deposited in the Heriot-Watt University Library, should be made available for loan or photocopying and be available via the Institutional Repository, subject to such conditions as the Librarian may require
5) I understand that as a student of the University, I am required to abide by the Regulations of the University and to conform to its discipline.

* *Please note that it is the responsibility of the candidate to ensure that the correct version of the thesis is submitted.*

Signature of Candidate*:*		Date:	07/05/2013

Submission

Submitted By *(name in capitals):*	SAURAV GOEL
Signature of Individual Submitting:	
Date Submitted:	07/05/2013

For Completion in the Student Service Centre (SSC)

Received in the SSC by *(name in capitals):*			
Method of Submission *(Handed in to SSC; posted through internal/external mail):*			
E-thesis Submitted (***mandatory for final theses***)			
Signature:		Date:	07/5/2013

Table of Contents

List of Tables

List of Figures

Abbreviations

3C-SiC	3C type silicon carbide
4H-SiC	4H type silicon carbide
6H-SiC	6H type silicon carbide
AFM	Atomic force microscope
ALMA	Atacama Large Millimeter / submillimeter Array
AMMPs	Advanced micro-machining processes
AMNFPs	Advanced micro-/nano-finishing processes
APS	Average particle size
BDT	Brittle-ductile transition
CBN	Cubic boron nitride
CIS	Critical indent size
CSP	Centro-symmetry parameter
CVD-SiC	Chemically vapour deposited silicon carbide
DBT	Ductile to brittle transition
DLC	Diamond like carbon
DXA	Dislocation extraction algorithm
E-ELT	European Extremely Large Telescope
EUV	Extreme ultraviolet
FCC	Face centred cubic
FIB	Focussed ion beam
FTS	Fast tool servo
HCP	Hexagonal close packed
HT	Hard turning
HPPT	High pressure phase transformation
IC	Internal combustion
IR	Infra red
LC	Load control
LLNL	Lawrence Livermore National Laboratory
MEMS	Micro-electro-mechanical system
MD	Molecular dynamics
MNM	Micro-/nano-machining
NEMS	Nano-electro-mechanical system
OFHC	Oxygen-free high thermal conductivity copper

PBC	Periodic boundary condition
PCD	Polycrystalline diamond
pH value	Power of hydrogen in water
RAF Growth	Repeated a-face growth
RB-SiC	Reaction-bonded silicon carbide
RDF / g(r)	Radial distribution function
SiC	Silicon carbide
SDM	Surface defect machining
SEM	Scanning electron microscope
SPDM	Single point diamond machining
SPDT	Single point diamond turning
STS	Slow tool servo
UPL	Ultra precision lathe machine
UPM	Ultra precision manufacturing
VAM	Vibration assisted machining
Vb	Tool flank wear width

Nomenclature

a	Lattice constant
a_0	Depth of cut
c	Critical crack length
d_c *or* t_c	Critical chip thickness
E	Elastic modulus of the material
f	Feed rate
f_{max}	Critical feed rate
G	Bulk modulus of the material
H	Hardness of the material
K_c / R	Fracture toughness of the material
K_b	Boltzmann constant (1.3806503×10^{-23} J/K)
l_c	Length of contact between cutting chip and tool
N	Spindle speed
P	Critical load of nano-indentation
R	Nose radius of the cutting tool
r	Inter-atomic distance
S	Specific energy required to propagate a crack
t_{max}	Maximum critical undeformed chip thickness
V	Cutting speed
Vp	Potential energy function
W	Width of cut
W_d / Z_{eff}	Ductile width of cut
Y_c	Critical crack length
ρ	Density of the material
σ_y	Yield stress for plastic flow

List of Publications by the Candidate

International Journals:

1. Goel S., Luo X. and Reuben R.L., Shear instability of nanocrystalline silicon carbide during nanometric cutting, Applied Physics Letters, 2012, 100(23), pp 231902
2. Goel S., Luo X., Comley P., Reuben R.L. and Cox A., Brittle-ductile transition during diamond turning of single crystal silicon carbide, International journal of machine tools and manufacture, 2013, 65(0), p 15-21
3. Luo X., Goel S., and R.L. Reuben, A quantitative assessment of nanometric machinability of major polytypes of single crystal silicon carbide, Journal of the European Ceramic Society, 2012, 32(12), p 3423-3434
4. Goel S., Luo X., and Reuben R.L., Wear mechanism of diamond tools against single crystal silicon in single point diamond turning process, Tribology International, 2013, 57(0), p 272-281.
5. Goel S., Luo X., Reuben R.L. and Pen H., Influence of temperature and crystal orientation on tool wear during single point diamond turning of silicon, Wear, 2012, 284–285(0), p 65-72
6. Goel S., Luo X., Reuben R.L. and Rashid W.B., Atomistic aspects of ductile responses of cubic silicon carbide during nanometric cutting, Nanoscale Research Letters, 2011, 6(1). p 589
7. Goel S., Luo X. and Reuben R.L., Molecular dynamics simulation model for the quantitative assessment of tool wear during single point diamond turning of cubic silicon carbide, Computational Materials Science, 2012, 51(1), p 402-408
8. Goel S., Stukowski A., Goel G., Luo X. and Reuben R.L., Nanotribology at high temperatures, Beilstein Journal of Nanotechnology, 2012, 3, p 586-588

9. Goel S., Luo X., Reuben R.L. and Rashid W.B., Replacing diamond cutting tools with CBN for efficient nanometric cutting of silicon. Materials Letters, 2012, 68(0), p 507-509
10. Goel S., Luo X., Reuben R.L., Rashid W.B. and Sun J., Single point diamond turning of single crystal silicon carbide: Molecular dynamics simulation study. Key Engineering Materials, Vol. 496, (2012), p 150-155, DOI:10.4028/www.scientific.net/KEM.496.150
11. Goel S., Luo X., Reuben R.L., Rashid W.B. and Sun J., Simulation study of cutting forces, stresses and temperature during nanometric cutting of single crystal silicon, Key Engineering Materials, Vol. 496, (2012), p 223-228, DOI:10.4028/www.scientific.net/KEM.496.223
12. Pen H.M., Liyang Y.C., Luo X., Goel S. and Ritchie J.M., Multiscale simulation of nanometric cutting of single crystal copper and its experimental validation, Computational Materials Science, 2011, 50(12), p 3431-3441
13. Rashid, W.B., Goel S., Luo X. and Ritchie J.M., An experimental investigation for the improvement of attainable surface roughness during hard turning process. Proceedings of the Institution of Mechanical Engineers, Part B: Journal of Engineering Manufacture, 2013, DOI: 10.1177/0954405412464217
14. Rashid W.B., Goel S., Luo X. and Ritchie J.M., The development of a surface defect machining method for hard turning processes, Wear, 2013, DOI: 10.1016/j.wear.2013.01.048
15. Goel S., Rashid W.B., Luo X., Jain V.K., Agrawal A. and Reuben R.L. , A theoretical assessment of the surface defect machining and hot machining of nanocrystalline silicon carbide, submitted for publication to Journal of manufacturing science and engineering published by ASME

16. Goel S., Stukowski A., Luo X., Agrawal A. and Reuben R.L., Anisotropy of single crystal 3C-SiC during nanometric cutting, submitted for publication to journal of modelling and simulations in material science and engineering published by IOP

International Conference Proceedings:

17. Goel S., Luo X., Stukoswki A. and Reuben R.L., Influence of nanoparticle coolant and crystal structure of the workpiece during nanometric cutting of silicon carbide, P 6.75- Proceedings of the 12th EUSPEN International Conference, Volume 2, Page 299-302, 2012, Stockholm, Sweden
18. Goel S., Rashid W.B., Mir A., Sun J. and Luo X., Development of the surface defect machining method for micro/nano scale material removal processes – accepted for publication in 13th EUSPEN International Conference, 2013, Berlin, Germany

Poster Publications:

1. Won Heidenhein scholarship award (Travel bursary of Euro 500 + Free conference Registration) for the conference paper and a technical poster on "Molecular dynamics simulation investigation on ultra precision machining of hard, brittle materials" at 13th EUSPEN International Conference held at Berlin, Germany, from 27th-31st May 2013
2. Presented an invited poster on Single point diamond turning of single crystal silicon carbide at House of Commons, Parliament of the UK, London on 18th March 2013

3. Presented a technical poster on "Crystal anisotropy of SiC during nanometric cutting" at 19th International conference on Wear of Materials at Oregon, Portland, USA from 14th to 18th April 2013
4. Won 3rd prize (including cash prize of 100 Euro) for the poster presented on "Single Point Diamond Turning of Silicon Carbide" at 12th EUSPEN International Conference held at Stockholm, Sweden from 4th July -8th July 2012
5. Presented a technical poster (Poster No. 59) at EPSRC organized International conference on "Manufacturing the future conference 2012" held at Loughborough University, UK during 19th -20th September 2012
6. Presented a technical poster at a knowledge exchange International conference in Edinburgh held at Heriot-Watt University, UK during 4th-5th October 2012 organized by KE Scotland society

Invited talks:

1. Delivered an invited talk at IIT Kanpur, India on "Wider spectrum of molecular Dynamics in the field of ultra precision manufacturing" on 3rd October 2011
2. Delivered an invited talk at Sharda University, Greater Noida, India on "Molecular Dynamics & single point diamond turning" on 10th October 2011
3. Delivered an invited talk at Bremen University, Germany on "MD simulation of hard, brittle materials" on 18th June 2012
4. Delivered an invited lecture at IIT Kanpur, India on "MD simulation of nanometric cutting of hard brittle materials" on 6th November 2012

Book Published:

Title: Wear Mechanism of Diamond Tools during Ultra Precision Machining: MD Simulation Study, ISBN No. 3844387447, Germany, 2011

Chapter 1 - Introduction

1.1 Background and significance

Due to its relatively low mass density and low cost, single crystal silicon is considered to be an ideal optical material for weight sensitive infrared (IR) applications and other high added value products such as X-ray optics and X-ray interferometers. On the other hand, NASA, USA has recently demonstrated that, due to its superior properties, such as chemical inertness, high thermal conductivity, high carrier saturation velocity, high specific stiffness (E/ρ) and high-temperature resistance [1], silicon carbide (SiC) is an appropriate choice to replace silicon for advanced ultra precision engineering applications especially in the electronic industry. Moreover, SiC is also recognized as a potential candidate for quantum computing applications as a substitute to diamond [2], in space-based laser mirrors [3] and for moulding dies used for hot-press moulding of aspherical glass lenses. Further demand is growing in weapons, aerospace, microelectronic and bio-medical applications as well as in "big-science" programmes such as the European Extremely Large Telescope (E-ELT), the Atacama Large Millimeter / submillimeter Array (ALMA) and next generation extreme ultraviolet (EUV) lithography steppers.

While some ultra precision products are becoming larger and larger (the size of a finished silicon wafer reached 300 mm at the year 2000), the sizes of many other precision components, such as fuel injectors and bearings, have been significantly reduced to meet the functional requirements and to reduce manufacturing and product costs. The need for tight dimensional tolerances and miniaturisation for such products is driven by the global mission to reduce emissions and increase the efficiency of IC-engines. This is just one example of how environment and sustainability issues are increasingly driving ultra precision technologies. Other examples can be found in

optical devices and computer chips, where the required tolerances are approaching the atomic length scale, thus requiring significant ultra precision manufacturing research in the fabrication of hard, brittle materials. Traditional machining methods for producing such parts rely on lapping and polishing, but these are not particularly successful for manufacturing complex shapes, such as aspheric, diffractive and "hybrid" components when judged in terms of quality and cost effectiveness.

Hard, brittle materials exhibit the so called "ductile-regime" in machining when the chip thickness is reduced to a few nanometres, thus permitting optical quality machined surfaces. There is no clear distinction between ultra precision engineering and nanotechnology. The early vision of Nobel laureate, Richard Feynman, of atom-by-atom construction, revealed in his much widely cited lecture "There's plenty of room at the bottom" would suggest that the second term is most often associated with additive manufacture. It is only more recently that technologies capable of controlling a single point diamond turning tool and workpiece have made it feasible to produce a deterministic finish on brittle materials with precision envisaged by Feynman. The process of material removal at the scale of a few atomic layers using a single point diamond cutting tool, single point diamond turning (SPDT), is one of the most efficient ultra precision material removal processes.

SPDT has remained one of the greatest advancements in the field of ultra precision engineering and is at the pinnacle of the turning process range in terms of machining accuracy and attainable machined surface finish [4]. Currently, with Fast Tool Servo (FTS), Slow Tool Servo (STS) or fly cutting techniques, SPDT can be used to machine freeform (non-rotationally symmetric) machined surfaces.

Hard, brittle materials present various technical challenges to manufacture, some of which are represented schematically in figure 1-1. From figure 1-1, it can be seen that

the ductile-regime machining of brittle materials involves a complex interplay of a number of processes at the atomic scale:

- catastrophic wear of the cutting tool during the process of machining
- unknown properties and extent of the deformation of the machined surface
- effect of the process variables and tool geometry on the cutting process in governing the tool life
- state of stress (local) to drive the high pressure phase transformation in the cutting zone
- movement of dislocations in the workpiece near the cutting zone
- effect of material's microstructures (both workpiece and cutting tool) on the cutting process and influence of crystal anisotropy

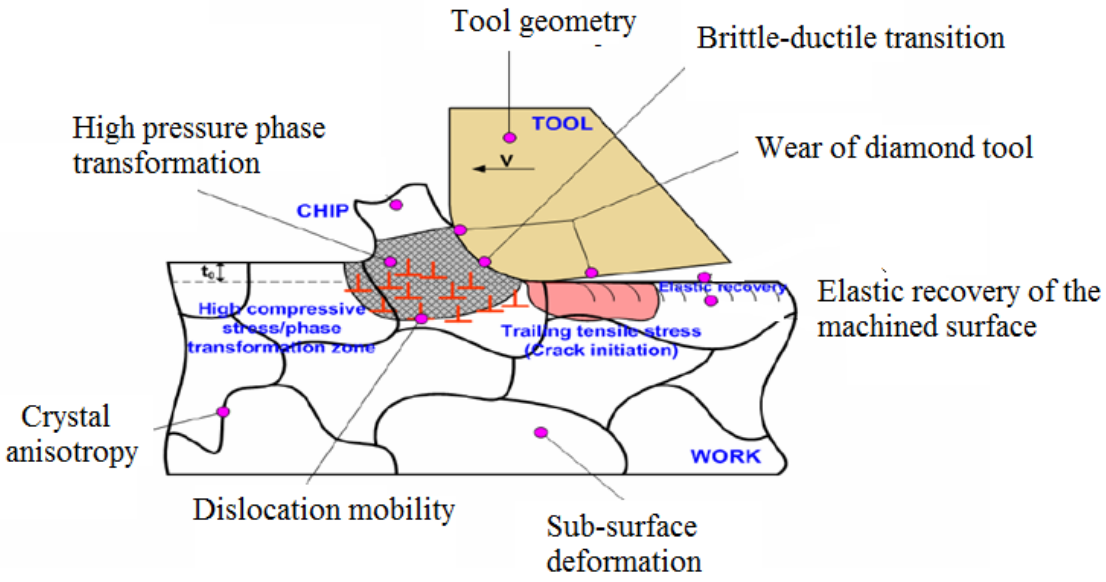

Figure 1-1: Various complexities inherent with the nanometric cutting of hard brittle materials – adapted [5]

A common consequence of failure to control these processes is the undesirable ductile-brittle transition or compromised tool life. In recent years, although a level of understanding of the chip formation mechanism and high pressure phase transformation in the cutting chips has been reached, this is some way short of an overall

phenomenological understanding of the complex interplay of all those aspects which affect tool wear and their influence on the dynamics of the process insofar as this affects the machined surface.

In this regard, this thesis aims to provide an understanding of the high pressure solid state physics of the cutting chips; specifically, the influence of microstructure and crystal structure of the tool and workpiece materials on sub-surface crystal deformation layer depth and on the phenomena involved in the tool wear mechanism. More detailed attention is paid to the phenomenology of the wear process in order to suggest measures for it suppression. In this way, a holistic view of nanoscale machining is also developed for the purposes of optimising tool life and improved machined surface quality.

1.2 Aim and objectives of the research

As discussed in section 1.1, the aim of this work is to provide an atomistic insight into the dynamics of nanometric cutting of hard, brittle materials. To accomplish this task, a molecular dynamics simulation model was developed to deliver a number of specific outputs. Besides the tool wear mechanism, the MD model was aimed at providing accurate understanding of the influence of crystal anisotropy, ductile characteristics of these brittle materials and sub-surface deformation underneath the machined surface of both silicon and silicon carbide.

In order to achieve this aim, following five objectives were set:

- Review of existing literature to develop an understanding of the previously published simulation models and identify any shortcomings of these models.
- Study and identification of the appropriate simulation inputs to simulate a more realistic nanometric cutting process using molecular dynamics (MD) simulation.
- Develop an MD simulation model of the nanometric cutting process considering the cutting tool as a deformable body. Analyse the simulation results to develop an understanding of the tribo-chemical processes.
- Perform experimental trials to validate aspects of the simulations.
- Make generic suggestions for suppressing tool wear.

1.3 Structure of the thesis

This thesis is divided into the following nine chapters:

Chapter 1 explains the relevance of the research in the current context of nanotechnology and describes the major objectives of this work.

Chapter 2 reviews the various kinds of ultra precision manufacturing process available to modern industry, including mechanical, chemical and physical machining processes and some of the hybrid machining processes. The chapter explains how the identification of "brittle-ductile" transition phenomena helped in the discovery and advancement of the single point diamond turning method and highlights the various challenges associated with the ductile-regime machining of hard, brittle materials.

Chapter 3 reviews critically what is known about the major factors which influence the ductile-regime machining of hard brittle materials, including both geometrical features of the cutting tool and the internal atomic scale geometrical features of the workpiece such as its microstructure, variations in the stacking sequence of the atomic planes

(polymorphism) and the influence of crystal anisotropy on the mechanism of nanometric cutting.

Chapter 4 describes how the molecular dynamics (MD) simulation was adapted to be useful for analysing ultra precision cutting. The basic concept and framework of the MD simulation approach is first introduced, followed by a discussion of the importance of the potential energy function, something which has not received any attention in previous studies. This chapter also provides a detailed description of the tools required for pre-processing and post-processing of the MD simulation results.

Chapter 5 describes the details of the simulation results obtained from the MD simulation of nanometric cutting of silicon using a diamond cutting tool. Along with a comprehensive discussion on the high pressure phase transformations of the silicon, this chapter provides a detailed insight into the likely wear mechanism of the diamond tool as indicated by the thermodynamics of the process and Gibb's free energy calculations.

Chapter 6 covers detailed aspects of nanometric cutting of silicon carbide arising out of the simulations. The ductile response of silicon carbide has remained a controversial issue in the literature and this is discussed in the first section. Details of crystal anisotropy of 3C-SiC are explained in the second section, while the two subsequent sections discuss the variations in the machining response of machining of RB-SiC and single crystal SiC. The last section offers a detailed explanation of the wear mechanism of the diamond tools and also presents a novel, generic flowchart to quantify tool wear from MD simulations.

Chapter 7 presents experiments on nano-scratching and single point diamond turning of single crystal 6H-SiC. The cutting forces and machined surface roughness were measured and, as with the theoretical model, evidence of brittle-ductile transition in SiC is demonstrated.

Chapter 8 presents a novel approach for nanometric cutting of hard, brittle materials which is given the name surface defect machining (SDM). Alongside the theoretical description and working principle of SDM, this chapter presents some preliminary MD simulation results for SDM of 3C-SiC.

Chapter 9 presents the assessment and conclusion of the whole research. Based on the simulations developed in the thesis, some measures to suppress the tool wear are highlighted. As well, some recommendations for work that could usefully be done in the future are made.

Chapter 2 - Literature review

2.1 Introduction

Machining by mechanical means has undergone prolific development since its introduction as metal cutting. One relatively recent development is the hard turning (HT) process where IT4 is now achievable with state-of-the-art HT techniques [6] compared to the earlier limitations reported by Konig *et al*. [7] where geometric tolerances corresponding to IT6 and the surface qualities of Rtm 2-3 µm were the best attainable. Over the past few decades, the emphasis in manufacturing research has shifted from macro- through micro- to nano-scale methods. Strenuous efforts are currently being made to reduce the scale of material removal down to the atomic level. Some ultra precision manufacturing (UPM) processes already involve material removal at the micro-/nano- scale and interest is turning towards ultra precision machining. Single point diamond turning (SPDT) is one such UPM process capable of removing material from the workpiece to the level of several atomic dimensions. This chapter presents a review of the various micro-/nano-manufacturing processes and highlights the current research status of SPDT of hard, brittle materials.

2.2 Micro-/nano-machining (MNM) processes

Davies *et al.* [8] has quoted Fortune's [9] statement that "*Ultra precision manufacturing is doing for light what integrated circuits did for electronics*" highlighting the precision of material removal possible using lasers.

Since then, several researchers have sought to define ultra precision machining [10], a selection of which follows:

Taniguchi (1983) [11] :
"*Ultra-precision machining is the process by which the highest possible dimensional accuracy is achieved at a given point of time*".

McKeown (1987) [12]:
"The role of ultra-precision machining in the manufacturing sector is to research, design, develop and commercialize processes, sensors, instruments, machines, control systems and materials in order to achieve further advances in technology, science and wealth creation".

Corbett *et al.* (2000) [10] :
Nano-machining is "the study, development and processing of materials, devices and systems in which structure of a dimension of less than 100 nm is essential to obtain the required functional performance".

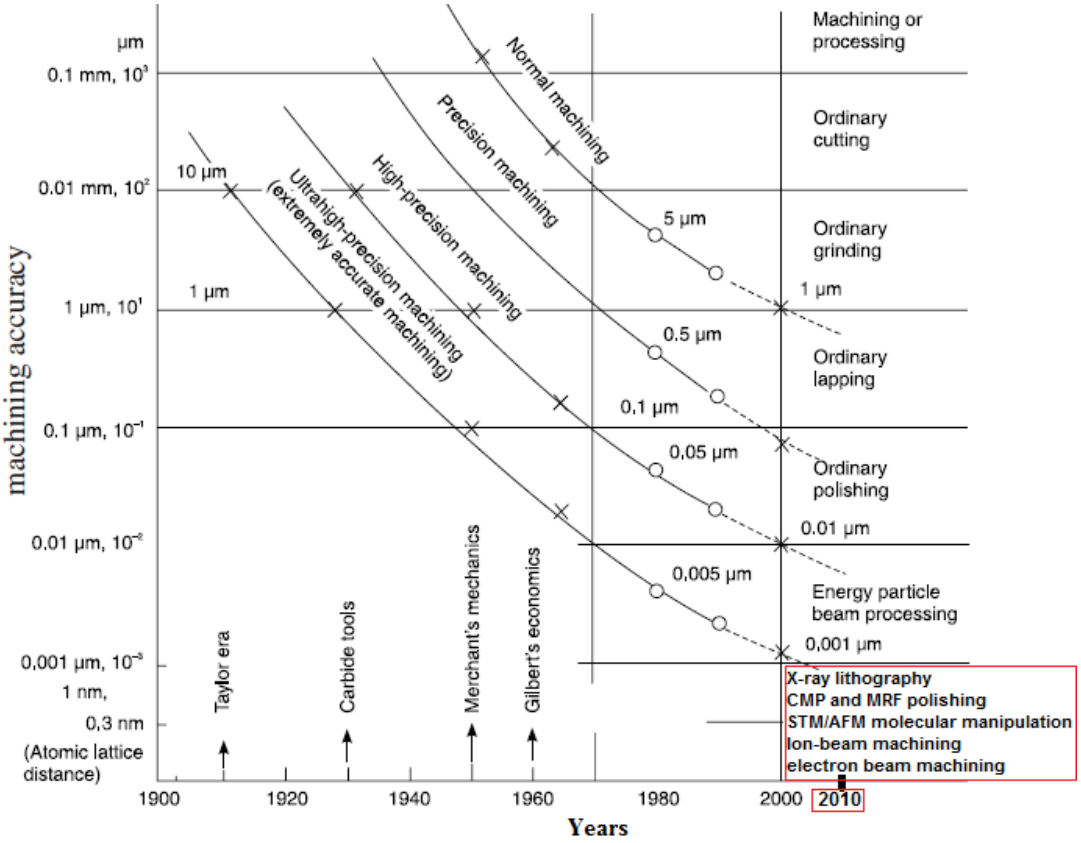

Figure 2-1: Evolution of machining accuracy - Taniguchi's prediction's [11] updated beyond 2000 to include state-of-the-art manufacturing processes (shown in red box)

During the 1980s, Taniguchi [11, 13] set out a predictive map of development in precision machining, figure 2-1, and this still seems to be hold as we approach 2020. Recently, Shore *et al.* [4] suggested that the Taniguchi chart is analogous to Moore's

Law, the mid-1960s prediction of microelectronics manufacturing precision for the coming 50 years. In either case, a sharp distinction is made in the attainable accuracy between macro- and micro- and nano- scale machining.

Although sometimes used synonymously, one major difference between the micro- and nano-machining is the size of the attainable chip thickness, e.g. a minimum ratio of the chip thickness to the cutting edge radius in micromachining has been estimated to be 0.293 whereas in nanometric cutting it could be down to 0.1 [14]. Besides this major difference, some other significant differences were highlighted by Brinksmeier during a talk at the Royal Society in 2011, and summarised in table 2-1.

Table 2-1: Differences between macro, micro and nano level machining processes [15]

	Macro-Machining	**Micro-machining**	**Nano-machining**
Size of machined area	1 to $10^5 cm^2$	1 to $10^5 mm^2$	1 to$10^5 \mu m^2$
Volume removal in one machining step	from 10^{-3} to $10^2 cm^3$	from 10^{-3} to $10^2 mm^3$	from 10^{-3} to $10^2 \mu m^3$
Material removal rate	from 10^{-5} to 1 $cm^3 s^{-1}$	from 10^{-5} to 1 $mm^3 s^{-1}$	from 10^{-5} to1 $\mu m^3 s^{-1}$
Relative figure error	from 10^{-5} to 10^{-3}	from 10^{-7} to 10^{-5}	from 10^{-5} to 10^{-3}
Surface roughness	up to 10 micron	up to 0.1 micron	0.1 to 10 nm

The 21st century has seen the rapid emergence of a variety of non-conventional micro/-nano-machining (MNM) processes capable of being applied to a range of engineering materials, including metals, ceramics, plastics and composites. Miniaturization of various aspects of manufacturing requires improvement in attainable accuracies and tolerances to the sub-micron range especially in the fields of optics, electronics, medicine, biotechnology, communications, and avionics in applications concerning fuel cells, microscale pumps, valves and mixing devices, fluidic microchemical reactors,

microfluidic systems, micronozzles for high-temperature jets, microholes for fibre optics, micromoulds and deep X-ray lithography masks etc. [14].

MNM processes can be divided into two broad categories:

- advanced micro-machining processes (AMMPs) to shape and size a component
- advanced micro-/nano-finishing processes (AMNFPs) for fine finishing of a component to the required tolerances [16]

As shown in figure 2-2, MNM processes can also be divided into four major categories based on whether they involve addition of material, removal of material or no nominal change in the amount of material during the process, the last with or without a melt stage. The categories involving no gain or loss of material, i.e. micro-thermo forming and micro-injection moulding, are most suited to the class of materials exhibiting low critical temperature, such as polymers. Micro-thermo forming is achieved by thermally softening the part to conform to a mould whereas micro-injection moulding involves the material being fed into a heated barrel, mixed, and forced into a mould cavity.

As shown in figure 2-3, the material removal processes can be classified further into mechanical, physical or chemical processes depending on the nature of the mechanism of material removal. While physical and chemical machining processes are restricted to specific materials and applications, mechanical micro-machining is considered to be almost universal in its applicability [15].

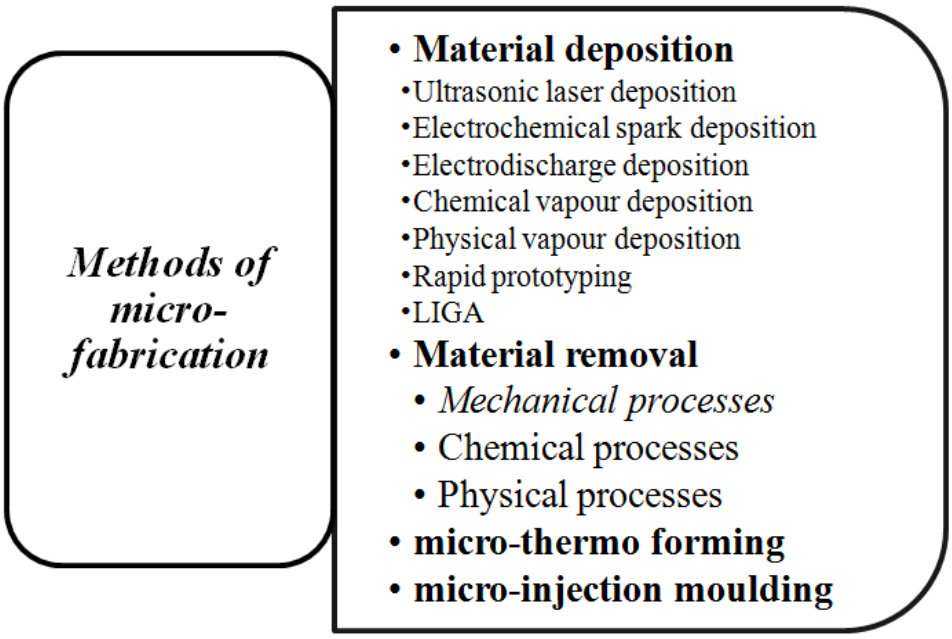

Figure 2-2: Classification of ultra precision manufacturing processes

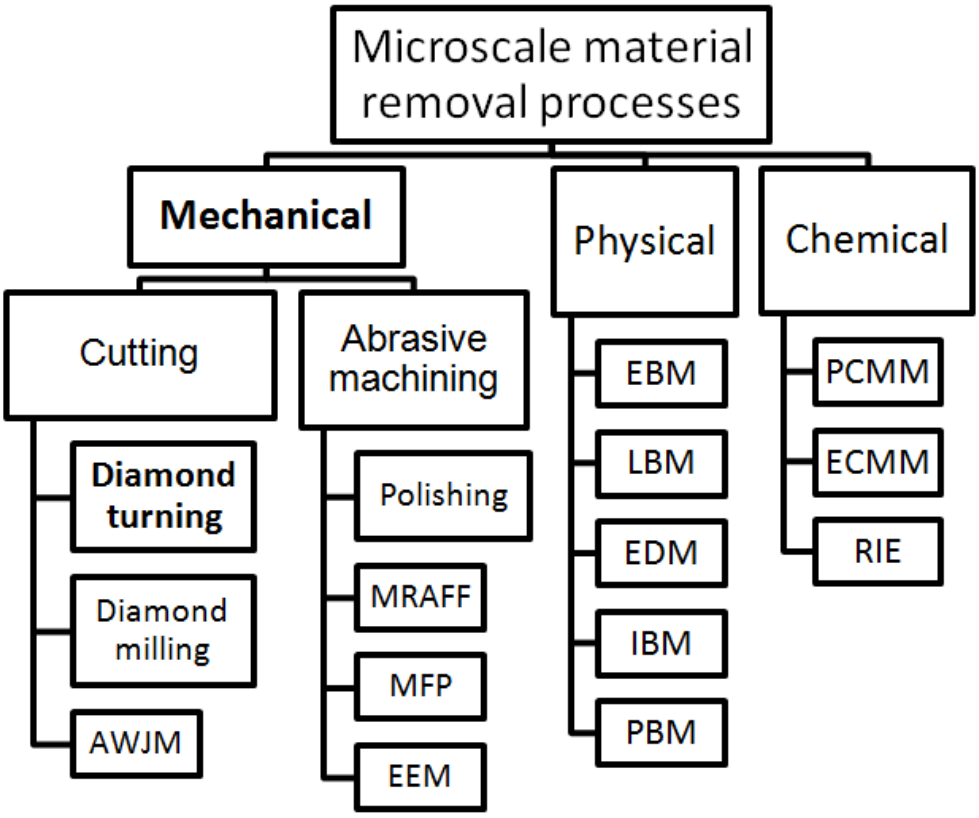

AWJM: abrasive water jet machining; MRAFF: magneto-rheological abrasive flow finishing; MFP: magnetic float polishing; EEM: elastic emission machining; EBM: electron beam machining; LBM: laser beam machining; EDM: electro discharge machining; IBM: ion beam machining; PBM: proton beam micromachining; PCMM: photo chemical micro-machining; ECMM: electro chemical micro-machining; RIE: Reactive ion etching.

Figure 2-3: Classification of various ultra-precision manufacturing processes

Over time, researchers have been able to integrate some of these manufacturing processes to harness the combined advantages of each. Such integrated processes are known as hybrid micro-/nano machining processes, some of these hybrid processes are shown in figure 2-4. Surface defect machining (SDM) is one such hybrid manufacturing process, which is particularly relevant to this research and is discussed in detail in Chapter 8.

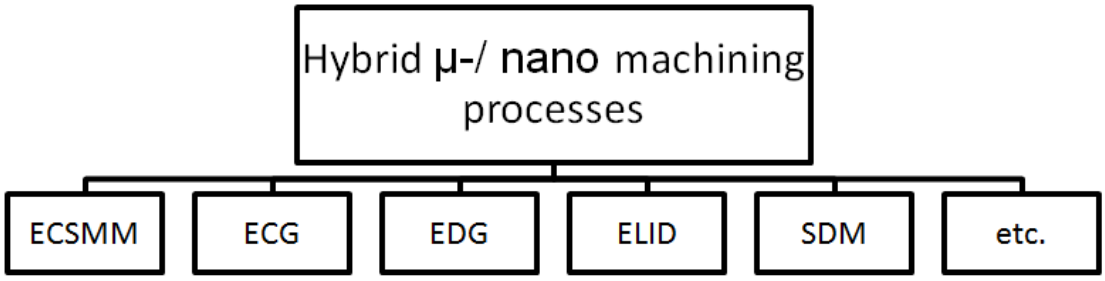

ECSMM: electro chemical spark micro-machining; ECG: electrochemical grinding; EDG: electro discharge grinding; ELID: electrolytic in-process dressing; SDM: surface defect machining

Figure 2-4: Hybrid micro-/nano machining processes

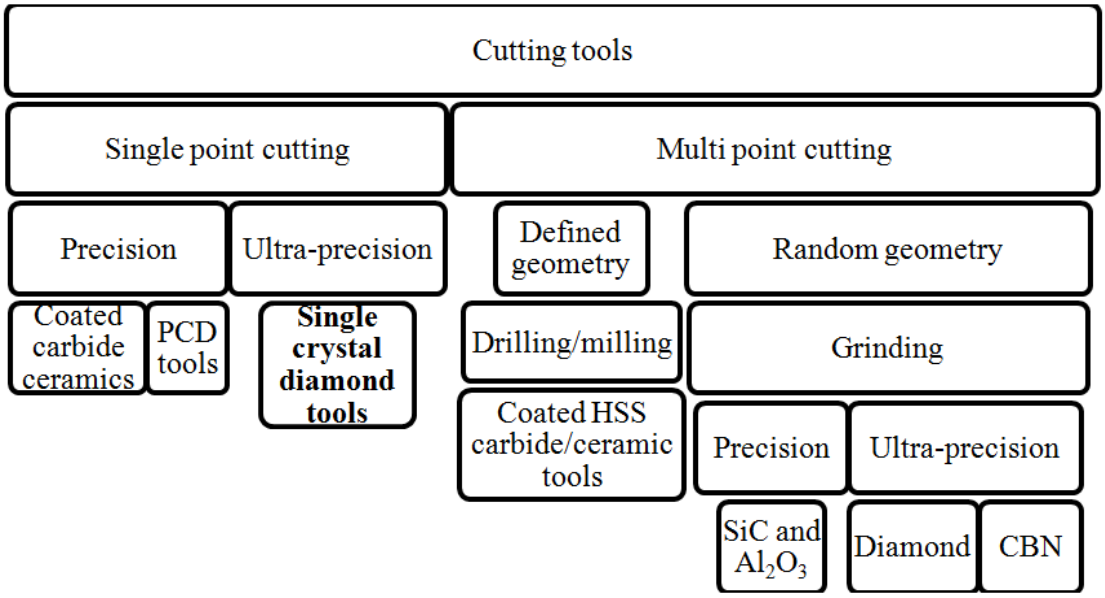

Figure 2-5: Classification of cutting tools

Mechanical micro-machining can be further subdivided into cutting and abrasive machining (figure 2-5) depending on the geometry of the cutting tool used for the removal of material i.e. single point cutting, multi point cutting and abrasive machining. The basic difference between them is that cutting as such employs a pre-defined and

known geometry of cutting tool whereas abrasive machining involves a relatively large number of arbitrarily oriented cutting tips and thus the engagement of the cutting tips with the workpiece occurs at random. Whereas abrasive machining provides very fine finished surfaces in an iterative manner, cutting offers a more efficient rate of material removal and deterministic form accuracy.

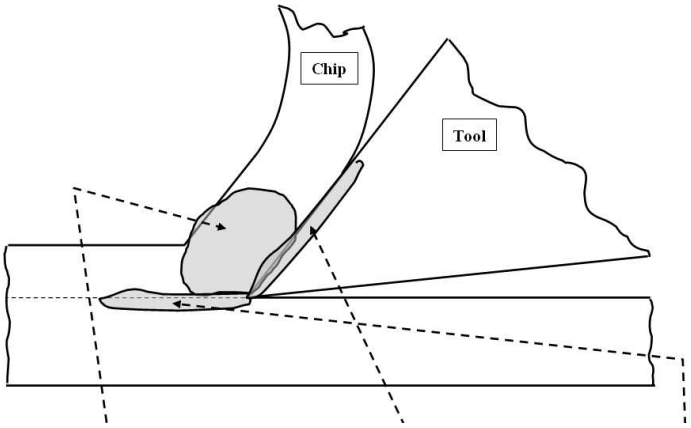

$$\underbrace{F_c V}_{\text{Total energy to cut}} = \underbrace{(\tau_y \gamma)(t_0 w V)}_{\substack{\text{Shear energy} \\ \text{(Plastic dissipation)}}} + \underbrace{[F_c \sec(\beta-\alpha)\sin\beta]\frac{V\sin\varphi}{\cos(\varphi-\alpha)}}_{\text{Frictional dissipation}} + \underbrace{RwV}_{\text{New surface formation}}$$

where R is the specific work of surface formation (fracture toughness), w the width of cut, V is the cutting speed, τ_y is the shear yield stress, β the friction angle, α the rake angle, t_0 the uncut chip thickness, F_c the cutting force, φ the shear plane angle and γ is the shear strain

Figure 2-6: Atkin's model of distribution of energy in nanoscale cutting [17] [1]

Due to the significant consumption of energy to manufacture any material through cutting and increasing concerns about energy consumption and CO_2 emissions, manufacturing research on the assessment of machining energy has attracted lot of attention. Atkin has proposed a model (shown in figure 2-6) to calculate the cutting energy in a turning operation. He divided the cutting energy into three major components; the energy required to shear the material, the energy dissipated due to friction between the cutting chips and the rake face of the cutting tool and the energy required to create the new surface. Recently, Gutowski *et al.* [18] presented a

[1] Readers are referred to the electronic copy of this thesis to interpret the correct colour legends.

thermodynamic analysis through which they highlighted that both ultra precision machining and injection moulding require low amounts of energy compared to other manufacturing processes, as shown in figure 2-7.

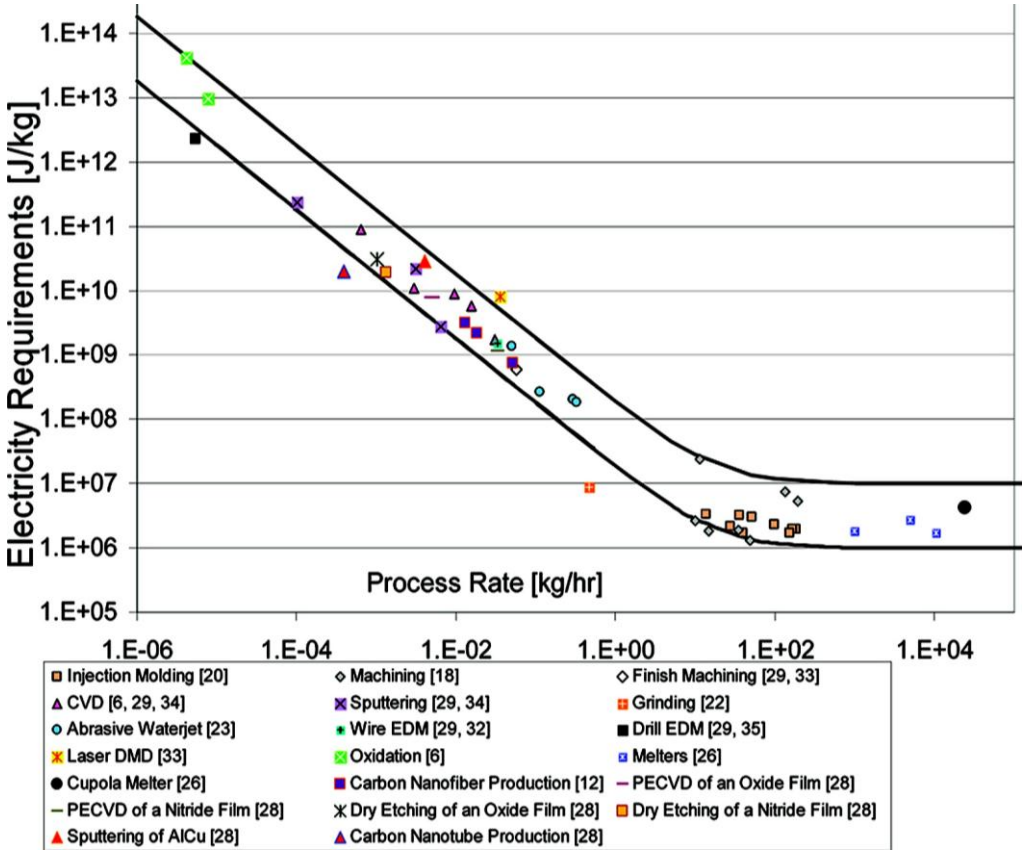

Figure 2-7: Work in the form of electricity used per unit of material processed for various manufacturing processes as a function of the rate of material processing [18]

From figure 2-7, it is apparent that the process of oxidation involves highest energy consumption. In contrast, ultra precision machining such as single point diamond turning (SPDT) involves low energy consumption. SPDT can thus be considered to suit to the long term requirement of a manufacturing method that is socially sustainable and environmentally green.

2.3 Emergence of SPDT to machine brittle materials

At its early stages of development, SPDT was limited to the machining of soft and ductile materials such as aluminium and copper. However, advances in optical and defence systems required precision manufacturing of hard brittle materials coupled with excellent optical properties. The materials used commonly by the optical, semiconductor and opto-electronics industries are silicon, silicon carbide and gallium arsenide. These materials are capable of transmitting light over a variety of wavelengths making them the obvious choice for optical applications over soft materials [19]. This requirement drove an extension of SPDT technology to the machining of hard, brittle materials. The key discovery was that, with careful selection of the process parameters, brittle materials can be machined in the "ductile-regime" where chip removal takes place by virtue of plastic deformation rather than by brittle fracture. Early attempts to understand the ductile behaviour of these brittle materials through interrupted cutting tests are well documented [20-21]. The first mathematical approach for quantifying the machining parameters and to make the SPDT operation more deterministic was presented by Scattergood and co-workers [22]. They developed mathematical formulas to determine the optimum feed rate and highlighted the importance of the critical chip thickness [23]. However, the estimated values of maximum feed rate obtained from their model were only accurate up to a certain extent, depending on the machining conditions [24]. Of late, the ductile-behaviour of brittle materials has been attributed to the high-pressure phase transformation (HPPT) [25] of the brittle material being cut. HPPT causes structural transformations and associated volume changes of the cutting chips. These transformations were not accounted for in earlier models and can contribute up to 25% of the prediction error [26] in the model proposed by Scattergood.

The mechanism of chip formation, the distribution of the cutting forces, the role of material microstructure and crystal anisotropy and the elastic recovery of the machined surface all changes through the transition of the scale of machining from the macro to the nano level. The foremost of these differences is the mechanism of chip formation which shifts from continuous to discrete as the scale goes down. The effect of cutting edge radius is also more important in nanometric cutting as there exists an upper bound edge radius beyond which an undesirable ductile-brittle transition (DBT) [27] occurs. There are a number of other factors which tend to influence the accuracy of SPDT as shown in figure 2-8.

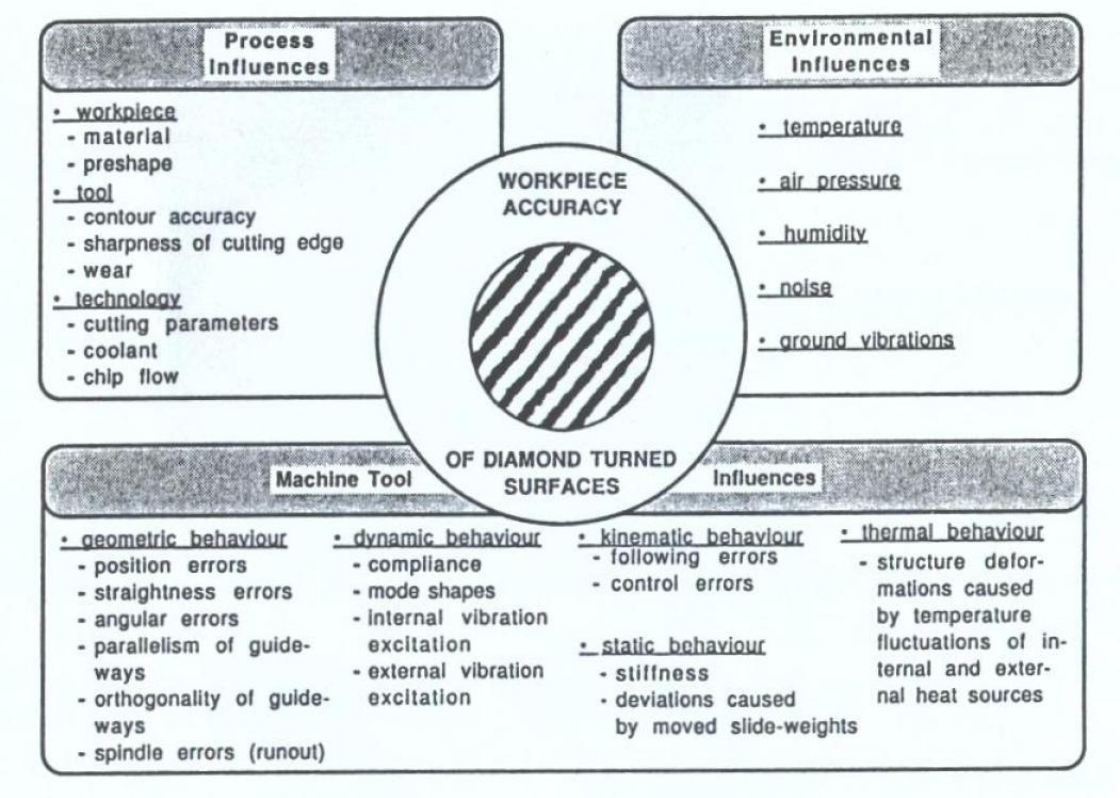

Figure 2-8: Factors which influence the attainable accuracy in diamond machining [28]

The factors affecting the tangible outcome of an SPDT operation i.e. the attainable accuracy can broadly be classified into three categories as follows:

- Process influences : material, tool and technology
- Machine tool influences : geometric behaviour, dynamic behaviour, thermal behaviour
- Environmental influences

Amongst other non-trivial factors shown in figure 2-8, tool wear is an obvious concern as it may cause a sudden transition of the material removal from ductile mode to brittle mode, thereby making a single point diamond machining process non-deterministic. The fracture damage that occurs on the machined surface due to the brittle-regime machining is often called pitting [23]. The following section elaborates details of the so called "brittle-ductile transition" mechanism often observed during nanometric cutting of hard, brittle materials.

2.4 Brittle-ductile transition during SPDT

Unlike most metals, brittle materials exhibit very low fracture toughness which means that they normally fracture with little or no plastic deformation, thus making them difficult to machine using conventional cutting conditions. It is, however, possible to machine such brittle materials using appropriate machining parameters but at a very fine scale of the order of several nanometres. Execution of such a machining process on brittle materials where the chips are generated through plastic deformation rather than fracture is known as ductile-regime machining. The possibility of machining brittle materials in the ductile-regime was first acknowledged by King and Tabor [29] as early as 1954 as a result of observations on frictional wear of rock salt. They observed that, although some cracks and surface fragmentation occurred during heavy abrasive wear,

there was some plastic deformation involved. Similarly, Bridgman *et al.* [30] recognized that a brittle material such as glass exhibited ductility under high hydrostatic pressure. Subsequently, Lawn and Wilshaw [31] observed the same ductile behaviour of glass during the nano-indentation testing which led to the identification of the elastic-plastic transition as explained in figure 2-9.

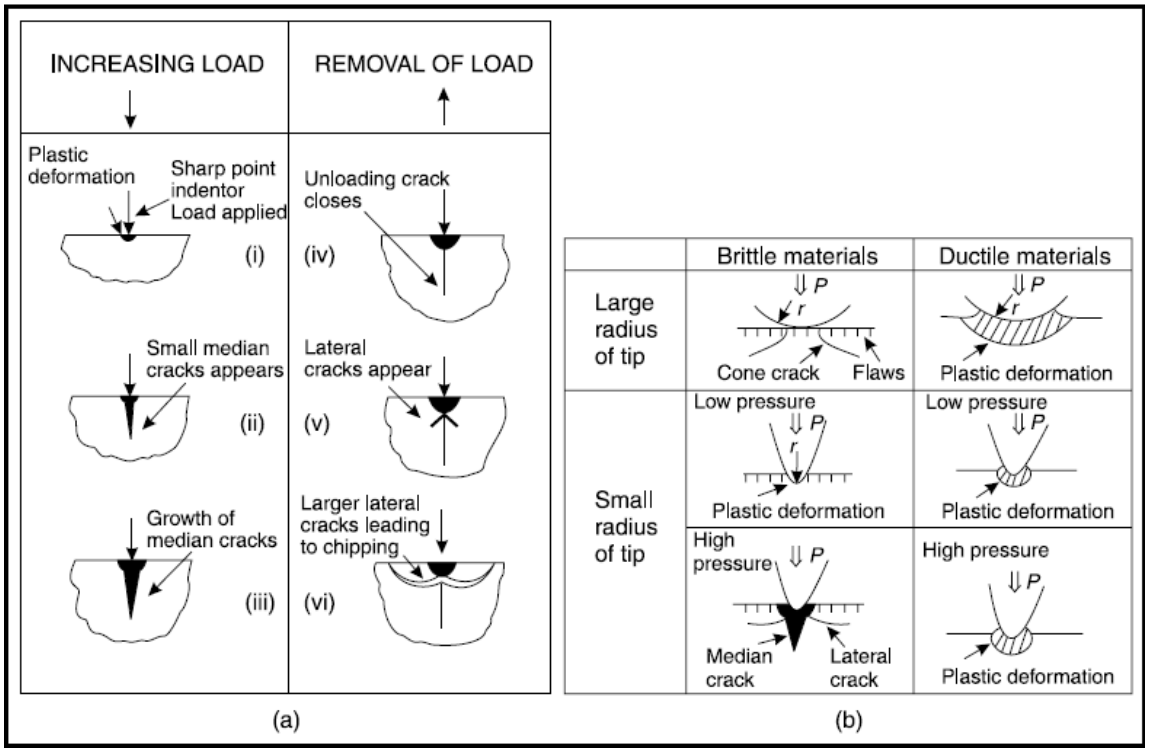

Figure 2-9: Elastic-plastic transition during nano-indentation of brittle materials [32]

An elaborated view of figure 2-9 is shown in figure 2-10 which shows schematically how ductile behaviour causes the material to expand within a radial core which exerts a uniform hydrostatic pressure on its surroundings. This radial core is encased within an intermediate "plastic region" which is surrounded by a so-called "elastic matrix". This qualitative identification of the elastic-plastic response of brittle materials during their nano-indentation was based on the fact that, under the influence of large hydrostatic stresses, almost any material including super-hard substances like diamond can be deformed plastically even at low temperatures [33]. In subsequent work, Lawn and Marshall [34] proposed empirical relationships between the indentation load, *P*, and the

crack length *c* and the fracture toughness and hardness of the substrate in an indentation test:

$$P = \lambda_0 \left[\frac{K_c^{\,4}}{H^3} \right] \qquad 2\text{-}1$$

$$c = \mu_0 \left[\frac{K_c^{\,2}}{H^2} \right] \qquad 2\text{-}2$$

where λ_0 and μ_0 are geometrical constants dependent on the indenter shape, *P* is the indentation load, *c* is the observed crack length, *Kc* is the fracture toughness (resistance to fracture) of the substrate material and *H* is its hardness, which is a measure of its resistance to the plastic flow.

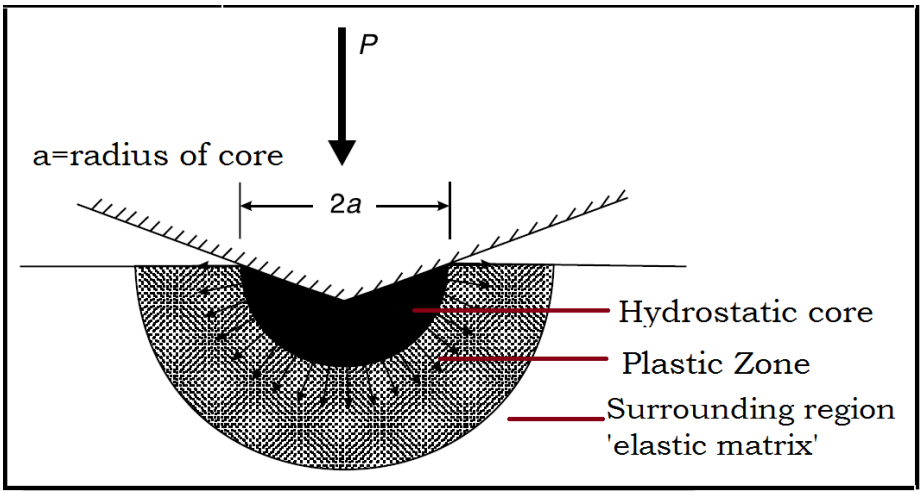

Figure 2-10: Model of elastic-plastic nano-indentation in brittle materials [31, 34]

The fracture toughness of the diamond cubic crystal structure has been suggested to be obtainable from the following formula [35]:

$$Kc^2 = \frac{4GEa_0}{72(1-2\upsilon)} \qquad 2\text{-}3$$

where a_0 is a constant, *G* and *E* are the bulk and elastic modulus, and υ is Poisson's ratio.

Further developments on machining brittle materials in the ductile-regime led to the identification of the critical indent size (CIS) [36], expressed as:

$$CIS = \mu\left[\frac{K_c}{H}\right]^2 \qquad 2\text{-}4$$

where $\mu \propto E/H$.

In the late 1990s, Blake and Scattergood [22] suggested that, despite the dynamic and geometric differences in the material removal mechanism during nano-scratching and a nano-indentation, there are essential similarities in both these processes. They identified that a critical chip thickness *dc* separates the regime of plastic deformation from brittle fracture material removal. Accordingly, they proposed a new machining model to explain the ductile regime machining of brittle materials, shown in figure 2-11 which has been validated later experimentally (as shown in figure 2-12). Since it was proposed, this theoretical machining model has been used widely as the machining mechanism of all brittle materials.

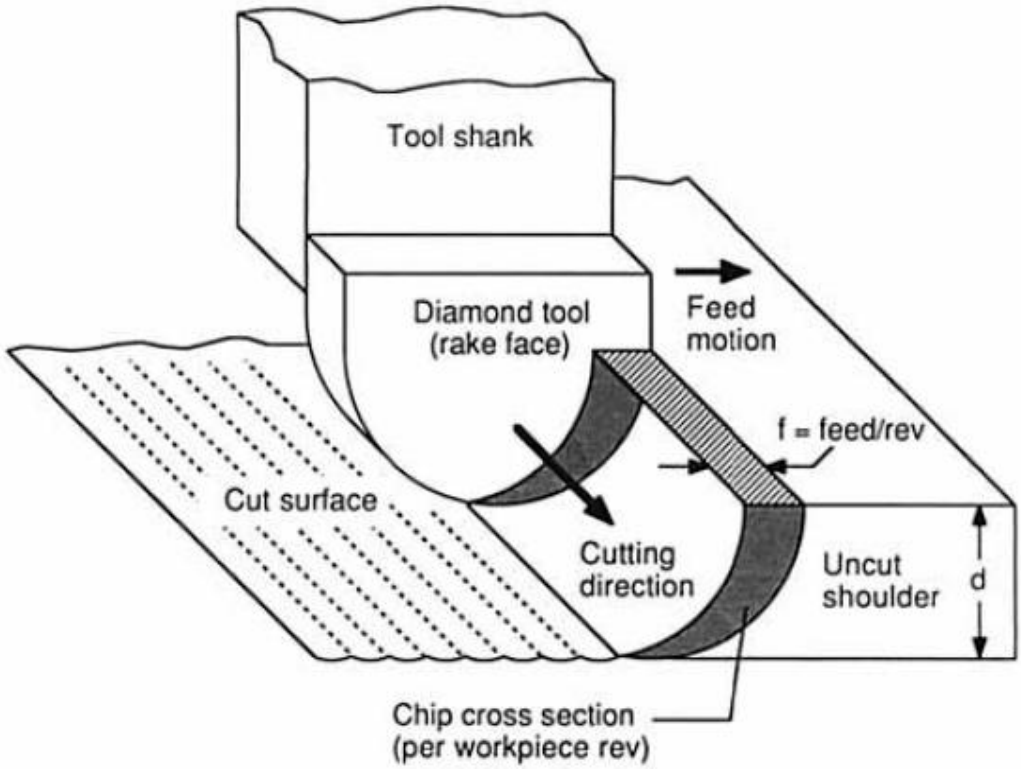

Figure 2-11: Ductile-regime machining model using a round nose cutting tool [22]

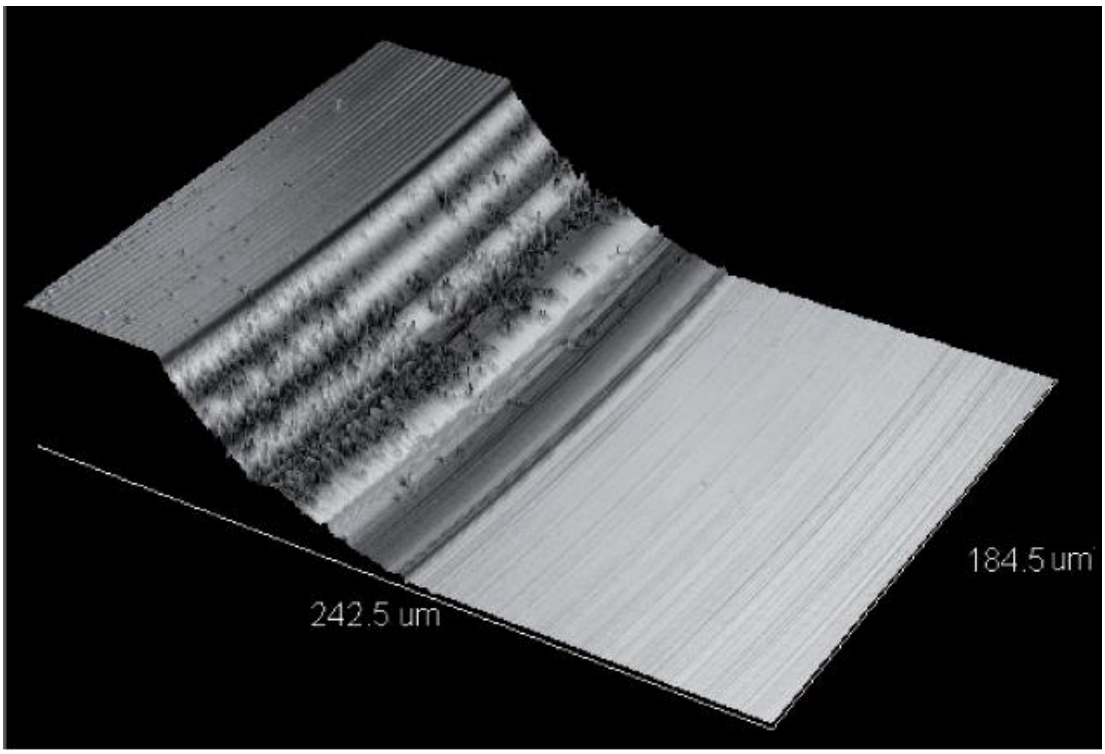

Figure 2-12: Three dimensional image of the uncut shoulder showing an occurrence of brittle-ductile transition in silicon [37]

A schematic cross-sectional view of the brittle-ductile transition is shown in figure 2-13, compared with a molecular dynamics (MD) simulation model from the current work for nanometric cutting of silicon carbide.

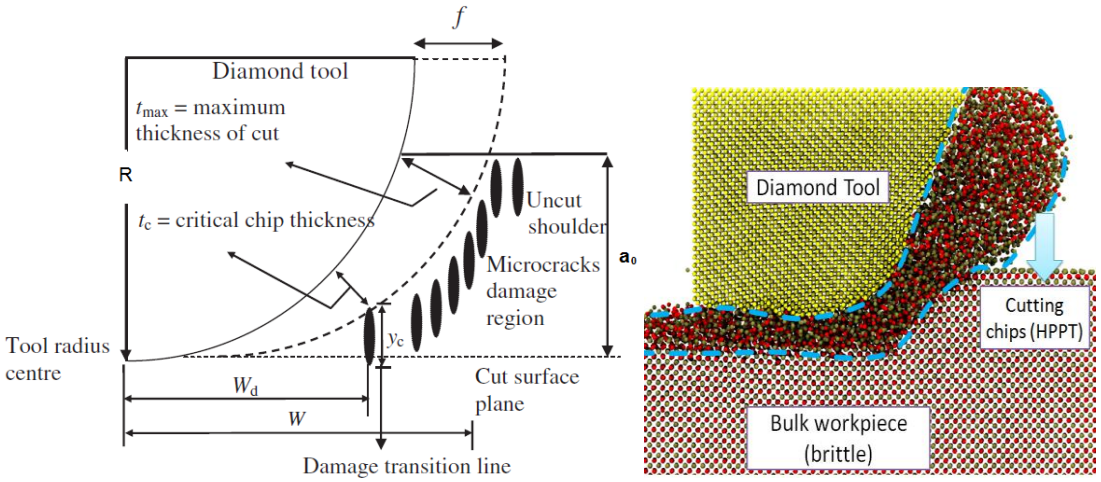

W: Width of cut, W_d: ductile width of the chip, f: feed rate, R: tool nose radius and y_c: critical damage depth, a_0: Depth of cut

Figure 2-13: Ductile-regime machining (a) analytical model [23] (b) MD model

Figure 2-13 illustrates an important dimension, which is the horizontal distance between the critical chip thickness and the tool nose centre denoted here by W_d (sometimes called Z_{eff}). For an SPDT operation, undesirable fracture damage is assumed to initiate at the critical chip thickness (d_c) which propagates up to a depth Y_c. The critical crack length (Y_c) is of particular importance as it varies along the nose radius as per the feed rate of the tool. As shown schematically in figure 2-14, *Yc* does not penetrate below the subsurface damage at smaller feed rates and hence does not affect the final machined surface. However, as the feed is increased, *Yc* moves toward the machined surface and thus cracks begin to propagate into the final cut surface, i.e. the machined surface starts showing undesirable brittle fractures and consequent damage to the machined surface.

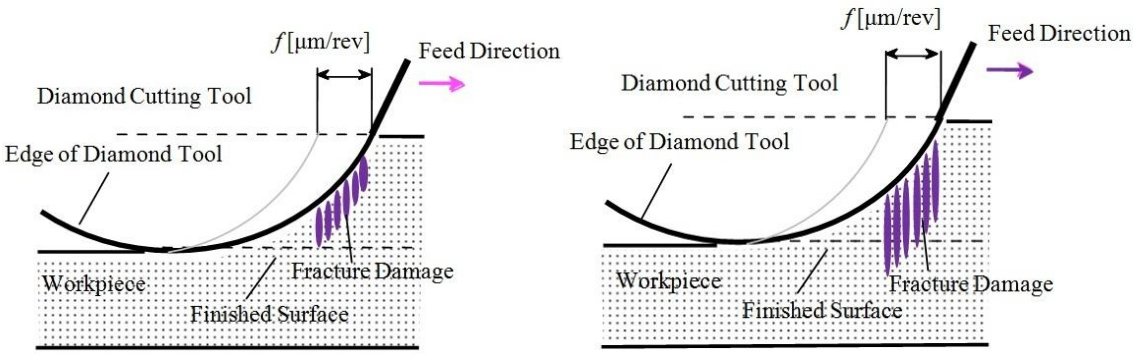

Figure 2-14: Schematic for diamond turning at (a) low feed rate (b) high feed rate

As long as the fracture damage does not penetrate to the final machined surface, ductile-regime machining can be executed consistently. It may be noted here that the fractured material in the remaining region of uncut shoulder is carried away by the tool in the succeeding passes and is therefore of no concern. This phenomenon gives rise to the important fact that materials exhibiting short critical crack lengths are more amenable to SPDT. Also, the critical chip thickness, d_c, represents the condition for any fracture initiation whereas *Yc* is an indicator of the average depth of fracture propagation. Both of these parameters are interdependent in a convoluted fashion depending on the local state of the stress in the cutting zone. Bifano *et al.* [21] suggested that, at smaller feed

rates, the energy required to propagate a crack is larger than the energy required for plastic yielding, so plastic deformation becomes the dominant mechanism of chip formation during ductile-regime machining.

2.5 Theoretical models of brittle-ductile transition

Griffith's criterion suggests that the propagation of brittle fracture involves the balance between the absorption of volumetric strain energy and the release of surface energy i.e. the energy required for plastic deformation is directly proportional to the volume of the material removed whereas the energy for brittle fracture is directly proportional to the cracked surface area. Therefore, the process of brittle material machining can be treated in terms of the minimum energy [26]. Thus, the BDT transition can be determined as the condition at which it will take more specific cutting energy to execute ductile-regime machining than it takes to execute brittle-fracture dominated machining. In a model using this approach [38], the consumption of energy involved during the machining of brittle materials was described as a function of the properties of the workpiece material, tool geometry and process parameters. Finally, the BDT could be identified in terms of a critical undeformed chip thickness.

Earlier, Nakasuji *et al.* [39] proposed a model of the brittle-ductile transition (BDT) by considering the forces giving rise to slip and cleavage as shown schematically in figure 2-15. They suggested that plastic deformation occurs in front of the cutting edge when the resolved shear stress exceeds a certain critical value in the direction of the shear plane, whereas cleavage takes place if the resolved tensile stress exceeds a certain critical value in the direction normal to the cleavage plane.

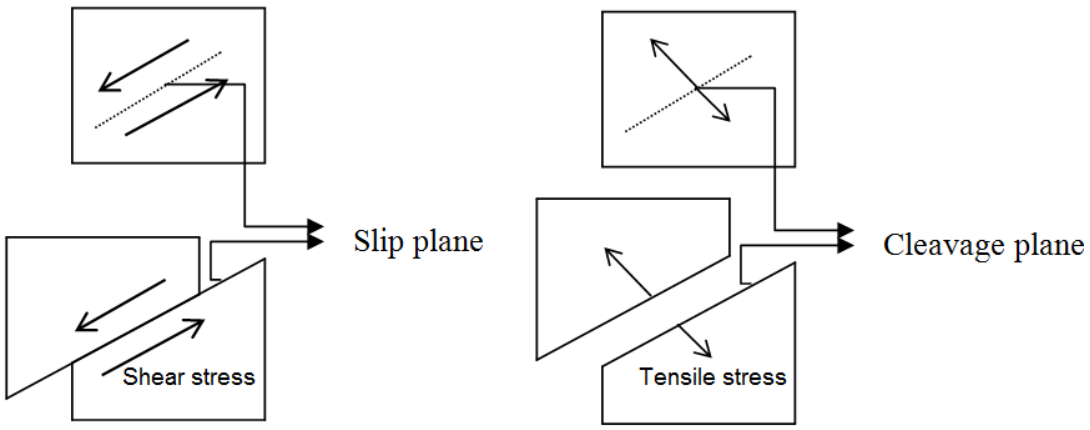

Figure 2-15: Slip and cleavage mechanisms of chip removal [39-40]

They also highlighted the importance of the size effect that exists at the nanoscale. They claimed that the critical values of stress for plastic deformation and cleavage are also governed by the density of lattice defects and dislocations present in the work material, a level of which exists in all practically available materials. With smaller uncut chip thicknesses, the size of the resulting critical stress field is small enough to avoid cleavage initiated at the defects, but, with larger uncut chip thicknesses, the larger critical stress field allows for sufficient nuclei for crack propagation, which initiate from defects within the material, as shown schematically in figure 2-16.

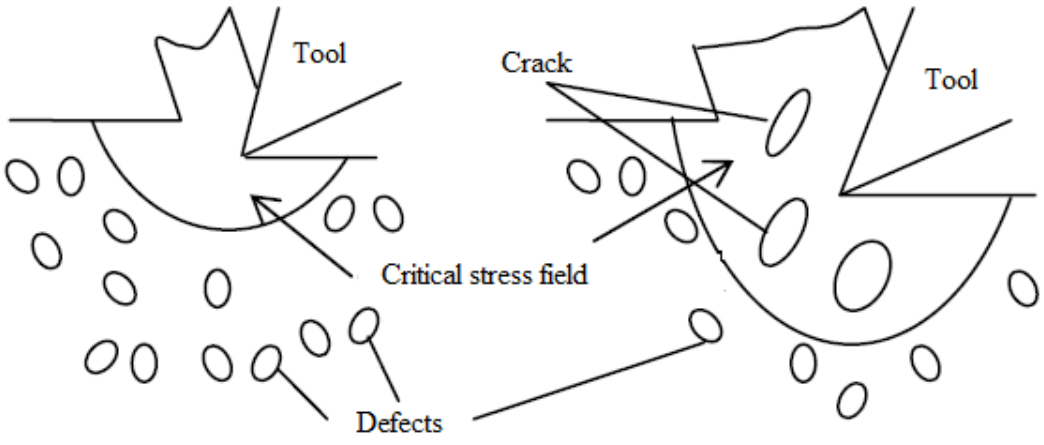

(a) small depth of cut (b) large depth of cut

Figure 2-16: Schematic representation of size effect for small-scale chip removal [39]

Conversely, the theory of plasticity suggests that the magnitude of hydrostatic stress determines the extent of plastic deformation prior to fracture, which in turn determines

material's ductility. Therefore, when sufficient hydrostatic pressure is generated by the tool edge radius in the cutting region, plastic deformation is more likely to occur than crack generation even at lower temperature, and therefore, ductile mode cutting of brittle materials can be achieved. The above proposition is considered to be the classical theory of the brittle to ductile transition in diamond turning. Indeed it has been cited [41] as a main reason for the requirement of a cutting edge radius on the diamond cutting tools rather than sharp-edged tools as shown in figure 2-17.

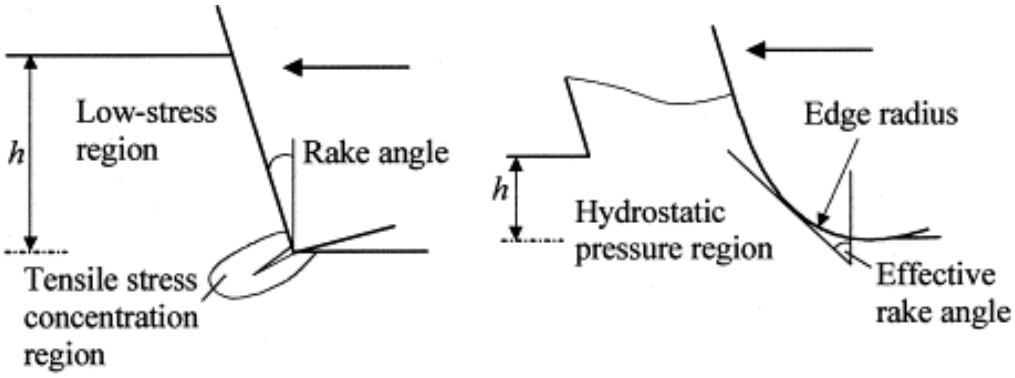

(a) Brittle regime (b) Ductile regime

Figure 2-17: Schematic illustration of the influence of the edge radius on SPDT [41]

Providing an edge radius on the cutting tool causes two particularly significant phenomena:

- edge roundness decreases the stress concentration and produces a hydrostatic stress field in the cutting region.
- the effective rake angle caused by the small radius becomes large and negative and, as a result, material in front of the cutting edge is pushed downward and compressive stresses (hydrostatic stress field) become dominant.

A similar effect was also observed during a molecular dynamics (MD) simulation study as shown in figure 2-18.

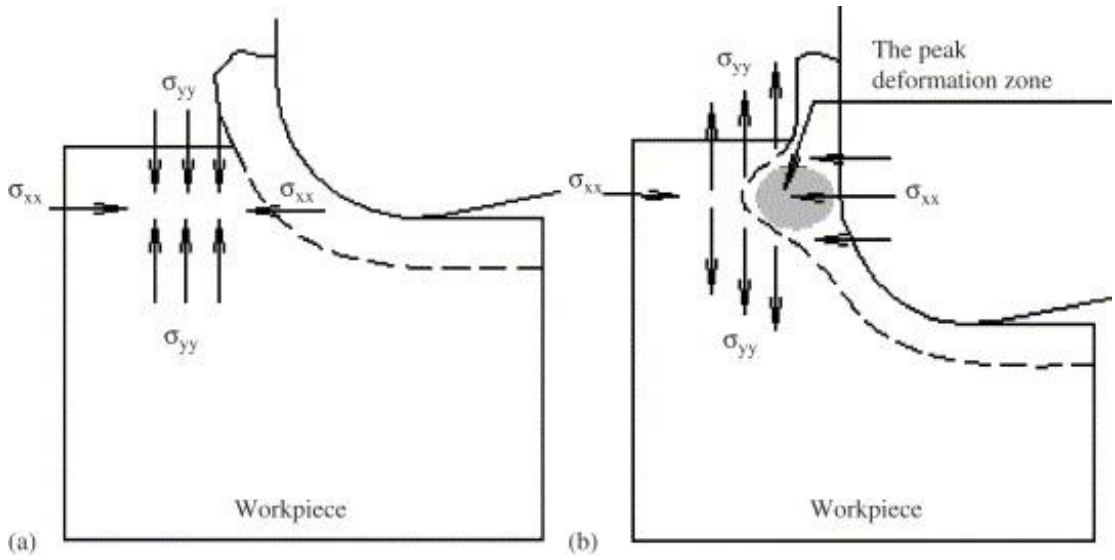

Figure 2-18: Chip formation modes (a) ductile (b) brittle [27]

For semiconductors, a strong correlation has been found between their nano-indentation hardness and their metallization pressure [42-43]. The metallization pressure (Herzfeld-Mott transition [44]) is the value under which brittle semiconducting material becomes metallic, i.e. the band gap vanishes because of the closure of valence-conduction band gap due to overlap of wave functions and hence delocalization of the valence electrons. It has been suggested that this process is facilitated by a high pressure phase transformation (HPPT) which has been demonstrated to be the outcome of shear strain rather than simple hydrostatic strain i.e. predominance of bond-bending over bond-stretching. Gilman [42-44] suggested that it is a change in bond angle rather than a change in bond length which appears to cause the metallization of semiconductors as observed during polishing of diamond [45]. He explained that, in a diamond cubic lattice, bond length can only bring about a change in volume, not necessarily shape, whereas a change in bond angle can change both shape and volume. Topologically, the diamond cubic structure (Si-I) is quite similar to the β-tin structure (Si-II) form of silicon. It is shown schematically in figure 2-19 that compressing the Si-I structure on the tetragonal axis by 50% will result in the transformation to the Si-II structure or

stretching of the Si-II by 200% will provide the Si-I lattice structure of silicon. During the process of transformation from Si-I to Si-II structure, the percentage change in bond angle can be up to 37% whereas the bond length varies only up to 4.4%.

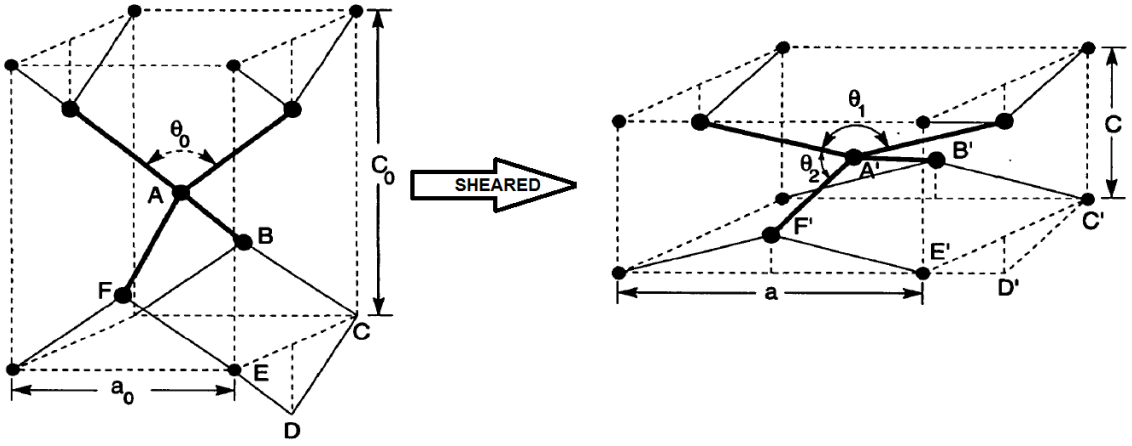

Figure 2-19: Shear transformation of Si-I (brittle) silicon to Si-II (ductile) silicon [44]

2.6 Simulation-based studies on SPDT

Yan *et al.* [46] have simulated SPDT of silicon using the FEM method and demonstrated two important phenomena as follows:

- Increase in the cutting edge radius causes a decrease in the cut chip thickness and a corresponding increase in the thrust force
- Lowering the cutting edge radius (below 200 nm) shifts the high temperature zone from the tool rake face to the tool flank face resulting in the transition of the wear pattern from crater to flank wear

Similarly, Patten and Jacob [47] have simulated SPDT of single crystal 6H-SiC by employing a Drucker-Prager (pressure sensitive) yield criterion in a commercially available FEM package. They found that the cutting forces agreed with those experimentally measured only under ductile-regime machining conditions and not brittle-regime. This limitation was attributed to the criterion used for yielding which does not include a fracture criterion or, by implication, a brittle material removal

mechanism. While FEM is a useful tool for gaining some insight into the cutting pressure under ductile-regime conditions and the effect of cutting edge radius, some of the important mechanisms, such as high pressure phase transformation, combined influence of the crystal anisotropy and cutting direction, mechanisms of tool wear, cannot be studied suitably using standard FEM simulation. For this reason, the contribution of molecular dynamics (MD) simulation to the field of SPDT is considered to be pivotal. At this time, MD simulation has already been recognized as a powerful simulation technique for giving insights into a variety of aspects of the material removal process.

MD simulation originated through the pioneering work of Alder and Wainwright in the late 1950s [48] but its adaptation to ultra precision machining took place at LLNL, USA during the late 1980s [49]. Belak, Shimada and Ikawa [50] pioneered the concept of MD in the framework of nanometric cutting followed by the work of Voter *et al.* [51]. Since then, Shimada and Ikawa [52], Rentsch *et al.* [53], Komanduri *et al.* [54], Luo *et al.* [55] and Cai *et al.* [56] have contributed significantly and have laid a sound foundation for the study of nanometric cutting processes using MD simulation.

In their seminal study, Belak *et al.* [57] reported the amorphisation of silicon chips and raised the possibility of melting of silicon under the influence of heat generated during the cutting processes. They also observed that the simulated silicon atoms cling quite tightly to the rake and flank faces of the cutting tool. This adherence of workpiece atoms to the cutting tool has also been observed by Maekawa *et al.* [58] for machining of copper. Ikawa *et al.* [50] explored the limits of thickness of cut attainable during the process of diamond turning. Combining their simulation work with the experimental facilities of LLNL, USA they successfully obtained 1 nm size of cut chip thickness on copper and demonstrated the feasibility of nanometric size chip removal through SPDT.

By converting an atomistic model into the equivalent continuum model, Inamura *et al.* [40] observed a high compression in the primary shear zone rather than a concentrated shear stress. They used the Plandtl-Reuss equations to suggest that the deformation of the workpiece in the primary shear zone could be due to shear plastic deformation resulted from levels above the yield shear stress. Nozaki *et al.* [59] used the Stillinger-Weber potential energy function to compare the performance of machining silicon on different planes to that of machining metals. They found that, unlike metal, the plastic deformation in silicon is highly confined resulting in the brittle nature of silicon. Interestingly, the machined surface was found to be smoother with increasing depth of cut.

Shimada *et al.* [60] examined the brittle-ductile transition phenomenon in silicon using MD simulation. Underneath, and in the vicinity of, the cutting tool (included angle 90°) they observed the movement of voids. They also found elastic and thermal shock waves to be generated and propagate in the substrate. However, when the depth of cut was in the nanometre range, they found that the potential energy was too small for the shock wave to supply the necessary energy to initiate a crack or to propagate a pre-existing crack. Komanduri *et al.* [61] have cited the work of Tanaka and Shimada who used a Tersoff potential energy function to simulate the cutting of silicon using MD. They, too, found that dislocations were absent in their simulations and consequently suggested that inelastic deformation *via* amorphous phase transformation are energetically more favourable mechanisms than plastic deformation involving the generation and propagation of dislocations.

2.7 Process and environmental variables in SPDT

The process variables of SPDT make it a difficult task to execute ductile-regime machining on brittle materials consistently. Some of these factors are discussed below:

2.7.1 Cutting edge radius, undeformed chip thickness, depth of cut and feed rate

Arefin *et al.* [62] have stressed the importance of the tool cutting edge radius and the maximum undeformed chip thickness of the workpiece. Based on their experimental work on silicon and a molecular dynamics simulation model [56], they suggested that the following condition must be satisfied in order to obtain ductile-regime machining of silicon:

807 nm > Cutting edge radius > Maximum undeformed chip thickness

They claimed that, as the tool cutting edge radius increases, the shear stress in the workpiece material around the cutting edge decreases down to a lower level, at which the shear stress is insufficient to sustain dislocation emission in the chip formation zone, and then crack propagation dominates [27]. Consequently, the chip formation mode changes from ductile to brittle which adversely affects the tool life. It may be recalled here that a tool with a very sharp edge may wear out quickly because of stress concentration and hence a finite edge radius is always preferable. Also, when the uncut chip thickness is less than the tool cutting edge radius, the thrust force increases more rapidly than the tangential cutting forces [63]. Recently, Patten and co-workers have examined the critical depth of cut at which ductile to brittle transition (DBT) occurs in single crystal 4H-SiC and single crystal 6H-SiC. They reported that 6H-SiC exhibits a DBT depth of only 70 nm [64] against the 4H-SiC where the DBT depth is up to 820

nm [65]. Similarly, the DBT depth of CVD 3C-SiC (polycrystalline) was found to be as 550 nm [66] whereas d_c in silicon was experimentally found to be 20-40 nm, depending on the crystal orientation [67].

Leung *et al.* [68] proposed that there exists a relationship between the critical depth in an indentation test and the critical depth of cut in machining. It must, however, be noted that, despite the similarities between the nano-indentation process and the nanometric cutting process, there are many differences between the two, some of which are summarised in table 2-2.

Leung *et al.* [68] also studied the influence of depth of cut during nanometric cutting of silicon experimentally. Using varying depths of cut, they observed a sharp transition of material removal from ductile deformation to brittle fracture. Based on further experimental work, they were able to plot a relation between the depth of cut and feed rate to distinguish brittle regime machining from ductile regime machining. Accordingly, they proposed a schematic diagram highlighting this regime map, as shown in figure 2-20.

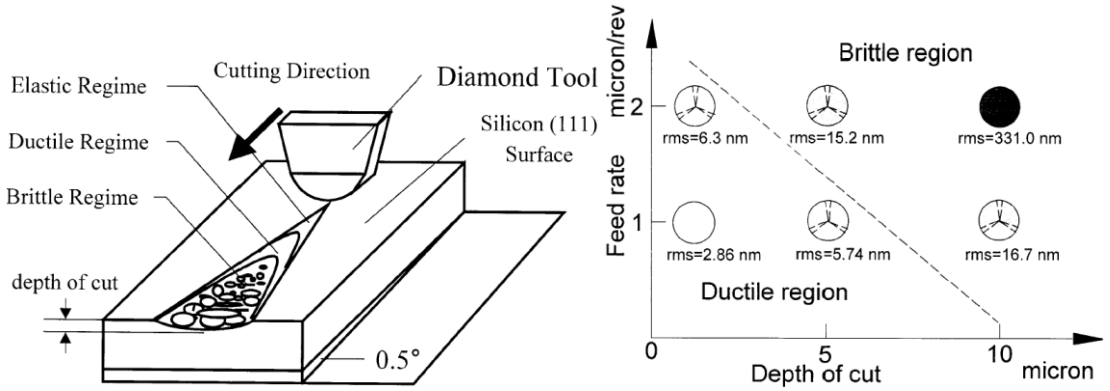

Figure 2-20 : Influence of depth of cut and feed rate on ductile-brittle transition [68]

Table 2-2: Differences between nano-indentation and nanometric cutting

S.No.	Differences	Nano-indentation	Nanometric cutting
1	Stress dominance	Compressive stress (Hydrostatic stress)	Shear stress (Deviatoric stress)
2	Effect of the process	Induced compressive strain which results in the pronounced change in the bond length	Induced shear strain results in pronounced change in the bond angle
3	Strain energy field	Dimension of the indentation is considered a criterion	Cognate to nano-indentation, depth of cut is normally chosen as a criterion
4	Contact of the tool	Point contact	Line contact
5	Process outcome	Pile-up formation (may be of irregular shape)	Both pile up and cutting chips (continuous or discontinuous type)
6	Wear of the tool	Trivial	Non-trivial
7	Cutting action	Role of the cutting edge radius is dominant during a nano-indentation process	Role of tool rake face is more dominant during the nanometric cutting
8	Direction of execution	On the same cutting plane, nano-indentation is usually done in the direction normal to the plane	On the same cutting plane, cutting is done along the direction of the cutting plane.
9	Duration of action	Indentation depth is usually the parameter used to specify the duration which is usually small in magnitude	Track length is usually specified to quantify the cutting length which is relatively quite large in magnitude.
10	Forces	Unidirectional loading and unloading forces are used to characterize the process	Two forces namely, tangential cutting forces and thrust forces are used to characterize the process.
11	Toolpath	The tool enters the substrate and retracts along the same tool path	Usually the tool is retracted at a different tool path otherwise; the finished surface may be destroyed by the tool.
12	Application	To measure the hardness or elastic modulus of the sample	To measure specific cutting energy and/or study the chip flow process

Komanduri *et al.* [61] used MD simulation to examine nanometric cutting of silicon. They suggested that a decrease in the *w/d* ratio (i.e. the ratio of width of cut to depth of cut) caused an exponential increase in the side flow of the material. Based on the simulation results, they suggested that a reduced width of cut will result in a reduced deformed layer depth on the machined surface of amorphous silicon. Also, some surface damage on the machined surface of silicon was found to be inherent with the nanometric cutting process irrespective of the depth of cut, width of cut and rake angle used. Based on these observations, they suggested that the difficulty in SPDT of silicon is not attributable to high cutting forces or specific cutting energy but to the problems of tool wear and subsurface deformation underneath the cutting tool.

2.7.2 Influence of the coolant

A coolant is normally used during any machining operation. Irrespective of the mode to supply i.e. mist, spray or as a layered coating, the primary functions of a coolant are:

- cooling
- lubrication
- assisting in chip removal from the cutting zone

As shown schematically in figure 2-21: cooling reduces the thermal load on the workpiece and the cutting tool; lubrication reduces the frictional contact between the tool and the workpiece; and viscous drag by the liquid coolant removes chips from the cutting zone of the workpiece. There is a variety of coolants used in machining, as shown in the bottom panel of figure 2-21. A comparison of water based coolants and oil based coolants has shown that water is a superior coolant to kerosene or oil based formulations for machining silicon [69]. Similarly, it has also been reported that cryogenic environments can significantly improve the life of the diamond tools [70].

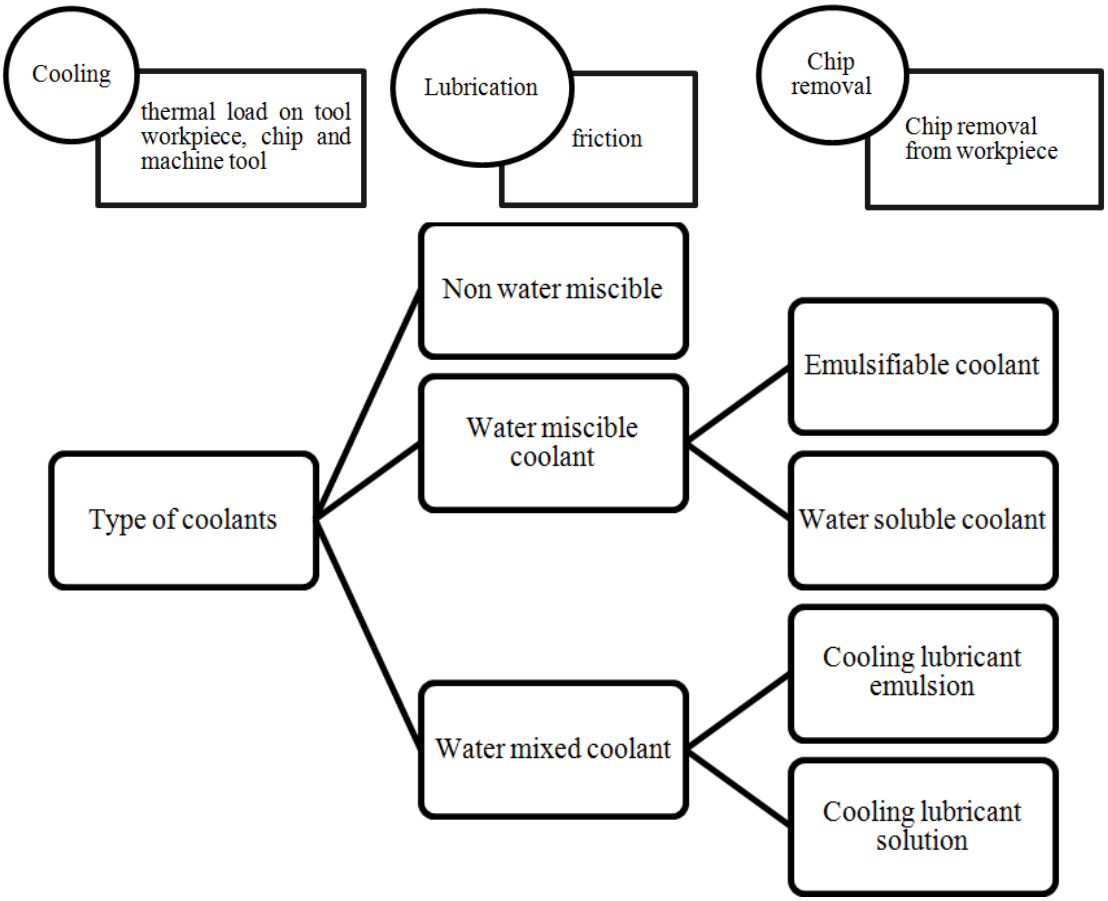

Figure 2-21: Role and type of coolants used in machining

Rentsch *et al.* [53] have studied the influence of cutting fluid using MD simulation. They considered a hypothetical cutting fluid around a copper block which was modelled using a Lennard-Jones interaction potential energy function. A snapshot from their work is shown in figure 2-22, where the effect of coolant on the chip generation process is demonstrated.

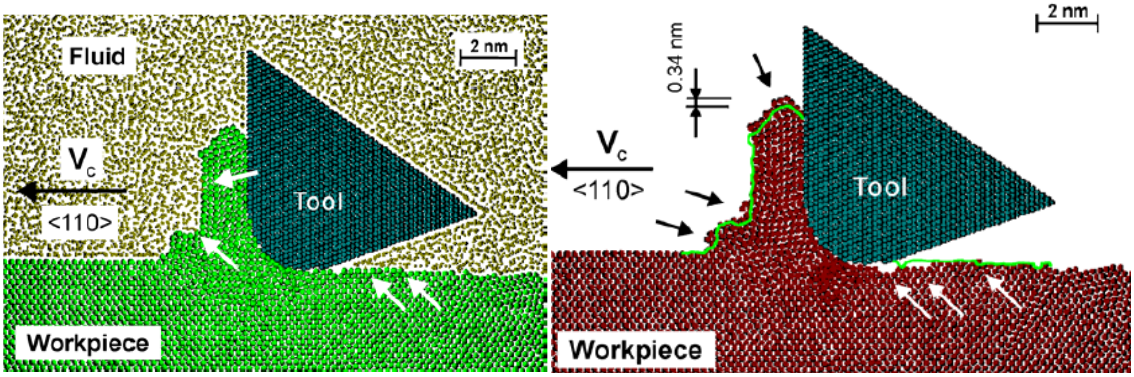

Figure 2-22: MD simulation of nanometric cutting of copper involving coolant [71]

Rentsch *et al.* [53] explained that the stress distribution in the workpiece remained unchanged irrespective of the cutting environment, but, conversely, the temperature distribution in the machining zone changed, albeit only in the area of local contact between the tool and workpiece. Thus, coolant can have a significant influence on the process of nanometric cutting.

2.7.3 Tool wear

Paul *et al.* [72] have presented a dedicated review on the wear of diamond tools during SPDT operations. With only a few exceptions, they proposed a hypothesis in which rapid chemical wear of the diamond tools was attributed to the presence of unpaired *d-shell* electrons in the substrate. They explained that the wear of diamond may be a consequence of any, or a combination of the following mechanisms:

- Adhesion and formation of a built up edge
- Abrasion, microchipping, fracture and fatigue
- Tribothermal wear and
- Tribochemical wear

Another, similar classification of the wear of cutting tools in general includes the following mechanisms [73]:

- Diffusion wear: Influenced by the chemical affinity between the workpiece and the cutting tool
- Abrasive wear: Influenced by the hardness of the workpiece and the cutting tool
- Oxidation wear: Influenced by the affinity of the cutting tool to the oxygen
- Fatigue wear (static or dynamic): Influenced by the thermo-mechanical effect and its duration

- Adhesion wear: Occurs at relatively low machining temperature when there are strong intermolecular attraction between the atoms of the cutting tool and the workpiece.

Wong [74] used around 150 single crystal diamond tools and classified tool wear into into six categories: i.e. normal wear, chipping, setting problems, line effects, chip dragging and fracture by inclusions in the work material. He noticed that diamond tools with shorter tool lives exhibited broader infrared absorption at 1365 cm^{-1}. Based on this observation, he postulated that the presence of the nitrate bond (N-O) in diamond tools induces unfavourable internal strains within the crystal lattice which may shorten the tool life.

Jasinevicius *et al.* [75] conducted an experiment in which they machined a single crystal silicon wafer with a worn diamond tool. Their results indicated that the worn tools can generate high stress levels with an increase in the penetration depth. If the compressive stresses are high enough and the tensile stresses are low enough, the onset of the phase transformation and then plastic deformation takes place prior to cracking.

Li *et al.* [76] noted that diamond tool wear starts with the appearance of nanoscale grooves on the tool flank, as shown in figure 2-23. These grooves form secondary cutting edges which tend to change the cutting mode from ductile to brittle fracture, thus further accelerating wear.

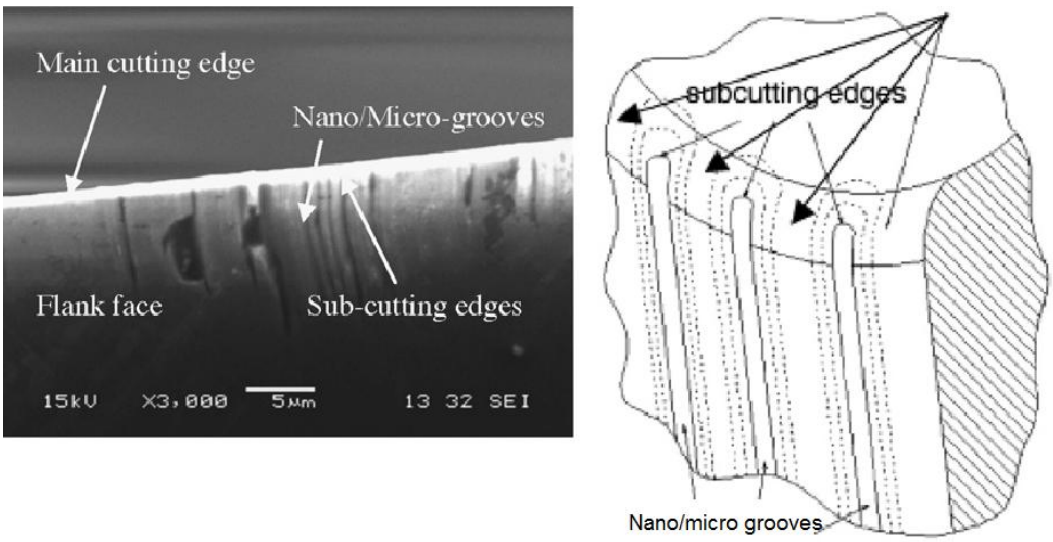

Figure 2-23: SEM image and schematic of the groove wear observed during SPDT [77]

Khurshudov *et al.* [78] conducted a nanoscratching experiment on a silicon wafer using a diamond AFM tip to measure the wear rate. They suggested that the diffusion rate of carbon from the diamond into silicon was quite high, and that this explained the high wear rate during the interaction of diamond and silicon. In addition, tool geometry, crystal orientation and the quality of the diamond gem have all been found to influence tool wear significantly [69, 79-81]. Also, natural mono-crystalline diamonds always contain a range of defects such as cracks, inclusions, lattice defects (including twins and dislocations) and impurities (including metal atoms, hydrogen, nitrogen or oxygen) [82]. Tool flank wear width (Vb) is normally used to quantify the flank wear, which is more pronounced during diamond turning of brittle materials.

2.8 Summary

This chapter has presented a critical literature review on the state-of-the-art of MNM processes. The survey traces the sharp transition in manufacturing accuracy from macro-manufacturing to nano-manufacturing, which occurred during the late 1960s. The branch of manufacturing dedicated to achieving nanometre level accuracy in

manufacturing is now recognized as ultra precision manufacturing. One key factor in this development is that machining by mechanical means, laser assisted machining and injection moulding all consumes less electrical energy than any other ultra precision manufacturing process. Developments in materials science and the corresponding requirements in advanced technology call for cost-effective manufacturing methods and, accordingly, the need for ultra precision machining of brittle materials arises. Various theories and postulates have been advanced over the last few decades regarding the ductile-regime machining of brittle materials and the potential problems of tool wear arising from the SPDT of hard brittle materials and these have been thoroughly reviewed.

SPDT has been shown to be among the most efficient material removal processes for brittle materials. Experiments have proved that samples of silicon machined using SPDT exhibit a surface quality corresponding to that achieved by optical polishing, i.e. an R_a = 0.6 nm and Peak to valley (PV) i.e. R_{max} = 6 nm, better than that obtained through grinding i.e. R_a = 7 nm and 64nm < R_{max} < 148 nm [83]. This performance is advanced further with the fact that SPDT offers flexibility of generated form, better step-definition, deterministic form accuracy and economy of fabrication time. Thus, SPDT is an obvious choice over other ultra precision manufacturing processes to machine hard, brittle materials. It was identified that the machining variables, such as critical undeformed chip thickness, feed rate, cutting edge radius and depth of cut, can all play an important role in influencing the machining regime but is interrelated in a very complex and dynamic manner. It was also recognized that, even when the SPDT operation is carried out in a controlled environment while keeping all the above variables fixed, the outcome of the process can still vary. Three reasons were identified for this; crystal anisotropy of the workpiece, influence of coolant and wear of the

cutting tool. Taken with the high tooling cost, short tool life causes undesirable ductile-brittle transition on the workpiece and consequent deterioration in the quality of the machined surface. It has finally been suggested that there is a strong need to understand further the wear mechanism of diamond tools during the machining of hard, brittle materials.

Chapter 3 - Major factors influencing ductile-regime machining

3.1 Introduction

The mechanism of nanometric cutting of hard, brittle materials is influenced by a number of variables such as machine tool performance, machining conditions, materials properties, and cutting tool performance (material microstructure and physical geometry of the contact). In this chapter, the focus is on how fundamental material properties and physical geometry of the cutting tool may alter the machining performance even when the SPDT is carried out in a controlled fashion. The purpose of this focus is to establish what understanding of machining conditions is required to setup a machining operation or simulation.

This chapter firstly identifies one common thing that all hard, brittle materials share. With an emphasis on the fundamental atomic understanding, the subsequent section characterizes the hard, brittle materials based on their hardness and Young's modulus. Towards the end, this chapter reviews the considerable body of research concerning the influence of crystal anisotropy and the influence of rake angle on the performance of nanometric cutting.

3.2 Composition cycle of hard, brittle materials

Principally, ultra-hard materials, materials whose hardness is attributable to covalent bonding, can be represented using the "composition cycle" shown in figure 3-1. This cycle consists of the four elements i.e. carbon (C), boron (B), silicon (Si) and nitrogen (N), the combination of any of which can produce a three-dimensionally covalently bonded compound exhibiting ultra-high hardness, e.g. Diamond, Cubic BN, SiC, Si_3N_4, B_4C and the recently recognized C_3N_4.

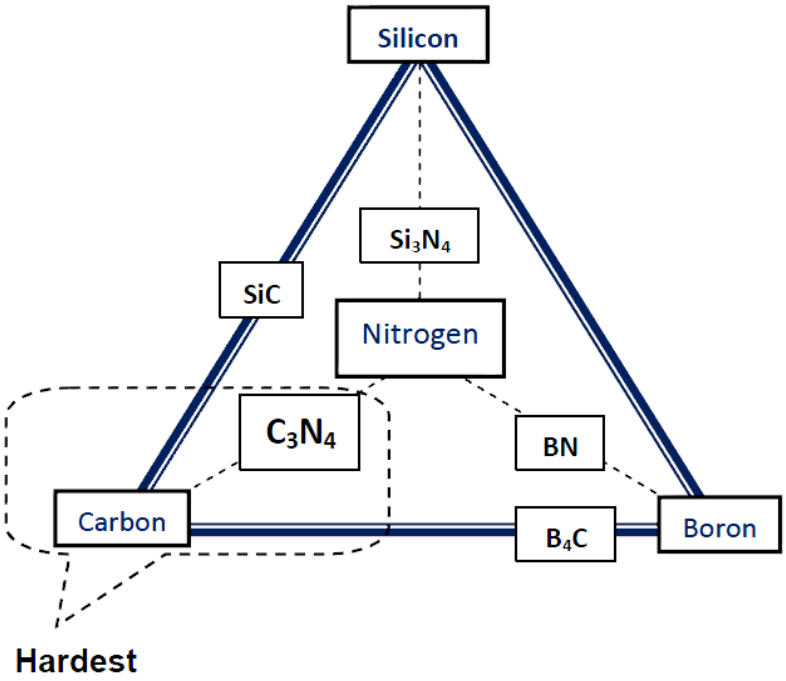

Figure 3-1: Composition cycle of ultra-hard materials (C–N–B–Si) [84]

Under ambient conditions, nitrogen is gaseous with only diatomic covalent bonds while boron, silicon and diamond naturally form 3-dimensionally covalent solids [84]. Due to its abundance on the earth crust and capability to form stable, solid oxides, silicon is very widely used, not least the electronics consumer market (because of its semi-conducting properties) [85] while, despite its natural rarity and difficulty to synthesis, the industrial use of diamond originates from its exceptional properties, such as thermal conductivity, wear resistance and its ability to form extremely sharp cutting edges [86]. Both diamond and silicon are classed as hard and brittle [87-88] due to their sp^3-bonded nature.

Two commercially available materials from the composition cycle, diamond (C) and cubic boron nitride (CBN), possess ultra high hardness (attributed both to their sp^3 bonding and relatively short bond length) and, for this reason, they are frequently used to manufacture cutting tips. While diamond resides in a cubic lattice structure, CBN possess a zinc-blende structure having boron atoms arranged in tetrahedra and nitrogen

atoms in the centres of these tetrahedra. Although, the chemical bond between the two carbon atoms in diamond is stronger than the corresponding iso-electronic bond between nitrogen and boron atoms, it is anticipated that cubic boron nitride "CBN" could be an alternative cutting tool material for high-temperature nanotribology applications, owing primarily to its superior thermal and chemical stability over diamond [89]. This is because of the differences in the surface chemistry of diamond and CBN. In the cubic crystal lattice of CBN, boron atoms have only three valence electrons on the surface while nitrogen atoms have five. However, two of these five electrons of nitrogen can form a stable pair, leaving three valence electrons for bonding with boron. Conversely, the diamond cubic lattice has four valence electrons; thereby a maximum of three electrons on the surface can have stable bonding between them. Consequently, there is the possibility that the remaining one or two electrons of each surface atom in diamond can bond with other atoms like iron, nickel and even silicon in a tribological environment, leading to chemical wear of the cutting tool. In contrast to diamond, CBN has fewer dangling bonds on the surface which makes its more resistant to chemical wear.

Figure 3-2 shows a property map of various hard materials with respect to their hardness and elastic modulus. Among the materials being investigated in this thesis, it can be seen from figure 3-2 that nanocrystalline diamond exhibits the highest hardness and Young's modulus followed by CBN, silicon carbide and, finally, silicon.

Whilst elastic modulus and hardness are useful assessing cutting tool material performance, their ratio has been highlighted as being of particular importance. For example, nano-scratching tests performed on a wide range of materials from polymers to metal have revealed that the extent of plastic deformation increases with increasing *E/H* ratio [90]. On the basis of such tests, it has been concluded that *E/H* provides a good criterion to assess the machinability of a material [91]. It has, however, since

emerged, that, even when if the *E/H* ratio along a certain crystal direction is high, this may not necessarily provide the plastic response required for good machining [37].

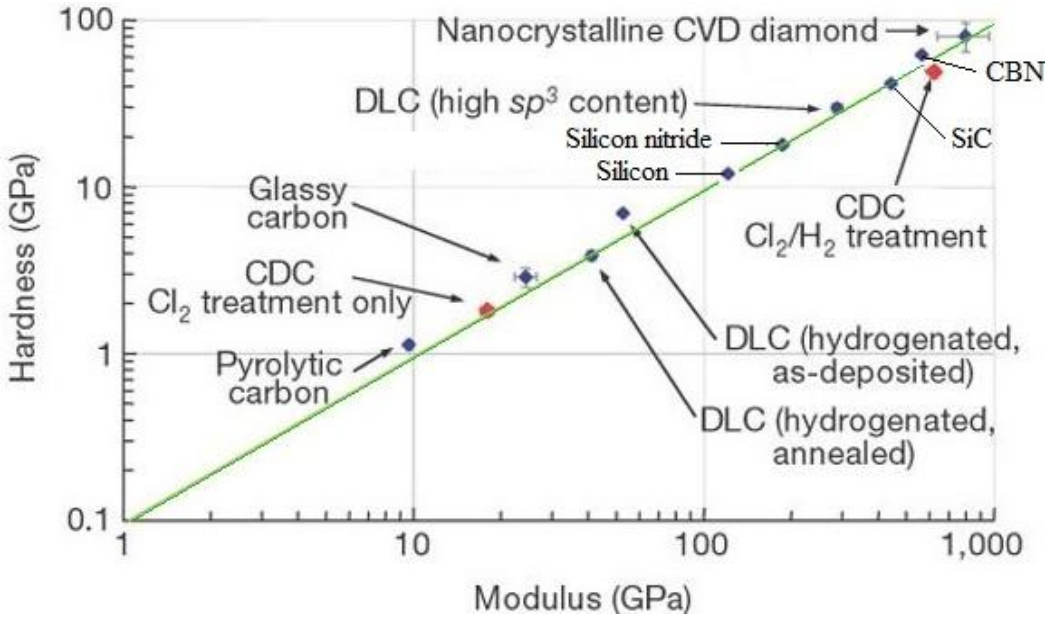

Figure 3-2: Variation in the hardness and Young's modulus of various materials [92]

This directional sensitivity may occur if there is a large difference in the hardness and transition pressure along a particular direction which may result in the initiation of undesirable fragile cracks. Puttick *et al.* [93] have noted, that, in such circumstances, yielding is expected rather than a crack propagation below a linear dimension Y_c. Mathematically, this may be expressed as follows:

$$Yc = \frac{\alpha ES}{\sigma_y{}^2} \qquad 3\text{-}1$$

where E is young's modulus, σ_y is the yield stress, S is the specific energy required to propagate a crack and α is a numerical parameter which depends on the type of process involved such as indentation, compression or scratching. Also, both diamond and CBN are capable of cutting silicon and even SiC, although the commercial availability of diamond as a cutting tool has promoted its significantly greater usage than CBN [89, 94]. Komanduri *et al.* [95] cited Tabor, who made a recommendation on the

selection of the cutting tools that their hardness should be about 5 times that of the workpiece. In the case of SiC as a workpiece and diamond as a cutting tool, the ratio is only about 4:1, owing to the high micro hardness of SiC (about 28 GPa) compared to diamond (100 GPa). Experimentally, this ratio was found to reduce to about 2:1 at relatively shallow depths of cut [26].

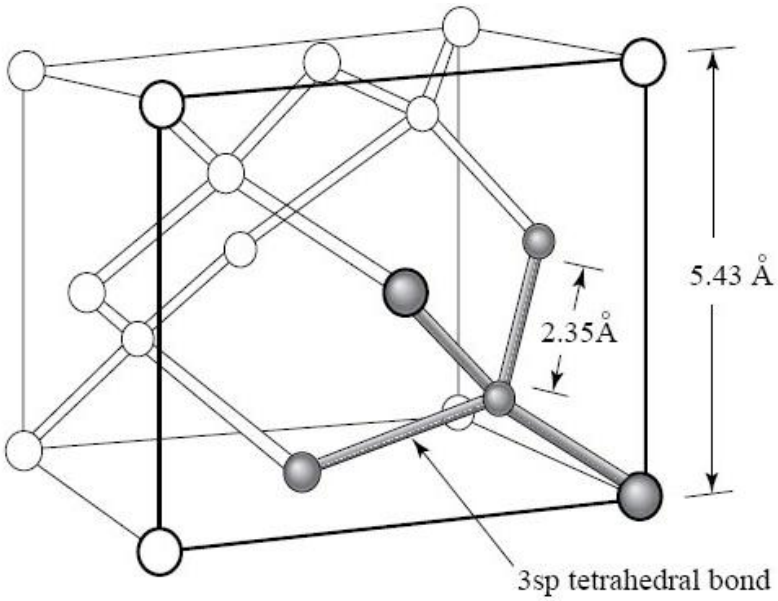

Figure 3-3: Cubic crystal structure of single crystal silicon [96]

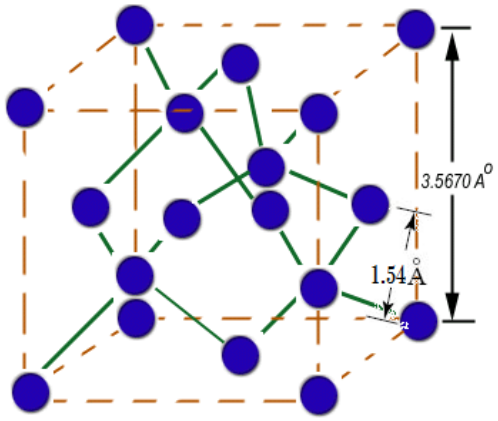

Figure 3-4: Cubic crystal structure of single crystal diamond [97]

Figures 3-3 and figure 3-4 show the diamond cubic crystal geometry of silicon and diamond respectively. The slip system in silicon is <110> (111), but this does not involve edge dislocations but is rather due to pure screw dislocations with Burgers

vectors at 60° to the dislocation line [61]. Besides continuing to be a main electronic material even in the 21st century [98] and currently constituting 90% of the total revenue of all semiconductor industries combined together [85], silicon exhibits tremendously desirable engineering properties such as low mass density, low cost and high refractive index which is preferable for weight sensitive infrared (IR) optics. Micro-electro-mechanical system (MEMS) accelerometers in cars, solar cells, renewable energy systems, micro-turbines, microfluidic chips and other high added value products such as X-ray optics and X-ray interferometers are some of the major examples where silicon finds applications outside electronics. Table 3-1 compares various properties of silicon with other optical quality materials, where it can be seen that silicon exhibit the highest Young's modulus couple with a relatively low mass density giving it an edge over other optical materials for many engineering applications.

Table 3-1: Physical properties of optical mirror materials [99]

Material	**Density** *(gm/cm^3)*	**Fracture toughness** *(MPa.m$^{1/2}$)*	**Coefficient of thermal expansion at 300K** (× *10^{-6} /K)*	**Young's modulus** (*GPa)*	**Poisson's ratio**
Silicon	2.3	0.9	2.6	135	0.27
Germanium	5.32	0.46	5.9	125	0.26
Zinc sulphide	4.08	0.8	6.8	75	0.27
Fused Silica	2.2	0.92	0.4	74.5	0.17
Zerodur	2.5	0.9	-0.1	91	0.24
Aluminium	2.7	24	23.4	69	0.33
Copper	8.9	26	17.6	117	0.36

Natural diamond exhibits significant variation in its physical, mechanical and chemical properties. Industrial characterization of diamond is usually based on the colour of the gem; a more quantitative assessment is possible using more sophisticated optical characterization but this is time consuming and costly. There are two broad classifications of diamond, the main features of which are shown in table 3-2.

Table 3-2: Classification of diamonds [82]

	Type I		**Type II (Extremely good heat conductors)**	
	I_a	I_b	II_a	II_b
Nitrogen (ppm)	~200-2400	~40	~8-40	~5-40
Boron (ppm)	None	None	None	~0.5
Remarks	Nitrogen exists in small geometrically clustered groups	Nitrogen exists as isolated substitution atoms	Chemically pure with very little nitrogen	Little nitrogen but contains substantial boron impurities

Unlike type II diamonds, type I diamonds have low dislocation density and a high density of platelets [100]. The presence of these platelets hinders the movement of dislocations in type I diamond making it even more difficult to cause plastic deformation. It has been demonstrated that type Ib diamond exhibits good repeatability of the tool life under identical test conditions whereas type IIb diamond is the most wear resistant of all categories of diamond.

3.3 Influence of polymorphism in silicon carbide

SiC exhibits one-dimensional polymorphism, all polytypes having the same planar arrangement of Si and C atoms but different stacking sequences. About 250 polytypes of silicon carbide (SiC) have been recognized by their energetic equivalence demonstrated through theoretical thermodynamic calculations [101]. The two major

polymorphs are α-SiC and β-SiC with hexagonal and zinc-blende lattice structures, respectively. The main engineering properties of β-SiC (3C-SiC) and α-SiC (6H-SiC and 4H-SiC) are listed in table 3-3, along with the corresponding values for single crystal silicon as a reference material.

Table 3-3: Engineering properties of various polytypes of SiC and silicon

Parameter	3C-SiC	4H-SiC	6H-SiC	Silicon	Diamond [102]
Lattice Parameter (Å)	a = 4.359[103]	a = 3.079[103] c = 10.254[103]	a =3.0817[103] c =15.1183[103]	5.43[104]	3.56
Mechanical Properties					
Bulk Modulus (K) (GPa)	225[105]	215[106]	215[106]	98[107]	442
Shear Modulus (G) (GPa)	124[108]	131.4[108]	131.4[108]	79.9[75]	478
Hardness (H) on (100) plane (GPa)	25-30[106]	26[109]	20-26[110]	9.8[75]	97
Poisson's Ratio (υ)	0.267[108]	0.231[108]	0.231[108]	0.27[75]	0.16-0.29
Young's Modulus(E) (GPa) "$E = 3K(1-2\upsilon)$"	314.55	347.01	347.01	135.24	1050
Fracture Toughness (K_c) ($MPa.m^{1/2}$)	2.02[111] 3.23 for CVD	1.9[112]	1.9[112]	0.9[113]	2-4
Electronic Properties [1, 114-117]					
Band Gap (eV)	2.3	3.2	3	1.1	5.45
Hole Mobility (cm^2 /V.s)	40	115	90	420	1600
Electron Mobility (cm^2 /V.s)	750	// c-axis: 800 ⊥ c-axis: 800	// c-axis: 60 ⊥ c-axis: 800	1200	2200
Thermal Conductivity (W/cm-K)	4.9	3-5	3-5	1.5	26
Electron Saturation Velocity ($cm/s\times10^7$)	2.5	2	2	1	2.7
Breakdown electric field strength ($V/cm\times10^6$)	1.8	// c-axis: 3 ⊥ c-axis: 2.5	// c-axis: 3.2 ⊥ c-axis: >1	0.6	10

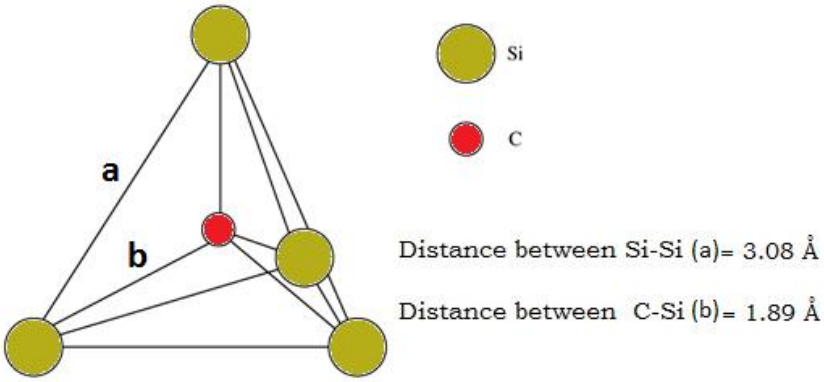

Figure 3-5: Tetrahedral geometry of SiC

It can be seen that the properties of the individual polytypes of SiC differ significantly despite the fact that all share the same tetrahedral geometry of silicon and carbon atoms as shown in figure 3-5. The difference in material properties of the various polytypes of SiC is fundamentally attributable to the difference in the stacking arrangement of SiC bilayers along the c-axis of β-SiC and along the (001) direction of α-SiC [118]. Figure 3-6 shows the stacking sequence of silicon and carbon atoms in 3-key polytypes of SiC.

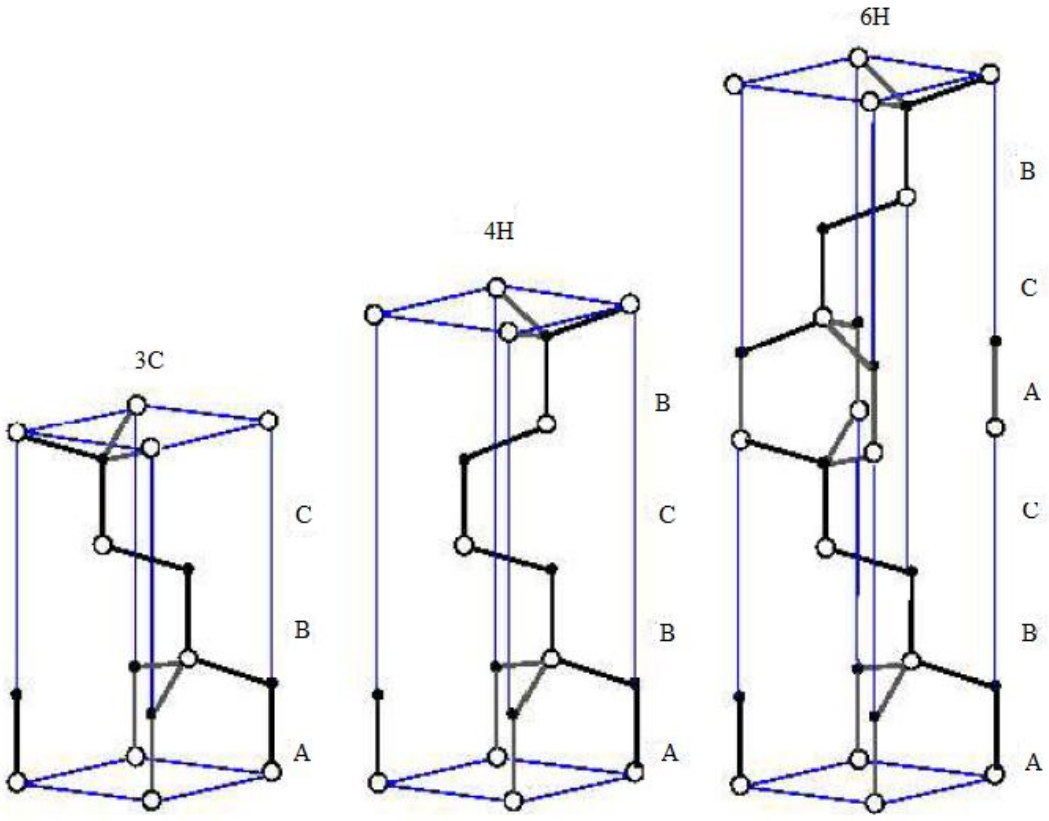

Figure 3-6: Stacking sequence of bilayers in three polytypes of SiC [117]

It can be seen from figure 3-6 that, if the first Si-C layer is labelled A, a close packed structure can be obtained by placing the next layer at either positions B or C. The various polytypes of SiC are simple permutations of three such positions. Thus defined, the stacking sequence is ABC in 3C-SiC, ABCB in 4H-SiC and ABCACB in 6H-SiC. Although SPDT of single crystal 6H-SiC [47, 119], CVD (polycrystalline) 3C-SiC [120], RB-SiC [121] and single crystal 4H-SiC [122] has been successfully demonstrated, a theoretical study of the machining mechanism at fundamental atomic level can answer some key questions which are difficult to observe on-line during experiments. For example, it is non-trivial to know if it is possible to generate defect-free surfaces in all the major polytypes of silicon carbide, and, if so, under what machining conditions. Also, it is of interest to know if some polytypes are more amenable to SPDT. Hence, it is worthwhile to investigate the SPDT mechanism for all polytypes of SiC simultaneously and to characterize the nanometric machinability of each material quantitatively in a way that it is indexed to silicon, which is a comparatively well-studied material offering a suitable reference.

Madar [123] has reported that a new process named “repeated a-face growth process (RAF)” has shown promise to develop virtually dislocation-free, large size SiC wafers. It was thanks to this development that SiC could at last be considered to outperform silicon based electronics components in the context of a range of commercial opportunities, as summarised in table 3-4 [124].

Table 3-4: Commercial applications of SiC [125]

S.No.	Properties of SiC	Applications	Realisation
1	High sublimation temperature	High temperature transducer elements	High temperature sensor diaphragms and resonators
2	Large band gap	High temperature electronics	Sensors for smart engines
			On chip signal conditioning
3	Low wear and high hardness	Enhanced durability/operation	Coated mechanical contacts
			Microfabricated bearings
4	Chemically inert	Stable in harsh environments	Valves/pumps for corrosives

3.4 Influence of the microstructure of the workpiece

The size of the grains in most commonly used engineering materials, such as steel, aluminum, silicon and even RB-SiC, is in the range of 100 nm to 100 µm which is around the feature size of micro-machined components. Therefore, various aspects of the workpiece material microstructure will be important in its machinability by SPDT. For example, when the depth of cut and the cutting edge radius are of the order of the workpiece material grain size, the cutting tool will experience varying resistance from different grains and across grain boundaries, which could be critical when it is necessary to generate a smooth surface on a polycrystalline material. Vogler *et al.* [126] investigated experimentally the effect of workpiece microstructure on the surface generation process in cutting and found that the machined surface roughness values for the various phases commonly found in ferrous alloys were larger than that of single-phase iron. They explained this finding by observing that, the chip-formation process

becomes discontinuous at the phase boundaries, causing the chip-formation process to become interrupted as the tool exits a phase more than at a homogeneous grain boundary. Consequently burrs form at the boundary of each phase in a multiphase material and not as much in a single phase material. A similar phenomenon occurs in nanoscale machining of polycrystalline materials where there is a dearth of slip systems, such as silicon carbide and silicon, as discussed in detail in section 6.6.

3.5 Influence of crystal orientation

Following crystallographic convention, this thesis, will use ( ) and < > notations to represent crystallographic plane orientations (direction of plane normals) and crystallographic directions, such as cutting and slip, respectively. Under normal conditions, natural silicon prefers a diamond cubic lattice structure with the (111) planes acting both as slip planes and cleavage planes. The Burgers vector of the diamond cubic lattice can be calculated as: $b_{(111)}= 1/2a$, $b_{(110)}= 1/\sqrt{2}a$ and $b_{(100)} = a$ where *a* is the lattice parameter. The angle between the (111) plane and the (100) plane in a diamond cubic lattice is 54.74° while the angle between the (110) plane and the (111) plane is 35.26°. A view to the unit cell of SiC is shown in figure 3-7.

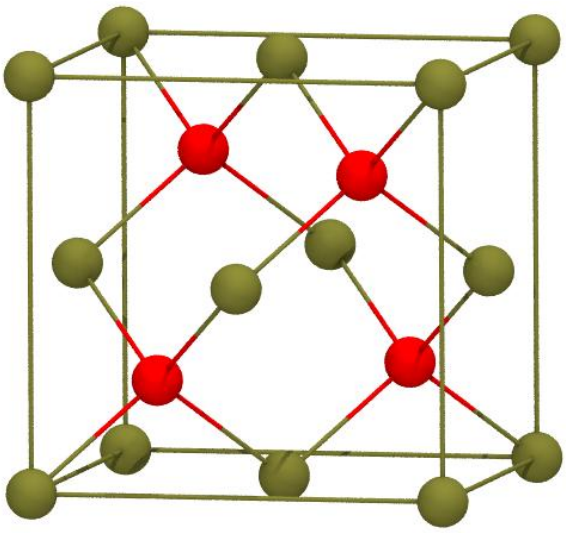

(a) Orthographic view of β-SiC

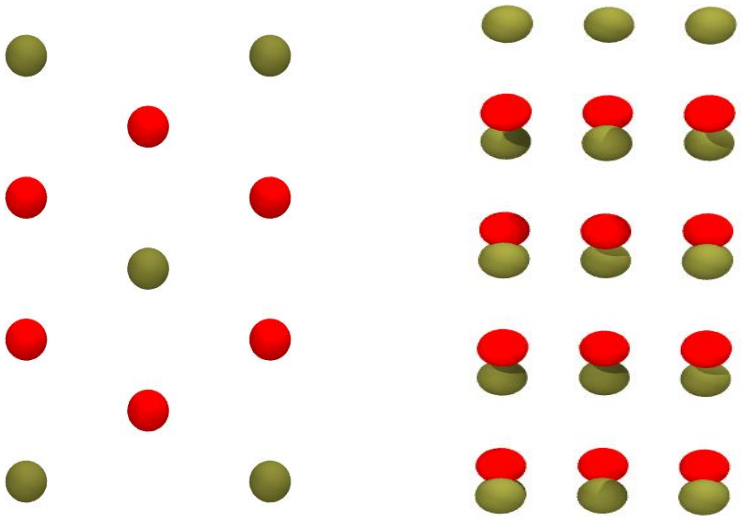

(b) View onto (001) plane of α-SiC (c) View onto (100) plane of α-SiC

Figure 3-7: Unit cell of SiC

Figure 3-8 shows schematically the changes in symmetry, atomic density and relationship to a number of possible cutting directions for three different crystallographic planes. As can be seen, the arrangement of atoms and, thereby the behaviour of the material under nanoscale cutting conditions, changes with respect to change in crystal setup (plane and direction). This is the reason why all the nanoscale mechanical properties, including the plastic response of brittle materials, change with respect to crystal orientations and direction of applied force.

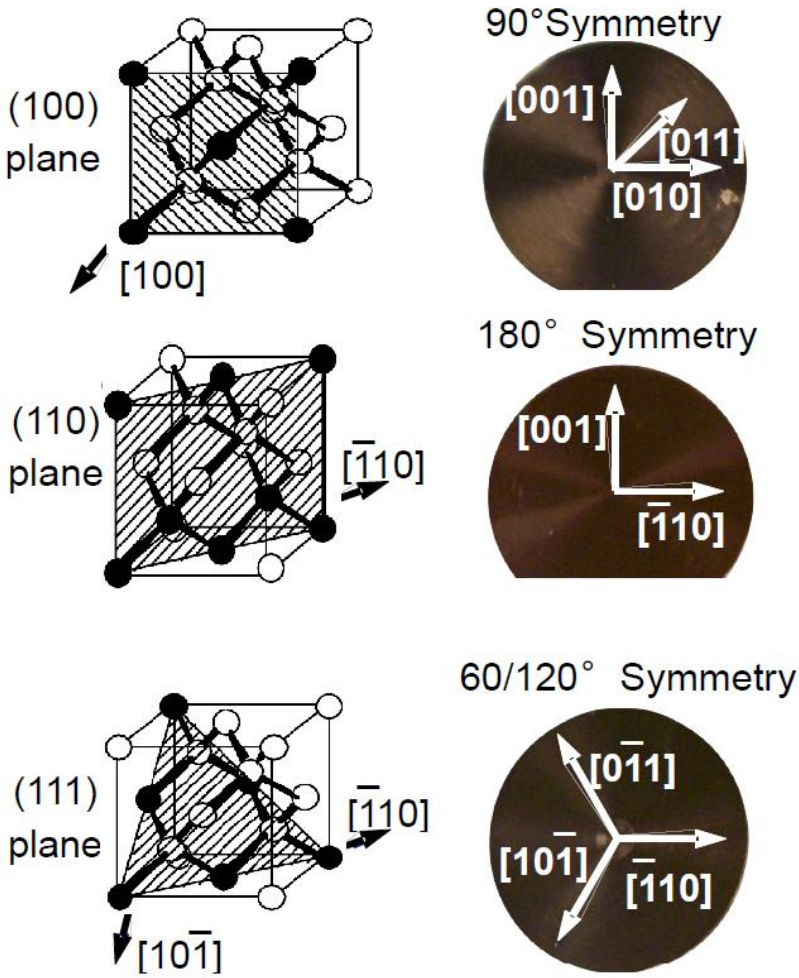

Figure 3-8: Schematic of various crystal orientations and cutting directions [127]

In figure 3-8, $\langle 1\bar{1}0 \rangle$ can also be read as <1-10>, these can be followed based on the standard notations used in material science or crystallography. Recent work by Wang *et al.* [35] on the influence of crystal anisotropy of silicon during its ductile-regime machining showed the (110) crystal orientation to support more dislocation movement than the (111) orientation. However, they recalled the findings of Marsh *et al.* [128] in which cleavage fracture occurs in a direction parallel to the (111) crystal plane while perpendicular to the (110) plane. Compared with other combinations for the same machining parameters, Wang *et al.* [35] obtained the best machined surface roughness of Ra 9.22 nm on silicon while cutting along the $\langle 1\bar{1}0 \rangle$ direction on the

(111) orientation. This result was consistent with earlier work of Shibata *et al.* [129] where a Schmidt-type slip orientation factor was proposed and the $\langle 1\bar{1}0 \rangle$ direction was recognized as the preferred cutting direction for silicon either on the (100) or on the (111) planes. It must be noted here that, while the (100) orientation permits a larger critical undeformed chip thickness, it is the (111) orientation which provides a better experimentally observed machined surface roughness during SPDT of silicon.

One of the most convenient ways of measuring the critical undeformed chip thickness of any material is through a fly cutting experiment in which the depth of tool engagement varies around the circumference of the tool path. An example of the result of one such test, provided by Connor *et al.* [80], is shown in figure 3-9:

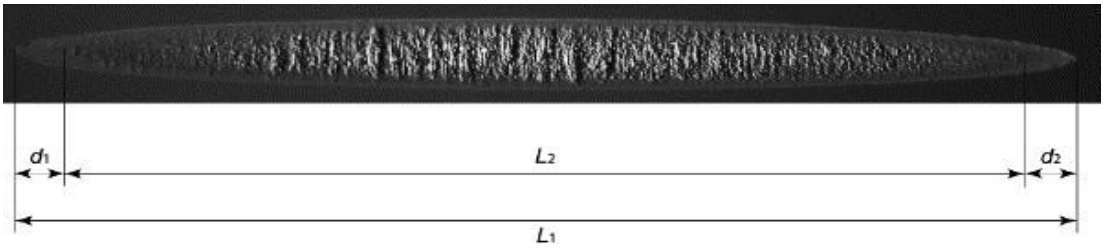

Figure 3-9: Scratch made on a silicon workpiece using fly cutting [80]

Using the parameters shown in figure 3-9, the critical undeformed chip thickness, t_c, can be calculated from:

$$t_c = \frac{2(L_1 d_1 + L_1 d_2 - d_1 d_2) - {d_1}^2 - {d_2}^2}{8R} \qquad 3\text{-}2$$

where R is the flycutter radius

These diamond flycutting experiments, performed up to a cutting speed of 5.6 m/s, showed that the critical chip thickness during ductile regime machining of silicon is at a maximum of 120 nm on the (100) planes and a minimum of 40 nm on the (110) planes [80]. The value of maximum critical chip thickness is reasonably consistent with the

value obtained by applying a simple mathematical formula to the optimised machining parameters suggested by Born and Goodman and shown in table 3-5 [130].

Table 3-5: Modified form of suggested parameters for machining silicon [130]

Parameter	**Value**
Feed rate (f)	6.35 μm/rev
Depth of cut (a_0)	1 μm
Cutting speed (V)	3.81 m/s
Rake angle of the tool	-45° or -30°
Clearance angle of the tool	10°
Tool nose radius (R)	5 mm
Critical undeformed chip thickness $= R - \sqrt{R^2 + f^2 - 2f\sqrt{2Ra_0 - a_0^2}} = 123\text{nm}$	

In quantitative (but not qualitative) contrast to the above, Jasinevicius *et al.* [37] have recently reported a maximum critical undeformed chip thickness of 285 nm on the (100) planes and a minimum of 115 nm on the (110) surface of silicon during SPDT with a **-5°** rake angle tool at a feed rate of 2.5 μm/rev and a depth of cut of 5 μm.

Ichida [131] recognized that an increase in the cutting velocity during ductile-regime machining of silicon enhances the upper bound of the critical chip thickness. Yan *et al.* [41] provided the quantitative illustration of critical undeformed chip thickness with crystallographic direction, shown in figure 3-10 and proposed that, in order to obtain homogeneous ductile crystal surfaces, the undeformed chip thickness (d_c) must be kept below the critical chip thickness for all the crystallographic orientations. Similarly, Zhang *et al.* [132] used large scale MD to simulate the machining of the (010) surface of copper along various cutting directions, as shown in figure 3-11. They noted that the 0° and 90° cutting directions offered least cutting resistance compared to 45°, which

offered the highest cutting resistance. However, the 45° cutting direction provided the best machined surface finish.

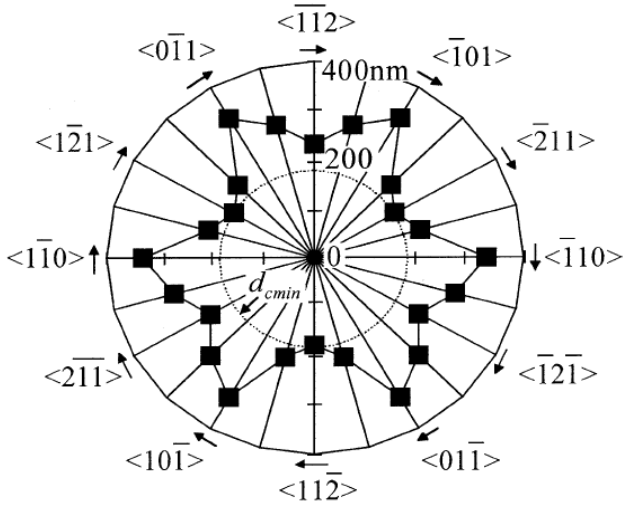

Figure 3-10: Crystallographic direction dependence of minimum undeformed chip thickness in silicon [41]

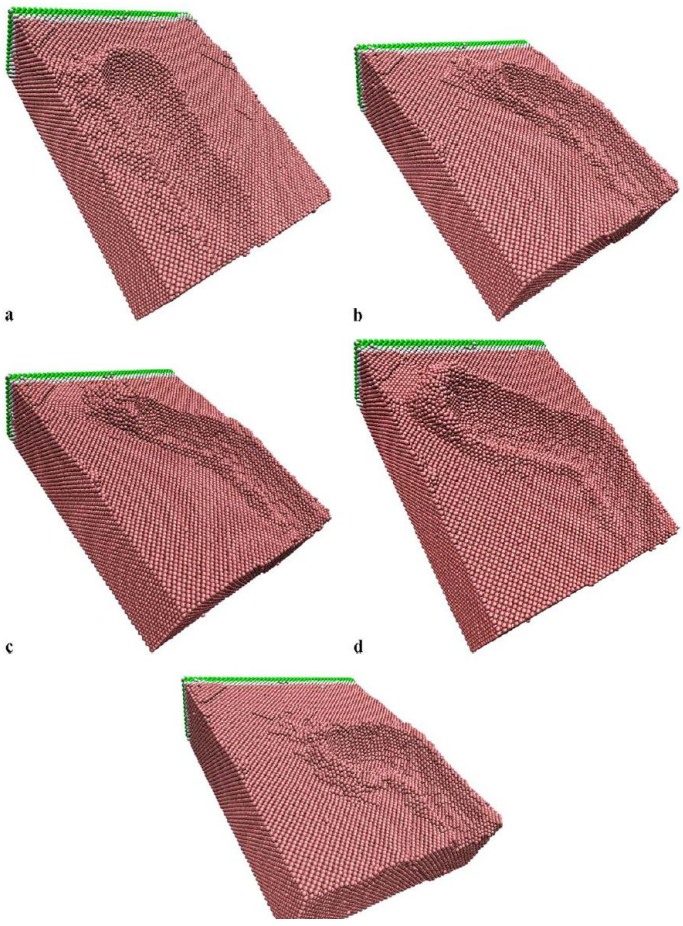

Figure 3-11: Simulated groove profiles on the (010) surface of copper for cutting directions: (a) 0° (b) 30° (c) 45° (d) 60° (e) 90° [132]

The results discussed above show that, while the critical undeformed chip thickness and the cutting edge radius clearly influence the regime of the machining of brittle materials [56, 62], substantial research is still needed to ascertain and establish a mathematical model.

Also, there is strong evidence in the literature that the crystal orientation of the cutting tool has a non-trivial influence on the tool life and the attainable machined surface roughness [82, 133-135]. An improved understanding of how to lap the diamond tools was presented by Zong *et al.*[134-135] using which they succeeded in machining the edge radius of a diamond cutting tool to an average surface roughness of 5 nm, a significant improvement on the industrial standard of 20-70 nm [54]. Figure 3-12 shows a generic scheme for re-lapping of worn diamond tools.

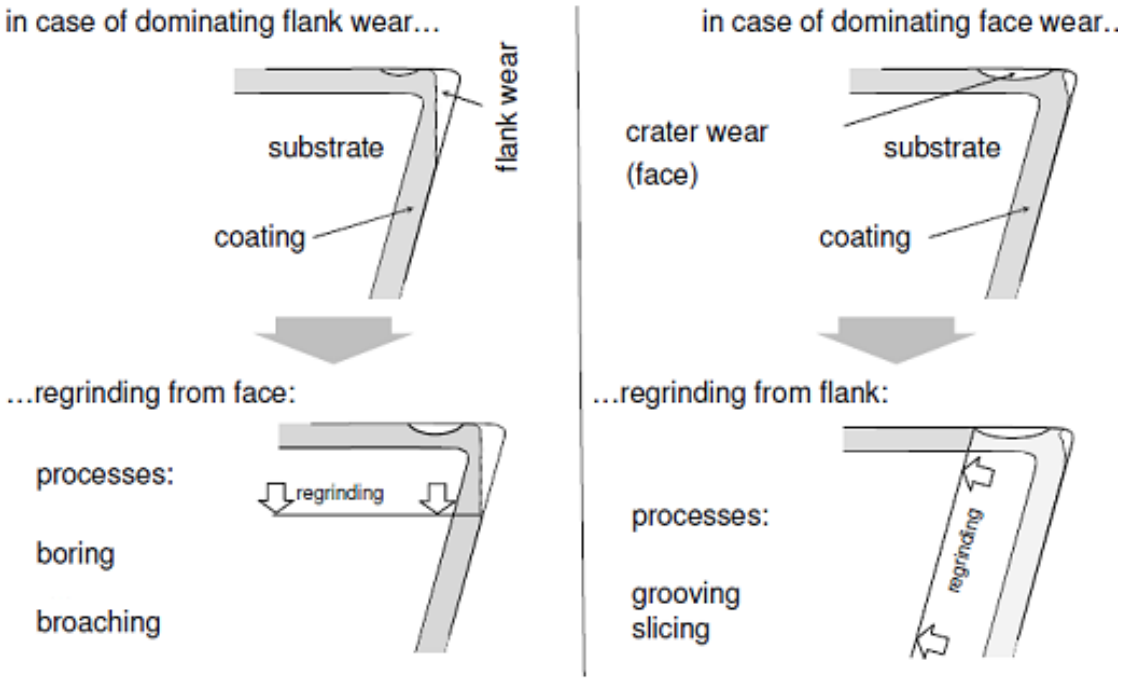

Figure 3-12: Procedure for lapping worn diamond tools

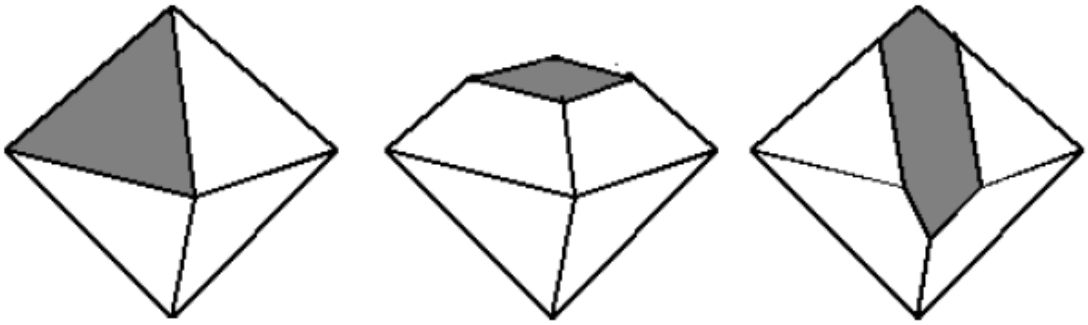

Octahedron (111) Cube (100) Dodecahedron (110)

Figure 3-13: Schematic showing (111), (100) and (110) planes of diamond

Diamond tool manufacturers usually select the crystallographic orientations of the tools based on the convenience of the polishing process. The three most commonly used planes of a diamond crystal are highlighted in figure 3-13. The (110) or (100) crystallographic planes are often chosen as the tool rake face with the axis of the tool and the tool shank parallel to <110> direction. However, it is possible that the optimum orientation for a particular tool may be a few degrees away from these crystallographic planes and directions. The crystallographic plane (110) is often used as the rake face and flank face of the diamond tools because it is easiest to shape by abrasion.

Over the years, much research work has been carried out to investigate the effect of crystallographic orientation on the performance of diamond tools. In order to obtain the best performance, the flank and rake face must be polished as smooth as possible to minimize friction and to ensure that the cutting edge remains smooth [136]. Figure 3-14 shows the two most popular commercially available orientations, cubic and dodecahedral.

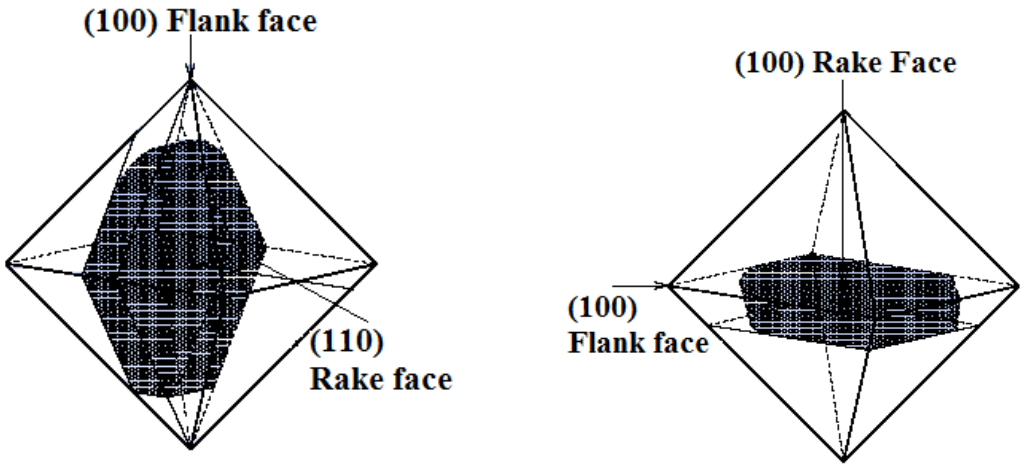

(a) Dodecahedral orientation (b) Cubic orientation

Figure 3-14: Popular crystal orientations for diamond tools (Courtesy: Contour Fine Tooling Limited, UK)

As long ago as 1975, Bex [137] demonstrated that diamond tools with the flank face oriented on the (100) plane had a wear rate of almost one-sixth times to those oriented on the (110) plane when used for machining Al-Si alloy. This observation was further supported by Casey *et al.* [138] based on tool wear experiments on LM13 (Al-12%Si), where tools with (100) rake face showed a tool life, by a factor of 7 higher compared with other orientations. In the same experiments, they further showed that the tool wear rate was independent of the cutting speed and that intermittency of cutting did not affect tool wear. Hurt *et al.* [139] investigated the effect of crystallographic orientation on wear characteristics of diamond tools during machining of oxygen-free high conductivity (OFHC) copper and gold. They found that diamond tools with cubic orientation exhibited higher wear resistance than the dodecahedral orientation. Also, cleavage fracture in a direction along the (111) crystal plane was responsible for the deterioration of the cutting edge of the tool for the dodecahedral orientation. Ikawa *et al.* [140] estimated the fracture strength of the cutting edge of diamond tools using a three-dimensional FEM model with crystallographic orientations (100), (110) and (111) as the rake faces. Based on the tangential stresses on rake face, they suggested

that the (100) crystallographic plane is more suitable as the rake face than the (110) plane for resisting chipping.

On the assumption that the friction between the diamond tool and the work material affects shear deformation, tool wear and machined surface quality, Yuan *et al.* [141] first observed the frictional characteristics between diamonds with (100), (110) and (111) crystallographic planes, and an aluminium alloy, copper, brass and cast iron. They next compared two diamond tools; one with (100) as the rake and the flank faces, the other with (110) as the rake and the flank faces. They carried out ultra-precision machining trials and found that the diamond tool with (100) as the rake and the flank possessed higher wear resistance and provided better machined surface quality than the (110) oriented tool. All of the above studies suggest that the cubic orientation gives better performance than the dodecahedral for turning of metals.

The research work reviewed above on the tool wear characteristics and the effect of diamond crystal orientation is mainly based on traditional cutting of nonferrous metals/alloys such as aluminium, brass and copper, where a diamond tool can last a cutting distance of up to a few hundreds of kilometres. For the machining of brittle materials, two independent papers have provided experimental evidence suggesting that the dodecahedral orientation can sometimes be better than the cubic orientation [82, 133]. Although this contradicts the theoretical findings [139, 142], it seems that, for a 0° rake angle tool, the dodecahedral orientation offers better wear resistance than the cubic orientation. However, evaluation of the relative wear resistance of the two orientations becomes rather more complex when the rake angle is negative. Although, particular reasons can be advanced for the above contradiction, it has been recognized of late that the best orientation of the diamond tool must be judged taking into account how the cutting tool is to be used [82].

3.6 Influence of the tool geometry

In a nanometric cutting operation, the cutting tool geometry plays a vital role as it directly affects the following outcomes [143]:

- Chip control
- Productivity of machining
- Tool life
- The direction and magnitude of the cutting forces and thus its components
- Quality of finish (surface integrity and residual stresses)

It has been demonstrated that the material removal at extremely fine depths of cut for certain atomic layers involves a high coefficient of friction which is dependent on the rake angle and independent of the thrust force of the cutting tool [144]. When the uncut chip thickness approaches the size of the cutting edge radius during SPDT, the rake angle of the cutting tool appears to determine both the direction and the magnitude of the resultant cutting force. Lucca *et al.* [145] demonstrated this phenomenon in SPDT trials on OFHC copper, where the cutting tool rake angle dictated the direction of the resultant force vector for smaller uncut chip thicknesses.

A schematic comparison of the cutting process using negative and positive rake tool is shown in figure 3-15. The use of a negative rake angle tools for SPDT operations has become something of a conventional belief for machining of brittle materials, for reasons explained earlier [54, 146]. The tangential force F acts along the wedge of the cutting tool so that the normal force acts onto the wedge face. Along these directions, the shear stress and compressive stress on the cutting tool vary during the course of machining. When positive rake angles are used, the normal force exerts a bending stress

on the cutting tip of the tool under which diamond, being highly brittle, may eventually chip off. When a negative rake angle cutting tool is used, this bending effect does not occur being replaced by compression on the cutting tool. Also, a negative rake angle cutting tool is believed to exert a hydrostatic stress state in the workpiece, which inhibits crack propagation and hence leads to a ductile response from brittle materials during their nanometric cutting [27, 39].

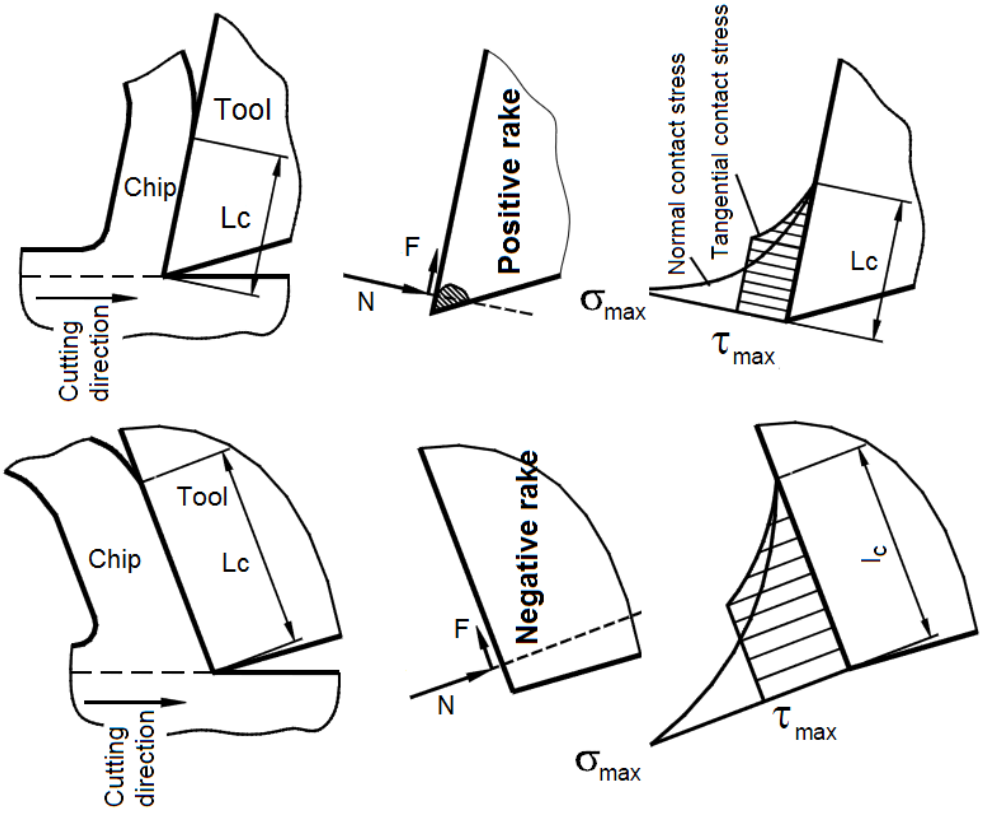

Figure 3-15: Difference in the force vector and stress distribution due to positive and negative rake angles [147] where l_c is length of contact between cutting tool and chip

Nakasuji *et al.* [39] mentioned that the effect of rake angle in cutting is analogous to that of apex angle of an indenter, low angles of approach resulting in relatively small hydrostatic stress fields which in turn enable ductile regime machining. Negative rakes of around -25° to -45° degrees with clearance angles of around 8° to 12° have been suggested for better tool life [95]. The reason offered for such a selection is that a high clearance angle reduces rubbing while a corresponding increase in rake angle provides

mechanical strength to the wedge of the cutting tool [148]. Interestingly, a research group at NUS, Singapore has found a 0° rake angle to provide superior performance than a +5° or -5° rake angle for machining of electroless nickel plate die material, at a fixed clearance angle of 8° [149]. For hard steels, the critical value of the rake angle (the dividing line between efficient and inefficient material removal) is 0° [150].

Table 3-6 summarises the work of the many researchers who have investigated the effect of the cutting tool rake and clearance angle. It has been demonstrated that, when the depth of cut is smaller than the edge radius, an effective rake angle is presented by the tool [151]. In such cases, a 0° rake angle tool already presents some negative rake and, indeed, has been found to provide a better finish than -25° or -30° rake angle tools. A simple calculation of the effective rake angle can be made with the help of the essential geometry shown in figure 3-16.

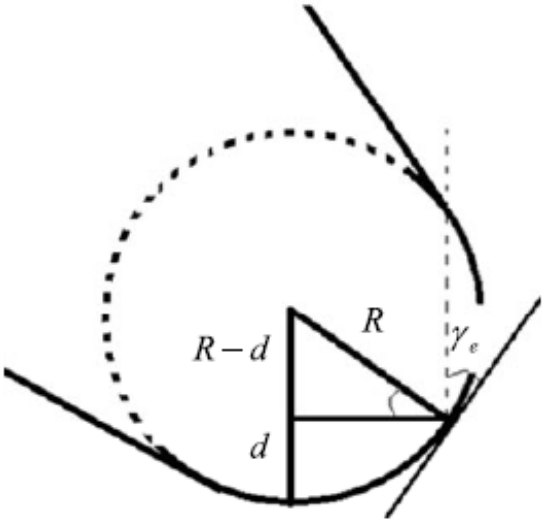

Figure 3-16: Schematic diagram showing effective rake angle [152]

From figure 3-16:

$$\sin\gamma = \frac{R-d}{R} = 1-\frac{d}{R} \qquad 3\text{-}3$$

where R is the tool nose radius, d is the depth of cut and γ is the effective rake angle.

Table 3-6: Influence of rake angle on the outcome of the SPDT of brittle materials

Work material and citation	Rake Angle	Clearance angle	Total included angle	Remarks/Observations
Germanium [23]	-30°	6°	114°	Better machining conditions (large feed rate) was obtained for -30° rake tool than -10° and 0° rake angle tool
Silicon [35]	-40°	5°	125°	Enabled better plastic deformation of the workpiece than that of (-25°) rake angle tool
Silicon [129]	-40°	10°	120°	A -40° rake angle tool provided purely ductile finished surface than a negative -20° angle rake tool
Silicon [153] and SiC [119]	-45°	5°	130°	With an adjustable arrangement for varying rake angle, a -45° rake angle tool was found to provide better response of the workpiece for ductile-regime machining
Silicon [154]	-25°	10°	105°	Performed better than –15° and -45° rake angle tool; however, inferior quality of gem was suspected to be the reason of poor performance of the diamond tool having -45° rake.
Silicon [68]	-25°	10°	105°	Provided a better machined surface finished in comparison to a –15° and 0° rake angle tool.
Silicon [151]	-30°	7°	113°	A range of rake angle between 0° and 60° rake angle was tested keeping other parameters unchanged and 30° rake was found superior
Silicon [155]	0°	Not specified	Not specified	An effective rake angle is presented by the tool when the depth of cut is smaller than the edge radius. In this condition, a 0° rake angle tool already presented some negative rake and was found to provide better finish than -25° or -30° rake angle tool however 0° rake angle tool permits reduced critical chip thickness and hence low material removal rate (MRR).
Silicon [156]	Varying tool rake and clearance		84°	Both tool rake angle and clearance angles were varied from −15° to −45° and from 21° to 51 ° respectively. A (-30°) rake angle tool permitted higher critical chip thickness while (-45°) angle tool enabled to reduce the microcracks.

Although it is evident from table 3-6 that the rake angle and the clearance angle have a significant influence on the critical undeformed chip thickness and the sub-surface lattice deformation layer depth, there is no systematic answer or model available yet which can be used to determine the best tool geometry for tool longevity.

Komanduri *et al.* [157] used molecular dynamics to simulate a wide range of rake angles to observe the mechanism of chip formation during nanometric cutting of silicon, a snapshot of which is shown in figure 3-17. They compared the chip formation process, to extrusion, particularly, for large negative rake angle tools, where the space available to accommodate departing chips decreases causing an increase in chip side flow. From their simulation results, they were able to explain that an increase in the negative rake angle results in a significant increase in the extent of sub-surface deformation.

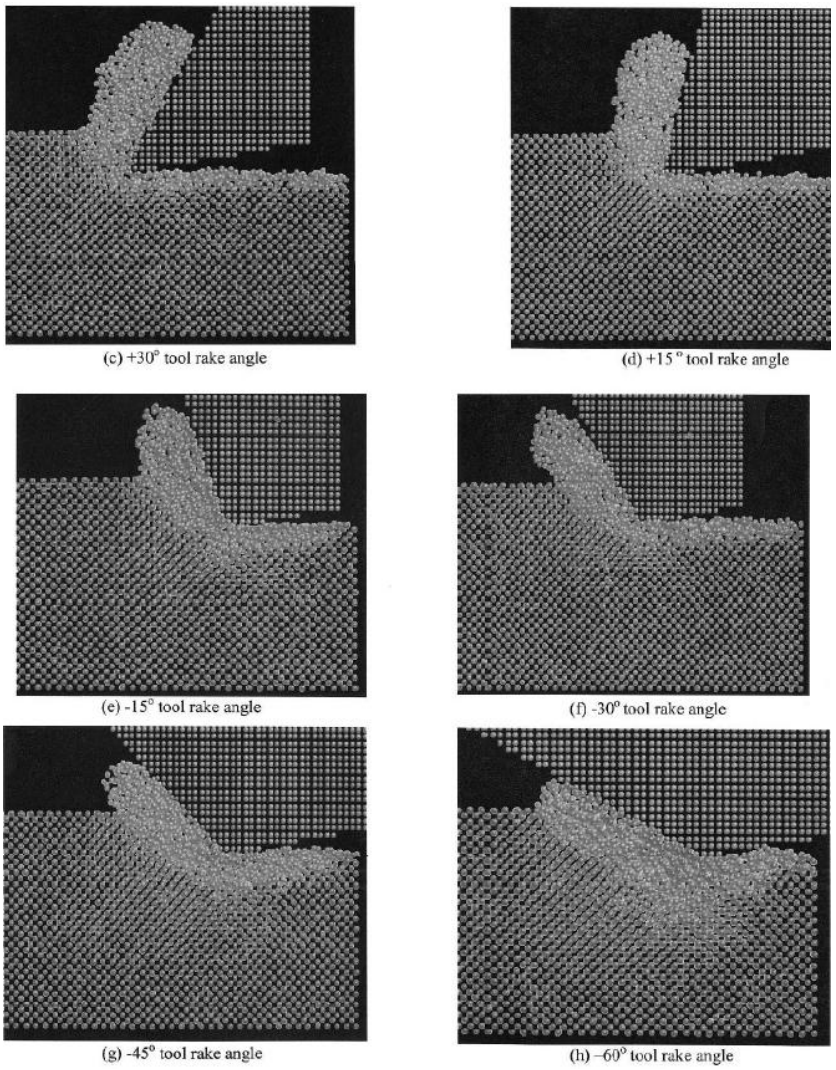

Figure 3-17: MD simulation of turning of silicon over range of rake angle [157]

3.7 Summary

This chapter has presented an extensive review and characterization of hard, brittle materials, including their polymorphism, crystal anisotropy and the effect that these have on machinability, particularly, the influence of the cutting tool rake angle. It was noted that polymorphism plays a key role in influencing the mechanical and physical properties of silicon carbide and that, for the various polytypes of silicon carbide an effect of this may be expected in nanometric cutting which needs to be investigated. The crystal anisotropy of a diamond tool is relatively well documented but the crystal anisotropy of silicon carbide during nanometric cutting is not known.

From the review it was also clear that the tool rake angle has a strong influence on ductile-regime machining and a tool rake angle in the range of -25° to -45° appears to be most conducive to achieving a ductile response from hard, brittle materials. It also appears that the geometry of the cutting tool used in a SPDT operation is analogous to the indenter used in an indentation experiment and that this analogue is valid down to the atomic level. Thus, ultra precision machining can be considered as an atomic level process which can be studied using molecular dynamics simulation.

Chapter 4 - Molecular dynamics simulation for nanometric cutting of hard, brittle materials

4.1 Concept, introduction and background

Molecular dynamics (MD) simulation is a combination of three distinct techniques, i.e. molecular modelling, computer simulation and statistical mechanics. MD simulation is a scientific algorithm through which an assemblage of atoms and/or molecules is given prescribed intermolecular interactions for a specified period of time to yield a trajectory of their movement. This is shown schematically in figure 4-1 for the example of nanometric cutting where the atoms within the workpiece and the cutting tool are at certain positions at time *t*. As the tool moves by a certain distance in time interval Δt, an atom *i*, acted on by the force F_{ij}, changes its position in the time interval $t+\Delta t$. Consequently, the new position of the atom *i* can be predicted using classical Newtonian mechanics.

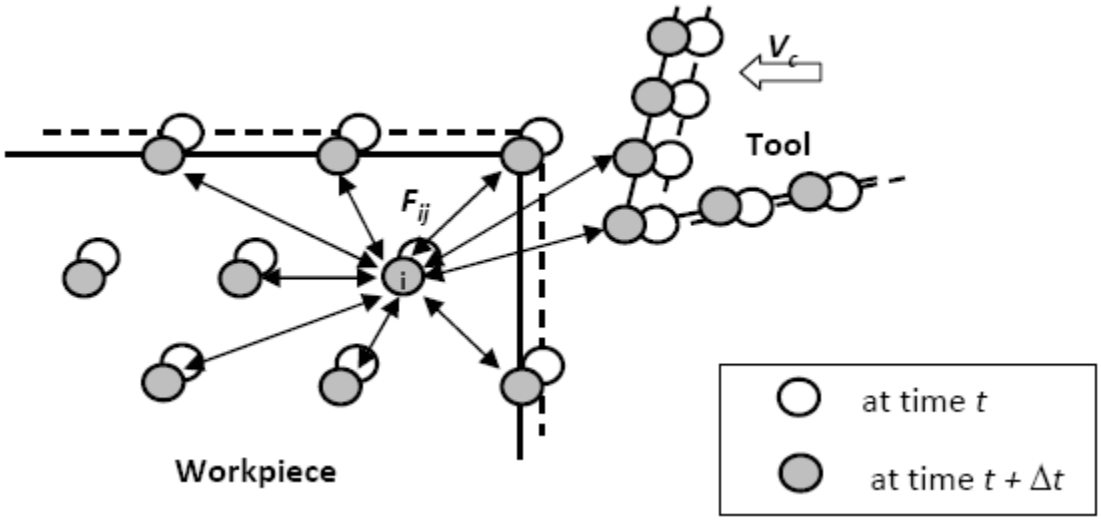

Figure 4-1: Principle of molecular dynamics simulation [158]

The idea that classical Newtonian mechanics, with a known potential and initial state of a system can effectively predict molecular motion is basically an eighteenth century concept dating to Rapaport [159] , who quoted Laplace:

"Given for one instance an intelligence which could comprehend all the forces by which nature is animated and respective situations of the beings that compose it intelligence sufficiently vast to submit these data for analysis it would embrace in the same formula the movements of the greatest bodies of the universe and those of the lightest atoms"

The implementation of MD simulation was first developed through the pioneering work of Alder and Wainwright in the late 1950s [48] in their study of the interactions of hard spheres. The principle of molecular dynamics is that Newton's second law of motion is assumed to be valid even at the atomic level. Newton's law can be written as follows:

$$m_i \frac{d^2 r_i}{dt^2} = F_i \qquad i = 1,2,....,n \tag{4-1}$$

where m_i is the mass of particle i and F_i is the force acting on it.

This equation can also be obtained from Lagrange's equation of motion which provides a more general framework for deriving equations of motion for systems of particles evolving under constraints.

4.2 Advantages and limitations of MD simulation

Unlike quantum mechanics, MD simulation disregards the details of the electronic motion and only considers the movement of atomic nuclei, thus permitting the study of relatively large systems. While MD offers many other technical advantages, it is restricted by the size of the simulation and the time to perform that simulation. A

summary of the key advantages and current limitations of MD in the context of nanometric cutting are presented in table 4-1.

Table 4-1: Advantages and limitations of molecular dynamics simulation

S.No.	Advantages	Limitations
1.	MD algorithm enables to take into consideration a more fundamental unit of matter i.e. atom and hence material properties are described naturally by their interaction potentials. Influence of crystal anisotropy, tribochemistry of the process and basic mechanisms underlying a wear process can thus be suitably studied through MD. Also, MD permits to investigate the theoretical approachable limits.	MD cannot predict the attainable experimental measure of machined surface roughness which is a prime requirement governing the choice of a material in an industrial application. Even if a theoretical value is estimated, it will always remain an ideal limit which can only be attained under ideal set of machining conditions.
2.	MD permits online monitoring of the machining processes with good temporal and spatial resolution in a reversible manner. Any time step can simply be reversed through a computer programme to analyse it at any given point of time.	Time to finish one simulation is a major challenge associated in performing a simulation with a realistic cutting speed and large size specimen.
3.	MD simulation avoids the use of expensive equipments and apparatus which are key requirements to perform nanometric cutting experiments. Besides, material once consumed will be required to reorder whereas MD can perform any number of trials with number of varying parameters.	Size of the workpiece and tool material cannot be varied to a larger (experimental) scale because of the current memory limitations associated with handling a large size data file.
4.	MD simulation offers repeatability of the process. This is to say that the type of workmaterial, cutting tool material, and the environmental conditions can all be kept intact and maintained at a pre-decided value.	Ongoing work on the development of potential functions is still restrictive to use variety of coolants during a simulation which is often a prerequisite in a real experiment.
5.	MD simulation provides flexibility to perform the simulation at any place as a computer system is mobile whereas an ultra precision machine tool (exhibiting high stiffness) demands static foundation and is thus static.	An advanced researcher can only perform an appropriate MD simulation as it requires accurate understanding of various disciplines whereas a machining trial can be performed by a relatively inferior knowledge.

4.3 Contribution of MD to the field of SPDT

It has been an important precursor to experimental studies of SPDT, which are not only expensive but also do not permit direct observation of all the events occurring at the atomic scale of time and length. This may be one reason why tool wear experiments conducted in the past were perhaps too long to permit any direct observation of the wear processes. An accurate understanding of the tribological phenomena occurring at an atomic scale requires an insight into the energetic, structural, dynamic and rheological aspects of the system [160]. Also, it has now been realized that it is not the atomic scale discreteness, but the atomic scale machined surface roughness, which causes the dramatic differences between the results obtained for nano-tribological problems using continuum mechanics principles [161]. Understanding the relevant atomic level phenomena is the key to obtaining full knowledge of the atomistic mechanism of ultra precision machining and this can be accomplished efficiently through the use of MD simulation [95, 162]. For instance, a recent study [163] has made use of an MD simulation to reveal the root cause of anisotropy exhibited by diamond. Also, in the absence of a large enough physical specimen of a material such as single crystal 3C-SiC, MD simulation is a viable option to advance the understanding of tool and substrate material selection and development in nanoscale cutting. An example of how MD simulation permits *in-situ* monitoring of all the events occurring within a short time range is the occurrence of the brittle-ductile transition in silicon [164] illustrated in figure 4-2.

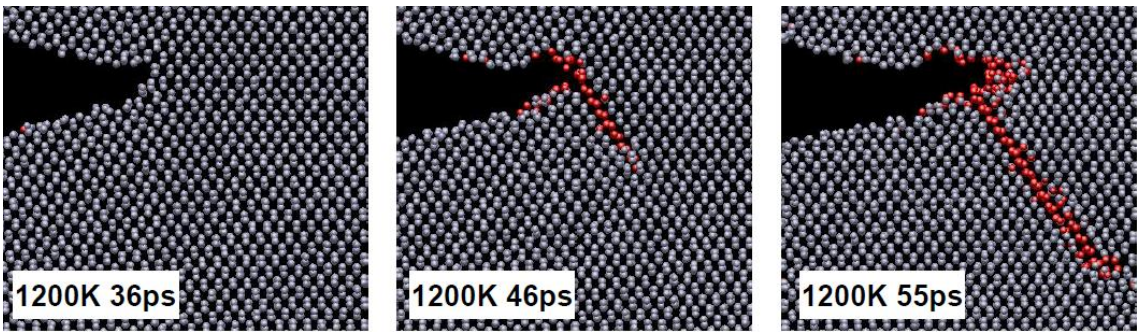

(a) Ductile failure *via* dislocation emission - Crack does not extend, but rather the lattice is sheared along the reddish region

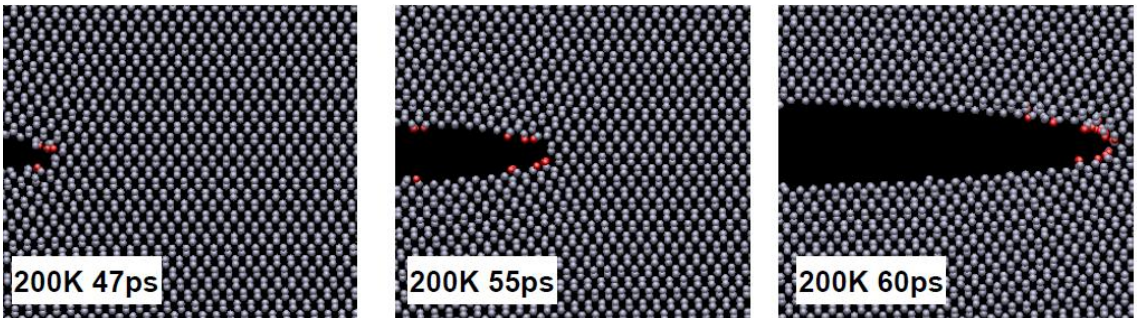

(b) Brittle cleavage failure – Crack extends suddenly and rapidly

Figure 4-2: Atomistic model of fracture in silicon [164]

From figure 4-2a, it can be seen that ductile failure results from dislocation emission and the material gets sheared along a direction which is energetically more favourable than crack propagation. In contrast, during the brittle cleavage fracture, as shown in figure 4-2b, the crack extends suddenly and rapidly along its original direction. It is thus evident that MD is capable of providing insights into material removal mechanisms in ultra precision machining.

4.4 Potential energy function

MD simulation requires a constitutive description of the terms in which the particles in a simulation interact. This interaction is governed by a potential energy function which approximately accounts for quantum interactions between electron shells and represents the physical properties of the atoms being simulated, such as its elastic constants and lattice parameters.

Potentials used in chemistry are generally called force fields, while those used in materials physics are called analytical potentials. Most force fields in chemistry are empirical and consist of a summation of forces associated with chemical bonds, bond angles, dihedrals, non bonding forces associated with van derWaals forces and electrostatic forces. The potential energy function *Vp* as illustrated schematically in figure 4-3 through ball and spring arrangements dictates the accuracy of an MD simulation and comprises the van derWaals interaction, electrostatic interaction, bonds, angles, and dihedrals/torsion.

$$V_p = \sum_{i<j} \sum 4\varepsilon_{ij}\left[\left(\frac{\sigma_{ij}}{r_{ij}}\right)^{12} - \left(\frac{\sigma_{ij}}{r_{ij}}\right)^{6}\right]$$

$$+ \sum_{i<j} \sum \frac{q_i q_j}{4\pi\varepsilon_0 r_{ij}}$$

$$+ \sum_{\text{bonds}} \frac{1}{2} k_b (r - r_0)^2$$

$$+ \sum_{\text{angles}} \frac{1}{2} k_a (\theta - \theta_0)^2$$

$$+ \sum_{\text{torsions}} k_\varphi [1 + \cos(n\varphi - \delta)]$$

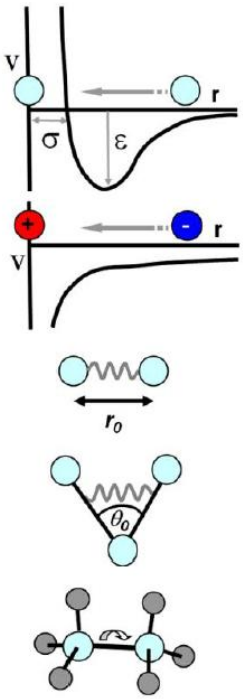

Figure 4-3: Potential energy function for molecular dynamics simulation [165]

Balamane *et al*. [166] have presented a comprehensive review of the potential energy functions that have been used for silicon. While the newly developed formalisms are providing more accuracy, they are sometimes computationally very expensive as shown in figure 4-4 and table 4-2.

Table 4-2: List of potential functions with respect to the time of introduction

S.No.	Year	Name of the potential function	Materials suited
1	1984	EAM: embedded-atom method [167]	Cu
2	1985	Stillinger-Weber potential [168-169]	Si
3	1987	SPC: simple point charge [170]	H_2O
4	 1988 1988 1989 1990 1994	BOP: bond–order potential • Tersoff-1 variant for silicon [171] • Tersoff-2 for better elastic properties of silicon [172] • Tersoff-3 for silicon, germanium and carbon [173-174] • Tersoff-4 for silicon and carbon [175] • Tersoff-5 for amorphous silicon carbide [176] • Refinements in Tersoff potential function [177-178]	 Si Si Si, Ge and C Si and C SiC
5	1989	MEAM: modified embedded-atom method [179]	Si and Ge
6	1990	REBO: reactive empirical bond order [180]	Carbon
7	2000	AIREBO: adaptive intermolecular reactive empirical bond order [181] (4 body potential function)	Hydrocarbons and Carbon
8	2001	ReaxFF: reactive force field [182] (Capable of bond breaking and bond-formation during the simulation)	Universal
9	2005	ABOP: analytical bond order potential [183] (3 body potential function)	Si and C
10	2007	COMB: charge optimized many-body [184]	SiO_2, Cu, Ti
11	2008	EIM: Embedded-ion method [185]	Ionic e.g. NaCl
12	2010	GAP: Gaussian approximation potential [186]	Universal
13	1998-2001	Other important potential functions relevant in contact loading problems [187-189]	Si, B and N

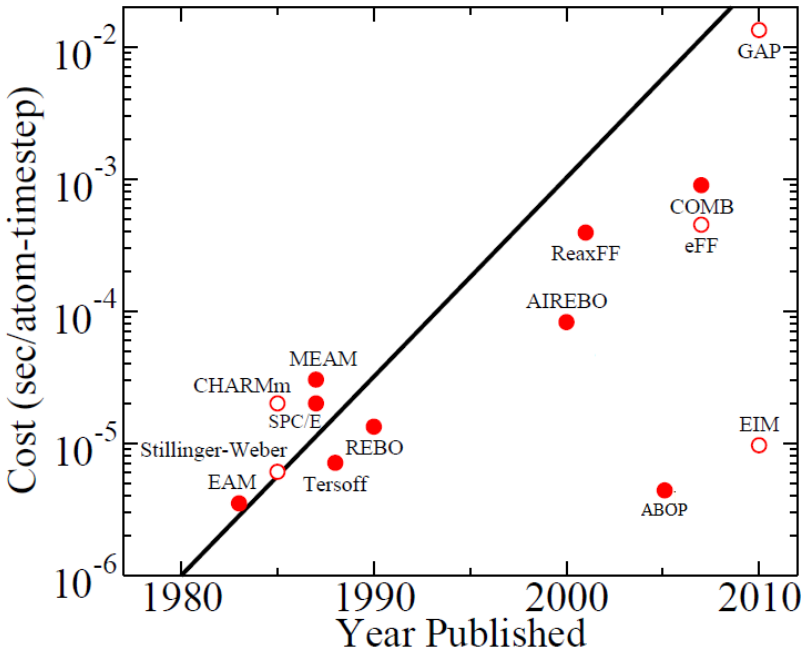

The black line represents a doubling in computational cost every two years, akin to Moore's Law for hardware complexity [190]

Figure 4-4: Single CPU cost in seconds/atom/time step for various potential functions

Table 4-3: Morse potential function for some metallic elements [144]

Element	Crystal structure	Lattice constant (Å)	D (eV)	a ($Å^{-1}$)	r_0 (Å)
Lead	FCC	4.95	0.2348	1.1836	3.733
Silver	FCC	4.09	0.3323	1.369	3.115
Nickel	FCC	3.52	0.4205	1.4199	2.78
Iron	BCC	2.87	0.4174	1.3885	2.845
Chromium	BCC	2.89	0.4414	1.5721	2.754
Molybdenum	BCC	3.14	0.8032	1.5079	2.976
Tungsten	BCC	3.165	0.9906	1.4116	3.032

Chemistry force fields commonly employ preset bonding arrangements (exceptions being *ab initio* dynamics and ReaxFF) and are thus unable to simulate the processes of chemical bond breaking and chemical reactions. One such example of a pair potential which was frequently used in early research work is the Morse potential function. Morse potential parameters for some example materials are shown in table 4-3.

A nanometric cutting simulation requires an interaction potential between the atoms of the cutting tool and the workpiece. For example, from table 4-3 one can describe the interactions within the atoms of the workpiece and the cutting tool but a parameter to describe an interaction between the atoms of the cutting tool and the workpiece is also needed. As an example, nanometric cutting of aluminium or copper using a diamond tool can be conducted using the Morse parameters shown in table 4-4.

Table 4-4: Morse potential parameters for nanometric cutting of metals [191]

Element	D (eV)	a ($Å^{-1}$)	r_0 (Å)
Cu-Cu	0.342	1.3588	2.866
Al-Al	0.2703	1.1646	3.253
C-C	3.68	2.2	1.54
Cu-C	0.087	1.7	2.05
Al-C	0.28	2.78	2.2

Unlike Morse potential functions, many of the potentials used in physics, such as those based on the bond order formalism can describe both bond breaking and bond formation. Covalent bonds have a strong directional dependence with some preferred angles between the bonds. For instance, the energy of three atoms (i, j and k) will not only depend on the inter-atomic distances but also on the angles between them (figure 4-5).

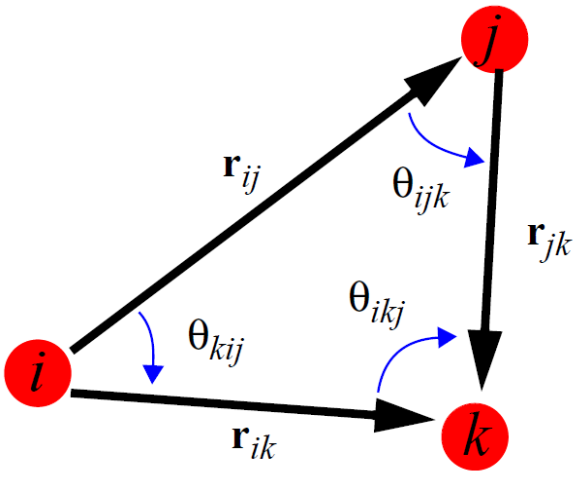

Figure 4-5: Configuration of three atoms for the development of a three-body potential function

The Tersoff or, more appropriately, "Tersoff-Abell" formalism is the most widely used bond order potential formalism and has become the basis for a huge number of potential functions. The Tersoff is a three-body potential function, while, the AIREBO function is a four-body potential function. Tersoff based his potential on an idea presented by Abell a few years earlier, a bond order potential (BOP) which has environmental dependence and no absolute minimum at the tetrahedral angle. Initially, Tersoff proposed two variants for pure Si, in which Si(B) describes well the surface properties of silicon while Si(C) describes well the elastic properties [171-172] of silicon. In its earliest form, Tersoff proposed the following formalism to describe the covalent bonding of silicon:

$$E = \sum_i E_i = \frac{1}{2}\sum_{i \neq j} V_{ij} \qquad 4\text{-}2$$

$$V_{ij} = fc(r_{ij})[a_{ij} f_R(r_{ij}) + b_{ij} f_A(r_{ij})] \qquad 4\text{-}3$$

repulsive part $\quad f_R(r) = A\exp^{(-\lambda_1 r)}$ $\qquad 4\text{-}4$

attractive part $\quad f_A(r) = -B\exp^{(-\lambda_2 r)}$ $\qquad 4\text{-}5$

potential cutoff function as:

$$fc(r)=\begin{cases}1 & r\le R-D\\ \frac{1}{2}-\frac{1}{2}\sin\left(\frac{\pi}{2}\frac{(r-R)}{D}\right), & R-D<r<R+D\\ 0 & r\ge R+D\end{cases} \quad 4\text{-}6$$

$$b_{ij}=(1+\beta^{n}\zeta_{ij}{}^{n})^{-1/2n} \quad 4\text{-}7$$

$$\zeta_{ij}=\sum_{k\neq i,j} fc(r_{ik})g(\theta_{jik})\exp(\lambda_3{}^{3}(r_{ij}-r_{ik})^{3} \quad 4\text{-}8$$

$$g(\theta)=1+\frac{c^{2}}{d^{2}}-\frac{c^{2}}{[d^{2}+(h-\cos\theta)^{2}\ ]} \quad 4\text{-}9$$

$$a_{ij}=(1+\alpha^{n}\eta^{n}{}_{ij})^{-1/2n} \quad 4\text{-}10$$

$$\eta_{ij}=\sum_{k\neq i,j} fc(r_{ik})\exp[\lambda_3{}^{3}(r_{ij}-r_{ik})^{3}] \quad 4\text{-}11$$

Here, the distance between atoms *i* and *j* is r_{ij} and the angle between bonds *ij* and *ik* is θ_{jik}. Inspection of the terms shows that there is an angular dependence, but, since it is embedded inside the b_{ij} term, it does not give a fixed minimum angle between the bonds. Table 4-5 lists the parameters given by Tersoff according to this formalism.

Table 4-5: Tersoff potential parameters for silicon [171-172]

	Si(B)	Si(C)
A(eV)	3264.7	1830.8
B(eV)	95.373	471.18
λ_1(Å^{-1})	3.2394	2.4799
λ_2(Å^{-1})	1.3258	1.7322
A	0	0
B	0.33675	1.0999×10^{-6}
N	22.956	0.78734
C	4.8381	1.0039×10^{5}
D	2.0417	16.218
H	0	-0.59826
λ_3(Å^{-1})	1.3258	1.7322
R(Å)	3	2.85
D(Å)	0.2	0.15
Remarks	Suited for surface properties	Suited for elastic properties

In subsequent years, Tersoff refined his formalism and proposed a few modifications to describe both Si and C along with their alloys. The new formalism took the following form:

$$E = \sum_i Ei = \frac{1}{2}\sum_{i \neq j} V_{ij}, \qquad V_{ij} = fc(r_{ij})[f_R(r_{ij}) + b_{ij} f_A(r_{ij})] \tag{4-12}$$

$$f_R(r_{ij}) = A_{ij} \exp(-\lambda_{ij} r_{ij}),\ f_A(r_{ij}) = -B_{ij} \exp(-\mu_{ij} r_{ij}) \tag{4-13}$$

$$fc(r_{ij}) = \begin{cases} 1 & r_{ij} < R_{ij} \\ \frac{1}{2} + \frac{1}{2}\cos[\pi \frac{r_{ij} - R_{ij}}{S_{ij} - R_{ij}}] & S_{ij} > r_{ij} > R_{ij} \\ 0 & r_{ij} > S_{ij} \end{cases} \tag{4-14}$$

$$b_{ij} = \chi_{ij}(1 + \beta_i^{ni} \zeta_{ij}^{ni})^{-1/2n_i},\ \zeta_{ij} = \sum_{k \neq i,j} fc(r_{ik}) \omega_{ik} g(\theta_{ijk}) \tag{4-15}$$

$$g(\theta_{ijk}) = 1 + \frac{c_i^{\,2}}{d_i^{\,2}} - \frac{c_i^{\,2}}{[d_i^{\,2} + h_i - \cos\theta_{ijk}]} \tag{4-16}$$

where E_i is the site energy-the sub-function, V_{ij} describes the energy between two atoms (*i* and *j*), (*i*, *j*, and *k)* label the atoms of the system, f_R represents a repulsive pair potential, f_A represents an attractive pair potential, f_C represents a smooth cut-off function to limit the range of the potential, r_{ij} is the length of the *i-j* bond, b_{ij} is the bond order term, ζ_{ij} counts the number of other bonds to atom *i* besides the *i-j* bond and θ_{ijk} is the bond angle between the bonds *i-j* and *i-k*. Here the indices *ij* represents the atom species. The mixing parameters between the two atomic species can be obtained from the mixing rules shown in the following equations:

$$\lambda_{ij} = \frac{\lambda_i + \lambda_j}{2} \tag{4-17}$$

$$\mu_{ij} = \frac{\mu_i + \mu_j}{2} \tag{4-18}$$

$$A_{ij} = \sqrt{A_i A_j} \tag{4-19}$$

$$B_{ij} = \sqrt{B_i B_j} \quad \text{4-20}$$

$$R_{ij} = \sqrt{R_i R_j} \quad \text{4-21}$$

$$S_{ij} = \sqrt{S_i S_j} \quad \text{4-22}$$

The parameter χ_{ij} determines the attractive interactions between two atoms. The potential function parameters given by Tersoff for the refined function are tabulated in table 4-6.

Table 4-6 : Tersoff potential parameters for silicon and carbon alloys

	Year 1989 [173-174]		Year 1990 [175]		Year 1994 [176]	
	Si-Si	C-C	Si-Si	C-C	Si-Si	C-C
A(eV)	1830.8	1393.6	1830.8	1544.8	1830.8	1544.8
B(eV)	471.18	346.74	471.18	389.63	471.18	389.63
$\lambda(Å^{-1})$	2.4799	3.4879	2.4799	3.4653	2.4799	3.4653
$\mu(Å^{-1})$	1.7322	2.2119	1.7322	2.3064	1.7322	2.3064
β	1.1×10^{-6}	1.5724×10^{-7}	1.1×10^{-6}	41.612×10^{-7}	1.1×10^{-6}	41.612×10^{-7}
n	0.78734	0.72751	0.78734	0.99054	0.78734	0.99054
c	100390	3804.9	100390	19981	100390	19981
d	16.217	4.3484	16.217	7.034	16.217	7.034
h	-0.59825	-0.57058	-0.59825	-0.33953	-0.59825	-0.33953
R(Å)	2.7	1.8	2.5	2.5	2.7	1.8
S(Å)	3	2.1	2.5	2.5	3	2.1
χC-Si	0.9776		0.9972		1.0086	

The Tersoff functions gained wide popularity in the 1990s for the purpose of simulations. However, one key drawback is that it poorly describes the graphite-to-diamond transformation. However, simply increasing the parameter *S* in the potential to 2.46 Å, improves this aspect [192]. Tersoff potential function does not describe well the dimer properties of silicon. To overcome this shortcoming, another potential function of almost same formalism which is an analytical bond order potential (ABOP) has been proposed [183]. ABOP is of the following form where the total energy can be expressed as:

$$E = \sum_{i>j} f_c(r_{ij})[V_R(r_{ij}) - \underbrace{\frac{b_{ij} + b_{ji}}{2}}_{\bar{b}_{ij}} V_A(r_{ij})] \qquad 4\text{-}23$$

where *E* is the cohesive energy which is the sum of individual bond energies with the following repulsive and attractive contributions:

$$V_R(r) = \frac{D_0}{S-1}\exp\left[-\beta\sqrt{2S}(r - r_0)\right] \qquad 4\text{-}24$$

$$V_A(r) = \frac{SD_0}{S-1}\exp\left[-\beta\sqrt{2/S}(r - r_0)\right] \qquad 4\text{-}25$$

where D_0 and r_0 are the dimer energy and bond length. The cutoff function is given by:

$$f_c(r) = \begin{cases} 1 & r < R - D \\ 0 & r > R + D \\ \frac{1}{2} - \frac{1}{2}\sin\left(\frac{\pi}{2}\frac{r-R}{D}\right) & |R - r| \le D \end{cases} \qquad 4\text{-}26$$

where the parameters *R* and *D* specify the position and the width of the cutoff region. The bond order is given by:

$$b_{ij} = \left(1 + \chi_{ij}\right)^{-1/2} \qquad 4\text{-}27$$

$$\chi_{ij} = \sum_{k(\neq i,j)} f_c(r_{ik})\exp[2\mu(r_{ij} - r_{ik})g(\theta_{ijk}) \qquad 4\text{-}28$$

and the angular function is given by:

$$g(\theta) = \lambda\left(1 + \frac{c^2}{d_2} - \frac{c^2}{d^2 + (h + \cos\theta)^2}\right) \qquad 4\text{-}29$$

The parameters of the potential energy function for carbon and silicon and their interactions in the ABOP formalism are shown in table 4-7.

Table 4-7: Potential function parameters of silicon and carbon [193]

	Si-Si	C-C	Si-C
D_0 (eV)	3.24	6	4.36
r_0 (Å)	2.222	1.4276	1.79
S	1.57	2.167	1.847
β (Å^{-1})	1.476	2.0099	1.6991
Γ	0.09253	0.11233	0.011877
C	1.13681	181.910	273987
D	0.63397	6.28433	180.314
H	0.335	0.5556	0.68
2μ (Å^{-1})	0	0	0
R (Å)	2.9	2	2.4
D (Å)	0.15	0.15	0.2

Finally, Pastewka *et al.* [194] have presented a state-of-the-art review, explicitly highlighting some of the important considerations needed to use a potential energy function to model phenomena such as fracture, wear or plasticity.

4.5 Preparations for the MD simulation

4.5.1 Equilibrium lattice parameter

The lattice parameter, *a*, of a solid corresponds to the length of the unit cell at the equilibrium volume. For simulation purposes, it is obtained by minimising the total energy of the cell volume. The lattice energy and hence lattice parameter may vary with the individual potential energy function. Using an inappropriate lattice parameter may affect the total energy content of the system and thus the specified uncut chip thickness,

cutting edge radius and other key measures may all vary during the process of equilibration, resulting in the erroneous simulation results. It is therefore important to use the equilibrium lattice parameter during the MD simulation.

The lattice energy Φ and the number density ρ are defined as:

$$\Phi = \frac{E_{pot}}{N} \tag{4-30}$$

$$\rho = \frac{N}{V} \tag{4-31}$$

where E_{pot} is the potential energy of the lattice and, N is total number of atoms in the simulation cell of volume V. The lattice parameter can be determined from the $\Phi(\rho)$ curve where Φ is minimum, $\Phi_{minimum}$, also known as the cohesive energy ($E_{coh,\ \min}$), defined as the minimum energy required for breaking the bonds of the solid to yield isolated atomic species. Under ambient conditions, both the silicon and diamond lattices prefer a diamond cubic (DC) structure. Accordingly, the cohesive energy (E_{coh}) for the DC structure of silicon and diamond were found for a range of lattice parameters. A fifth order polynomial trendline was fitted to the resulting values of cohesive energy (E_{coh}) as a function of lattice parameter to calculate the minimum cohesive energy ($E_{coh,\ min}$). For example, the minimum cohesive energy for silicon - 4.629595 eV was observed at a lattice parameter a = 5.432 Å, against the experimental lattice parameter 5.43095 Å [195]. For diamond, the minimum cohesive energy $E_{coh,min}$ = - 7.3705142 eV was observed at a lattice parameter a = 3.5656 Å again comparing well with the experimental value of 3.56683 Å [195].

4.5.2 Boundary conditions

A schematic diagram of the nanometric cutting simulation model used in this work is shown in figure 4-6. Both the nano-crystalline workpiece and the diamond cutting tool

were modelled as deformable bodies in order to permit tribological interactions between them. The model developed used here fixes the bottom and outer sides of the substrate as these have been suggested to be appropriate boundary conditions for nanometric cutting [196].

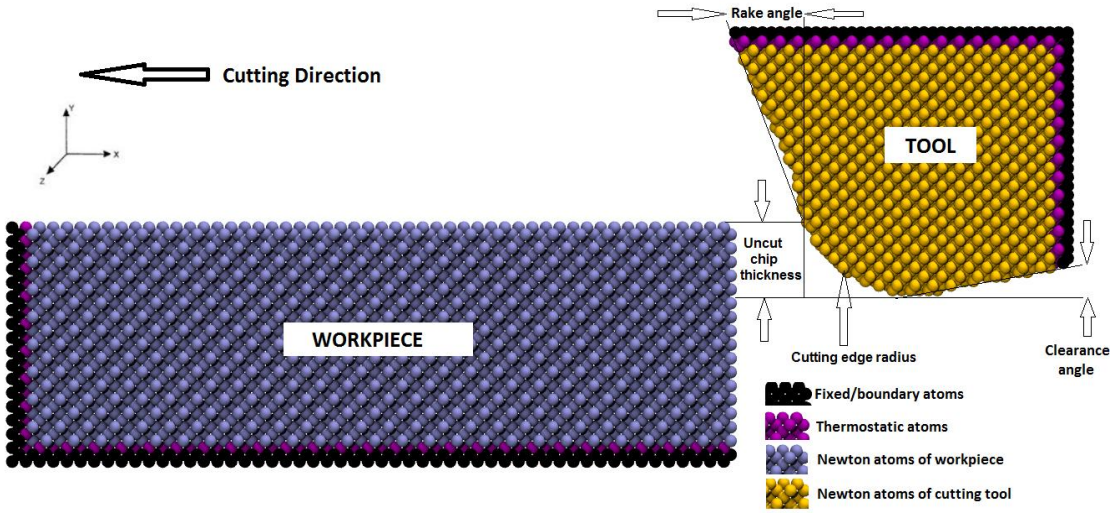

Figure 4-6: Schematic of MD simulation model

The MD model also incorporates a negative tool rake angle, as this is generally recommended for machining hard brittle materials [54, 146].

The atoms of the cutting tool and the workpiece were allocated into one of three different zones: Newton atoms, thermostatic atoms and boundary atoms. The boundary atoms were assumed to remain unaffected during the simulation and were kept fixed in their initial lattice positions, serving to reduce the boundary effects and maintain the symmetry of the lattice. In conventional machining operations, the energy from plastic deformation in the primary shear zone and friction at the tool-chip interface generate heat, which is carried away by chips, lubricant and by conduction into the tool and workpiece. The nanometric cutting model is, however, extremely small and is not capable of dissipating the cutting heat itself. The velocity of the thermostatic atoms is therefore re-scaled to a temperature of 300K at each step of the computation to dissipate the Joule heat.

MD simulations are usually implemented considering a system of N particles in a cubic box of length L. Since N is typically of the range of 100 to 10000, very far from the thermodynamic limits, it is necessary to use a periodic boundary condition (PBC) in all three directions to avoid surface effects. The PBC is the most popular boundary condition in MD. To use PBC in a simulation of *N* atoms confined to a volume *Vn*, we imagine that *Vn* is only a small portion of the bulk material, called the primary cell, where the bulk is considered to be composed of the primary cell surrounded by replicas called image cells. The image cells are of the same size and shape as the primary cell, each containing *N* atoms, themselves images of the atoms in the primary cell as illustrated schematically in figure 4-7.

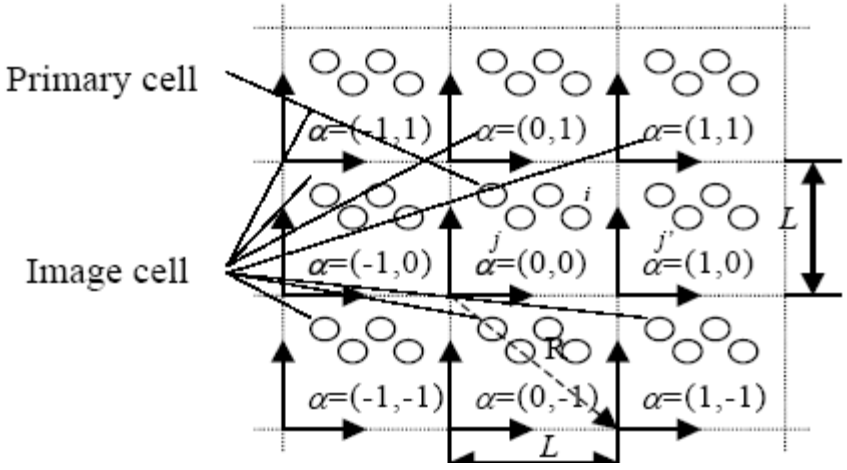

Figure 4-7: Periodic boundary condition [197]

An important consideration in using a PBC involving two different lattices with periodic boundaries is that the periodic cell dimensions must be chosen such that the lattice constants are in integer proportion: $L_z = n_1 \times a_1 = n_2 \times a_2$ where L_z is the cell size (in, say, the z direction), n_1 and n_2 are integers and a_1 and a_2 are the two lattice constants. In general, there is no exact solution to this equation, but for large enough system, n_1 and n_2 it can be approximated reasonably well. Similarly, change in crystal orientation also requires adjustment in crystal orientation.

For example, a workpiece may be oriented on (111) orientation either by writing orient (x -2 1 1) orient (y 1 1 1) orient (z 0 1 -1) or by describing orient (x -1 1 0) (y 1 1 1) (z 1 1 -2) In both cases, the z orientation is different to be fitted in the simulation box. For the former case, the equivalent lattice length in z direction must first be calculated by multiplying $\sqrt{2}$ with the lattice length of the crystal in (100) orientation which must then be fitted with the tool box z dimension. Similarly for the latter case, the equivalent lattice length would be $\frac{\sqrt{1^2+1^2+2^2}}{2}$ multiplied by the lattice length of the crystal in (100) orientation which has to be than fitted with the periodic box dimension of the tool. Similarly, other orientations could be (orient x 1 -1 0) (orient y 1 1 -2) (orient z 1 1 1) and (orient x -1 1 -2) (orient y 1 1 0) (orient z 1 -1 -1). In both cases, z orientation is (111), i.e. the equivalent lattice length in z direction must first be calculated by multiplying $\sqrt{3}$ with the lattice length of the crystal in (100) orientation followed by fitting that dimension with the global box size.

The initial positions can be randomly assigned avoiding overlaps or, for dense systems, the initial configuration can also be constructed by assigning the atoms to coordinate of a lattice (figure 4-8a), which can be done by energy minimization. The velocities can be assigned using a Maxwell-Boltzmann distribution.

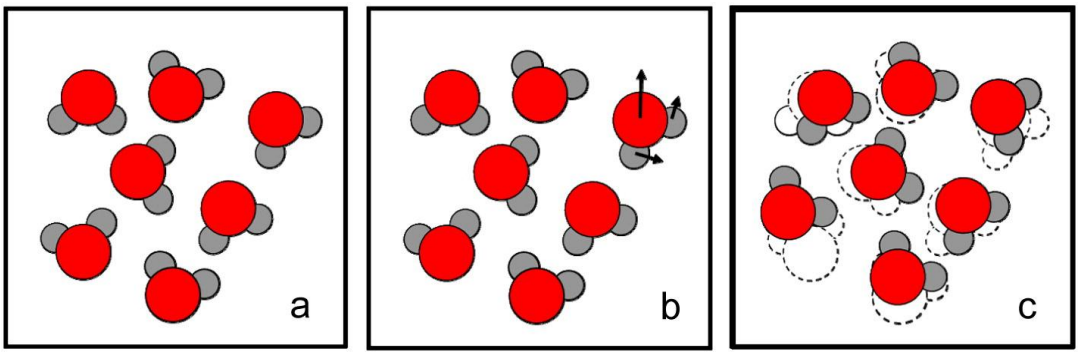

Figure 4-8: Illustration of molecular dynamics simulation procedure (a) The initial positions of the molecules are specified (b) Force on each atom due to the other atoms in its neighbourhood is calculated. (c) Potential energy function predict the newer positions and velocities of the atoms at a specified time [165]

After minimization, the velocities of all the atoms need to be scaled to a desired temperature. This is achieved by a process of equilibration, during, which the total energy is not conserved and the trajectories cannot be used to compute any properties (figure 4-8b). Once sufficient time has been given for equilibration, then velocity scaling is removed and the system follows NVE dynamics (figure 4-8c). During this phase, if the system is far from equilibrium, potential energy will be converted into kinetic energy or *vice-versa* and so, the temperature changes until it becomes stationary. The amount of time required for equilibration depends on the system being investigated as well as the initial configuration of the system.

4.5.3 Ensembles

An ensemble is an important parameter in a MD simulation and can simply be considered as a large number of replications of a cell with a limited number of atoms. Those repeating cells will not necessarily be the same, unless they have the same thermodynamic properties. It is therefore necessary to use an appropriate ensemble there most common of four which are; NVE, NVT, NPT and NPH.

An isolated system is described by three quantities, the total energy (E), the total volume (V) and the number of atoms (N). These are extensive quantities in that they are proportional to the size of the system as opposed to intensive quantities, such as temperature, which are independent of system size. A system with all these three extensive quantities fixed is called micro-canonical (NVE) ensemble.

In this work, the large scale atomic/molecular massively parallel simulator (LAMMPS) [198] was used to perform the MD simulation while Visual molecular dynamics (VMD) [199] and the Open visualization tool (OVITO) [200] were used for the visualization of the atomic trajectories. In LAMMPS, NVE simply involves an integration with respect

to time using Verlet's algorithm [159]. NVT, on the other hand, does both the time integration and also manipulates the acceleration of atoms in such a way that a bulk system with a finite number of particles behaves as if it was (homogeneously, i.e. no temperature gradient) connected to a (near) infinite heat sink or source. Thus, NVE is the microcanonical ensemble in which the total energy of the system is conserved, whereas NVT is a canonical ensemble which prescribes the (average) temperature of the system and hence the total energy is not conserved here. Newton atoms were allowed to follow unchanged Newtonian dynamics to ensure that the deformation process is not affected by any artificial dynamics whereas thermostatic atoms were constrained with the NVT dynamics.

4.6 Post processing of results

4.6.1 Identification of phase transformation in brittle materials

Mechanical micromachining involves a number of processes occurring simultaneously i.e. movement of dislocations, brittle fracture, tribochemistry and phase transformation of the material. Of all these mechanisms, the phase transformation of brittle materials under high surface pressures is of particular interest in the field of nanometric cutting as this opens up the possibility of obtaining a ductile response from brittle materials [201]. However, with the notable exceptions of silicon and germanium, brittle materials have not been studied much from this point of view [202]. Perhaps the main reason for this limited progress is that such a non-trivial scientific problem requires the bringing together of at least three disparate disciplines, materials science, micro-mechanics and solid state physics. An understanding of high pressure phase transformation is, however, necessary so that the deviatoric stress conditions can be controlled in order to drive phase transformation in brittle materials and so enable their ductile-regime machining.

From the MD simulation point of view, it is challenging to assign a definite phase to the material and a combination of several methods may sometimes be needed to understand and analyse the material's phase under a given set of conditions. A state-of-the-art review covering the relevance, importance and application of these methods as well as some new methods such as Vornoi analysis and Neighbour distance analysis has recently been presented by Stukowski [203]. Some of these methods are briefly discussed below with an emphasis on their applications as part of an MD simulation of nanometric cutting.

4.6.1.1 Coordination number

Cheong *et al.* [204] showed that the Si-I to Si-II phase transformation in silicon causes a change in the inter-atomic distance from 2.35 Å to 2.43 Å and 2.58 Å, respectively. Early research has established that this change in inter-atomic distance is associated with a change in the coordination number of silicon from 4 to 6 [61] which means that the number of nearest neighbour atoms in pure silicon changes from 4 to 6 to signify ductile-regime machining. However, it has been pointed out by Gilman [44] that the coordination number of Beta-silicon (Si-II) cannot be perfectly 6 because there is always a difference of 5.6% between consecutive nearest neighbour atoms. Since, this anomaly has persisted for a decade, it was considered more appropriate to assess the HPPT state of the material by applying other methods than coordination number.

4.6.1.2 Radial distribution function

The radial distribution functions (RDF), also called pair distribution functions or pair correlation functions, are the primary linkage between macroscopic thermodynamic properties and intermolecular interactions.

As illustrated in figure 4-9, blue colour atom is the central atom from which neighbour distance is measured, green colour atoms are the atoms which counts as the first neighbour distance atoms and white colour atoms are rest of the atoms in a system. If the atoms in a space are distributed homogeneously, then the RDF, $g(r)$, gives the probability of finding the centre of an atom in a shell dr at a distance r from the centre of an atom chosen as a reference point. The number of atoms $dn(r)$ at a distance between r and $r + dr$ from a given atom is expressed as follows:

$$dn(r) = \frac{N}{V} g(r) 4\pi r^2 dr \qquad 4\text{-}32$$

where N represents total number of atoms, V is the model volume and $g(r)$ is the radial distribution function.

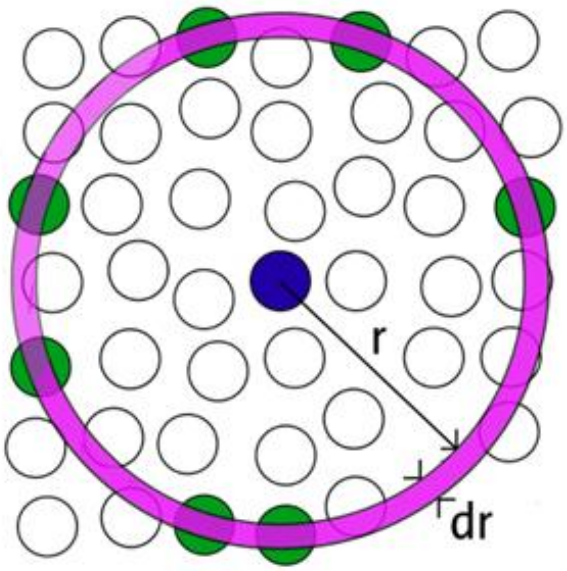

Figure 4-9: Schematic diagram of radial distribution function [205]

4.6.1.3 Angular distribution function and Ackland analysis

Analogous to the radial distribution function is the angular distribution function where the inter-atomic distance is replaced by the inter-atomic angle or bond angle. A classic example of the usefulness of this function is in distinguishing between the FCC and HCP crystal structures, which is tedious using coordination number alone, whereas they can easily be distinguished using a bond angle distribution functions. During the nanometric cutting of brittle materials, the change in bond angle can be as large as 37% in comparison to the corresponding change in bond length (only upto 4%). Therefore, because the angular distribution function is a much more robust and sensitive measurement than the RDF, an advanced algorithm named "Interactive structure analysis of amorphous and crystalline systems" (ISAACS) was used in the current work. Alternatively, this could also be accomplished by performing an "Ackland analysis" [206], available within the LAMMPS itself.

4.6.1.4 Centro-symmetry parameter

Dislocations play a crucial role in governing the plastic response of brittle materials. The thermal vibration of atoms at finite temperatures makes it difficult to observe dislocations in changing temperature environments, so the commonly used methods for tracing such dislocations and other lattice defects are coordination number, slip vector and centro-symmetry parameter (CSP). Although CSP was originally developed for BCC and FCC lattice structures but CSP parameter can also be applied to a diamond cubic lattice by considering the diamond cubic lattice as two identical FCC lattices.

Owing to thermal vibration of atoms, CSP has been proposed as the most effective measure [207].

A CSP can be computed using the following formula:

$$CSP = \sum_{i=1}^{N/2} \left| \overrightarrow{R_i} + \overrightarrow{R_{i+\frac{N}{2}}} \right|^2 \qquad 4\text{-}33$$

where N nearest neighbours of each atom are identified and R_i and $R_{i+N/2}$ are vectors from the central atom to a particular pair of nearest neighbours. Thus, the number of possible neighbour pairs can be given by $\frac{N \times (N-1)}{2}$ [208].

4.6.2 Calculation of cutting forces

Figure 4-10 shows schematically the main parameters affecting the process of nanometric cutting of anisotropic brittle materials, including a schematic representation of the crystal orientation [163, 209-211]. Regardless of whether the process is conventional turning or single point diamond machining, the cutting force remains one of the most fundamental parameters characterizing the process performance. As shown in the bottom panel of figure 4-10, two coplanar forces acting on a cutting tool fundamentally govern the cutting action of the tool, namely the tangential cutting force (F_c) and the thrust force (F_t). The third component shown, thrust force, F_z, acts in the direction orthogonal to the X and Y planes and mainly influences surface error as it tends to push the tool away from the workpiece. The tangential force causes displacements in the direction of cut chip thickness and its variation therefore relates to chatter.

From LAMMPS perspective, the calculation of cutting force for a diatomic pair potential is straightforward and can be done using a “compute group/group command”. This command, however, cannot normally be used with a many-body potential function as it only includes a pair potential portion and not the embedding term. However, this task can be accomplished manually by using an “fcm command” in conjunction with a “setforce command”.

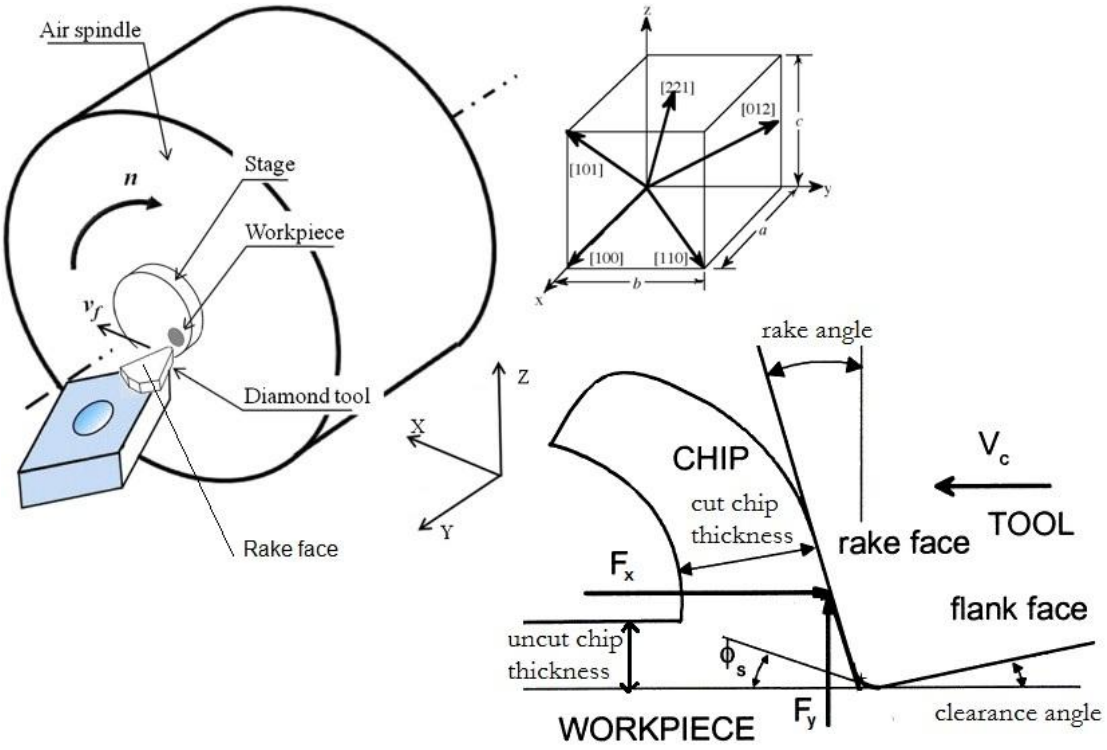

Figure 4-10: Schematic diagram of chip formation during SPDT - adapted from [212]

4.6.3 Calculation of machining stresses

The state of stress acting in the machining zone is shown schematically in figure 4-11 for both 2-D and 3-D stress systems. The stress tensor for an atom *i* can be calculated from equation 4-34.

$$S_{ab} = -\left[\begin{array}{l} mv_a v_b + \frac{1}{2}\sum_{n=1}^{Np}(r1_a F1_b + r2_a F2_b) + \frac{1}{2}\sum_{n=1}^{Nb}(r1_a F1_b + r2_a F2_b) + \\ \frac{1}{3}\sum_{n=1}^{Na}(r1_a F1_b + r2_a F2_b + r3_a F3_b) + \frac{1}{4}\sum_{n=1}^{Nd}(r1_a F1_b + r2_a F2_b + r3_a F3_b + r4_a F4_b) \\ + \frac{1}{4}\sum_{n=1}^{Ni}(r1_a F1_b + r2_a F2_b + r3_a F3_b + r4_a F4_b) + \sum_{n=1}^{Nf} ri_a Fi_b + Kspace(r_{ia}, F_{ib}) \end{array}\right] \quad 4\text{-}34$$

where *a* and *b* denote *x,y,z* to generate the 6 components of the symmetric stress tensor.

The first term in equation 4-34 is the contribution from the kinetic energy of atom *i*. The second term is a pair-wise energy contribution where *n* loops over the *Np* neighbours of

atom i and $r1$ and $r2$ are the positions of the two atoms in the pair-wise interaction. $F1$ and $F2$ are the forces on the two atoms resulting from the pair-wise interactions. The third term is a bond contribution over the N_b bonds of atom i. In a similar manner, N_a angle, N_d dihedral, N_i improper interactions and N_f internal constraints of atom i are accounted in the subsequent terms while the *Kspace* term represents long-range Coulombic interactions. It must be noted here that the three body potential function such as Tersoff potential function and ABOP potential function do not include Kspace terms in the stress computation. The above expression is however written only with an intention to comprehensively express the mathematical formula to determine the stresses at atomic scale.

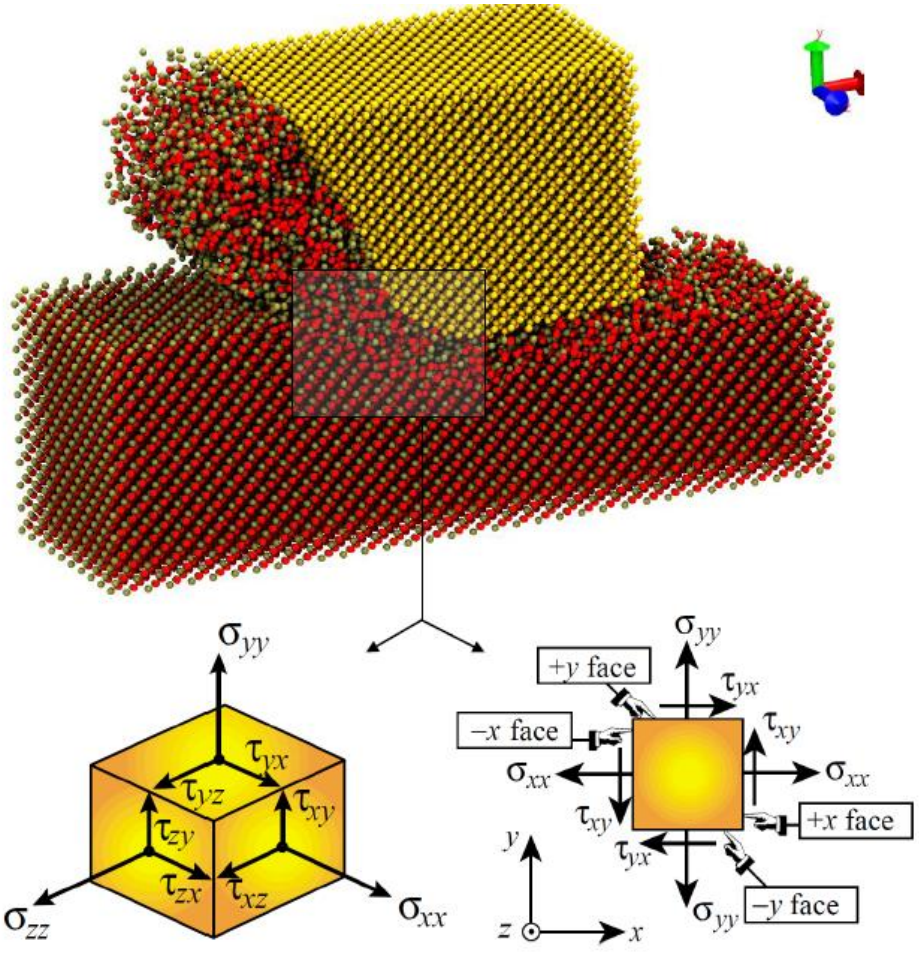

Figure 4-11: Stresses in the cutting zone

In a material continuum, hydrostatic stress is associated with a change of volume leading to classical thermodynamic phase transition, whereas the von Mises stress

(corresponding to maximum deviatoric strain energy) measures the deformation due to shear that governs the change in shape usually by the activation of a defect transport mechanism [213], most commonly dislocation movement. During the simulation run, the hydrostatic stress (σ_{hydro}) and von Mises stress (σ_{vonmis}) were computed using the following equations:

$$\sigma_{hydro} = \frac{\sigma_{xx} + \sigma_{yy} + \sigma_{zz}}{3} \quad 4\text{-}35$$

$$\sigma_{von\,Mises} = \sqrt{\frac{(\sigma_{xx} - \sigma_{yy})^2 + (\sigma_{yy} - \sigma_{zz})^2 + (\sigma_{zz} - \sigma_{xx})^2 + 6(\sigma_{xy}^2 + \sigma_{yz}^2 + \sigma_{zx}^2)}{2}} \quad 4\text{-}36$$

One fundamental problem in the computation of atomic stress is the fact that the volume of an atom does not remain fixed during deformation. To mitigate this problem, an elemental atomic volume was considered in the cutting zone for the computation of the stress tensor. The total stresses acting on that element were computed and were divided by the pre-calculated total volume of that element. In LAMMPS, this can be done using a "stress/atom" command followed by a "reduce sum" command.

4.6.4 Calculation of the temperature in the cutting zone

Due to the nature of the statistical mechanics in which an ensemble is defined, the instantaneous values for the atoms differ from the bulk property of the substrate. This phenomenon is called fluctuation. Temperature is also an ensemble property and so measurement of the temperature is not straightforward. The suitability of any method used to measure the temperature depends primarily on how many atoms are being analysed and how fast the released energy is dissipated by the surroundings. The velocity of the atoms is normally used to compute the average temperature of the atoms using the relationship between kinetic energy and temperature:

$$\frac{1}{2}\sum_i m_i v_i^{\,2} = \frac{3}{2} N k_b T \qquad 4\text{-}37$$

where N is the number of atoms, v_i represents the velocity of i^{th} atom, k_b is the Boltzmann constant (1.3806503×10^{-23} J/K) and T represents the atomistic temperature. During the process of nanometric cutting, the instantaneous fluctuations in kinetic energy per atom could be very high so these are averaged temporally and/or spatially over few timesteps and reassigned to each atom at every N steps to be converted into equivalent temperature. The movement of the tool will also contribute to the kinetic energy so the component of tool displacement should be subtracted beforehand. In general, LAMMPS computes the temperature of a group of atoms by using a "compute ke/atom" command followed by applying a "fix ave/atom" command.

4.6.5 Quantification of tool wear

The two most common allotropes of carbon, diamond and graphite, have different coordination numbers. In diamond, each carbon atom is at the centre of a tetrahedron formed by four other carbon atoms, so the coordination number is four. Graphite is made of two-dimensional layers in which each carbon atom is covalently bonded to three other carbons. Atoms in other layers are further away and are not in the nearest neighbour category, so the coordination number of a carbon atom in graphite is 3.

This information is very helpful not only in verifying the mechanism of tool wear but also to quantify the tool wear if the number of carbon bonds in the tool changes from 4 to 3 during the graphitization process.

During graphitization, the number of atoms presenting a coordination number of 4 in the diamond tool decreases with a corresponding increase in the number with a coordination number of 3. A few atoms on the cutting tool would have a coordination number of 3 at the start of simulation representing dangling bonds on the rake and flank

faces. To eliminate the effect of these dangling bonds on the conclusion, the number at the start of simulation can be assumed as the datum and subtracted from the number of atoms with 3 fold coordination during the simulation. Thus, a graph can be plotted indicating the percentage rate of graphitization or percentage progress of tool wear with the progressive advancement of the tool. Such a model can be used to characterize the tool wear during MD simulations. The computation of displacement of the tool atoms using the "displace/atom" command of the LAMMPS software which computes the current displacement of each atom from its original coordinates, including all effects due to atoms passing through periodic boundaries, is another useful measure of the extent of deformation of tool atoms. Number of atoms separated from the tool can be multiplied with the atomic volume of the material to obtain volumetric wear rate.

4.7 Summary

This chapter has provided a detailed description of the molecular dynamics simulation. Starting with an introduction to the concept and the background to its development, it goes on to provide the basis of the calculations required to perform an MD simulation of the nanometric cutting process. The chapter first introduces the advantages and the current limitations of MD simulation. This comparison justifies the choice of the potential energy function to perform an appropriate simulation. It was recognized that most of the previous research is done using a Morse potential function which is more appropriate for diatomic molecules than for hard, brittle materials which are covalent. The strong need for an appropriate potential function was highlighted and a thorough review of this type of formalism has been presented. It is shown that molecular dynamics simulations have been used to advance knowledge of the mechanisms of nanometric cutting over the past few decades. Taking the example of the brittle-ductile

transition, it has also been shown that it was only through molecular dynamics simulations that a conceptual understanding of this phenomenon is gathered.

It is also noted that, in order to replicate simulation results or to perform other simulations, the simulation conditions need to be understood very well. Accordingly, the preparations required for a simulation and the post-processing tools are also comprehensively described, including measurement of cutting forces using the three-body potential function, use of a periodic boundary condition and measurement of stresses during a simulation. A novel method has been described to quantify the tool wear from a MD simulation.

Chapter 5 - MD simulation results for the nanometric cutting of silicon

5.1 Introduction

Machining silicon in the ductile regime involves a number of simultaneously occurring processes, high pressure phase transformation (HPPT), wear of the cutting tool, movement of dislocations, all of which are influenced by the crystallographic structure and orientation of both the cutting tool and the workpiece. HPPT in silicon is already very well documented, although tool wear has received relatively little attention up to now. In the few reported studies so far of wear of diamond tools the results are inconsistent, most likely because the experimental conditions were quite different, a circumstance often encountered in machining. A good understanding of the wear characteristics of single crystal diamond tools during ductile mode cutting of brittle materials such as silicon can be used to enhance machining performance as well as to prolong tool life. Because of the anisotropy in the mechanical properties of single crystal diamond as well as some of the conflicting results of tool wear studies, as seen in the literature review, it is crucial to determine the phenomenological cause of tool wear. This chapter describes the molecular dynamics simulations aimed at studying crystal anisotropy, high pressure phase transformation and tool wear during the ductile-regime machining of silicon.

5.2 Influence of the crystal anisotropy

It has been found that the crystallographic directions corresponding to minimum values of the effective resolved shear stress are those with maximum hardness [80]. Also, the pressure required to drive phase transformation in silicon is sensitive both to the crystal

orientation and the cutting direction, i.e. the <001> cutting direction produces better metallic response than the <110> cutting direction on the (100) orientation of silicon [214] whereas the (111) orientation requires less transformation pressure than the (100) orientation [215]. Jasinevicius *et al.* [37] conducted experimental trials to investigate why two different cutting directions on the same orientation gave different machining outcomes, particularly that the soft direction i.e. <110> produced worse surfaces than the hard direction, <100>, on the same orientation (001). Based on their experimental results, they suggested that the difference between the high pressure phase transformation pressure of the workpiece and the hardness of the workpiece in the soft direction is larger which requires more energy to drive HPPT. Hence, brittle mode becomes dominant along the soft direction..

Table 5-1: Variables used in the MD simulation model

Workpiece dimensions	42.0743 nm ×4.6353 nm × 3.5656 nm
Cutting edge radius	1.313 nm
Uncut chip thickness / in-feed	1.313 nm
Crystal Orientation	Three simulation cases were tested: i. Cubic orientation of tool with cutting direction <-110> while workpiece was machined on (111) orientation. ii. Cubic orientation of tool with cutting direction <100> while workpiece was machined on (010) orientation. iii. Dodecahedral orientation of tool with cutting direction <-110> while workpiece was machined on (111) orientation.
Tool rake and clearance angle	-25° and 10°
Equilibration temperature	300 Kelvin
Cutting velocity	100 m/s
Timestep	0.5 femtoseconds

The diamond tool also shows a high degree of crystal anisotropy. Uddin *et al.* [210] have recommended the dodecahedral orientation while Cheng *et al.* [55] have suggested using the cubic orientation, both in the interest of enhancing tool life. Accordingly the present work considers three simulation cases with different combinations of crystal orientations to investigate their influence on the thrust forces during nanometric cutting of silicon. The simulation was performed with the parameters shown in table 5-1.

The evolution of thrust forces with change in crystal orientation is believed to be a useful measure for identifying appropriate crystal orientations for practical purposes. Table 5-2 and figure 5-1 show the results obtained for the thrust forces while cutting silicon using different combinations of crystal orientations of tool and workpiece. It can be seen that the time rate of change and magnitude of thrust force was least while using the (111) orientation of the workpiece with cubic orientation of the diamond tool.

Table 5-2: Calculation of cutting forces with different crystal orientation

S.N.	Orientation of silicon workpiece	Cutting direction	Orientation of diamond tool	Magnitude of thrust forces observed:
1	(111)	<-110>	cubic	minimum
2	(010)	<100>	cubic	intermediate
3	(111)	<-110>	dodecahedral	maximum

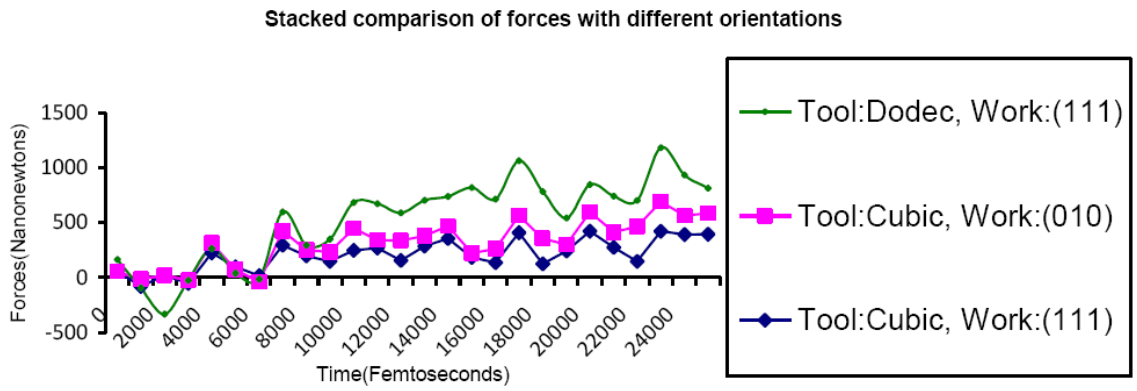

Figure 5-1: Variation in the thrust forces during nanometric cutting of silicon

While the simulation reveals that the cubic orientation of the diamond tool performed better, the discussion in section 3.4 indicated that it is actually the magnitude of the negative rake angle which dictates whether or not the dodecahedral or cubic orientation will perform better. One observation which is clear from the MD simulation is that the machining of silicon on the (111) plane along the <-110> cutting direction consumes least energy which is in accordance with the majority of published work.

5.3 Machining stresses

Figure 5-2 shows a schematic representation of the stress tensor in 3D and 2D acting on an elemental volume of the silicon workpiece in the cutting zone. The evolution of the various stresses acting on this elemental volume of silicon over the simulated period is shown in figure 5-3. It is evident that silicon experiences a peak compressive stress of up to 18 GPa in the direction of the tangential cutting force, σ_{xx} and this is the largest component of the stress tensor. This is followed by σ_{yy} at around 16 GPa (also in compression) and τ_{xy} at around 8 GPa. Moreover, silicon encounters a significant deviatoric stress, which could bring about shear induced metallisation [44]. Both the hydrostatic and the von Mises stresses hover around 14 GPa. The above stress state and the indicative magnitude are quite consistent with the values previously reported as required to cause the HPPT of silicon from its stable diamond cubic structure to the metallic Si-II structure, which is discussed in more detail in section 5.4.

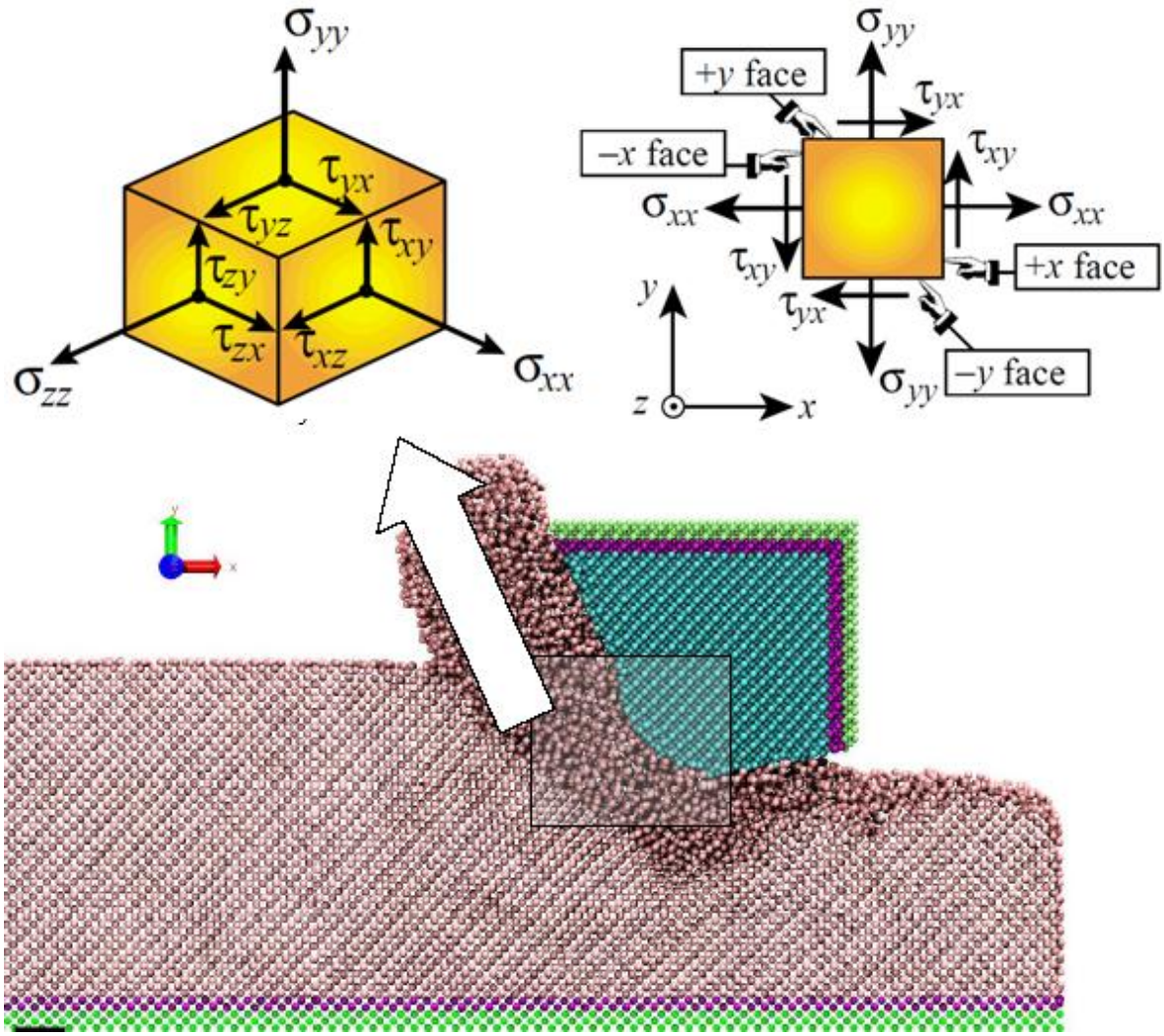

Figure 5-2: Stresses acting in the machining zone during nanometric cutting [216]

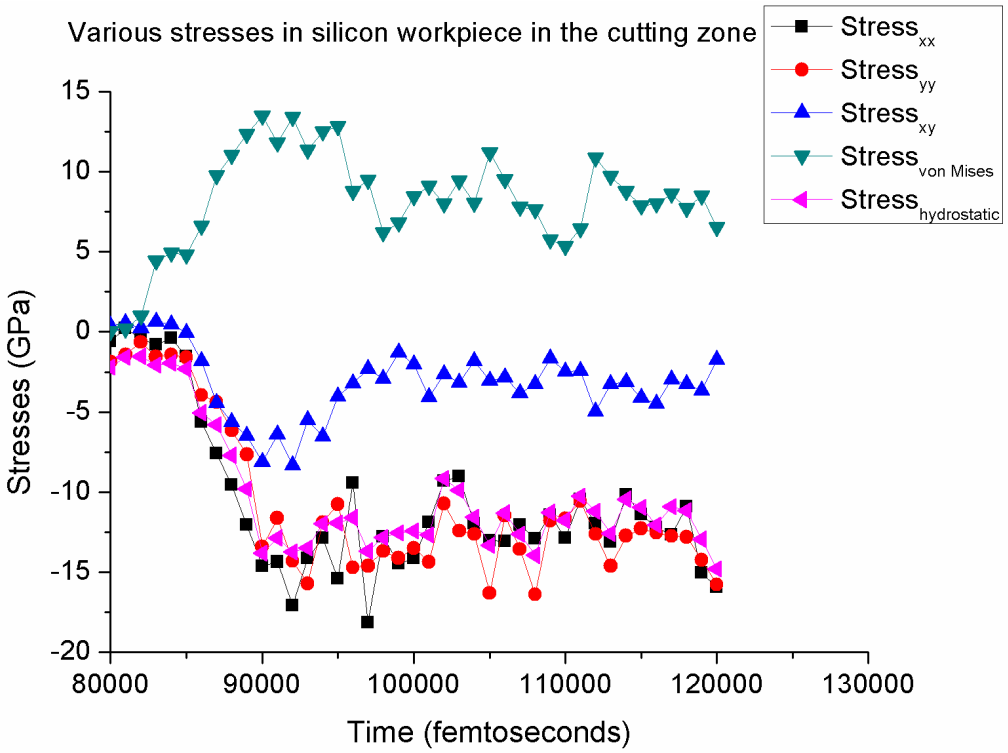

Figure 5-3: Stresses in silicon during its nanometric cutting

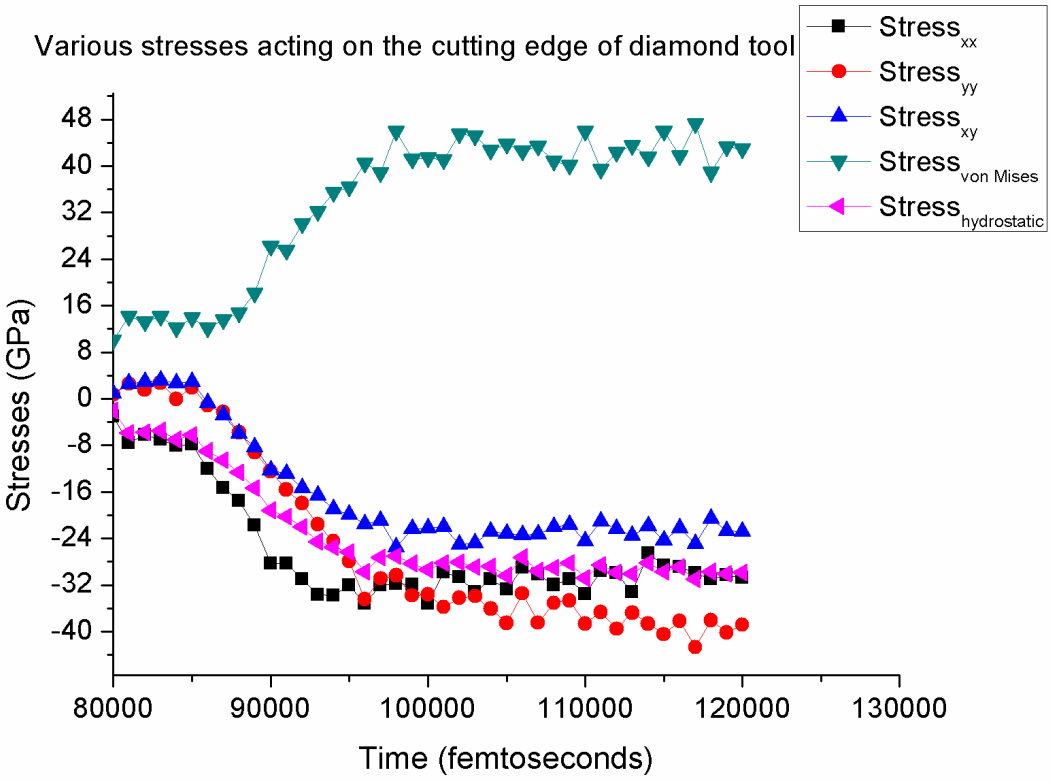

Figure 5-4: Stresses acting on the cutting edge of the diamond tool during SPDT of Si

Figure 5-4 shows the evolution of the stresses acting on the cutting edge radius of the diamond tool over the simulated period. It can be seen that the maximum magnitude of both σ_{xx} and σ_{yy} fluctuates between -30 GPa and -40 GPa indicating a high degree of compression of the diamond tool. A similar variation in the magnitude of the hydrostatic stress and von Mises stress acting on the diamond tool is also apparent from figure 5-4. The shear stress was, however, found to be of the order of 20 GPa which is close to the magnitude of the shear stress that acts on diamond during its polishing with another diamond [163]. Figure 5-5 shows a prediction [217] of the stresses required to drive a metallic-phase transformation in diamond (290 GPa). It can be seen from figure 5-4 that the von Mises stress acting on the diamond tool during machining of silicon was well below value of 290 GPa, indicating that diamond does not undergo a metallic phase transition while machining silicon. Also, it is now known that the minimum shear stress required to cause a phase change in carbon from its diamond lattice structure to its stable *hcp* graphite structure is around 80–100 GPa [218-219] which is much higher than the cutting stresses observed from figure 5-4. This suggests that perhaps tribochemistry is the main mechanism governing the wear of diamond tools during nanometric cutting of silicon rather than HPPT of diamond.

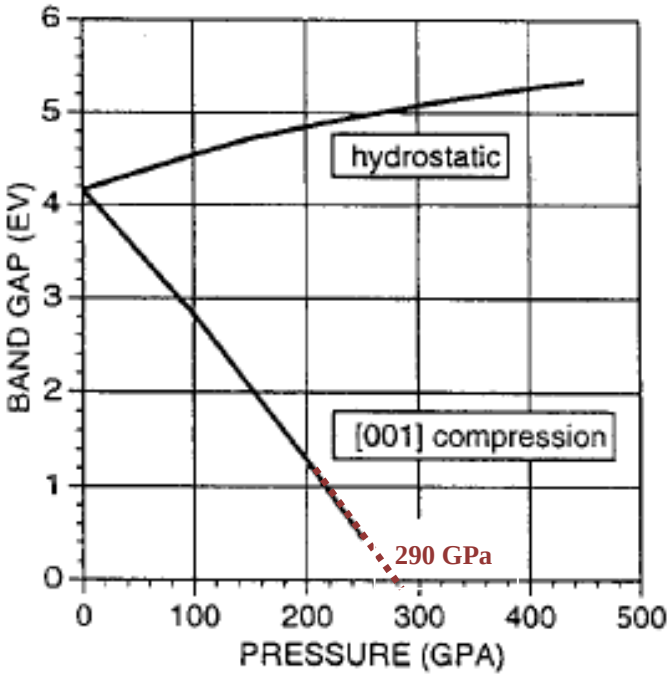

Figure 5-5: Change in the band gap of diamond due to the stress conditions [44]

5.4 High pressure phase transformation of silicon

As explained earlier, it is high pressure phase transformation (HPPT), now known as the Herzfeld-Mott transition, which causes metallization of brittle materials during their nanometric cutting. Such transformations are classed as metallic because they cause closure of the valence-conduction band gap due to overlap of wave functions and hence delocalization of the valence electrons [217].

Domnich *et al.* [98, 220] have stated that, under the influence of a hydrostatic pressure of 9-16 GPa, bulk silicon experiences a high pressure phase transformation resulting in the transformation of the Si-I (cubic diamond structure) into a more dense metallic Si-II phase having a β-tin structure [221]. The reverse transformation depends on the mode of unloading/release of the pressure. For instance, on slow decompression, Si-II transforms to Si-XII or r8 (rhombohedral structure with 8 atoms per unit cell), which corresponds to a volume increase of around 8%. On further pressure release, the degree of rhombohedral distortion diminishes gradually, producing a mixture of Si-XII and Si-III

or bc8 (body centred cubic structure with 8 atoms per unit cell), with some Si-XII persisting to ambient pressure. This cycle is schematically represented in figure 5-6. The pressure required to produce a metastable amorphous semiconductor phase upon unloading is about 7.5–9.0 GPa [37] and it is the corresponding change in volume from Si-II (more dense and low volume) to a-Si (more structural volume) which causes expansion and the consequent elastic recovery of the machined surface after the tool passes. However, the extent of this elastic recovery reduces with increasing E/H ratio of the materials involved [90].

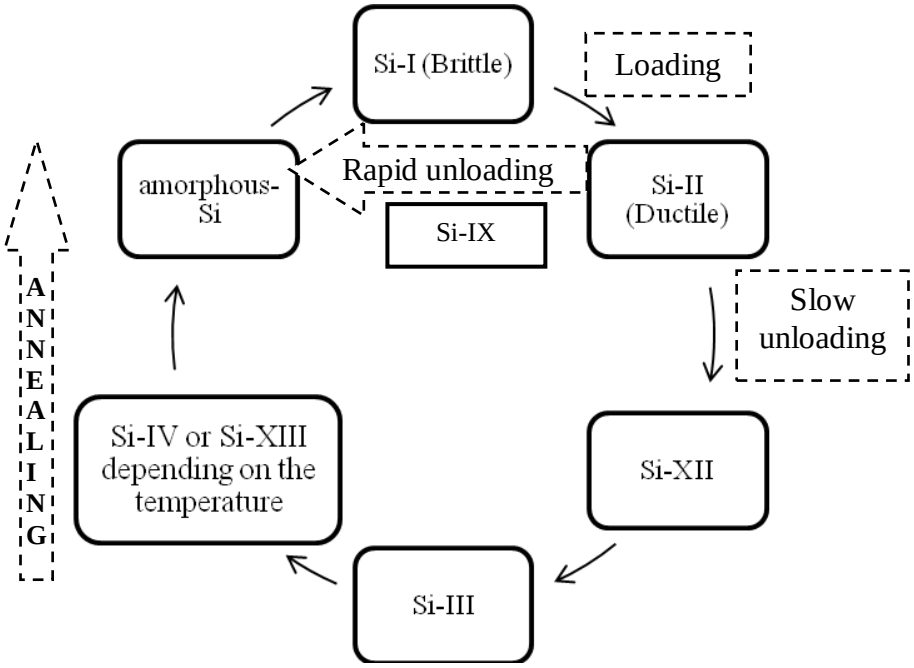

Figure 5-6: Phase transformations in silicon during its contact loading [222]

The phases involved in the response of silicon during its cutting in the ductile regime are summarised in table 5-3 [223] and their roles explained hereunder. High shear stress underneath the cutting tool leads to the metallization of Si-I to Si-II, which can be deformed plastically akin to a metal machining process [224]. Si-II phase subsequently transforms either into a-Si or a mixture of Si-III and Si-XII, depending on the cutting conditions. These back transformations are accompanied by an increase in volume of ~10% and contribute to the elastic recovery of the machined surface after the tool

passes. It is also noteworthy that the geometry of the diamond tool also affects the transformations. For example, Gogotsi *et al.* [225] have used a nano-scratching test to demonstrate the influence of the geometry of the indenter in driving the various phases during contact loading of silicon on the (111) crystal orientation, the outcome of which is shown in table 5-4.

Table 5-3: HPPT of silicon during its contact loading – adapted [98, 223, 226]

Phase of Silicon	**Lattice structure**	**Pressure (GPa)**	**Lattice parameter (Å)**	**Raman band (cm^{-1})**	**Relative volume**
Pristine Si-I (brittle)	Diamond cubic	0-12.5	a =5.42	521	1
Si-II (Metallic)	(Beta-tin)	9-16	a=4.69 c=2.578	137,375	0.78
Si-XII	R8, Rhombohedral	12-2	a=5.609 γ=110.07	184, 350, 375, 397, 435, 445, 485	0.9
Si-III	bc8 (BCC)	2.1 – 0 (ambient)	a=6.64	166, 384, 415, 433, 465	0.92
Si-IV	Hexagonal diamond	Martensitic transformation from Si-I	a=3.8 c=6.629	510	~0.98
Si-IX	St12, tetragonal	Upon rapid decompression from Si-II	Information not available yet		~0.88
Si-XIII	New martensitic phase, Raman peaks at 200, 330, 475 and 497				
a-Si	Raman bands at : TA-160, LA-300, TO-390, LO-470				

While pristine silicon experiences HPPT, which is responsible for its ductility, this is not the case with its nanoparticles. In contrast to bulk silicon, ductility in silicon nanoparticles is attributed to dislocation driven plasticity [227-228] rather than HPPT. Therefore, processes like high pressure phase transformation, movement of dislocations and micro fracture can all coexist and compete with one another during the contact loading of silicon and other brittle materials. This research area is now emerging as a new field of knowledge and is being referred to as High Pressure Surface Science [202].

Table 5-4: Comparison of the ductile response of silicon with different tools [225]

Category	Conical tool	Pyramidal tool (Vicker indenter)	Spherical tool (Rockwell indenter)
Shape	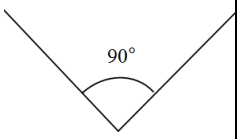	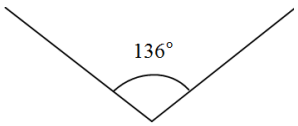	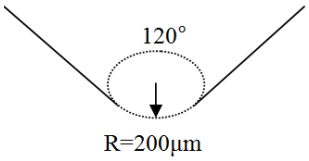
Rake angle	-45°	-68°	Variable from about -60° to -90°
Material removal	Yes	Yes	No
Si Phases	Si-III, Si-XII, Si-IV and a-Si	Si-III, Si-XII, Si-IV and a-Si	Si-III, Si-XII and a-Si
Maximum stress	Near the edge	Near the edge	In the middle

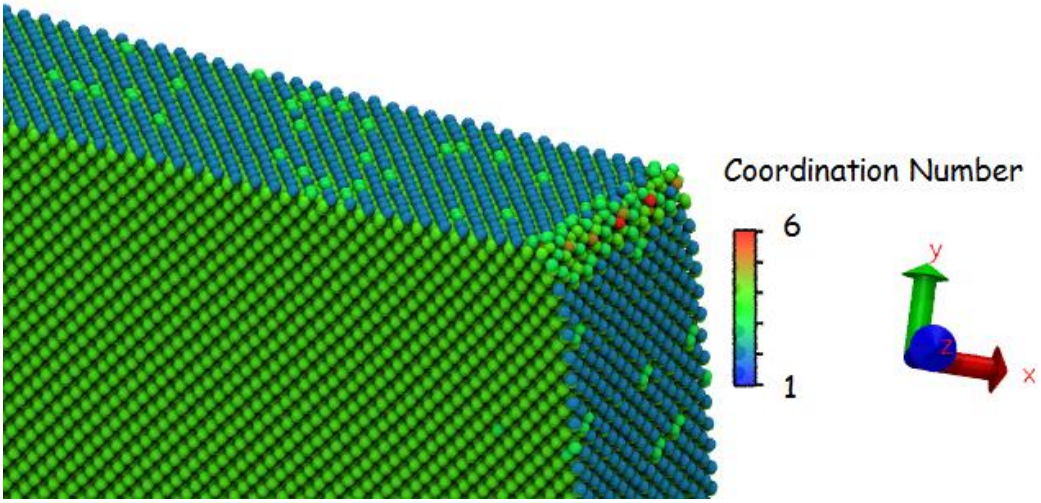

Figure 5-7: Change in coordination number of silicon during nanometric cutting of Si

Figure 5-7 shows the variation in the coordination number of silicon during its nanometric cutting after the tool has advanced by 1 nm while the workpiece is machined on the (010) surface along the <100> cutting direction using the cubic orientation of the tool. It can be seen that the bulk of the single crystal silicon has a coordination number of 4 which is indicative of a covalently bonded system in a diamond cubic structure. Coordination values of 1 and 2 represent termination of bonds (dangling bonds) on the

surface of the silicon workpiece. During nanometric cutting, the number of atoms with a coordination value of 4 decreases with a corresponding increase in the number of atoms with coordination values of 5 and 6. A change in coordination value from 4 to 6 during nanometric cutting indicates the formation of the Si-II metallic silicon structure as has been observed in the past. Essentially, pristine silicon has an atomic volume of 18.38 $Å^3$ with atoms having a bond length of 2.35 Å. The high-pressure (metallic) phase of silicon, i.e. Si-II, has an atomic volume of 14.19 $Å^3$. Also, Si-II has a bct structure with lattice constants a=4.686 Å and c=2.585 Å and (c/a ratio of 0.5516). Therefore, HPPT transformation of silicon is accompanied by a reduction in the atomic volume from 18.38 $Å^3$ to 14.19 $Å^3$ per atom which means a volumetric reduction of about 22.8% where the Si-II structure has four nearest silicon neighbour atoms at 2.43 Å and the two next neighbours at a distance of 2.585 Å.

As discussed earlier, Gilman [46] stated that the value of coordination number of Si-II cannot be perfectly 6 because there is always a difference of 5.6% between the consecutive nearest neighbour atoms. It is therefore worthwhile confirming the HPPT of silicon using a RDF, which is shown in figure 5-8.

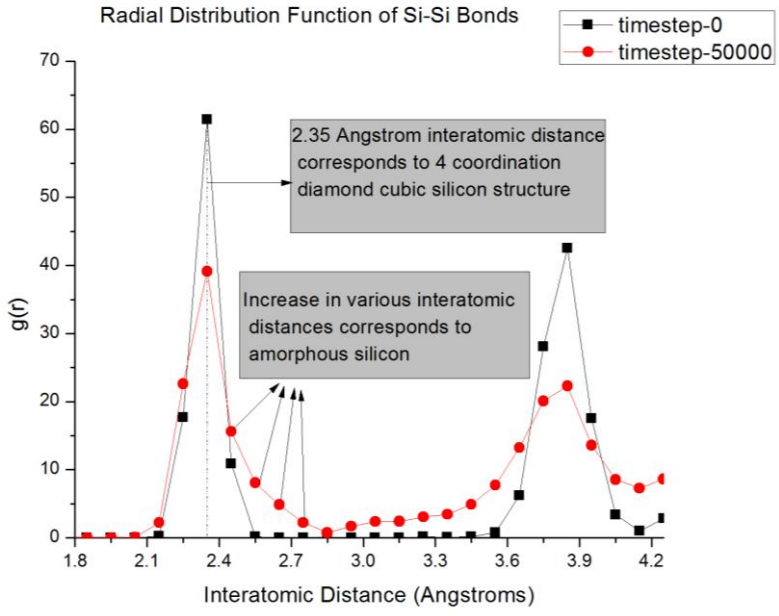

Figure 5-8: Radial distribution function of Si-Si during nanometric cutting of Si

As can be seen from figure 5-8, the RDF before nanometric cutting has a first sharp peak at an inter-atomic distance of 2.35 Å and a second peak at 3.85 Å, which is the inter-planar spacing in the tetrahedral geometry of silicon. Once cutting commences, the peak widens significantly involving various inter-atomic distances at the expense of the number of atoms having an inter-atomic distance of 2.35 Å, reconfirming polymorphic transformation induced amorphization of silicon.

Figure 5-9 shows a snapshot taken from the MD simulation corresponding to the same parameters of machining for which the measurement of coordination number in figure 5-7 is shown. It highlights the variation in centro symmetry parameter (CSP) after the tool has advanced by 1 nm where a zero value of CSP corresponds to an atom surrounded by other atoms on a perfect lattice and a positive value of CSP corresponds to lattice disorder including the surface atoms. The higher positive value of CSP in the cutting zone is another confirmation of lattice disorder during nanometric cutting of silicon. Unlike the coordination number, the value of CSP does not suggest any phase change of the material and may take any value, depending on the cutting conditions. However, a comparison of figures 5-7 and 5-9 clearly suggests that there is a lot more consistency in the colour of surface atoms in the CSP measure than the coordination number. This, in turn, confirms that CSP is the more effective measure of lattice disorder in a thermally sensitive environment.

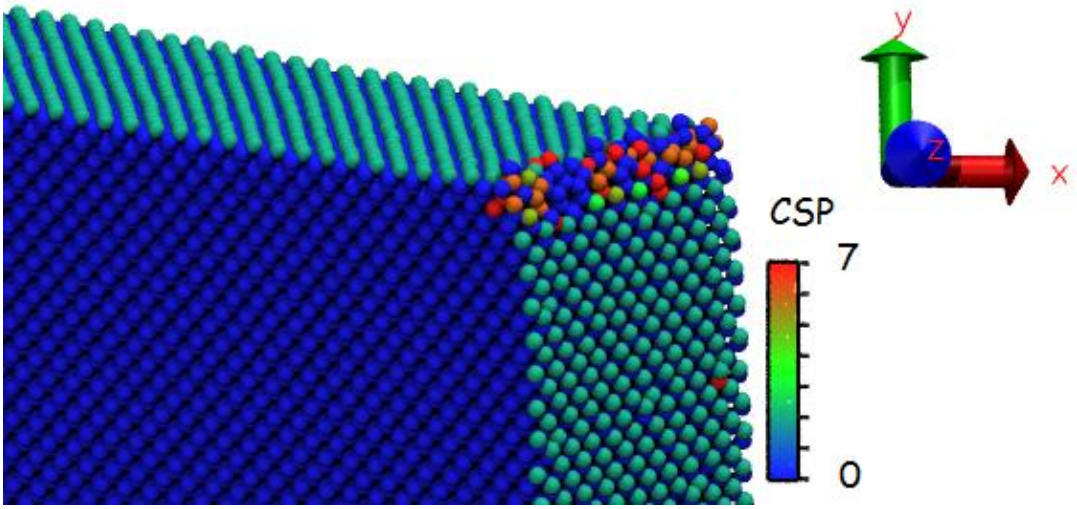

Figure 5-9: Change in centro-symmetry parameter during nanometric cutting of silicon

To gain further insights into the phase change and tool wear, a snapshot was captured from the simulation after a significant cutting length and this is shown in figure 5-10. It can be seen from figure 5-10 that, alongside HPPT, a few atoms also show a coordination value of 1 or 2 in the cutting zone and on the finished surface which signifies the formation of dangling bonds of silicon during cutting. These are highly reactive sites which combine chemically with the nascent surface of the diamond tool to form a stable compound of diamond and silicon discussed in detail in the next section.

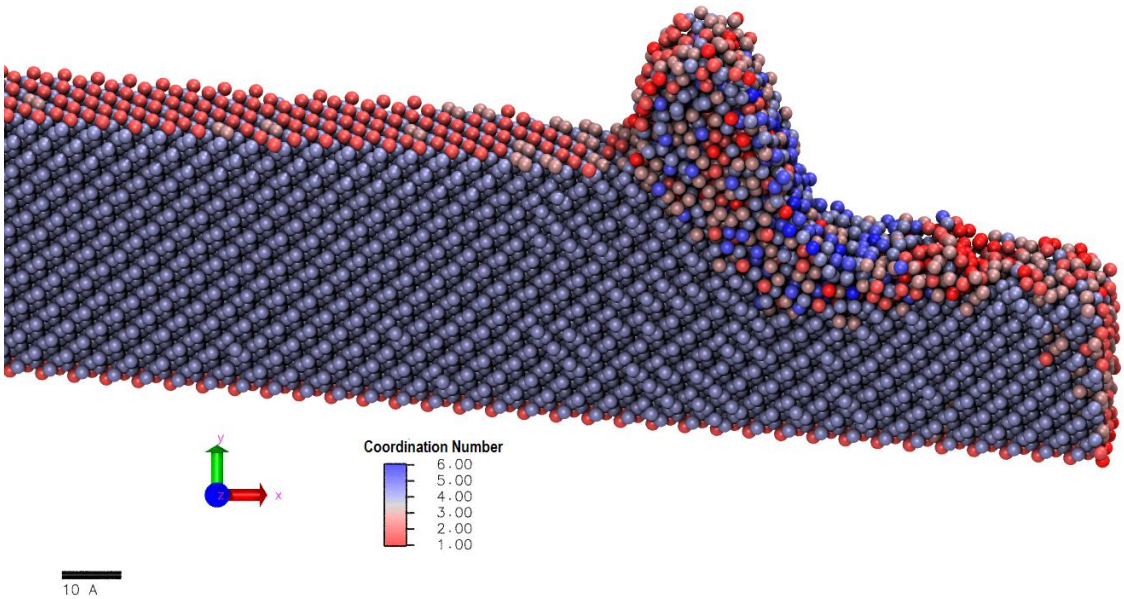

Figure 5-10: Detailed view of change in coordination number during nanometric cutting of silicon

5.5 Wear mechanism of diamond tools

A good understanding of the wear mechanism is an essential step in the identification of the measures needed to suppress wear and so enhance tool life. Much work has been done in the past on the characterization of tool wear in SPDT through observations and measurements of worn tools following experimental machining trials. An important consideration, neglected in the past, is that, at a constant spindle rotation speed, the surface cutting speed varies from maximum on the outside of the workpiece to zero at the centre. Thus, the obvious differences in wear behaviour due to different cutting speeds have not been accounted for hitherto. Early characterization of tool wear has used qualitative descriptors, such as; normal wear, chipping, setting problems (not related to diamond tools), line effects, chip dragging and fracture [74]. A brief summary of past tool wear studies performed using MD simulation and their conclusion is given in table 5-5.

Table 5-5: MD studies of tool wear during SPDT

Potential function for tool-workpiece interaction	Material	Author, Year and country	Tool consideration	Conclusion of the study concerning cause of tool wear
LJ	Silicon	J. Belak, 1990, USA [49, 57]	Deformable	SiC asperity was observed during SPDT of silicon
Morse	Copper	K.Maekawa, 1995, Japan [58]	Deformable	Interdiffusion and readhesion
Tersoff	Silicon	R.Komanduri, 1998, USA [54, 61]	Rigid	-
MEAM	Silicon	X.Luo, 2003, UK [55]	Deformable	Thermo-chemical mechanism
Morse	Silicon	M.B. Cai, 2007, Singapore [77, 229]	Deformable	Formation of dynamic hard particles
MEAM	Iron	R. Narulkar, 2008, USA [86]	Deformable	Graphitization of diamond
Morse	Silicon	Z. Wang, 2010, China [230]	Deformable	No mechanism has been described

As is evident from table 5-5, there is considerable disagreement amongst the conclusion of these studies concerning tool wear during SPDT of silicon. While Cheng *et al*. [55] have identified a thermo-chemical mechanism as governing wear, Maekawa *et al*. [58] have suggested inter-diffusion and re-adhesion. A theory, in which formation of "dynamic hard particles" causes tool wear has also been proposed [77, 229], but it lacks experimental evidence. Thus, the MD simulations that have been applied so far have not elucidated a convincing mechanism of tool wear during SPDT of silicon. It is also pertinent to note that the MD simulations performed by most of the researchers have used a Morse potential function to describe tool-workpiece interactions [58, 229-230] which is more appropriate for diatomic molecules. A study made by Komanduri *et al.* [61] used a Tersoff potential function but assumed the tool to be a rigid body so tool wear could not be studied. The simulation performed in the current work involves the use of a three-body potential function and is thus capable of providing a much better insight into the wear process. The radial distribution function between the silicon workpiece and the diamond tool extracted from the simulation is shown plotted at regular intervals in figure 5-11. This plot allows the tracking of the chemical activity between the diamond tool and silicon workpiece during cutting.

At timestep 0 in figure 5-11, *g(r)* is 0 which means there is no chemical bonding between Si and C before the physical contact between the tool and the workpiece. With tool advancement a first peak at an inter-atomic distance of 1.9 Å and a second peak at around 3.08 Å both grow to a relatively constant level of around 0.6.

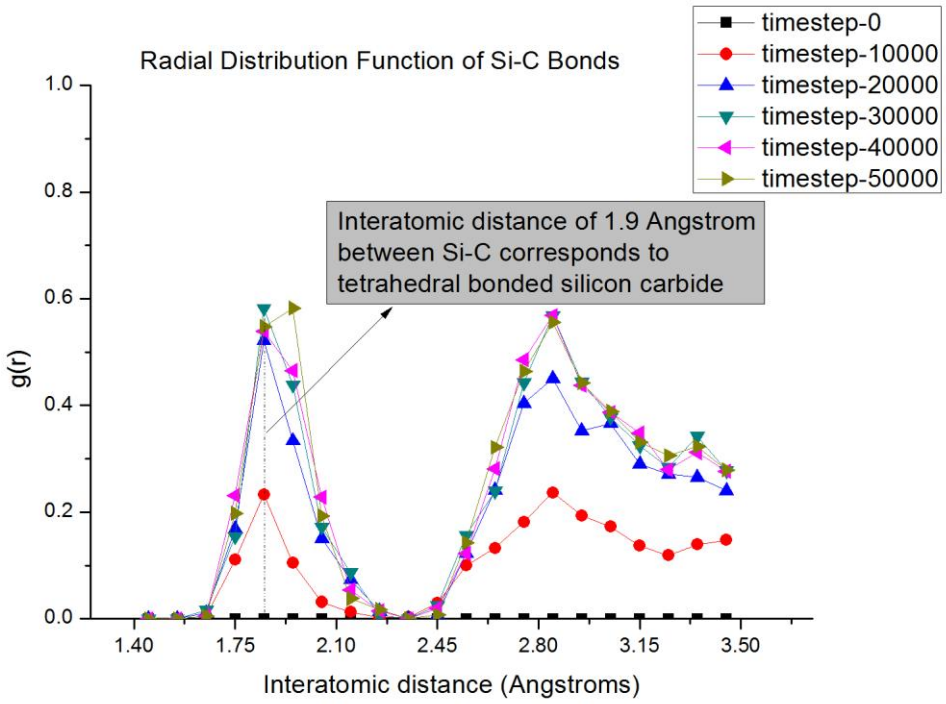

Figure 5-11: Radial distribution function between Si-C during nanometric cutting of Si

It is well known that tetrahedral silicon carbide (SiC) possesses the same bond length and interplanar spacing and so this is a clear indication of the formation of silicon carbide during the SPDT of silicon. The close contact between the workpiece and tool results in a locally high temperature which, in the actual machining environment, is supplemented with the presence of ambient oxygen. The highly reactive freshly generated dangling bonds of silicon will tend to combine with the atmospheric oxygen to form silicon dioxide as the free energy is negative at all temperatures [231]. However, the reaction mechanism thereafter may either be through a single phase solid state reaction or through a multiphase reaction as shown in table 5-6.

Table 5-6: Reaction mechanism for formation of silicon carbide

Process	Chemical Reaction	Free energy change for the reaction
Single Phase Reaction		
Formation of Silicon carbide	Si (s,l,g) + C → SiC [232]	$\Delta G_T^O = 499820 - 149T \ J/mol$
Multiphase Reaction		
Formation of Silicon Dioxide	$Si + O_2 \rightarrow SiO_2$ [232]	Free energy change in negative in all cases [231]
Formation of Silicon oxide	$SiO_2 + C \rightarrow SiO + CO$ [232]	$\Delta G_T^O = 670402 - 327T \ J/mol$
Formation of Silicon carbide	$SiO + 3CO \rightarrow SiC + 2CO_2$ [233-234] or SiO (g) + C (s) → Si (g) + CO (g) [232] Si (g) + C (s) → SiC (S) [232]	

Figure 5-12 shows the free energy change for the two routes as a function of process temperature and hence shows the precedence with respect to temperature. It can be seen from figure 5-12 that, in either case, the free energy change is positive and hence the reaction will not be spontaneous. Also, the solid state single phase reaction between silicon and carbon is thermodynamically more favourable up to a temperature of 959 K and, beyond a temperature of 959 K, the silicon dioxide path is energetically the more favourable route towards the formation of silicon carbide, which implies that the presence of oxygen at a temperature above 959 K will accelerate the formation of

silicon carbide. It is therefore necessary to know the cutting temperature in order to establish the route to the formation of silicon carbide. The temperature distribution on atoms obtained from the simulation of nanometric cutting of silicon is shown in figure 5-13.

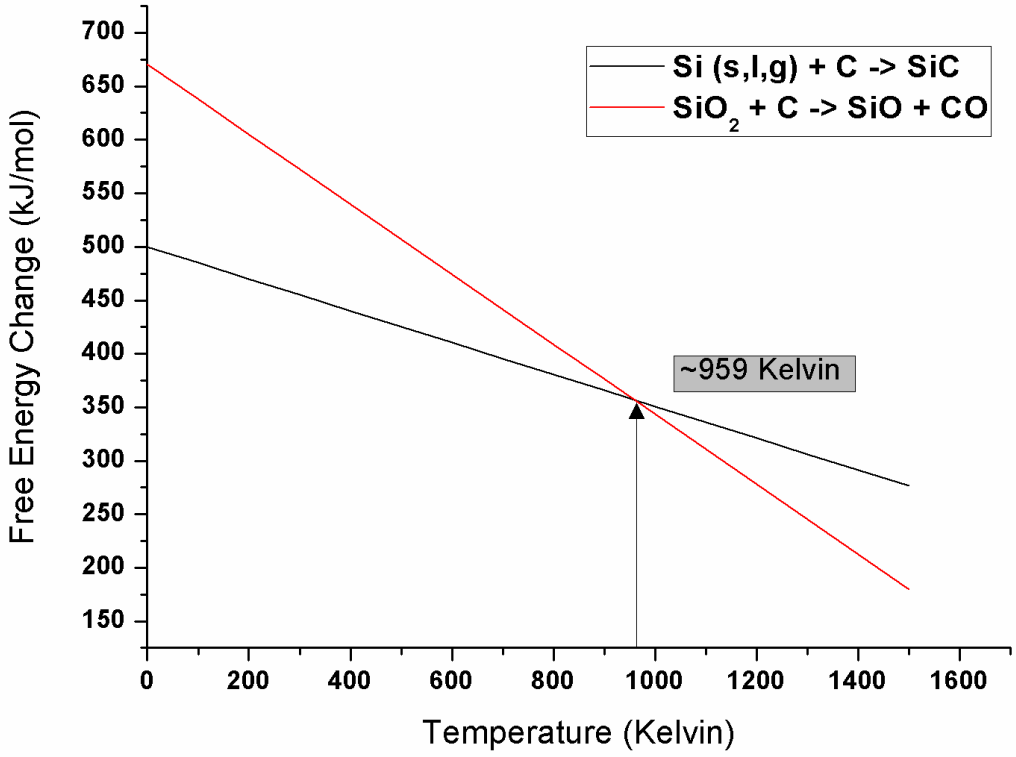

Figure 5-12: Gibb's free energy change for the formation of SiC

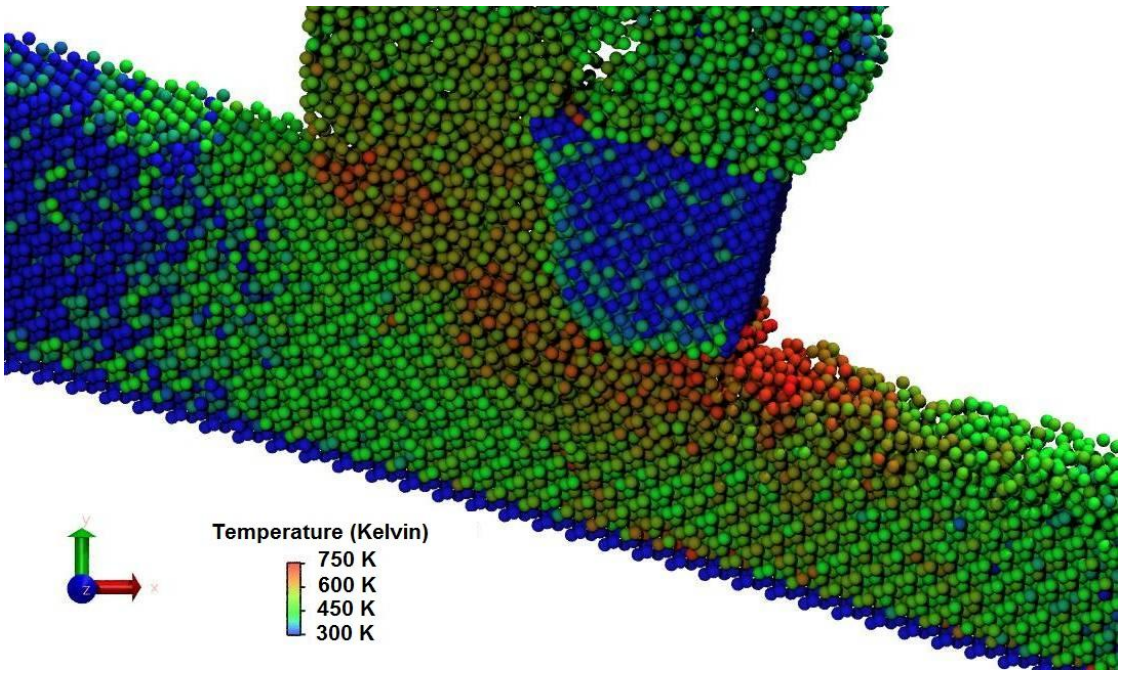

Figure 5-13: Temperature distribution on atoms during SPDT of silicon [235]

The maximum temperature on the tool tip was observed to be around 380 K while that on the workpiece was observed to be in the primary shear zone and on the finished surface approaching 750 K at a (high) cutting speed of 100 m/s. Since, the local temperature is well below 959 K, even at such a high cutting speed, it is reasonable to conclude that the formation of silicon carbide will proceed by single phase solid state chemical reaction between dangling bonds of silicon having coordination number 1 or 2 and highly chemically active nascent surface/dangling bonds on the diamond tool during their surface contact, and that this will be stimulated further by the cutting stresses. Pastewka [62] has carried out an MD simulation of polishing of a diamond crystallite with another diamond crystallite at a sliding speed of 20 m/s. He has similarly concluded that the tribochemistry plays a significant role in governing the wear rate of diamond, as shown in figure 5-14.

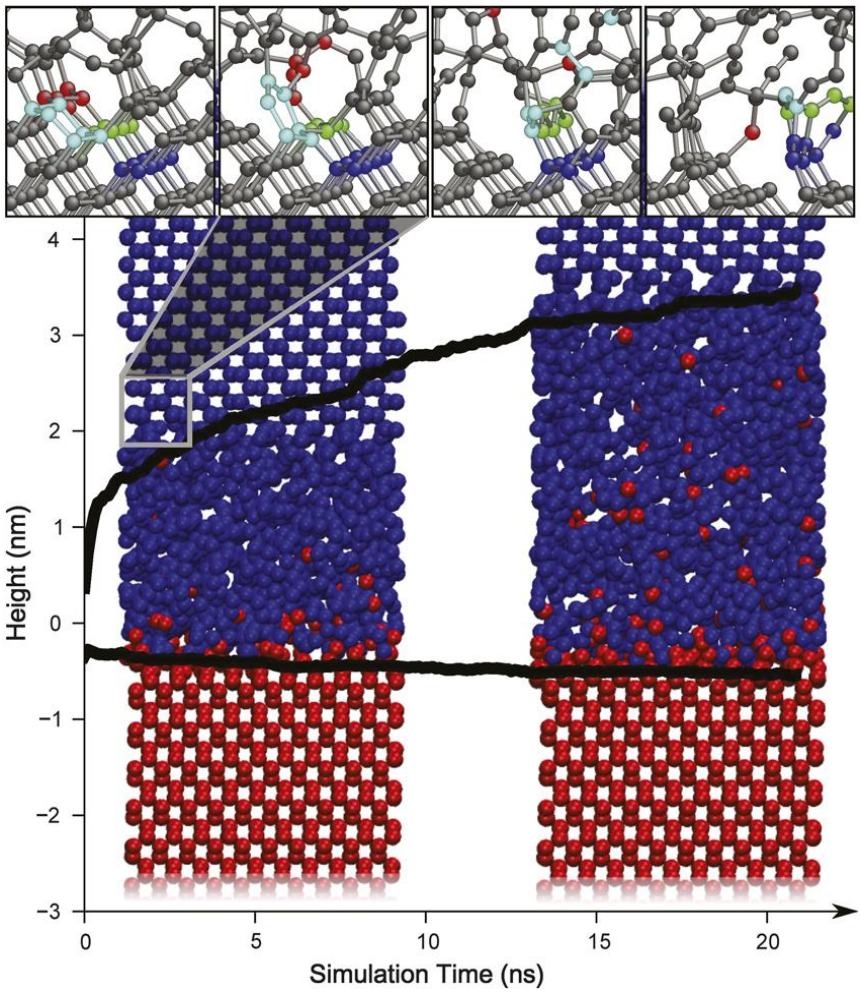

Figure 5-14: Sliding of diamond over another diamond at 20 m/s [194]

The various colours used in figure 5-14 indicate whether the atom was initially bound to the top or bottom crystallite of diamond while the black line shows the evolution of an amorphous interface of carbon atoms during the polishing process. A layer of ‘‘pilot’’ atoms that move around on the ordered phase repeatedly attracts the crystalline surface atoms. Since, the amorphization of the ‘‘pilot’’ atoms changes over time, the plucking forces also change. A surface atom is lifted into the amorphous phase when the pulling force becomes larger than the cohesive force holding the carbon atom into the diamond crystallite. This layer is subsequently removed by the ambient oxygen [236]. Quite similar to this phenomenon is the plucking of surface atoms from the diamond tool to form a thin film of SiC on silicon during machining. Jasinevicius *et al.* [37] have reported the formation of an amorphous layer to a depth of 340 nm on the machined surface of silicon. An interesting aspect of their research is that the microhardness of the diamond-turned silicon was lower than that of the pristine silicon which was attributed to the presence of the amorphous layer. This presented an anomaly compared to the machining of metals where the outermost layer of the machined surface always becomes harder due to work hardening whereas the machined silicon becomes softer. Mechanical machining generally introduces a barrier layer, known as a Beilby layer (tribomaterial), which exhibits a different refractive index from that of the substrate [83], as shown schematically in figure 5-15.

Thus, SiC can either be formed in the cutting chips or as a thin film on the surface of the diamond tool. In either of these cases, it will result in the formation of vacant sites on the diamond tool which have been identified as groove wear [76]. Also, the freshly formed SiC film will scrape off during continuous frictional and abrasive contact during SPDT of silicon. It is also important to note here that, during nano-scale ductile cutting of brittle materials, the undeformed chip thickness varies from zero at the centre of the tool tip to a maximum value at the top of the uncut shoulder.

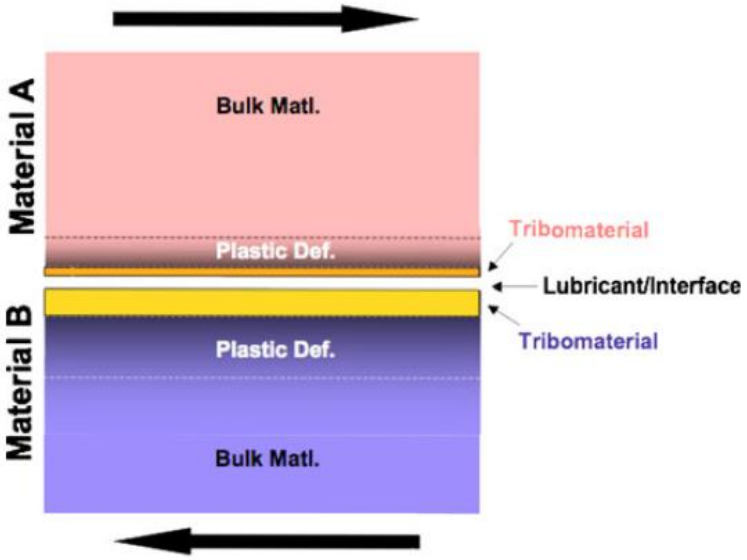

Figure 5-15: Schematic of a simple system consisting of a harder material 'A' sliding on a softer material 'B'. Near to the sliding interface, a Beilby layer of tribomaterial develops [237]

Thus, a 'zero-cutting zone' exists, within which no chips are produced. In this special zone, the tool acts more like a roller than a cutter and continuously slides on and burnishes the machined surface. A schematic diagram of this is shown in figure 5-16 [210].

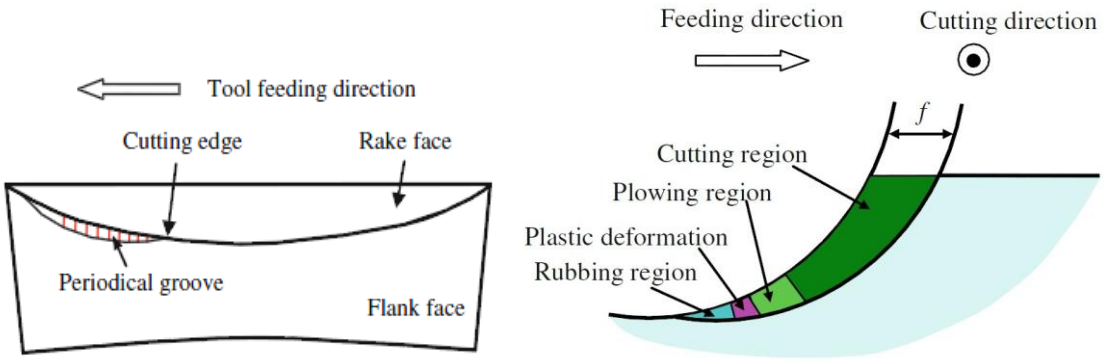

Figure 5-16: Schematic of the groove wear [238]

Figure 5-16 shows that the cutting edge of the tool continues to recede and the flank wear region becomes predominant. This can be represented and understood as a kind of stagnation, as shown in figure 5-17, where there exists a point on the cutting edge radius where the tangential velocity of the workpiece becomes zero [239]. It is of interest to

note that, below the stagnation point, the material gets compressed downwards in the wake of the tool, whereas, above the stagnation point, shear of the material is more pronounced than compression. Consequently, the sheared material is carried away as cutting chips.

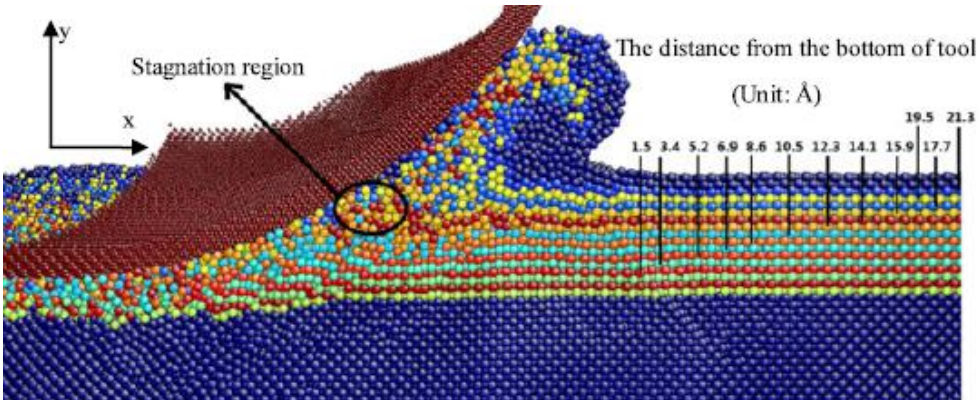

(a) MD model [152]

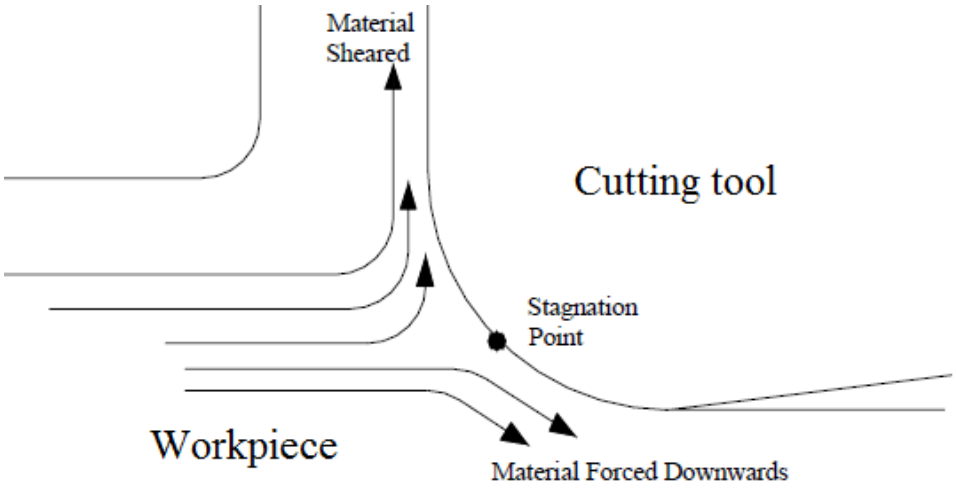

(b) Schematic model

Figure 5-17: Stagnation point on the cutting tool during SPDT

The flank wear region then causes a reduction in the clearance angle, which gives rise to increased frictional resistance. This is the reason for the observation of a relatively high temperature at the tool flank compared with the rake face. This phenomenon is in contrast to conventional machining where the tool rake face is at a higher temperature than the tool flank face. This is because of the large amount of the energy released from the cutting chips and the consequent heat dissipated into the tool rake face. In contrast,

during SPDT, the effect of frictional heat between the tool flank face and the finished surface of the workpiece is more than that on the tool rake face. Due to the high temperature on the flank face, the chemical kinetics between silicon and carbon atoms become more favourable at the flank face than the rake face. Subsequently, abrasion due to continuous frictional contact with the flank face further enhances the wear rate there, making the ratio rake wear to flank wear very small. The plucking of surface atoms from the diamond tool and subsequent abrasion between a thin layer of SiC and the cutting tool gives rise to associated sp^3–sp^2 disorder on the diamond tool as shown in figure 5-18.

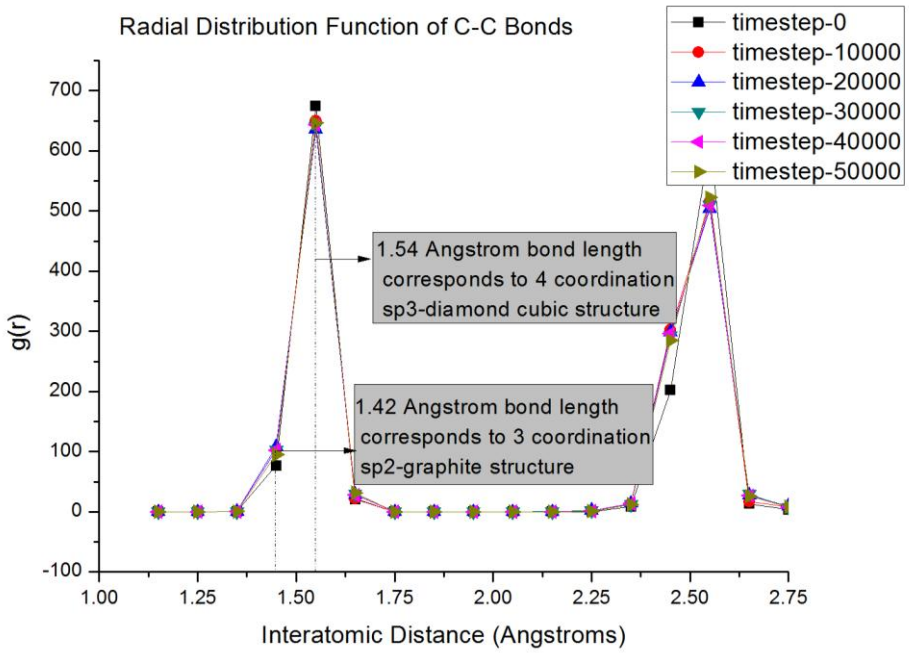

Figure 5-18: Radial distribution function of C-C bonds during SPDT of silicon

Figure 5-18 shows the RDF of the C–C bonds of the diamond tool. It can be seen that the peak at the inter-atomic distance of 1.54 Å (the known bond length of diamond) decreases during the simulation with a corresponding increase at the bond length of 1.42 Å, confirming sp^3–sp^2 disorder of the diamond. It is therefore reasonable to conclude that both processes i.e. formation of SiC and sp^3–sp^2 disorder of diamond proceed in tandem and which represent the fundamental cycle of wear of diamond tools during

SPDT of silicon. It is worth noting that, although high cutting speed was used in the MD simulation, the outcome of the process (i.e. the formation of SiC and sp^2 carbon) are also observed experimentally during machining of single crystal silicon [240] at a practical cutting speed.

5.6 Summary

From the literature review, it was recognized that the effect of crystal anisotropy on SPDT of silicon is well studied. For example, the <1-10> cutting direction on the (111) orientation has been suggested to provide superior quality of the machined surface during experimental SPDT studies on silicon and this is consistent with theoretical work in which the <1-10> direction was recognized as the preferred cutting direction either on the (100) or on the (111) crystal orientation.

This chapter concentrates on extracting information concerning the stress state and mechanism of tool wear during SPDT of silicon by analysing the MD simulations. The stress state of the cutting tool suggests that diamond does not undergo any metallic phase transformation during SPDT of silicon. However, the stress state of the silicon in the machining zone was found to be in the range of reported values of the pressure required to cause a Herzfeld–Mott transition (metallisation) of silicon in the cutting zone. Tribochemistry (formation of silicon carbide) through a solid state single phase reaction up to a cutting temperature of 959 K in tandem with sp^3–sp^2 disorder of diamond represents the basic wear mechanism of diamond tools against silicon during the SPDT process. The increased frictional contact and resulting abrasion between the tool flank face and the machined surface was found to be the main reason for higher temperatures at the tool flank face than at the tool rake face. This promotes both the formation of SiC and abrasion, which explains observations of relatively high flank wear compared to rake wear during SPDT of silicon.

Chapter 6 - MD simulation results for the nanometric cutting of silicon carbide

6.1 Introduction

Ductile-regime machining of silicon carbide is potentially subject to the same complexities as for silicon, i.e. interactions between; high pressure phase transformation (HPPT) / movement of dislocations, effect of crystal anisotropy and wear of the cutting tool, and process conditions. However, a ductile phase of silicon carbide is not as clearly defined as silicon and, furthermore, a very limited amount has been published on single point diamond turning of silicon carbide, even less on tool wear.

This chapter presents the MD simulation results concerning; the ductile response of SiC, crystal anisotropy in 3C-SiC, influence of polymorphism in SiC and the mechanism of wear of the cutting tool. A new parameter is devised here to index the machinability of various polytypes of SiC. Besides quantification of the sub-surface crystal lattice deformed layer depth, this chapter also presents the results for the differences in the machining of single crystal SiC and polycrystalline silicon carbide. Finally, a novel method to quantify the tool wear is presented.

6.2 Ductile characteristics of silicon carbide

Unlike silicon, the ductile response of silicon carbide has not been studied much. In the limited amount that has been published so far, there is considerable disagreement on the cause of ductility of silicon carbide, as summarised in table 6-1. Early studies on the ductility of SiC suggested that SiC undergoes a phase transformation from its stable structure to a β-tin structure [241] while others suggested just amorphization of 3C-SiC [242-243] or its transformation from its stable zinc-blende lattice structure to a rocksalt

structure [105, 244-245]. Similarly, 6H-SiC and 4H-SiC have been reported to transform to a polycrystalline phase [246], exhibit no high pressure phase transformation [121, 247], or allow dislocation nucleation followed by propagation within the zinc-blende phase [248]. One research group [249] has continued to place a major emphasis on dislocation driven plasticity in silicon carbide as the reason for its ductility during nanoindentation, but there is also a strong claim for high pressure phase transformation of silicon carbide during nanometric cutting in the literature [119].

Table 6-1: Previous studies concerning ductility of SiC

Material simulated	Author, Year	Process studied	Conclusions
3C-SiC	Yoshida, 1993 [247]	Pressure loading	No HPPT
3C-SiC	Tang, 1995 [242]	Nano-scratching	Shear instability induced amorphization
3C-SiC	Shimojo, 2000 [105]	Pressure loading	Rocksalt structural transformation
3C-SiC	Szlufarska, 2005 [243]	Nano-indentation	Amorphization of SiC
3C-SiC	Noreyan, 2005 [244]	Nano-scratching	Rocksalt structural transformation
3C-SiC	Szlufarska, 2009 [248]	Nano-indentation	Dislocation nucleation within the zinc-blende phase without any phase change
6H-SiC	Patten, 2005 [119]	Single point diamond turning	HPPT
6H-SiC	Yan, 2010 [246]	Nano-indentation	Transformation to polycrystalline phase

It is noteworthy that an experimental study revealed that the rocksalt structural transformation in 3C-SiC requires a transformation pressure of 100 GPa [247] against numerically predicted values of 64.9 GPa [242] and 66 GPa [250]. In contrast, the first machining trial on SiC reported a cutting pressure of only 25-35 GPa [47, 119], rather lower than the predicted value of 60 GPa based on the Herzfeld's theory [42]. Although

the high pressure phase of SiC was not recognised at that time, indirect evidence from the analysis of the cutting chips was indicative of HPPT of SiC during its cutting [119]. It was noted during the current investigation that, in common with diamond, SiC requires less force for bond-bending than bond stretching which is the opposite to other semi-conductors such as Si, Ge, Si_3N_4 or GaAs [45, 251]. Also, it was highlighted earlier that compression differs from hydrostatic pressure [252] as it may have a component of deviatoric stress which can cause shear induced metallization *via* changes in bond angle [44]. The fact that SiC undergoes amorphization under compression, such as in nano-indentation, unlike silicon which undergoes polymorphic phase transformation seems to stem from the chemical ordering effect between the silicon and carbon atoms within SiC. Moreover, the moving line contact between the tip of the cutting tool and the workpiece during nanometric cutting differs from the point/planar contact during nano-indentation [253] so nanometric cutting conditions result in an increased energy transfer compared with the nano-indentation process. If the propensity to a Herzfeld-Mott transition is a function of the nano-indentation hardness of a material [42], the question arises as to whether or not 3C-SiC will show a rocksalt transformation or any other metallic phase during nanometric cutting. From the MD simulation, the magnitude of the peak von Mises stress was found to be around 56 GPa while cutting 3C-SiC on a specific crystal orientation. This value of transition pressure was found reasonably consistent with predictions [42, 106] based on the nano-indentation hardness of materials. However, the transition pressure of 3C-SiC was found to be substantially lower than 100 GPa, which is the reported minimum pressure required to cause SiC to transform from its diamond cubic lattice to the rocksalt structure [247]. This suggests that the rocksalt structural transformation does not take place during nanometric cutting of SiC, and that it is certainly not responsible for the ductile response of 3C-SiC.

The shear stress, τ_{xy}, in the workpiece for both silicon and 3C-SiC were also calculated. For silicon, τ_{xy} was around 6.7 GPa while, in 3C-SiC, it was 32.5 GPa. Interestingly, this shear stress in a 3C-SiC workpiece in the cutting zone was significantly higher than that (15 GPa) exerted on a diamond grit during polishing with another diamond [163]. This observation immediately raises a concern over the stability of the SiC lattice structure, since such a shear stress could certainly cause its metallization through a change in bond angle [44]. It was therefore relevant to compute the change in bond angle during nanometric cutting in order to gain some insights. For a better understanding, a comparison of the angular distribution functions of silicon bonds and Si-C bonds during nanometric cutting of silicon and silicon carbide before and after cutting for both Si and SiC is shown in figure 6-1.

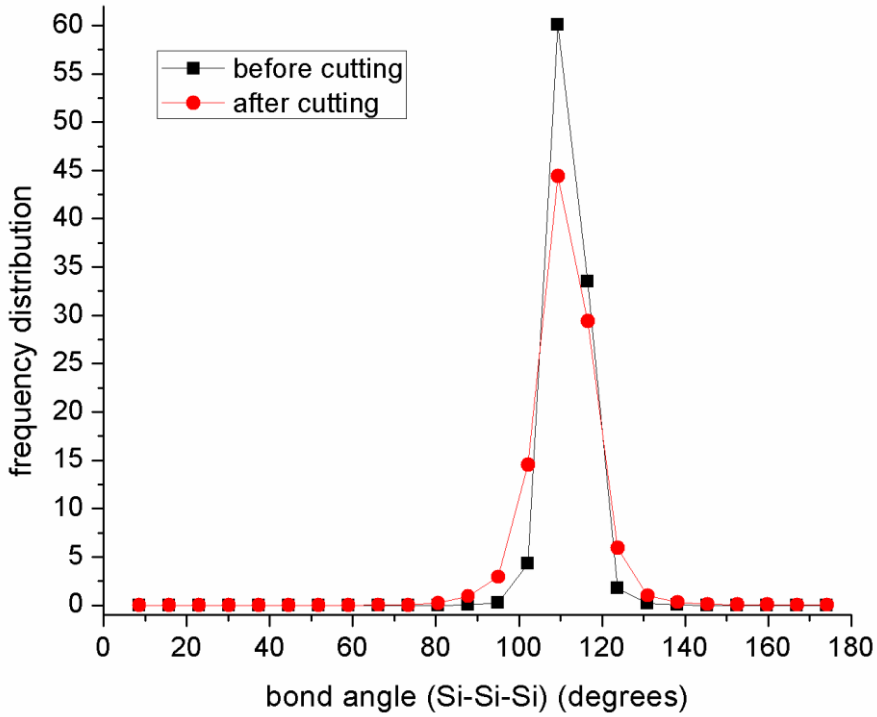

(a) Si-Si-Si

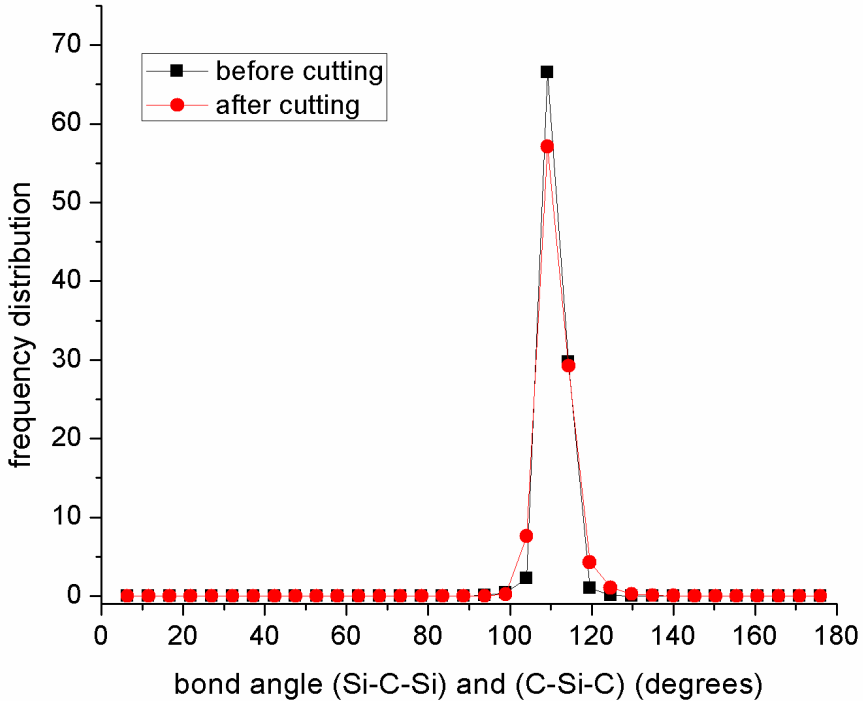

(b) Si-C-Si and C-Si-C

Figure 6-1: Angular distribution functions of silicon and silicon carbide before and after nanometric cutting

It is evident from figure 6-1 that, before cutting, there is a sharp peak in the bond angle distribution at 109.5° which corresponds to the known bond angle for both silicon and silicon carbide. However, after cutting, the bond angle distribution has broadened somewhat with angles for silicon appearing in the range of 80° to 140°. This wide range in bond angle is consistent with amorphization of silicon during nanometric cutting as discussed in the previous chapters. By contrast, the bond angle in 3C-SiC exhibited only two values (other than 109.5°), 105° and 120°. This limited number of bond angles in 3C-SiC is an indication that unlike silicon, SiC does not undergo polymorphic phase transformation during its nanometric cutting. Additional confirmation of morphological change can be seen in the changes in C-C-C bond angle and in dihedral angle (Si-Si-C-C) brought about by the nanometric cutting process, shown in figure 6-2 and figure 6-3. There is a distinct shift in C-C-C bond angle and Si-Si-C-C dihedral angle towards a value of 120° from the original value of 109.5°.

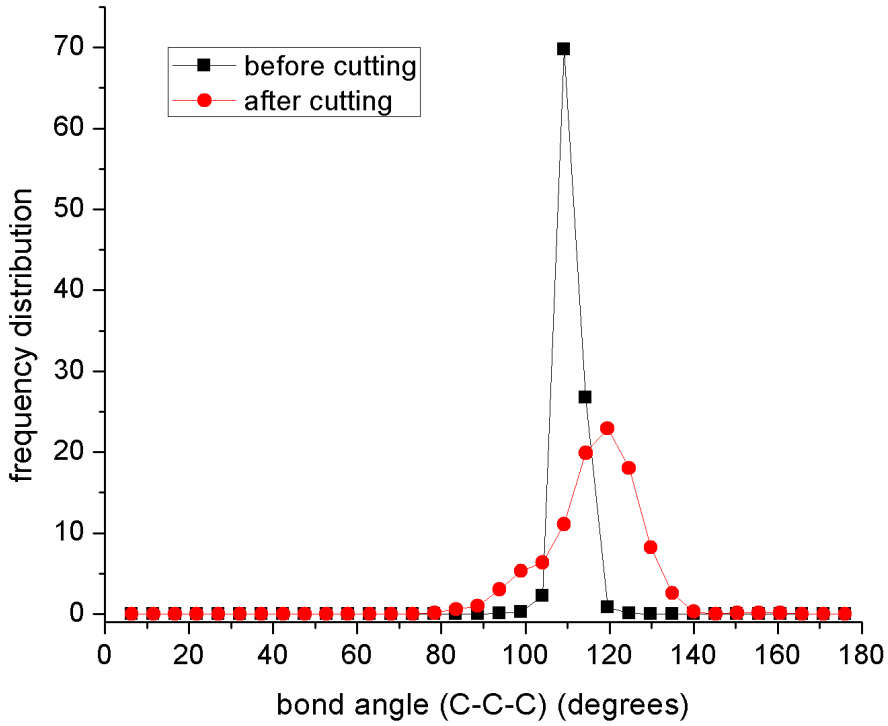

Figure 6-2: Angular distribution function of C-C-C after cutting of silicon carbide

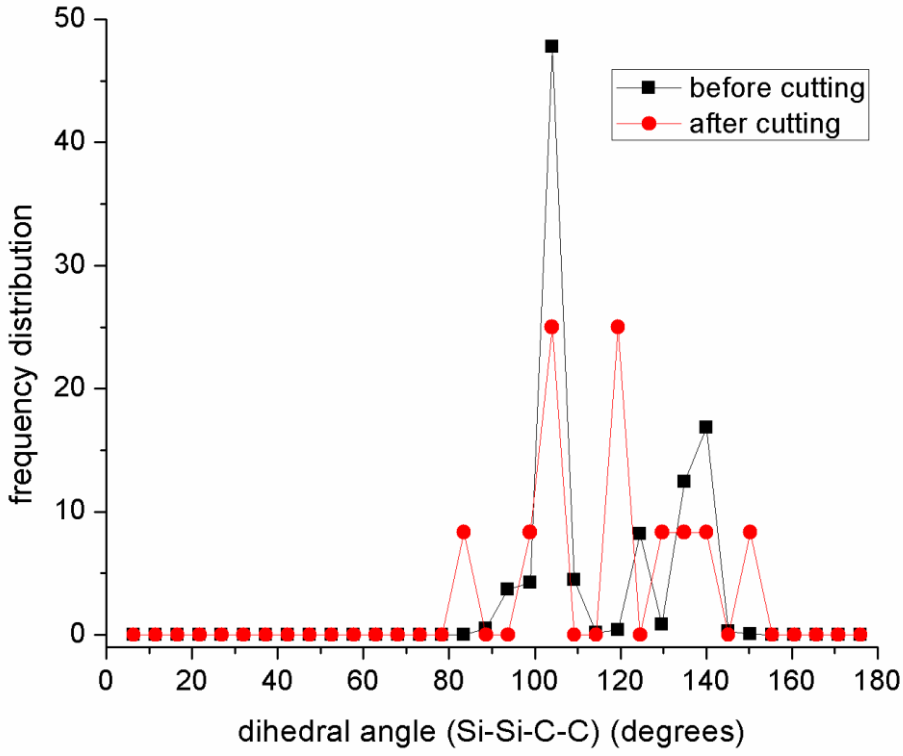

Figure 6-3: Change in dihedral angle after cutting of silicon carbide

This change in bond angle distribution (109.5°→120°) suggests a transformation from sp^3 to sp^2 bond in the 3C-SiC [125] which could be brought about by the intense shear

stresses. The structure formed during this transition can be understood by the analysis of the radial distribution function, $g(r)$, shown in figure 6-4.

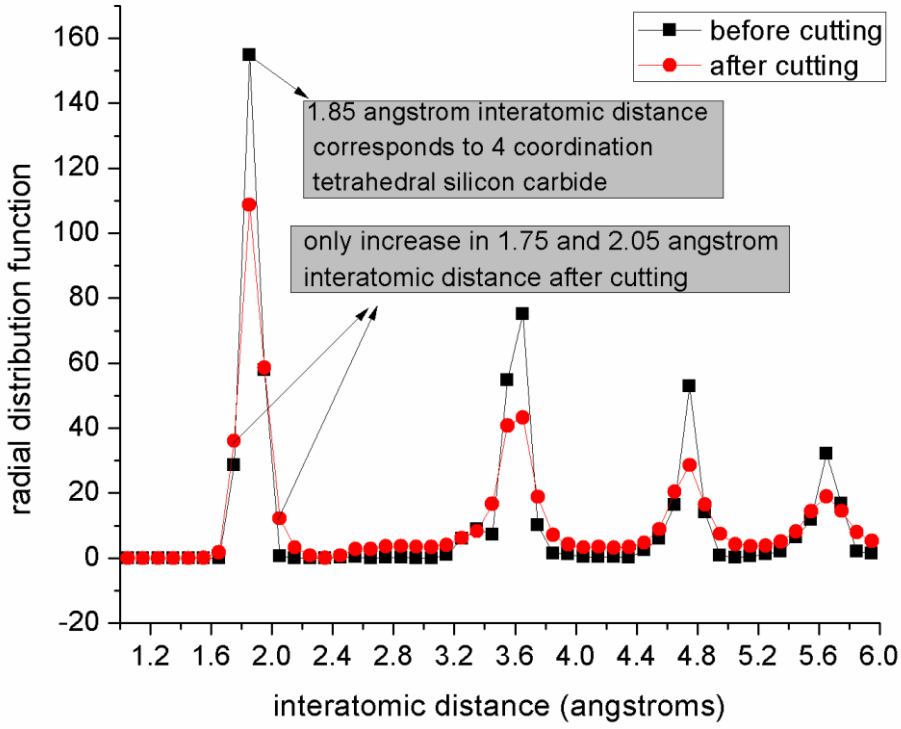

Figure 6-4: Radial distribution function of 3C-SiC during nanometric cutting

As can be seen, there is an increase in $g(r)$ for SiC bonds at two interatomic distances, 1.75 Å, which is the reported length of Si=C double bonds [88] and 2.05 Å. The analysis of $g(r)$, bond angle and dihedral angle, suggests that the transition of sp^3-SiC to sp^2-SiC can schematically be represented as shown in figure 6-5a. Carbon atoms are smaller than silicon atoms and are more electronegative [254] which causes the transformed structure (sp^2 form of SiC) to be chemically ordered even during its reconstruction. The geometry obtained in figure 6-5a is difficult to realize through experiments [255], but, the relevant inter-layer spacings have been obtained experimentally as 0.38 nm [256] as shown in figure 6-6.

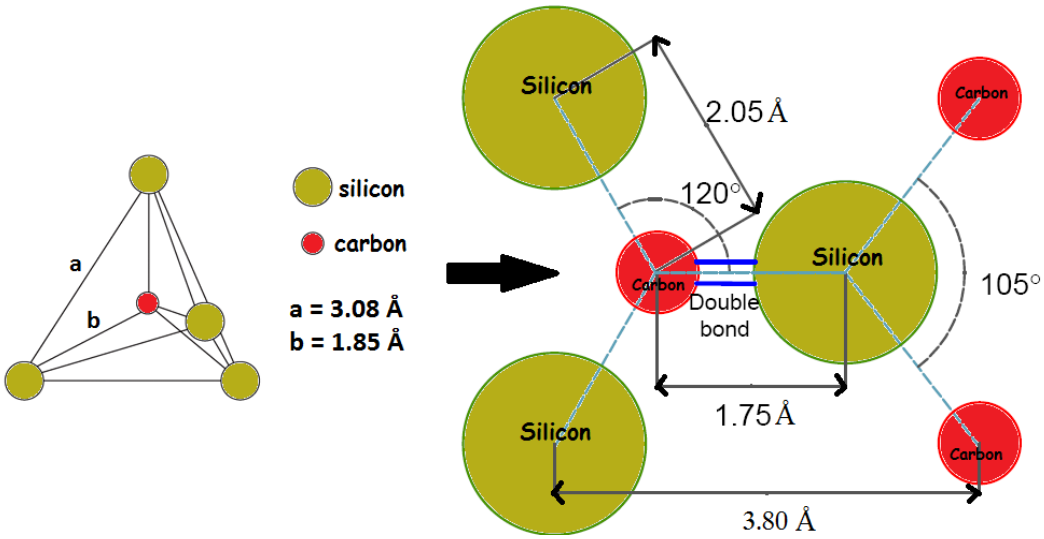

(a) sp^3-sp^2 transformation in 3C-SiC

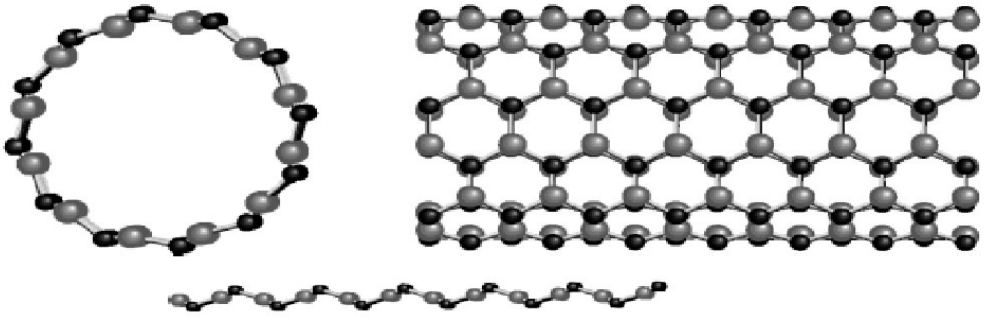

(b) Single wall SiC nanotubes with chirality (6,6 ordered) having energy of 0.49 eV per SiC atomic pair and Si-C bond length between 1.79-1.80 Å [255]

Figure 6-5: Phase transformation in 3C-SiC and relevant chemical structure [257]

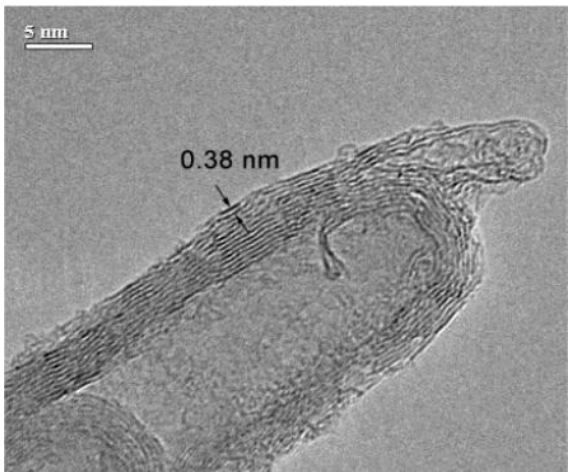

Figure 6-6: High-Resolution Transmission Electron micrograph of SiC nanotube with inter-layer spacing of 3.8 Å [256]

The inter-layer spacing in figure 6-6 is attributed to a π-like bond and can be obtained by applying simple trigonometry to the proposed lattice structure as follows:

$$x = 2.05 \times \frac{\sin 30^0}{\sin 90^0} = 1.025\text{Å} \quad \Rightarrow \text{Total inter-layer spacing} = 1.75\ \text{Å} + 2x = 3.8\ \text{Å}$$

An interesting observation relevant to this phenomenon is the mechanism of deformation on either the (111) or the (110) plane which is the natural shear plane during nanometric cutting. It is likely that this would have involved in inter-plane polarization, the two surfaces having atomic charges at the extremes between silicon and carbon. The resulting structure can be stabilized *via* charge transfer between the opposite diameters of silicon and carbon (~0.27|e|[26]) or a phase transition from the würtzite to the graphite structure [88]. It is further interesting to note that molecular stability calculations [28] have predicted the existence of a SiC graphene tube with a sp^2 structure as shown in figure 6-5b. This structure is not entirely planar but is rippled with Si atoms in a single plane and C atoms in alternate rows, above and below the Si atoms. A chiral vector defined by a pair of integers *(n,m)* appearing in a translation vector $c = na+mb$, where *a* and *b* are the two vectors defining the primitive cell of graphene, can be used to represent such structures. The effect of this chiral vector is that the structure will be conductive, i.e. metallic, as long as $(n - m)$ is a multiple of 3. It has also been suggested that the chemically ordered SiC nanotubes of "armchair" (6,6) type are slightly (by 0.05 eV/SiC atom pair) more stable than (12,0) SiC nanotubes [255] and both are conductive as $(n - m)$ is a multiple of 3. Further, the fact that the band gap has vanished in this form of sp^2 SiC satisfies the Herzfeld-Mott transition criterion. Hence the sp^3-sp^2 transition in 3C-SiC is consistent with a ductile or metallic response of SiC during nanometric cutting in contrast to previous studies suggesting the rocksalt structural transformation.

Recent work on the HPPT [258] using UV micro Raman spectra from the machined surface of a 6H-SiC wafer has revealed a local sp^2 environment seen as a dark spot,

figure 6-7. In accordance with the MD studies, the Raman spectra suggest sp^3-sp^2 transformation of SiC during its nanometric cutting. A reverse transformation is likely to happen upon release of the cutting load.

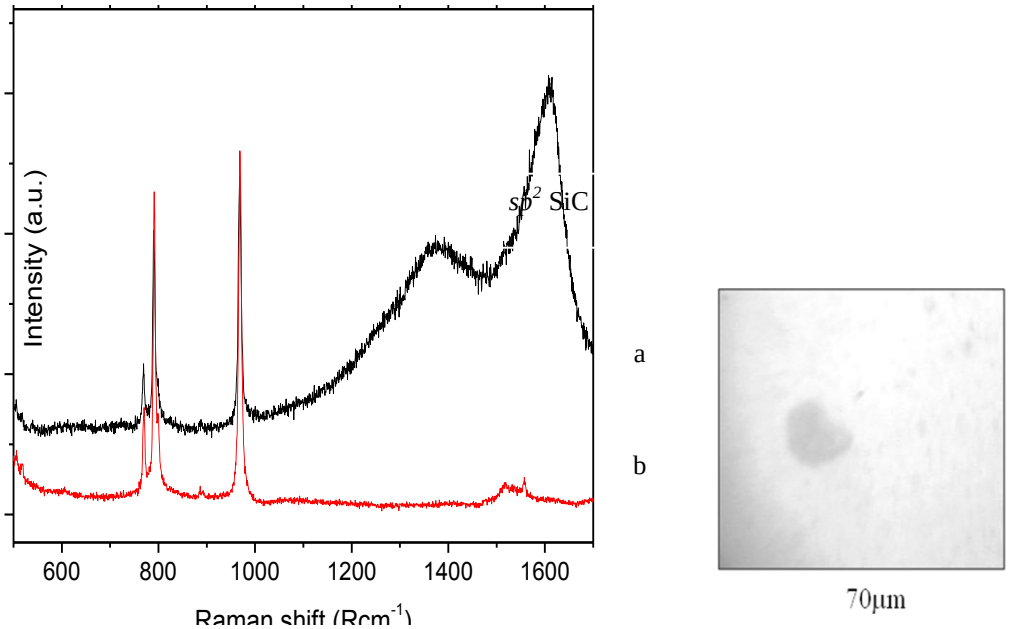

Figure 6-7: UV micro Raman spectra of (a) black line - dark spot found on the machined surface (b) red line - compared to the machined surface of a 6H SiC wafer [258]

In contrast to the above results, Levitas *et al.* [259] have recently identified a new phase of 6H-SiC which they have named the high-density amorphous (hda) phase of SiC. They used X-ray diffraction to monitor the crystal structures in a rotational diamond anvil cell which creates both hydrostatic pressure and shear rotation and found that the newly identified phase forms at a pressure of 30 GPa and 2160° of anvil rotation. Although, they only observed this phenomenon on 6H-SiC, they have suggested that the results would be similar for 3C-SiC on account of the small energy difference.

6.3 Crystal anisotropy in 3C-SiC

3C-SiC is the only polytype (among the 250 recognized so far [260]) of SiC which resides in a diamond cubic crystal structure . Early recommendations were to select the

cutting tool and the workpiece such that the ratio of their hardnesses is at least 5:1 [26, 122]. However, in the case of a SiC workpiece and a diamond tool, this ratio is only about 4:1, based on the high micro hardness of SiC (about 28 GPa) compared to diamond (100 GPa). Experimentally, this ratio has been found to reduce to only about 2:1 at relatively shallow depths of cut [26]. Hence, nanometric cutting of 3C-SiC by a single point cutting tool is expected to be surrounded by many technical challenges. One way to resolve this potential problem would be to identify an appropriate combination of crystal orientation and cutting direction to cut 3C-SiC. Crystal orientation of the workpiece has a significant effect on its cutting behaviour [261] and hence a properly selected crystal setup could benefit the tool life and the attainable machined surface roughness. Also, nanometric cutting involves significant plastic deformation ahead of the cutting tool and elastic recovery of the machined surface underneath the clearance face of the tool so the variation in the elastic modulus with crystallographic orientation will influence the machined surface finish, sub-surface integrity and residual stresses on the finished surface. While knowledge of the extent of anisotropy of 3C-SiC during nanometric cutting is important, it is also important to know the variation in the Young's modulus of 3C-SiC along three major crystallographic orientations. For this reason, experimentally known elastic constants were used to calculate the Young's modulus on different crystal orientations of 3C-SiC. Table 6-2 provides the mathematical formulae and the calculated values of the Young's modulus and Poisson's ratio. It is evident from table 6-2 that the maximum Young's modulus of 3C-SiC is on the (111) crystal orientation (557 GPa) while the minimum is on the (100) crystal orientation (314 GPa).

Table 6-2: Directional dependence of elastic properties of single crystal 3C-SiC

3C-SiC properties	Reference	Values
Elastic constant C_{11}	Experimental data [183]	390 GPa
Elastic constant C_{12}	Experimental data [183]	142 GPa
Elastic constant C_{44}	Experimental data [183]	256 GPa
Young's modulus (E_{100})	$C_{11} - 2\frac{C_{12}}{C_{11}+C_{12}}C_{12}$	314 GPa
Young's modulus (E_{110})	$4\frac{(C_{11}^{\ 2} + C_{12}C_{11} - 2C_{12}^{\ 2})C_{44}}{2C_{44}C_{11} + C_{11}^{\ 2} + C_{12}C_{11} - 2C_{12}^{\ 2}}$	467 GPa
Young's modulus (E_{111})	$3\frac{C_{44}(C_{11}+2C_{12})}{C_{11}+2C_{12}+C_{44}}$	557 GPa
Poisson's ratio	$\frac{C_{12}}{C_{11}+C_{12}}$	0.267
Crystal anisotropy	$\frac{E_{111}-E_{100}}{E_{111}}$	0.436

The values of calculated Young's modulus shown in table 6-2 are also consistent with the experimental values obtained by NASA, USA [262]. Table 6-2 suggests that 3C-SiC exhibits a high degree of crystal anisotropy to the extent of 43.6% although it is not known how this anisotropy can be translated to favourable combinations of crystal orientation and cutting direction in 3C-SiC. To interpret the simulation results it is, of course, important to understand the crystal geometry of 3C-SiC. Based on the known geometry of the diamond cubic lattice, the lattice structure of 3C-SiC on different crystal planes can be schematically represented as in figure 6-8 in which atoms that lie on the same crystallographic plane are coloured black for the ease of counting. Based on figure 6-8, calculations can be made as shown in table 6-3 highlighting the number of

atoms on a crystal plane, atomic density per unit area, minimum distance between the two atoms on a plane and distance between the adjacent planes of 3C-SiC.

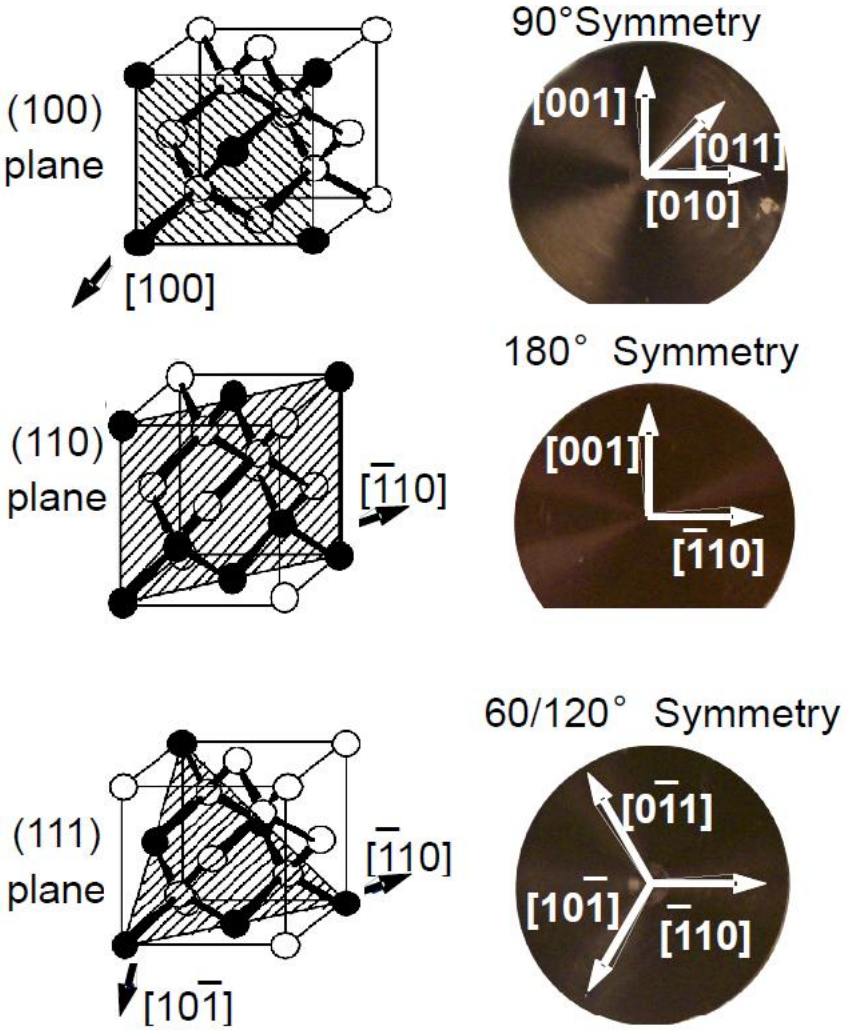

Figure 6-8: Schematic illustration of various crystal setups in 3C-SiC

Table 6-3: Properties of 3C-SiC with respect to various crystal orientations

Orientation	Number of atoms on the plane	Atomic projection area	Atomic density per unit area	Minimum distance between the two atoms lying on the same plane	Distance between two adjacent planes
Cube (100)	$\frac{4}{4}+1=2$	a×a $=a^2$	$2/a^2$ =0.1052	a/2 = 2.18 Å	a = 4.36 Å
Dodecahedron (110)	$\frac{4}{4}+2+\frac{2}{2}=4$	√2a×a $=\sqrt{2}a^2$	$4/\sqrt{2}a^2$ **=0.1488**	a/4 **= 1.09 Å**	1.707a **= 6.16 Å**
Octahedron (111)	$\frac{1}{6}\times 3+3\times\frac{1}{2}=2$	$=\frac{\sqrt{3}}{2}a^2$	$4/\sqrt{3}a^2$ = 0.1215	√3a/4 =1.89 Å	0.577a = 2.514 Å

It can be seen from table 6-3 that 3C-SiC possesses the highest atomic density and the farthest distance between two adjacent planes on the (110) crystal orientation, thus making the (110) plane more compliant than the other two crystal planes. Also, the minimum distance between two atoms on this plane is the shortest one of the three, making it energetically more favourable for deformation to occur on this crystal plane. Both 3C-SiC and diamond share this lattice structure in their sp^3 bonded state. However, unlike 3C-SiC, anisotropy of diamond during its machining is well documented [45, 102, 163, 263]. To investigate the effect of crystal anisotropy in 3C-SiC, two simulation trials of nanometric cutting of 3C-SiC were performed using different machining parameters.

Table 6-4: Process variables used in the MD simulation of nanometric cutting of 3C-SiC

Details	**Simulation trial case-1**	**Simulation trial case-2**
3C-SiC workpiece size	14.26nm×4.635nm×variable z dimension to avoid pbc mismatch	30.1nm×11.13nm× variable z dimension to avoid pbc mismatch
Uncut chip thickness (d) (nm)	1.312	1.9634
Cutting edge radius (r) (nm)	2.297	1.9634
d/r ratio	0.57	1
Cutting tool rake angle and clearance angle	-25° and 10°	-30° and 10°
Equilibration temperature	300 Kelvin	
Cutting velocity	10 m/s	4 m/s
Crystal Setup combinations	**Crystal orientation**	**Cutting direction**
Case-1	(111)	<-110>
Case-2	(111)	<-211>
Case-3	(110)	<-110>
Case-4	(110)	<001>
Case-5	(001)	<-110>
Case-6	(001)	<100>
Case-7	(11-2)	<1-10>
Case-8	(110)	<-11-2>
Case-9	(1-20)	<210>

Table 6-4 shows the details of the workpiece, uncut chip thickness, cutting tool, the nine distinct combinations of crystal orientation and cutting direction, *d/r* ratio and other relevant parameters used for the simulation trials. Snapshots from the MD simulation for each crystal setup are reproduced in figure 6-9, depicting the chip formation mechanism and consequent deformation of the 3C-SiC workpiece. In figure 6-9, green and red colours correspond to silicon and carbon atoms constituting the crystalline 3C-SiC workpiece while dark blue colour represents carbon atoms within the diamond cutting tool respectively. Atoms of 3C-SiC which have typically undergone a severe structural transformation and have lost their diamond cubic crystal lattice structure are coloured in cyan to separate the non-crystalline region with the crystalline region. It is evident that the cutting chips started to flow on the rake face of the cutting tool after having undergone a severe structural transformation. This transformation in 3C-SiC has been attributed to sp^3-sp^2 transition which brings Herzfeld-Mott transition [42], responsible for the ductility of 3C-SiC during its nanometric cutting. In the following sections, characteristics of the cutting chips on three major crystal orientations are discussed (figure 6-9a – figure 6-9i). In these figures, atoms are coloured as per the following scheme: Green/Red atoms are silicon and carbon atoms forming the crystalline 3C-SiC structure, Cyan coloured atoms are the mixture of both Si and C atoms which have undergone structural transformation and have lost the pristine diamond cubic lattice structure. Dark blue colour atoms belong to the diamond cutting tool.

(a) Crystal setup 1: Crystal orientation (111) cutting direction<-110>

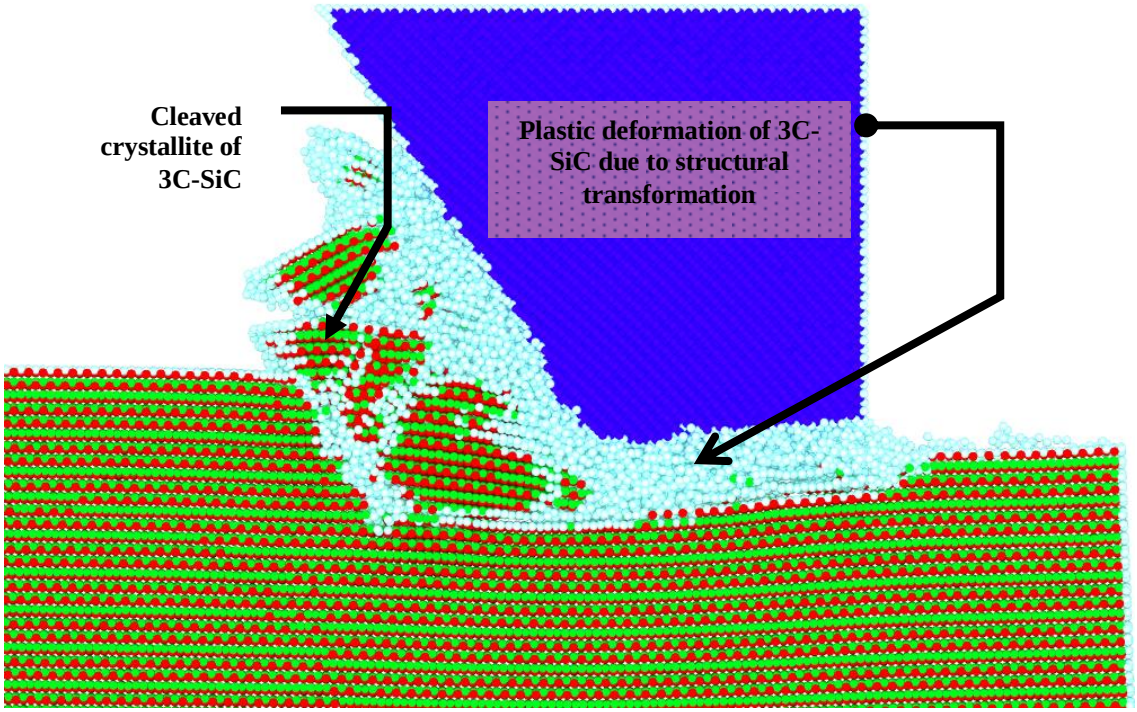

(b) Crystal setup 2: Crystal orientation (111) cutting direction<-211>

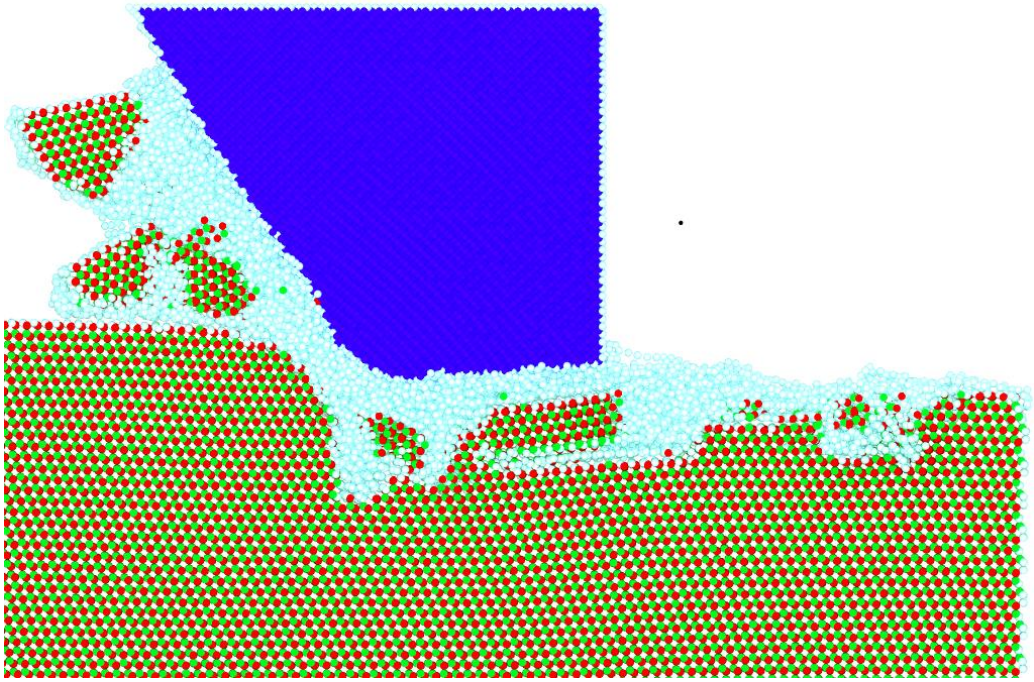

(c) Crystal setup 3: Crystal orientation (110) cutting direction<-110>

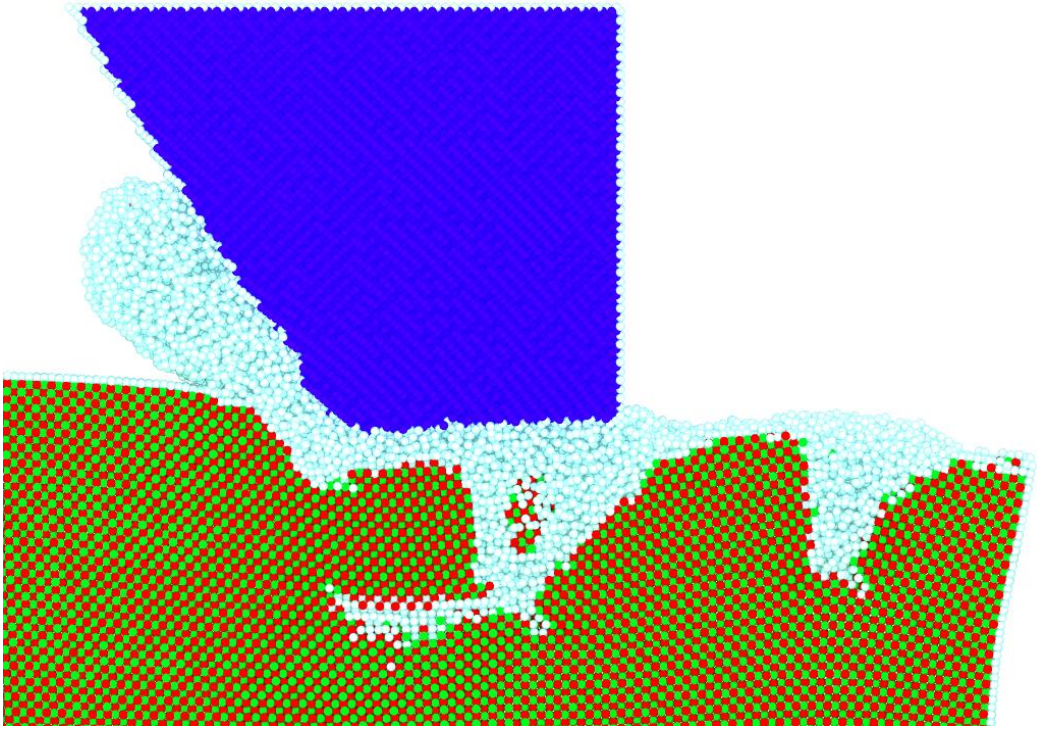

(d) Crystal setup 4: Crystal orientation (110) cutting direction<001>

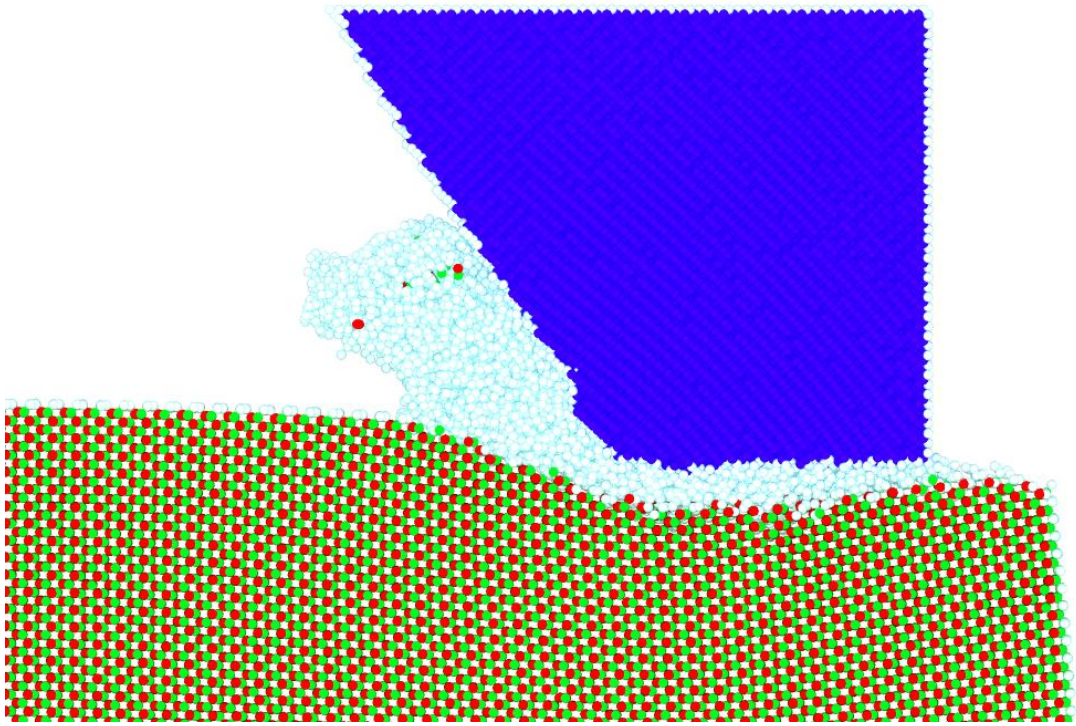

(e) Crystal setup 5: Crystal orientation (001) cutting direction<-110> (Partial and perfect dislocations highlighted)

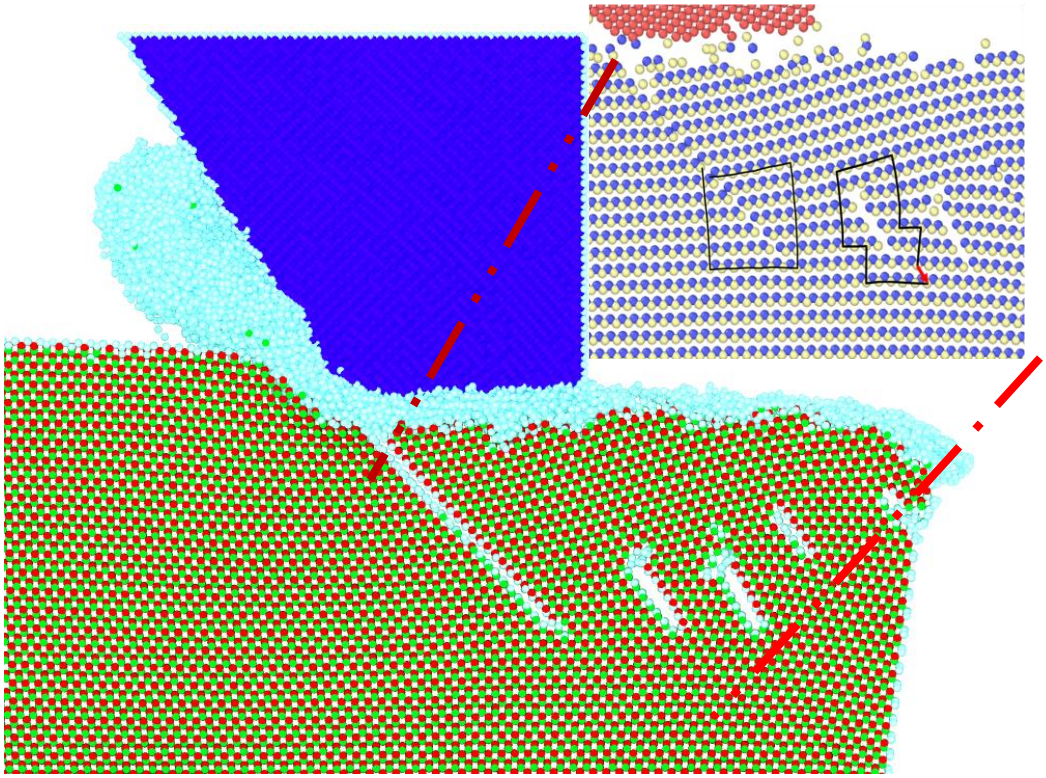

(f) Crystal setup 6: Crystal orientation (001) cutting direction<100>

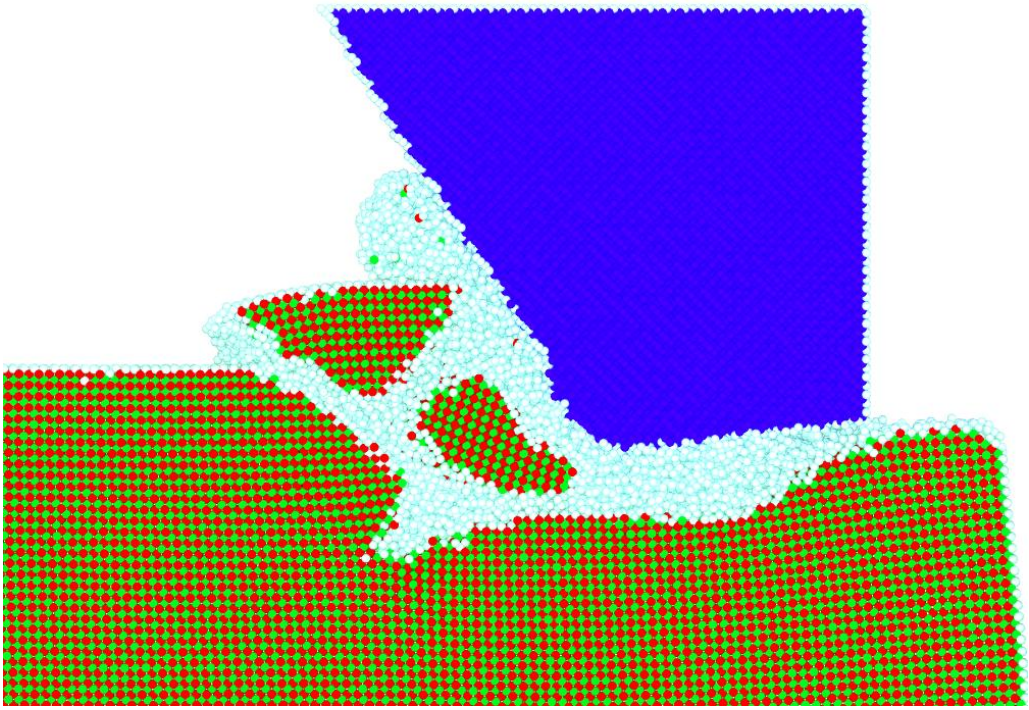

(i) d/r =1 and cutting velocity of 4 m/s

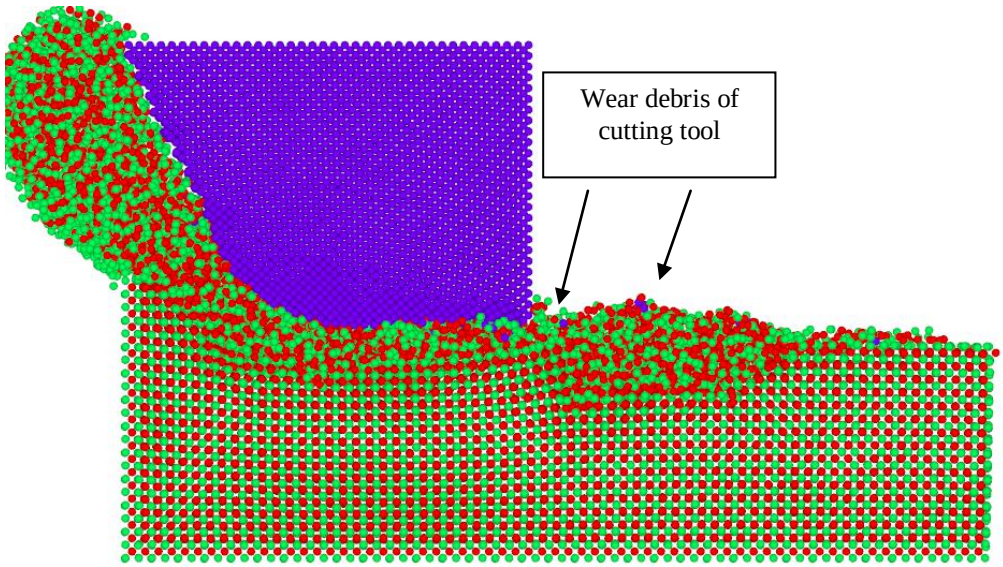

Here atoms having lost their pristine diamond cubic structure are not coloured to highlight wear of the cutting tool.

(ii) d/r =0.57 and cutting velocity of 10 m/s

(g) Crystal setup 7: Crystal orientation (11-2) cutting direction<1-10>

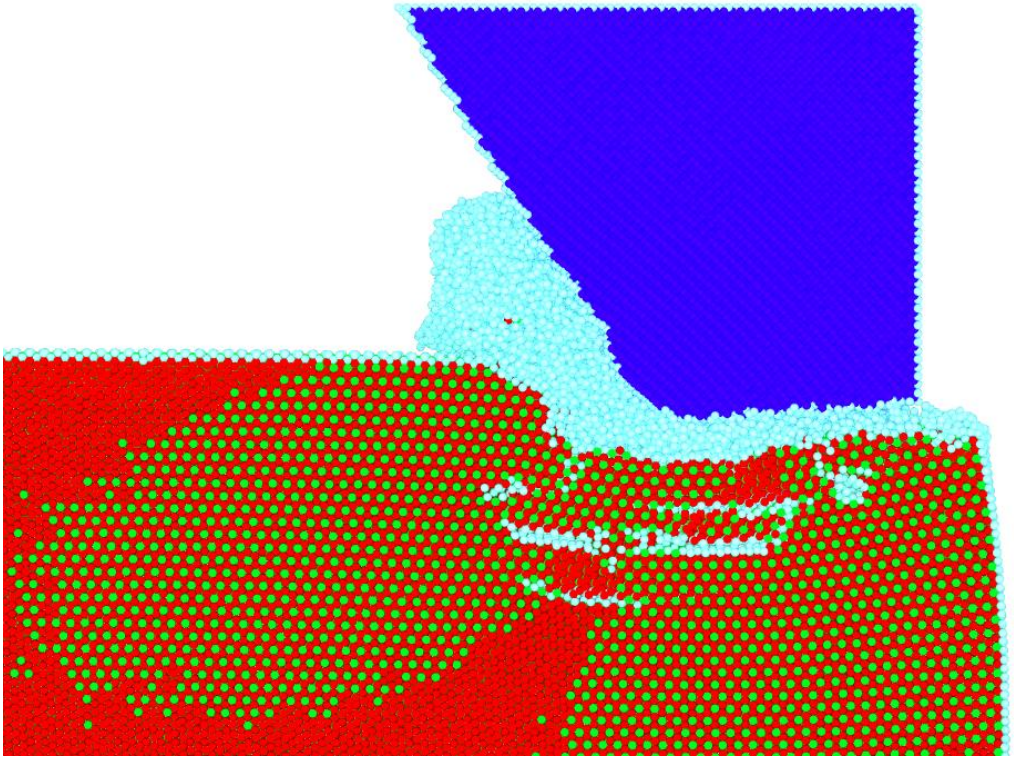

(h) Crystal setup 8: Crystal orientation (110) cutting direction<-11-2>

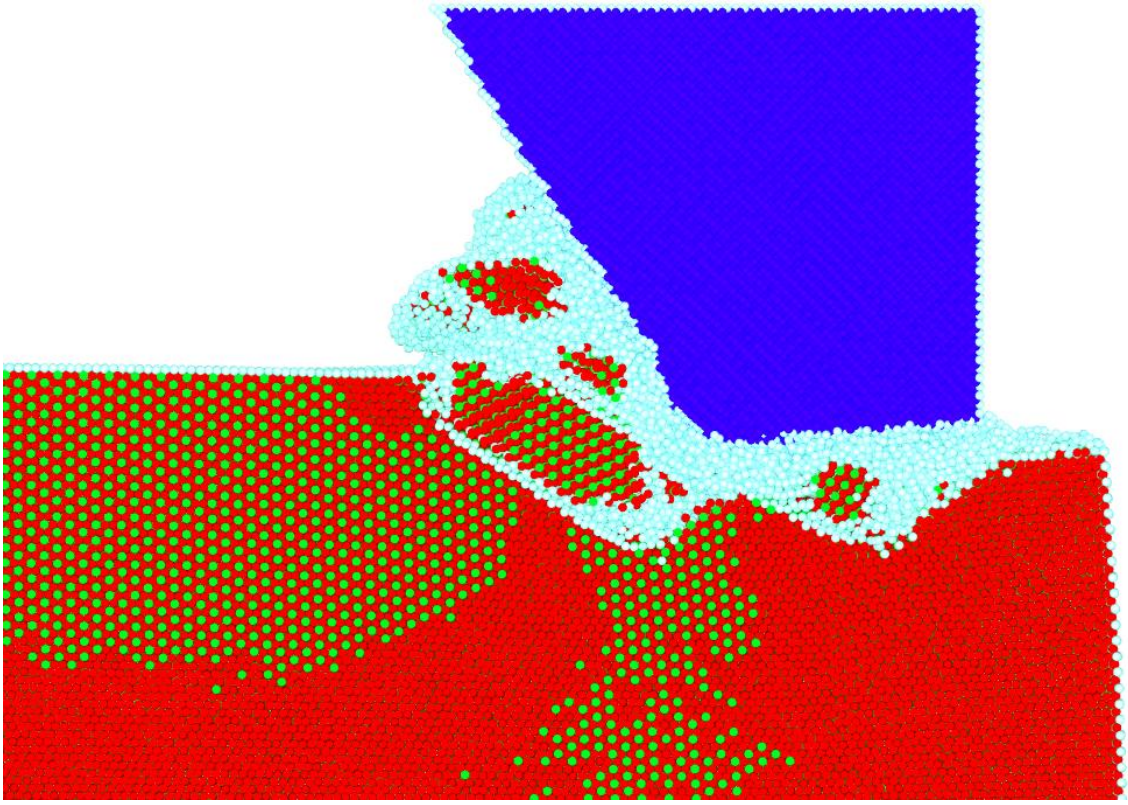

(i) Crystal setup 9: Crystal orientation (1-20) cutting direction<210>

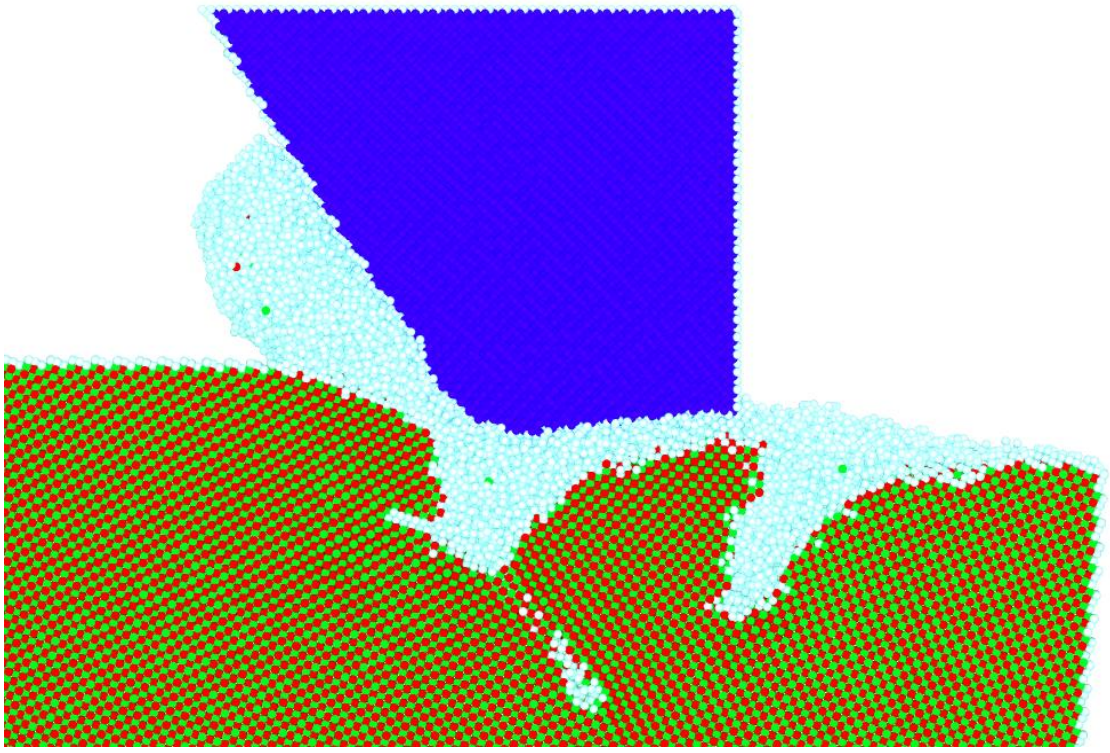

Figure 6-9: Snapshots from the MD simulation of nanometric cutting of 3C-SiC in nine different combinations (figure 6-9a – figure 6-9i) of crystal setups.

6.3.1 Cutting chips due to cleavage on (111) crystal orientation

Irrespective of the cutting direction, a mechanism of cleavage was observed to occur ahead of the cutting tool while cutting 3C-SiC on (111) crystal orientation. An atomic structure identification method (neighbour distance analysis [203, 264-265]) has been used to identify atoms that form a perfect diamond cubic lattice structure to separate it with the non crystalline region (cyan colour atoms). It is evident from figure 6-9 (crystal setup 1 and crystal setup 2) that few small crystallites of 3C-SiC in the cutting chips have retained their original crystalline lattice structure. The presence of such crystallites in the cutting chips without undergoing structural transformation is reminiscent to the mechanism of cleavage observed during the polishing of a diamond on (111) orientation [102]. With the proven evidences that structural transformation is a necessary requirement to generate the ductile response from a single crystal brittle material [201, 216, 222, 266], the above observation suggest that cleavage is a dominant mechanism of material removal on (111) crystal orientation of 3C-SiC during its nanometric cutting. Hence, it shows that material removal mechanism on (111) orientation of 3C-SiC, in common with diamond, is dominated by cleavage.

6.3.2 Mechanism of material removal on the (110) crystal orientation

Nanometric cutting (figure 6-9) on crystal setup 3, crystal setup 4 and crystal setup 8 was performed on (110) crystal orientation in different cutting directions i.e. <-110>, <001> and <-11-2> respectively. In the first case i.e. case 3, it can be seen that no cleavage took place however; an undesirable sub-surface deformation exhibiting a typical ‘V-shape’ is apparently evident. In case 4, the cutting mechanism was found to be dominated purely by the structural transformation of the cutting chips without

showing occurrence of any cleavage. For this reason, minimum or no sub-surface deformation was observed in case 4. This can thus be regarded as an amenable scratching direction in 3C-SiC. In case 8, alongside structural transformation, some remnants of cleavage were observed with apparent crystal sub-surface deformation exhibiting a typical 'V-shape'.

6.3.3 Mechanism of material removal on the (001) crystal orientation

Nanometric cutting (figure 6-9) in case 5 and case 6 was performed on (001) orientation and <-110> and <100> cutting directions respectively. In the former case, although the dominant mechanism of material removal was structural transformation but one stacking fault with one partial dislocation of unidentified Burgers vector was observed leading to the appearance of stacking faults. These were observed to extend deep into the sub-surface and were also present on the edge of the workpiece where the cutting commences. This could lead to the possibility of the chipping of the edge of the workpiece and can be regarded as the entry failure of the cutting tool into the workpiece. In the later case, i.e. in case 6, an occurrence of the cleavage was observed while the cutting was performed at a velocity of 4 m/sec, whereas no cleavage was observed on the same configuration while cutting was performed at a cutting velocity of 10 m/sec. It is further interesting to note that the same crystal setup of 3C-SiC while cutting at 100 m/sec showed no characteristics of cleavage. Therefore, it appears that the transition of material removal on (001) <100> from structural transformation to the cleavage could likely be an outcome of lower cutting velocity or an increase in the *d/r* ratio from 0.57 to 1.

Table 6-5 summarizes the outcome of the simulation results in all the nine cases and also indicate corresponding values of local shear stress in the machining zone obtained

from the simulation. It can be seen from table 6-5 that case 4 and case 6 showed lower shear stresses required to cut 3C-SiC, suggesting that these are more amenable scratch directions in 3C-SiC.

Table 6-5: Mode of material removal with respect to various crystal setups

Crystal setup	**Crystal orientation**	**Cutting direction**	**Remarks on material removal mechanism**	**Shear stress in the machining zone of 3C-SiC (GPa)**
1	(111)	<-110>	Cleavage is dominant	38
2	(111)	<-211>	Cleavage is dominant	35
3	(110)	<-110>	Structural transformation with visible sub-surface damage	26
4	(110)	<001>	Solely due to structural transformation with no sub-surface damage	29
5	(001)	<-110>	Dominated by structural transformation with number of visible dislocations underneath the machined surface	37
6	(001)	<100>	At low cutting speed : Remnants of cleavage were observed At high cutting speed : Structural transformation was dominating	23
7	(11-2)	<1-10>	Structural transformation with minimum visible sub-surface damage	26
8	(110)	<-11-2>	Both cleavage (small extent) and structural transformation visible	37
9	(1-20)	<210>	Structural transformation with high degree of sub-surface damage	28

6.3.4 Analysis of dislocations

In this work, the DXA algorithm is used to identify dislocation lines and to determine their Burgers vectors, which are tabulated in table 6-6. Few cases where major dislocations were identified are shown in figure 6-10 in conjunction with figure 6-9. These snapshots provide useful information e.g. nature of the deformation of 3C-SiC, topography of the machined surface, regions of sub-surface damage, occurrence of cleavage through identification of cleaved crystallites and dislocations with quantitative details of the Burgers vector. Burgers vector is the most important characteristic feature of a dislocation, which defines the nature and magnitude of slip. This could in turn help to trace the occurrence of glide/shuffle mechanisms which could help in assessment of their contribution in governing the observed ductility in 3C-SiC as has been reported by some authors [211, 243, 248].

A complex interplay of crystal orientation, cutting speed, uncut chip thickness, cutting edge radius are known to influence the machining outcome even when the machining is carried out in a controlled environment. Hence, an alteration in these parameters during the course of machining may influence the activity of dislocation nucleation, making it somewhat a stochastic process in the context of nanometric cutting. This could potentially be considered as one of the reasons that the dislocations captured in the current work differs from another recent work [267]. However, in its current form, dislocation analysis provides substantial amount of information. For example, in case 4 and case 6 no dislocation event was identified suggesting that the observed ductility in 3C-SiC during nanometric cutting on these crystal setups was solely due to structural transformation of the cutting chips. Similarly, the volume of cleavage on (111) orientation was observed to be far higher in comparison to other crystal setups which is indicative of the fact that cleavage is dominant in 3C-SiC on this orientation irrespective

of the cutting direction. One important information from precision engineering perspective is that the machined surface in Case 1, Case 4 and Case 6 appears to be smoother compared to other combinations of cutting orientation and cutting directions. These setups can thus be classed as amenable cutting setups to cut 3C-SiC. The Burgers vector of the observed dislocations in all cases was captured as shown. However, the observed dislocations were of sufficiently smaller length to cause any glide or shuffle in 3C-SiC. Hence, the ductility observed was not on account of these dislocations but was an outcome of the structural transformation of 3C-SiC.

Table 6-6: Identified Burgers vectors

Crystal setup	**Crystal orientation**	**Cutting direction**	**Burgers vector**
1	(111)	<-110>	½<110> (in the cleaved crystallite) and not in the workpiece
2	(111)	<-211>	No dislocations
3	(110)	<-110>	½<110>
4	(110)	<001>	No dislocations
5	(001)	<-110>	A stacking fault and a partial dislocation (with unknown Burgers vectors) was observed
6	(001)	<100>	No dislocations
7	(11-2)	<1-10>	½<121>
8	(110)	<-11-2>	½<110> forming junctions with some ½<112> and ½<303> dislocation segments
9	(1-20)	<210>	<100>

(a) Crystal setup 3: Crystal orientation (110) cutting direction<-110>

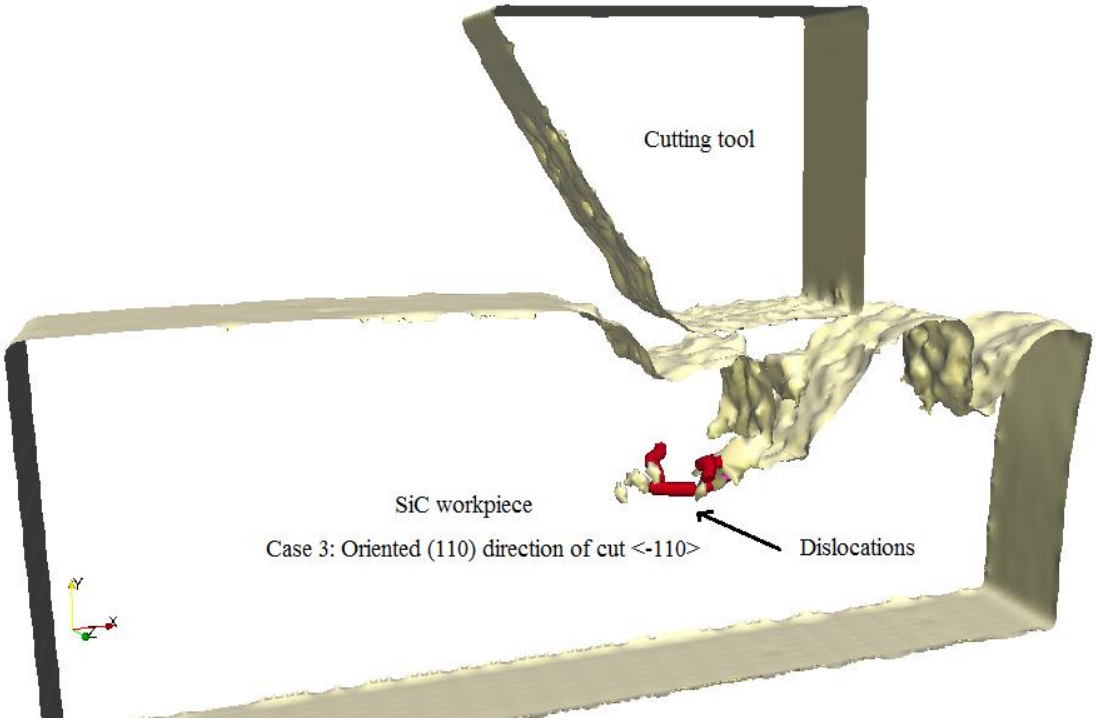

(b) Crystal setup 5: Crystal orientation (001) cutting direction<-110>

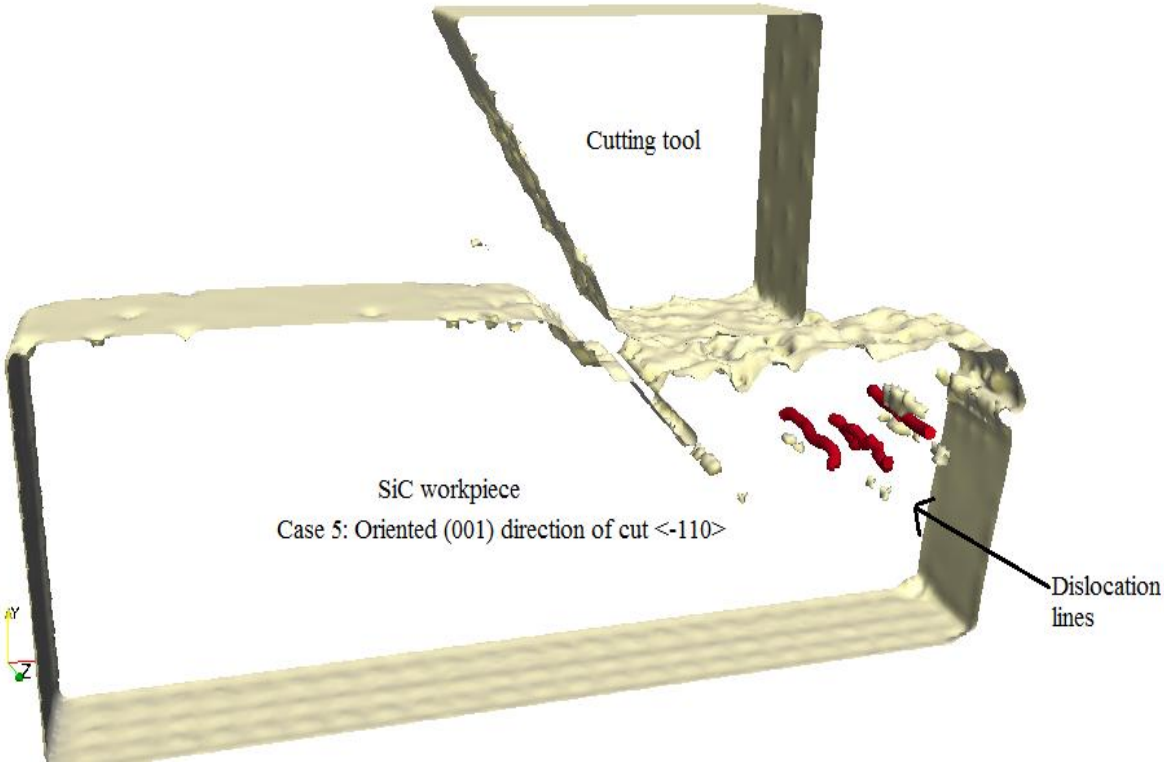

(c) Crystal setup 8: Crystal orientation (110) cutting direction<-11-2>

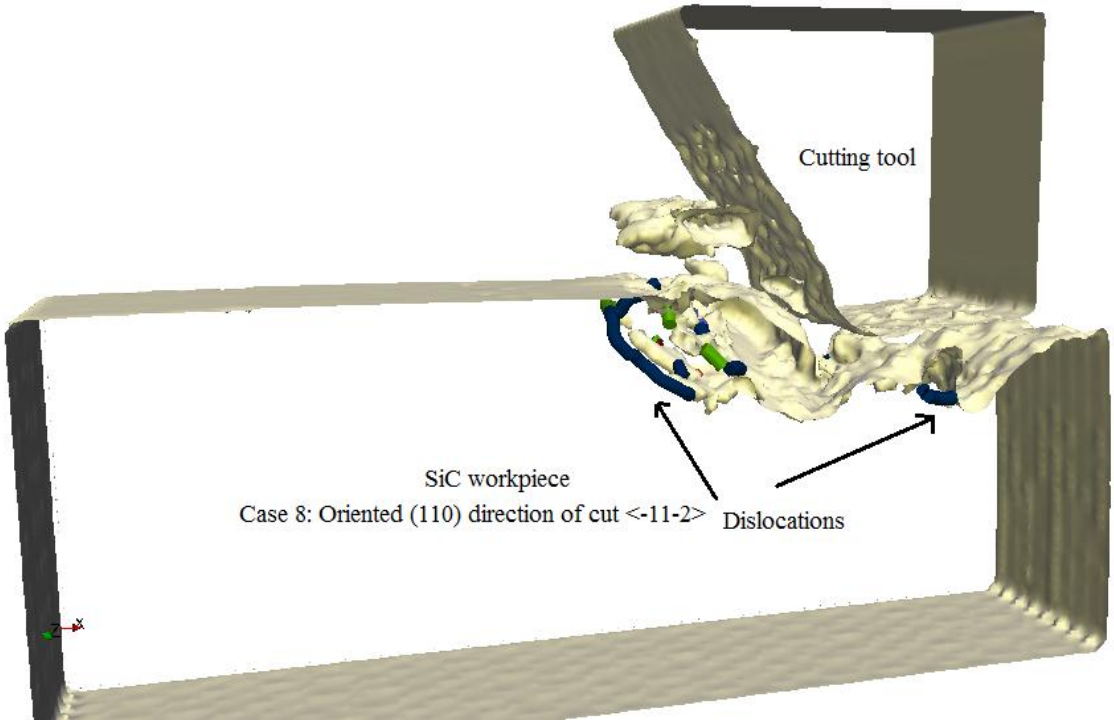

(d) Crystal setup 9: Crystal orientation (1-20) cutting direction<210>

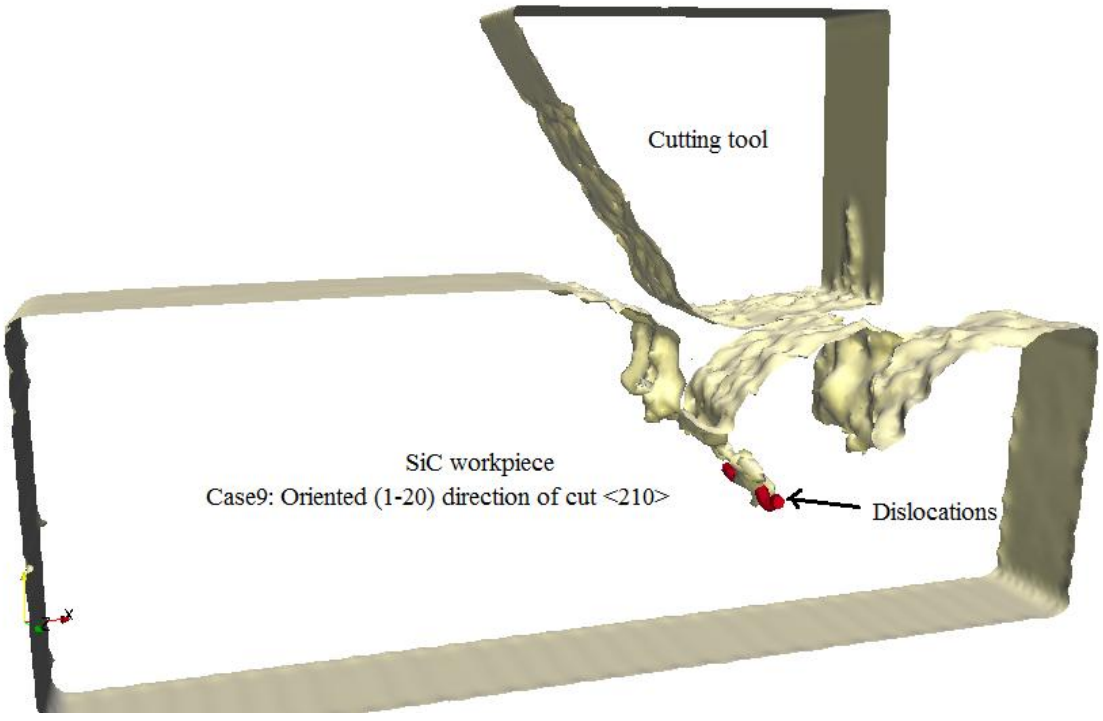

Figure 6-10: Output of the DXA algorithm showing dislocations during nanometric cutting of 3C-SiC in selected combinations of crystal orientation and cutting directions. The geometric boundaries of 3C-SiC and diamond crystallites are shown, while the geometric boundaries of the disordered phase are not visible in these visualizations.

A quantitative measure of the simulation results such as thrust forces (F_y or F_t), tangential cutting forces (Fx or Fc), resultant forces and coefficient of kinetic friction (F_c/F_t) are tabulated in table 6-7 which are plotted in figure 6-11 for comparison purposes.

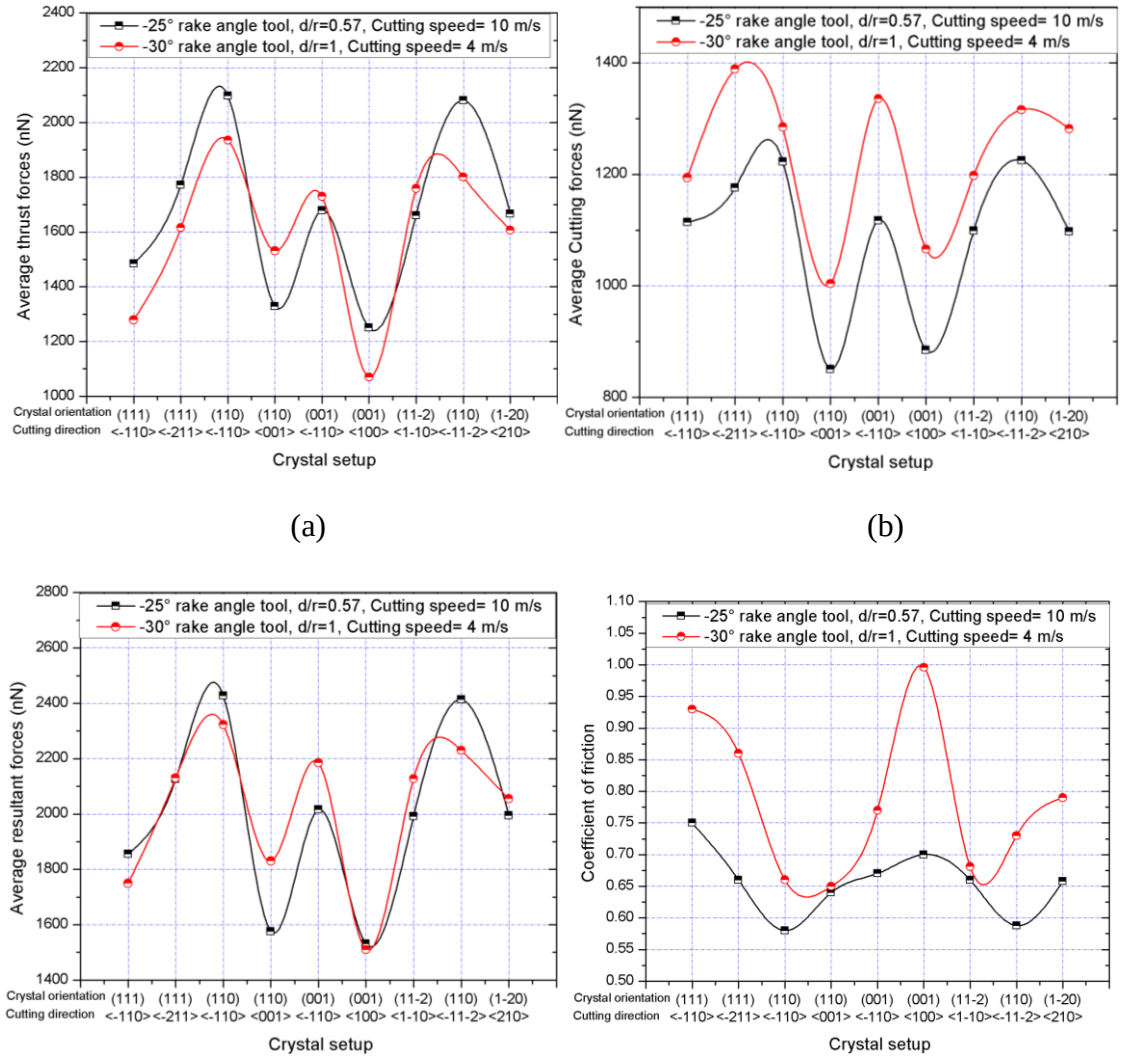

Figure 6-11: Variation in cutting forces and friction coefficients

Table 6-7: Percentage variation in the machining forces and friction coefficient

Crystal orientation		111*	111*	110	110	001	001	11-2	110	1-20	% anisotropy variation
Cutting direction		-110	-211	-110	001	-110	100	1-10	-11-2	210	
Average thrust force (F_t) nN	Set 1	1484	1772	2098	1328	1679	1250	1661	2081	1667	40.4%
	Set 2	1279	1616	1936	1531	1730	1070	1759	1801	1607	44.73%
Average cutting force (F_c) nN	Set 1	1114	1176	1223	850	1117	885	1099	1225	1097	30.61%
	Set 2	1194	1389	1285	1004	1316	1066	1198	1316	1282	23.71%
Average resultant force nN	Set 1	1855	2126	2428	1576	2016	1531	1991	2414	1995	36.94%
	Set 2	1749	2130	2323	1830	2185	1510	2128	2230	2055	35%
Coefficient of kinetic friction (F_c/F_t)	Set 1	0.75	0.66	0.58	0.64	0.67	0.7	0.66	0.588	0.658	17.14%
	Set 2	0.9 3	0.86	0.65	0.65	0.77	0.996	0.681	0.73	0.79	34.73%

*Mechanism of material removal on (111) plane was cleavage/fracture dominant which is the reason that whenever fracture occurs the cutting forces dropped and appears to be lower here. Therefore, machining outcomes on (111) crystal orientation were not considered in the calculation of anisotropy.

Although different d/r ratio, different tool rake angle and different cutting speeds were used in the two trials, the trend of the variation and the extent of variation in the plots shown in figure 6-11 were eventually found to exhibit the same pattern. As evident, the

thrust forces were found to be maximum for the crystal setup (110) <-110> while minimum for (001) <100>. From these values, the extent of anisotropic variation in the thrust forces was observed to be around 45%. Similarly, the tangential cutting forces were found to vary by 30% whereas the resultant force showed the extent of anisotropy of up to 37%. Contrary to the similar variation of the machining forces in both trials, friction coefficient showed significant variation. For example, a small variation in the friction anisotropy of upto 17% was noticed for high cutting speed of 10 m/sec and d/r ratio of 0.57 in contrast to a variation of friction anisotropy of upto 35% at a low cutting speed of 4 m/sec and d/r ratio of 1. The former part of the figure 6-12 shows the variation in the peak temperature of the workpiece with respect to the change in crystal setup and the latter part of the figure 6-12 shows the variation in the average of the peak temperature of the atoms in the cutting edge radius of the tool. It can be seen from a comparison of both these figures that the trend of the plot in both simulation trials is quite similar. It is further evident from former part of figure 6-12 that the local temperature in the workpiece rose upto 2000-2200 K when the cutting was performed on (111) crystal orientation. It is noteworthy to refer to the earlier discussions on the occurrence of cleavage on (111) crystal orientation. An occurrence of cleavage releases a tremendous amount of elastic energy in the form of heat which gets transmitted both to the workpiece and to the cutting tool. Consequently, the local temperature of the workpiece in this particular case increases to about 2200 K while cutting tool edge temperature increases to around 520 K observed while cutting on the (111) orientation. Interestingly, strength of materials having large ratio of covalent bonding do not get effected at elevated temperatures as much as ionic bonded materials [268]. This is also the reason why SiC exhibits lower coefficient of thermal expansion and high thermal conductivity. The ratio of covalent to ionic bonding in SiC is about 1:9 which justifies that it is the concentrated shear rather than the adiabatic shear which drives ductility in

SiC during its nanometric cutting [212]. Along the easy cutting directions, the temperature rise in the workpiece was only upto 600K. Also, during cutting on easy cutting directions i.e. case 4 and case 6 least temperature on the cutting tool was observed whereas case 3, case 5 and case 8 showed a somewhat higher temperature on cutting tool and workpiece.

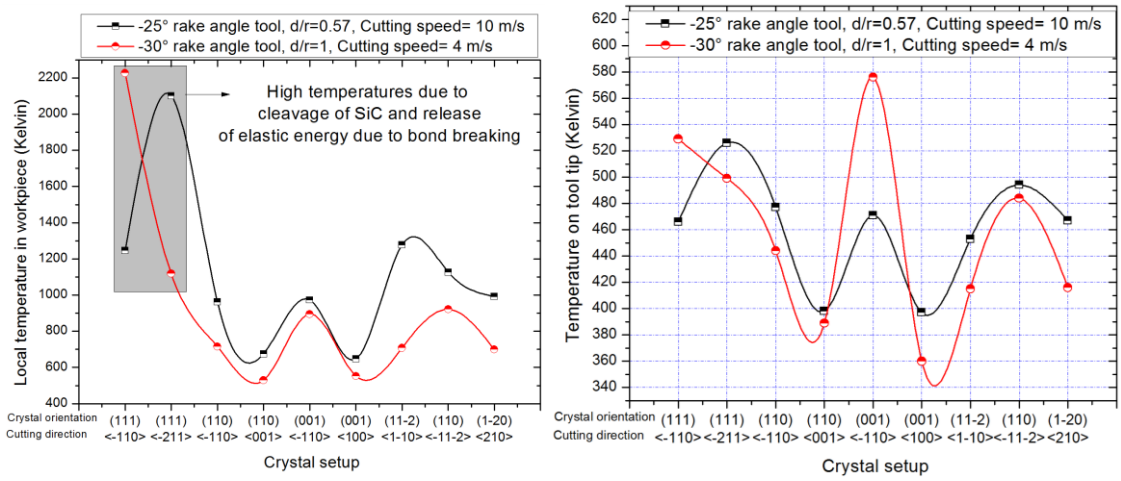

Figure 6-12: Variation in the temperature in the machining zone

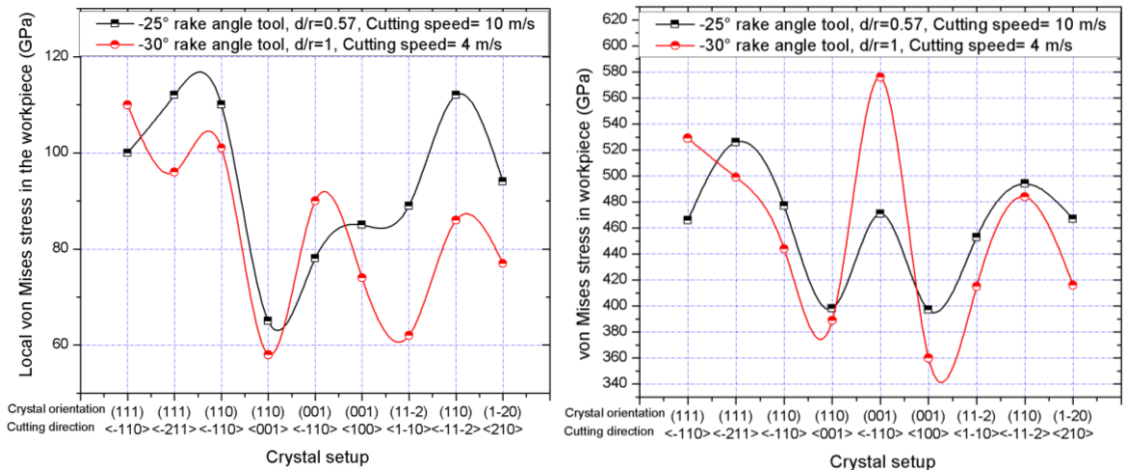

Figure 6-13: Variation in the von Mises stresses

* Mechanism of material removal on (111) plane was cleavage/fracture dominant which is the reason that the cleavage energy gets transformed to cutting heat and is apparent from the results.
+ reflects stress concentration responsible for the occurrence of cleavage

Table 6-8: Percentage variation in temperature and stresses while cutting 3C-SiC

Crystal orientation		111*	111*	110	110	001	001	11-2	110	1-20
Cutting direction		-110	-211	-110	001	-110	100	1-10	-11-2	210
von Mises stress in the machining zone of the workpiece (GPa)	Set 1	100	112^{+}	110	65	78	85	89	110^{+}	94
	Set 2	110^{+}	96	101	58	90	74	62	86	77
von Mises stress on the cutting edge of the diamond tool	Set 1	343	350	380	322	343	300	322	354	355
	Set 2	400	419	386	386	412	325	337	380	388
Average temperature in the machining zone of the workpiece (Kelvin)	Set 1	1247	2102	962	675	973	648	1277	1127	992
	Set 2	2227	1119	715	529	896	553	708	921	699
Average temperature on the cutting edge of the tool (Kelvin)	Set 1	466	526	477	398	471	397	453	494	467
	Set 2	529	499	444	389	576	360	415	484	416

Figure 6-13 in conjunction with table 6-8 shows the variation in the von Mises stresses in the machining zone. A high magnitude of von Mises stress of upto 112 GPa can be seen when cutting was performed on (111) orientation unlike case 4 (easy cutting direction) where this magnitude was only upto 58 GPa. Thus, it appears that it is the high stress concentration that is responsible for the occurrence of cleavage on (111) crystal orientation. Knowhow of stress state on the cutting tool is very promising information. In this context, machining stresses that acted on the cutting tool during

nanometric cutting of 3C-SiC on crystal setups (110) <001> and (001) <100> were found minimum and were of similar magnitude. In common with 3C-SiC, these two crystal setups are once again known to be soft cutting directions for easy material removal in diamond. The automated dislocation algorithm (DXA) showed no sign of dislocations while machining on (001) <100> and (110) <001> setups whereas multiple number of dislocations were observed on another crystal setups, although they were not found responsible to bring ductility in 3C-SiC via glide/shuffle mechanisms.

6.4 MD Simulation of polymorphs of SiC

Table 6-9: Process variables used for MD simulation model

Workpiece material	Number of atoms in the workpiece	Number of atoms in the diamond cutting tool
3C-SiC (14.2624 nm × 4.6353 nm × 4.2787 nm)	28600	21192
6H-SiC (14.2624 nm × 4.6353 nm × 5.1347 nm)	31999	25607
4H-SiC (14.2624 nm × 4.6353 nm × 3.92216 nm)	27360	19426
Silicon (14.2624 nm × 4.6353 nm × 4.2787 nm)	14840	21192
Equilibrium lattice parameters used for the workpiece(Å)		
a= b=c= 4.321 ; α = β= γ= 90°		3C-SiC
a= b=3.07; c=14.26 ; α = β= 90° ; γ= 120°		6H-SiC
a= b=3.07; c= 9.856 ; α = β= 90° ; γ= 120°		4H-SiC
a= b=c= 5.432 ; α = β= γ= 90°		Silicon
Crystal orientation of diamond tool		Cubic
Crystal orientation of workpiece		(010)
Cutting direction		<100>
Cutting edge radius (nm)		2.2974
Uncut chip thickness / in-feed (nm)		1.3128
Cutting tool rake and clearance angle		-25° and 10°
Equilibration temperature		300 Kelvin
Cutting velocity		100 m/s
Timestep		0.5 femtoseconds

This section covers observations and discussion of the significance of the MD simulations results of major polymorphs of SiC by comparing the cutting forces, cutting hardness, chip morphology, workpiece deformation, temperature in the cutting zone and, finally, the tool wear. The simulation parameters used for the evaluation of the performance of the nanometric cutting of the various polytypes of silicon carbide are listed below in table 6-9. Figure 6-14 shows schematically the orientation of the components of cutting force acting on the tool. The "tangential cutting force" (*Fc*) acts in the *x* direction, the "thrust force" (F_t) acts in the *y* direction and F_z acts in the direction orthogonal to the X and Y planes.

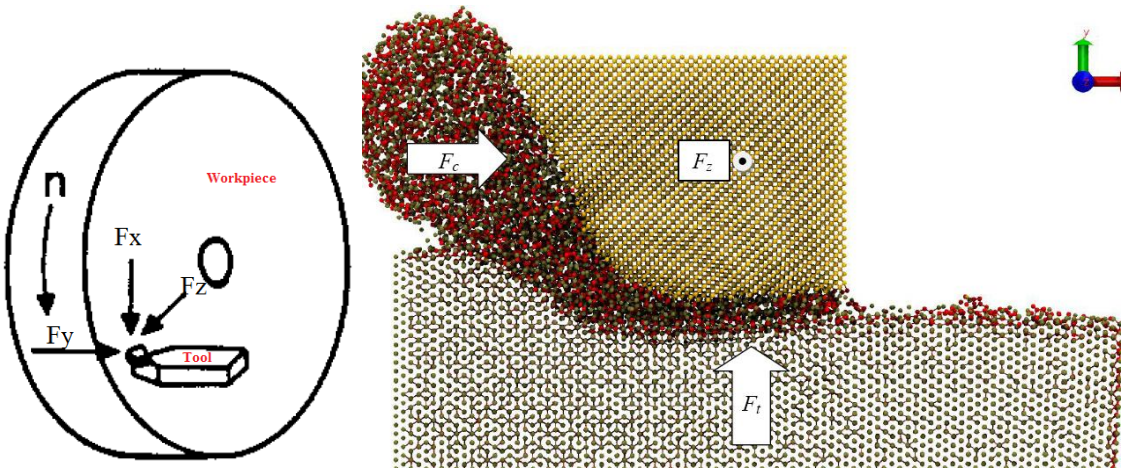

Figure 6-14: Cutting forces during nanometric cutting

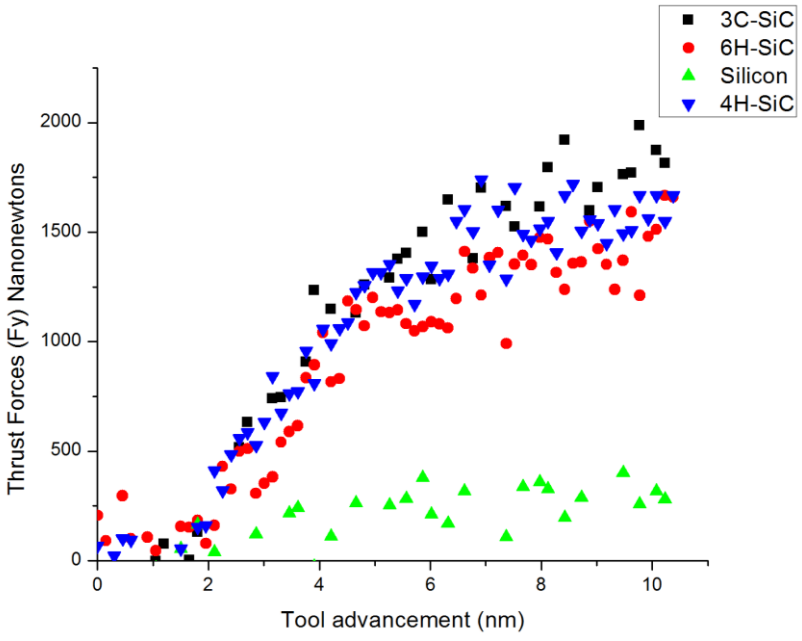

(a) Evolution of thrust forces

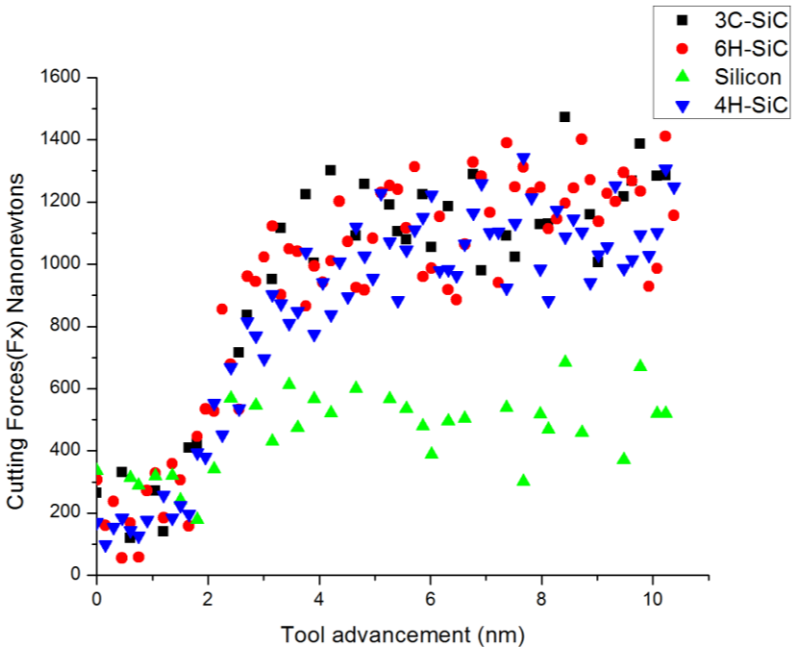

(b) Evolution of tangential cutting forces

Figure 6-15: Comparison of thrust and tangential cutting forces

A comparison of the main components (thrust and tangential cutting forces) for 6H-SiC, 4H-SiC, 3C-SiC and silicon is shown in figure 6-15. It can be seen from figure 6-15 that the magnitudes of the forces are significantly higher for all polytypes of SiC compared to silicon and, as with the thrust force (*Fy*), the highest in magnitude is for 3C-SiC, followed by 4H-SiC and 6H-SiC respectively. The magnitudes of *Fx* were however, found to be in a different order, the highest being for 3C-SiC, followed by 6H-SiC and 4H-SiC. Figure 6-16 shows an individual comparison of the thrust and cutting force development. It seems that in the current configuration, F_c is higher than F_t for machining silicon, whereas the reverse is the case for SiC polytypes.

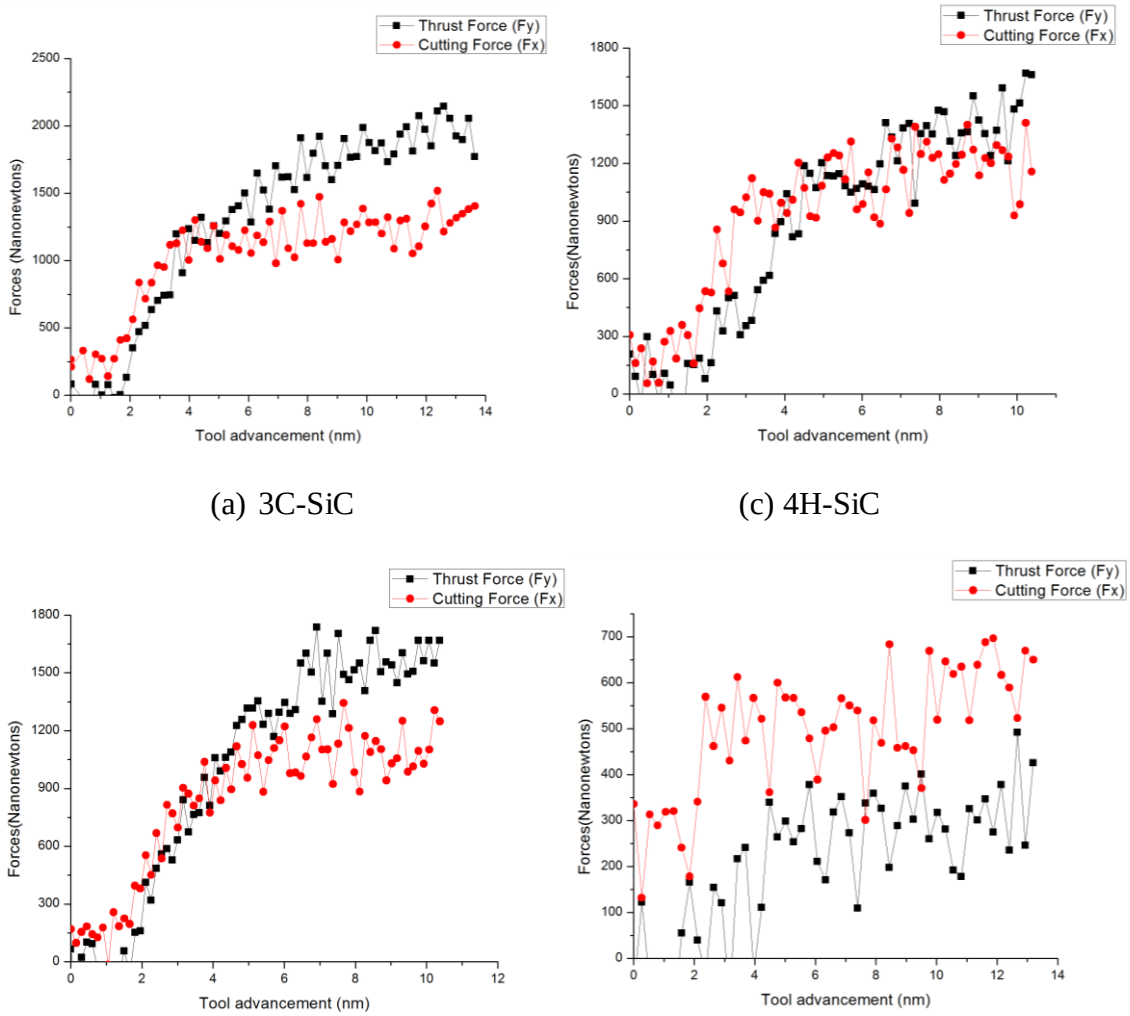

Figure 6-16: Comparison of forces on individual material during nanometric cutting

In conventional cutting, the dominance of cutting forces over thrust forces is attributed to the large shear plane area which results from a decrease in the shear angle. Patten *et al.* [153] have demonstrated that an increase in the negative tool rake angle increases the thrust force compared to the tangential cutting force. It is of further interest to note that higher cutting forces were observed while cutting 6H-SiC with a tool having a negative rake angle of -45° [119]. However, the cutting tool deployed in that study had a very large clearance angle (40°) and hence it experienced lower thrust forces than cutting forces. In the current case, neither thrust force nor cutting force seems to be a clear criterion to assess the relative machinability of the material. This difficulty in the

evaluation of the machinability can, however, be overcome using the "cutting hardness" which appears to be a new and novel quantitative indicator of the cutting resistance of a material irrespective of the machining parameters, expressed as follows:

$$\text{Average Cutting Hardness} = \frac{\text{Resultant force}}{\text{Volume of material removed}} = \frac{\sqrt{Ft^2 + Fc^2}}{bdl} \qquad 6\text{-}1$$

where F_t and F_c are the thrust and tangential cutting forces, respectively, b is the width or depth of cut, d is the uncut chip thickness and l is the length of cut. The evolutions of cutting hardness for 3C-SiC, 4H-SiC, 6H-SiC are shown in figure 6-17, compared with the reference material, silicon.

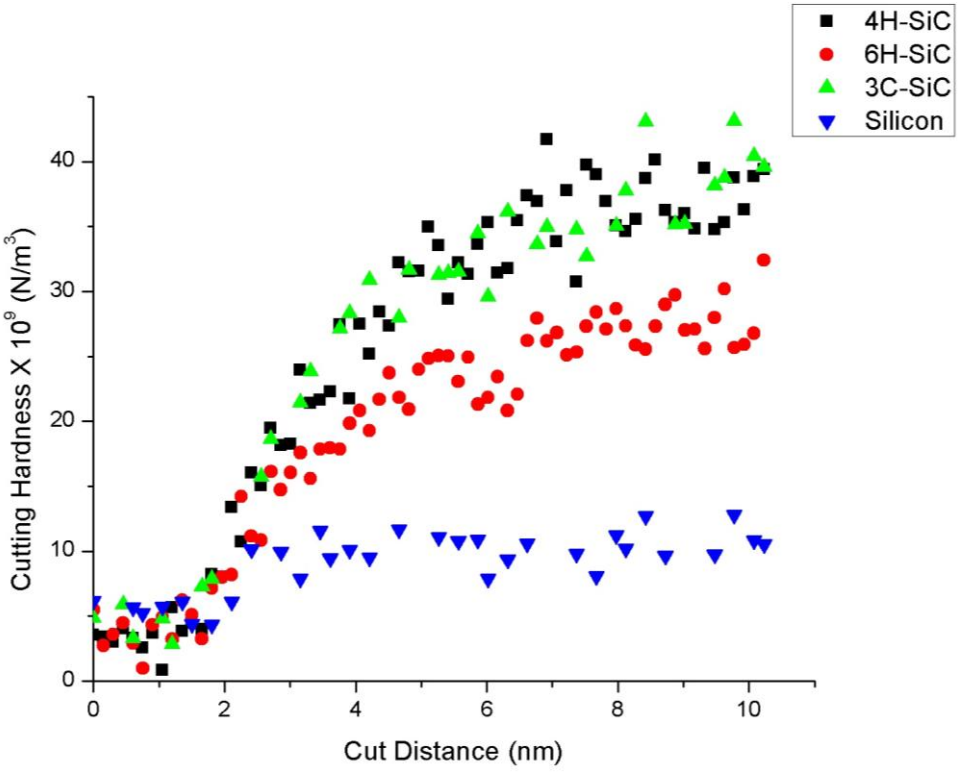

Figure 6-17: Cutting hardness of various polytypes of SiC compared with silicon [260]

The average values of cutting hardness over the 10 nm tool advancement for silicon, 3C-SiC, 6H-SiC and 4H-SiC were found as 9.1, 26.4, 19.2 and 25.5 respectively, so 3C-SiC offered the highest cutting resistance (~2.9 times that of silicon) followed by 4H-SiC (~2.8 times silicon) and 6H-SiC (~2.1 times silicon). The ratio of transition pressure and cutting hardness were found to be 2.25, 2.15, 1.75 and 1.42 for 6H-SiC, 3C-SiC,

4H-SiC and silicon respectively. A study made during the 1970s reported this ratio in carborundum as 1.6952 which looks in reasonable agreement with the value of 1.75 obtained for 4H-SiC. Figure 6-18 shows the average rise in the temperature of cutting edge of the tool and on the workpiece as the tool moves through each of the workpiece materials.

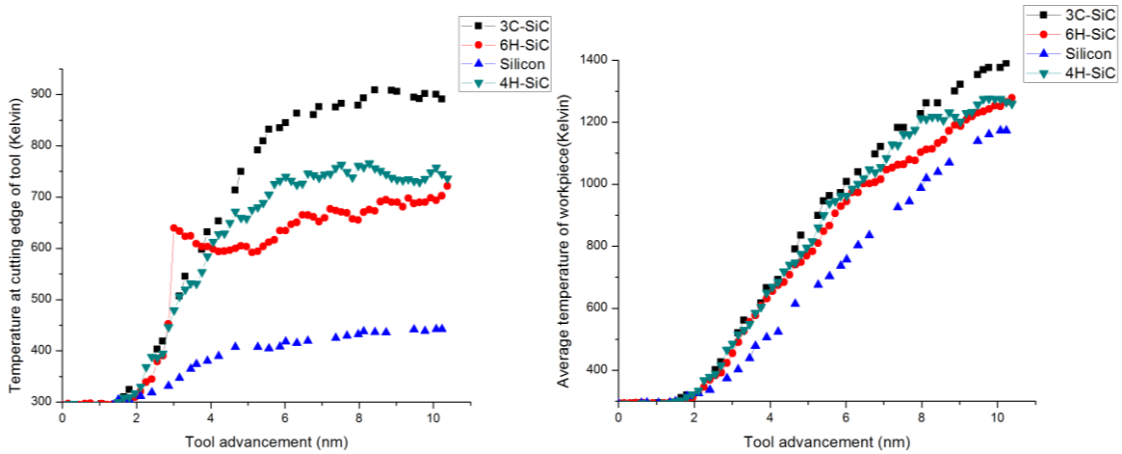

Figure 6-18: Comparison of temperature evolutions during nanometric cutting

3C-SiC showed the highest temperatures both on the cutting edge and the workpiece followed by 4H-SiC, 6H-SiC and silicon, so that all polytypes of SiC result in higher cutting temperatures than single crystal silicon. A high temperature in the cutting zone reduces the life of diamond tools [269] as it reduces hardness through graphitization of the diamond, a process which is accelerated further in the presence of properly directed shear stresses [252]. This mechanism can be supported by the analysis of radial distribution function, as discussed in the next section. High temperature is of course known to compromise the life of diamond tools, and an appropriate coolant may help to ameliorate this and provide improved surface roughness as well [270-271].

6.5 Sub-surface crystal lattice deformed layer depth and residual stresses

The depth of the sub-surface crystal lattice deformed layer is very critical information required at each step of the manufacturing process. The machined surface (typically up to a depth of 50 nm in silicon) obtained after the diamond turning differs from the pristine material due to the effects of the residual stresses and high temperature in the localized cutting zone. Severe plastic deformation compounded with high temperature and pressure underneath the cutting tool results in alteration of the microstructure in the sub-surface of the machined component. Depending upon the characteristics of the sub-surface, this may influence the component life by its effect on service life, fatigue and creep. Therefore, it usually requires a post machining operation such as chemical etching or chemo-mechanical polishing process to remove such deformed lattice layer depth induced by the mechanical micromachining process [83]. A good combination of machining parameters, crystal orientation and cutting direction can help to reduce this deformed layer depth and offset the time and the cost associated with such secondary post-machining fine finishing processes.

Monnoye *et al.* [272] has cited that different experimental methods e.g. Normarski observation, transmission electron microscopy, Rutherford backscattering, photon backscattering, KOH etching, Raman scattering and even positron annihilation have been used to identify the sub-surface deformation layer depth but it is too complicated to trace the details of sub-surface deformation using experimental methods. Since all the machining parameters in the MD simulation can be maintained at a same level, a measure of the sub-surface deformation can provide a useful index. This can help to understand if a specific material is apt to undergo large deformations irrespective of the machining parameter employed. On an experimental side, Raman peak in the current work is also found to be yet another convenient and quick way to measure residual

stresses. For example, a freshly polished diamond tool was examined using a digital microscope which was then examined using Raman spectroscopy, the results of which are shown in figure 6-19 and figure 6-20 respectively.

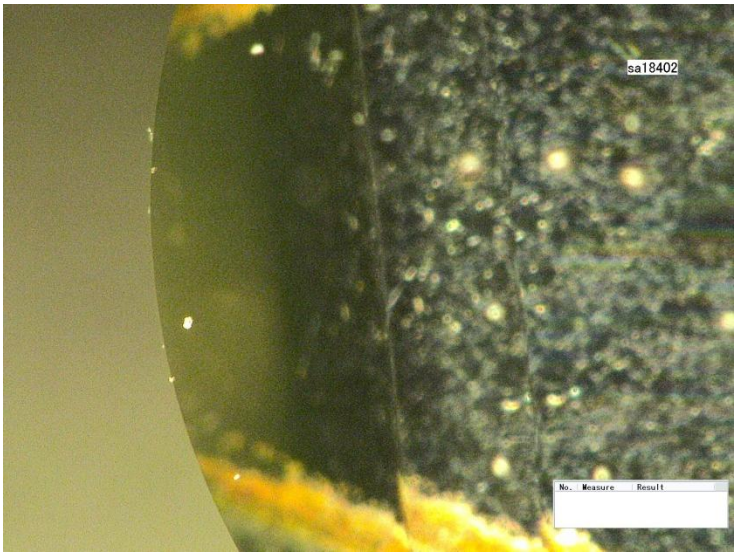

Figure 6-19: Examination of the cutting edge of a diamond tool using digital microscope at 150 X Zoom (Keyence- VHX-500F)

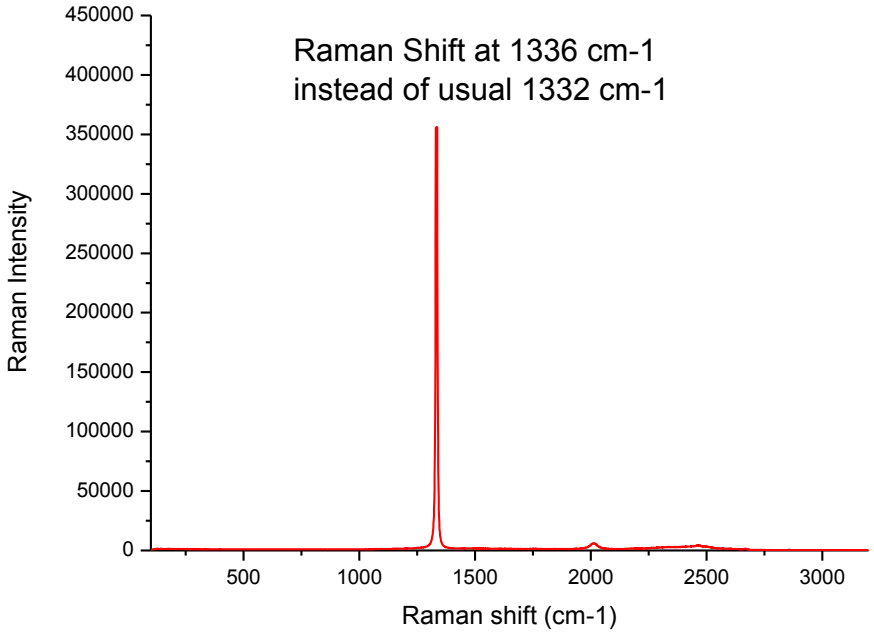

Figure 6-20: Raman analysis of a freshly prepared diamond cutting tool

As can be seen from the figure 6-19, the cutting edge of the freshly prepared diamond tool was finished smoothly. The corresponding Raman peak for a freshly prepared

diamond tool (residual stress free) is accordingly expected to show the peak at 1332 cm^{-1}. However, as shown in figure 6-20, the Raman peak during experimental measurement was found to be shifted towards right side i.e. at 1336 cm^{-1} signifying the existence of the compressive residual stresses on the edge of the cutting tool. A shift of this peak on the left hand side would have meant the existence of tensile residual stresses. With this information, a simple mathematical equation may be applied to quantify the extent of the residual stresses:

$$\omega = \omega_0 + 0.43P \quad \text{6-2}$$

$$1336 = 1332 + 0.43P \quad \text{6-3}$$

where ω is the actual Raman peak obtained from the experiment, ω_0 is the ideal Raman peak of the stress free diamond and *P* is the residual stress in kbar in the material being analysed from the Raman analysis. Thus, the residual stress in the diamond cutting tool was estimated to be about 0.93 GPa.

Lucca *et al.* [273] conducted experimental trials to investigate the depth of the subsurface damage during ultra precision machining of fine grain copper over the range of uncut chip thicknesses 0.01–10 mm. They suggested that the depth of the plastically deformed layer is strongly affected by the tool edge radius and was unaffected by the uncut chip thickness. In the current simulation, although both SiC and silicon show curly chip formation, the extent of this varies and the finished surface and subsurface obtained after machining differs significantly. The chip shapes in figure 6-21, 6-22, 6-23 and 6-24 shows that chip formation has taken place in all four materials by deformation rather than fracture, i.e. that ductile-regime machining could be achieved in all four materials.

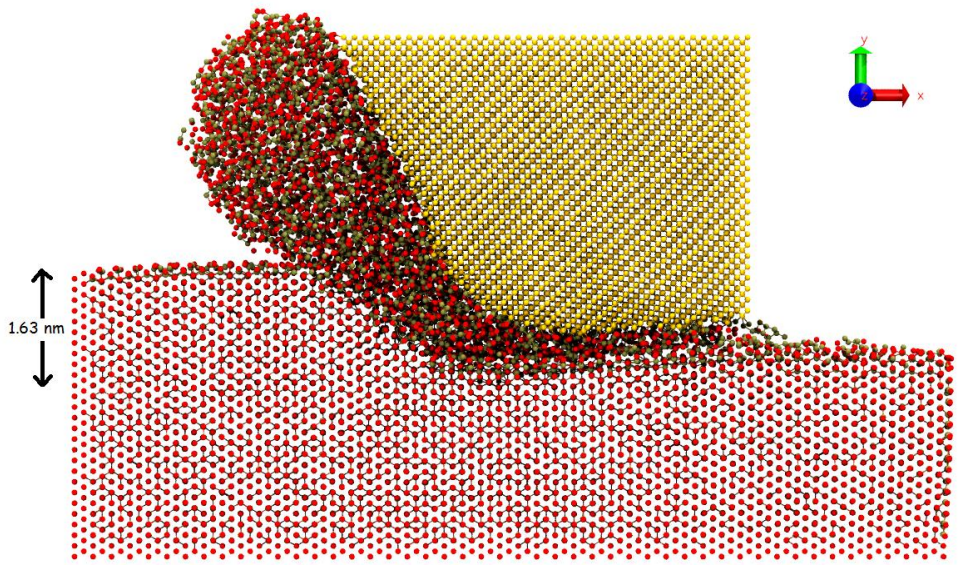

Figure 6-21: Sub-surface crystal lattice deformed layer depth and chip morphology of 4H-SiC

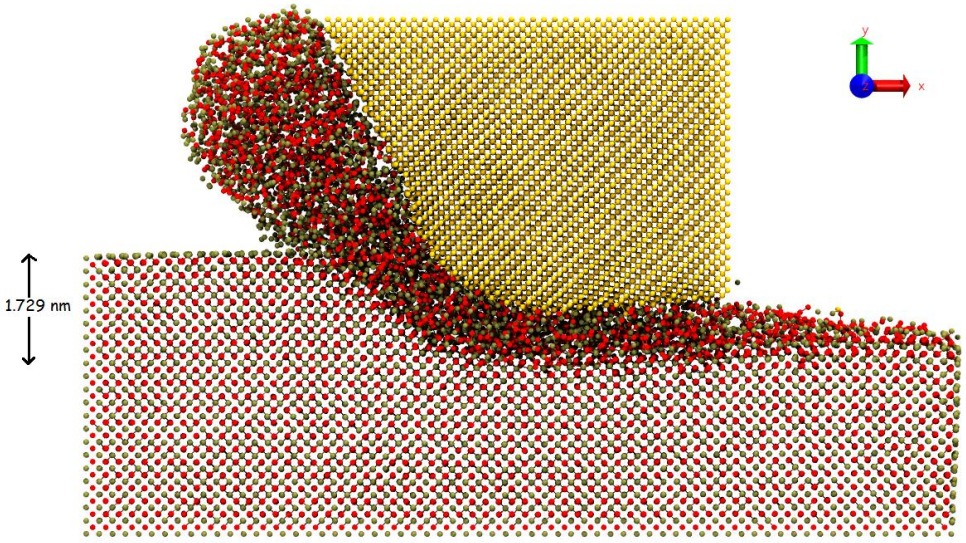

Figure 6-22: Sub-surface crystal lattice deformed layer depth and chip morphology of 3C-SiC

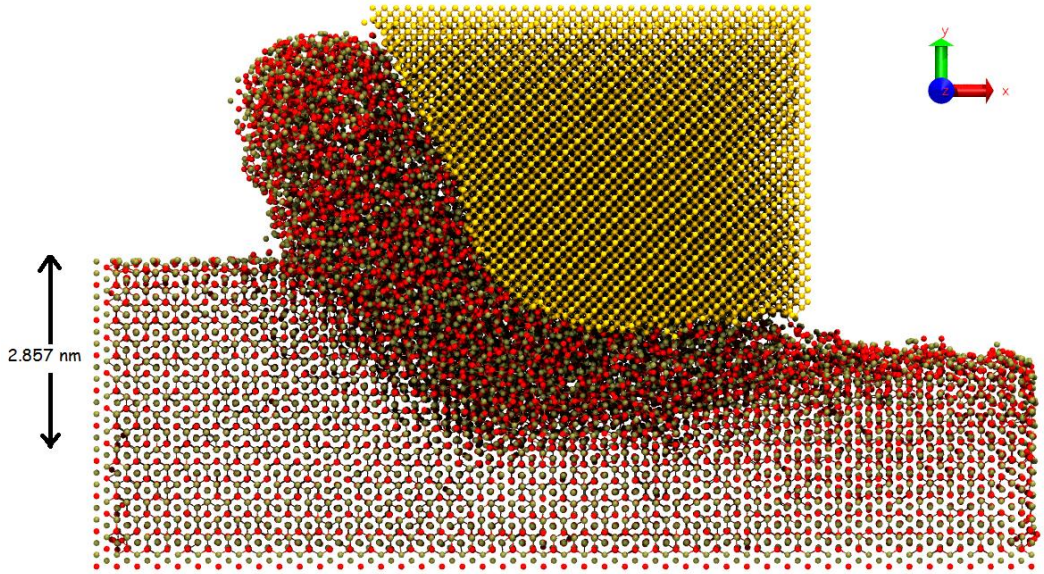

Figure 6-23: Sub-surface crystal lattice deformed layer depth and chip morphology of 6H-SiC

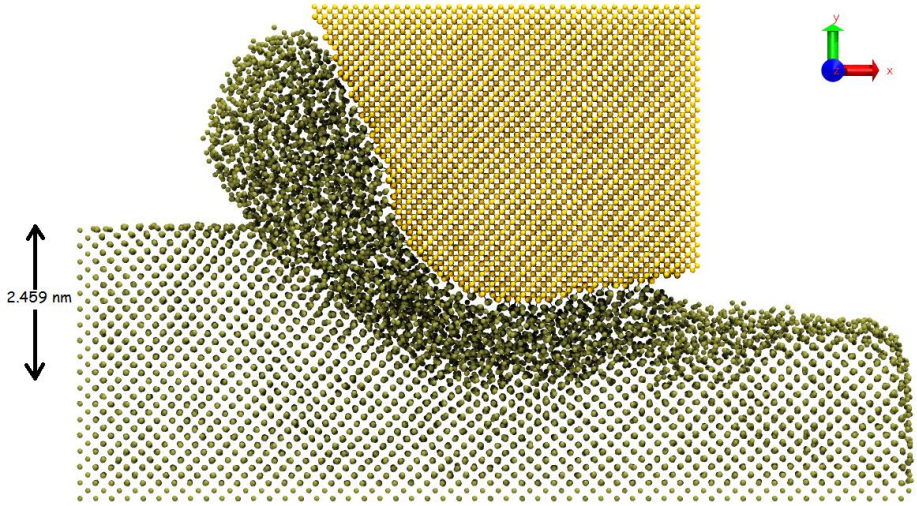

Figure 6-24: Sub-surface crystal lattice deformed layer depth and chip morphology of silicon

These figures also show an estimate of the sub-surface deformation depth below the uncut surface directly under the final tool position for all the polytypes of SiC and silicon. The quality of the finished surface (indicated by the deformed layer depth) appears to be the best on 4H-SiC, followed by 3C-SiC, silicon and, finally, 6H-SiC whose sub-surface is heavily distorted. This can be quantified by subtracting the uncut chip thickness from the estimated measurement, giving maximum sub-surface deformed

layer depths from the finished surface of 0.32 nm, 0.42 nm, 1.54 nm and 1.15 nm accounting for about 1.24, 1.32, 2.18 and 1.87 times the uncut chip thickness for 4H-SiC, 3C-SiC, 6H-SiC and silicon, respectively. Whereas the nanometric cutting and nano-indentation differs, the sub-surface deformation measured experimentally during nano-indentation on 6H-SiC, found to be 2.5 times of the maximum indentation depth [246] provides further evidence that 6H-SiC is apt to undergo large sub-surface deformations during contact loading. To further confirm these findings, the critical crack length, which is dependent on the fracture toughness and hardness of the SiC workpiece has been calculated as shown in table 6-10.

Table 6-10: Calculation of critical crack length [31, 34]

S.No.	Material	Fracture Toughness ($MPa.m^{1/2}$)	Hardness (GPa)	Critical crack length (micron) $c^* = 120\left[\frac{K_c^{\,2}}{H^2}\right]$
1.	3C-SiC	2.02	26.4	0.7025
2.	4H-SiC	1.9	25.5	0.6667
3.	6H-SiC	1.9	19.2	1.1751
4.	Silicon	0.9	9.1	1.1737

Amongst the other polytypes, 3C-SiC has the maximum fracture toughness and maximum hardness while 6H-SiC has the least hardness and shares the same fracture toughness as 4H-SiC. The ductile regime machining model [22] assumes that fracture damage starts at a critical chip thickness so that smaller critical crack lengths are desirable in order that a crack free machined surface is obtained making 4H-SiC the preferred choice over other polytypes for SPDT. Thus, both MD and the ductile regime

machining model suggest that 6H-SiC give the poorest and 4H-SiC the best sub-surface conditions.

6.6 Difference in machining of single crystal and polycrystalline SiC

Unlike machining single crystal semiconductors, Yan *et al.* [121] found that the reaction bonded SiC (RB-SiC) do not undergo any phase transformation during its SPDT. They further highlighted that the machined surface roughness on RB-SiC was significantly high. Quite similar to this observation was the outcome of the study of Patten and co workers who have observed very high machined surface roughness while machining 3C-CVD-SiC [120]. Both these materials, i.e. CVD-SiC and RB-SiC share one common credential that these are polycrystalline materials while most of the observations stated earlier are valid only for single crystal materials. This raises a key question on how the mechanism of chip formation changes while machining a polycrystalline material. To answer this question, an MD simulation model for the nanometric cutting of polycrystalline sample SiC workpiece with a cutting speed of 5 m/s, uncut chip thickness of 1.31 nm, negative rake diamond tool having cutting edge radius of 2.3 nm and total included angle as 105° was developed [274]. Figure 6-25 and figure 6-26 shows a comparison of the responses of single crystal (SC) 3C-SiC and polycrystalline (PC) 3C-SiC before and during the nanometric cutting process.

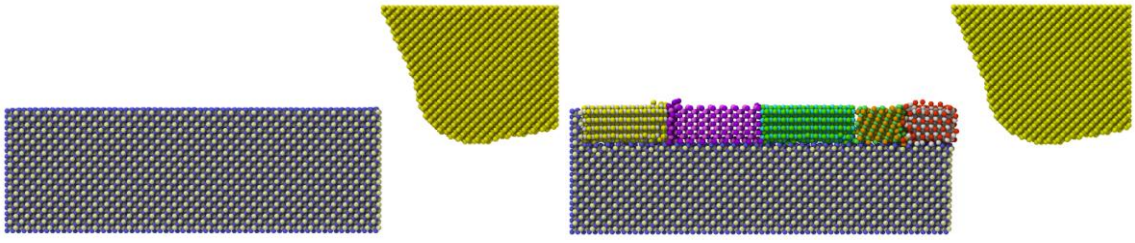

(a) Snapshot of SC-3C-SiC (b) Snapshot of sample PC-3C-SiC

Figure 6-25: Snapshot from simulation after equilibration of both the SiC workpiece

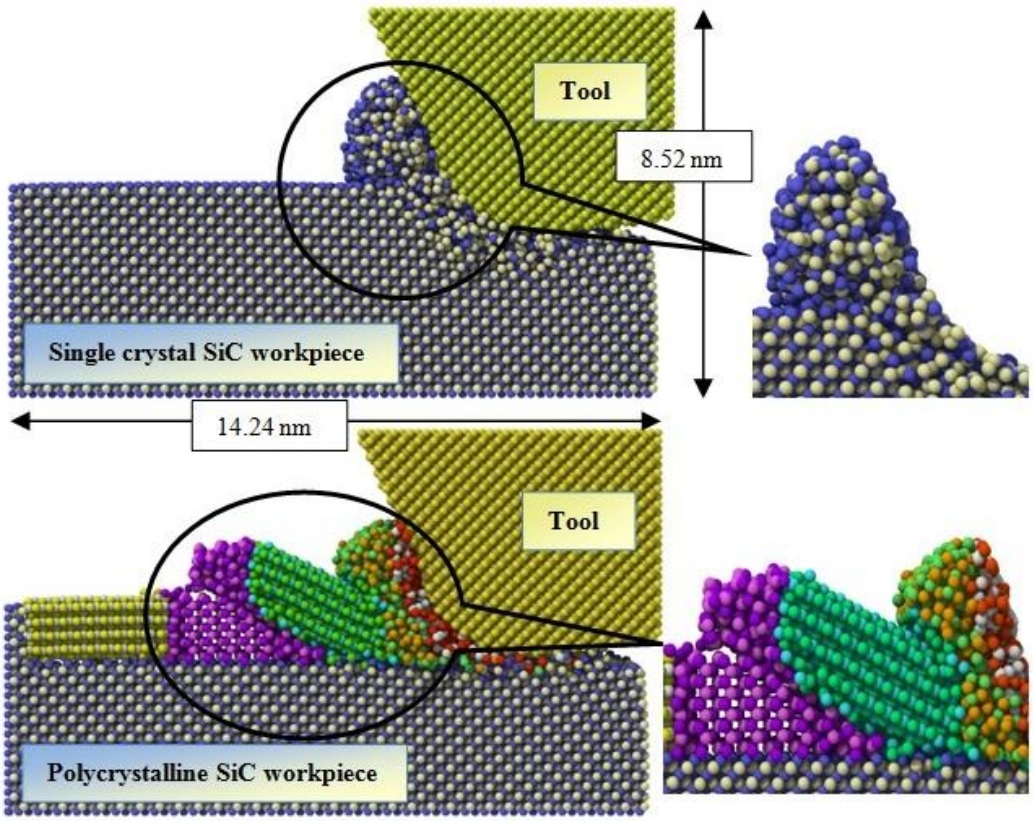

Figure 6-26: Snapshot from simulation showing response of SiC workpiece during cutting

As evident from figure 6-26, the absence of grain boundaries causes tremendous lattice distortion which is responsible for the structural transformation of the cutting chips in single crystal SiC. Such phase transformations are, however, obstructed by the presence of grain boundaries during machining of polycrystalline workpiece such as RB-SiC. In an RB-SiC workpiece, the grains of SiC are oriented along different crystal orientations. Since grain orientation changes from one crystal to another in polycrystalline SiC, the cutting tool experiences work material with different crystallographic orientations and directions of cutting. Thus, some of the grain boundaries cause the individual grains to slide along the easy cleavage direction. This causes the build-up of stresses at the grain boundaries. Consequently, the cutting chips in RB-SiC are not deformed by plastic deformation alone rather a combination of the phase transformation at the grain boundaries and the slip of the grains both precede in tandem. This is the reason that

silicon bonds underwent amorphization while no phase transformation of 6H-SiC grains was observed during diamond turning of RB-SiC [121].

Since the occurence of cleavage in polycrystalline SiC occurs in a random manner depending on the ease of lowest cleavage energy offered by a particular grain, this explains the observation of slightly higher surface roughness in a polycrystalline material than that in a single crystal material. This has been schematically presented in figure 6-27.

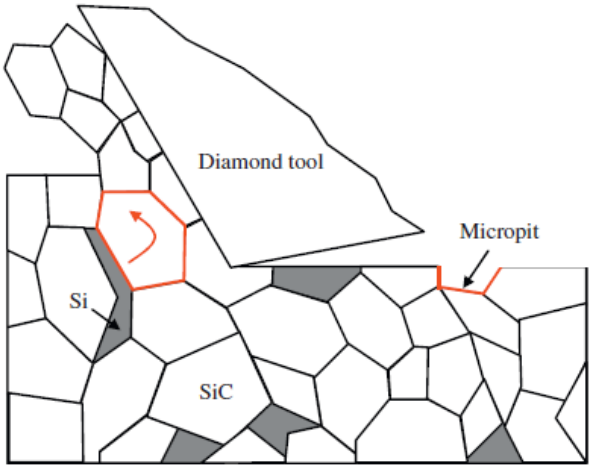

Figure 6-27: Effect of grain boundaries on the nanometric cutting of SiC [121]

Also, the average specific cutting energy for both the configurations was computed. Specific energy is defined as a ratio of the work performed (cutting force × distance travelled) by the cutting tool to the volume of material removed. The value obtained for polycrystalline 3C-SiC was found as 115 GPa which is relatively lower than the average specific cutting energy for single crystal 3C-SiC i.e. 150 GPa. This is for the fact that sliding along the easily cleavable direction in a non-uniform lattice will require least energy in comparison to cut a continuous and uniform crystal lattice on a relatively harder direction of cut. The above mechanism also explains that why RB-SiC [121] and CVD-3C-SiC [120], despite providing high surface roughness, were observed to be relatively more machinable than the single crystal SiC in the previous experiments.

6.7 Wear mechanism of diamond tools

Wear of diamond tools is an undesirable problem in SPDT not only because of the replacement cost but also because of its spurious effects on the attainable machined surface finish. In-process degradation of the diamond tool due to wear may alter the tool–workpiece contact and hence the machining conditions which can cause a sudden transition of material removal mechanism from ductile mode to brittle fracture in the cutting region with consequent deterioration to machined surface finish. A good understanding of the wear mechanism is an essential step in identifying mitigation measures.

An important explanation of periodic wear during diamond turning of RB-SiC has been provided by Zhang *et al.* [238] as shown in figure 6-28 and 6-29. They have stated that the wear marks on one side of the tool looked uniform and symmetrical. The wear lands were basically found to be fine microgrooves of uniform pitch and depth which were named as "periodical groove wear". Their careful inspection of the worn tools revealed that the width of the microgroove was equal to the feed/revolution signifying that the groove wear is an outcome of the replication of the tool feed on the machined surface. This mechanism not only prevails in SiC but also on other nominal hard brittle materials as the region below the cutting region i.e. plowing region, plastic deformation and more specifically the rubbing region continue to undergo tremendous friction resistance with the workpiece. During this process, the feed marks of the tool are in resonance with the wear marks left on the cutting tool.

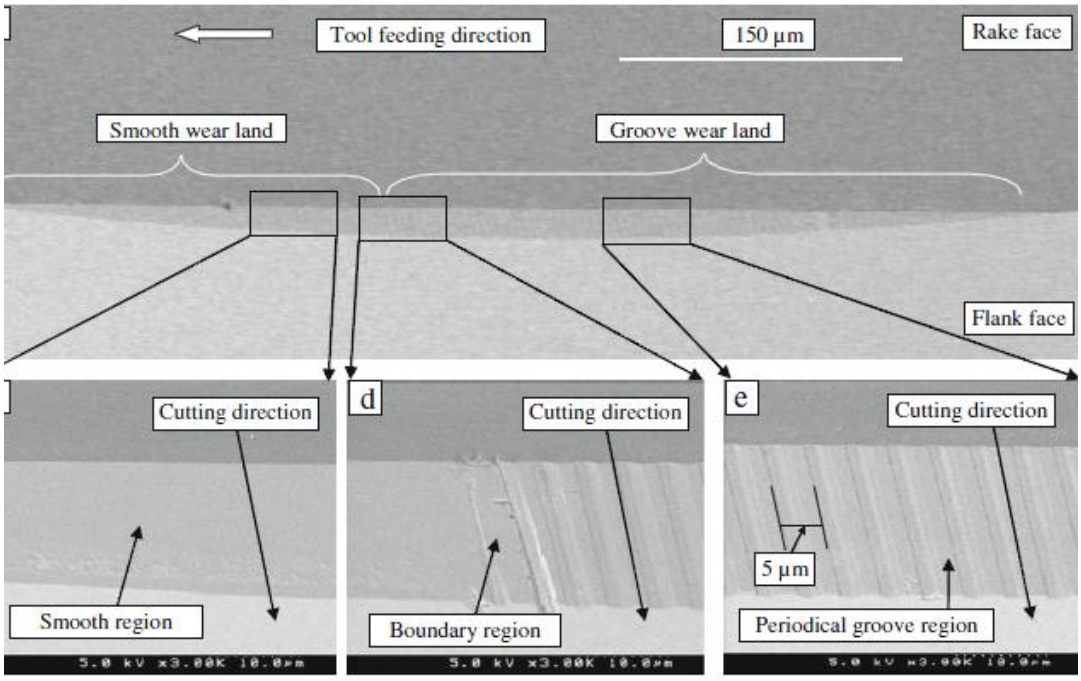

Figure 6-28: Schematic diagram of flank wear during SPDT [238]

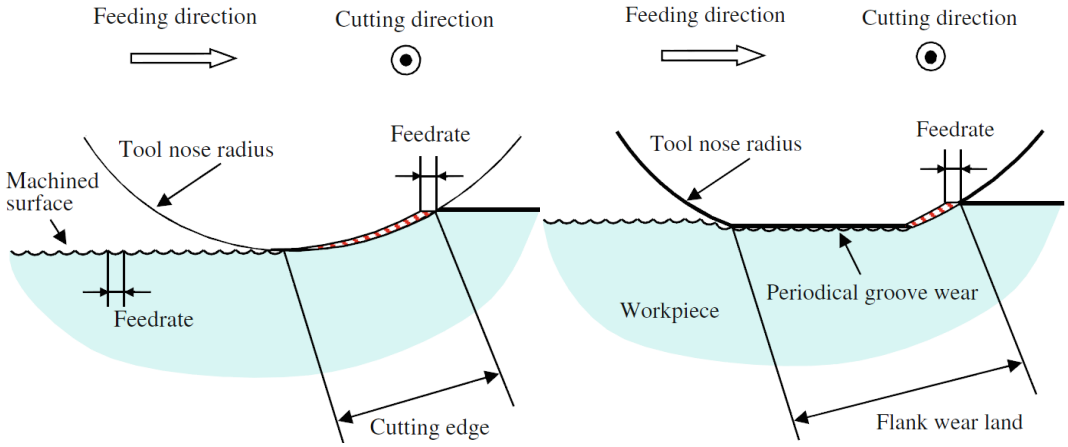

(a) New cutting tool (b) Worn cutting tool with flank wear

Figure 6-29: Schematic diagram of diamond turning [238]

Despite this explanation, the basic cause of wear process which is vital for phenomenal understanding of tool wear is yet to be investigated. Current simulation results were used to gain insights on the tool wear during nanometric cutting of SiC. It is widely accepted that measurement of the variation in inter-atomic distance during machining simulations provides useful insights into the wear mechanism.

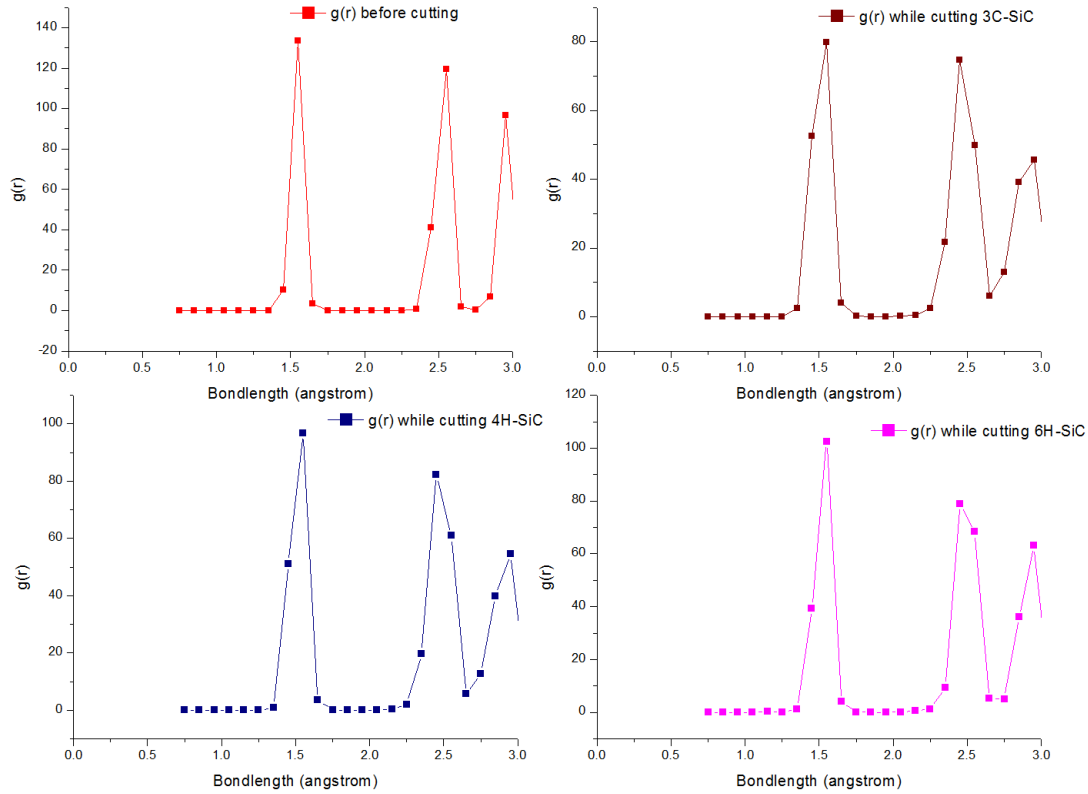

Figure 6-30: Radial distribution function of diamond tool before and during nanometric cutting of various polytypes of SiC

For this purpose, the radial distribution function for diamond tool was plotted before and during the nanometric cutting as shown in figure 6-30. It can be seen that before cutting, the radial distribution function, g(r), has a peak at 1.54 Å which is the known bond length of diamond while a few bonds on the surface (dangling bonds) result in a small peak at 1.42 Å. During machining, with the progressive advancement of the tool, this small peak continues to grow at the expense of the number of atoms with a bond length of 1.54 Å. This observation is common for all the polytypes of SiC but with varying magnitude. Thus, g(r) confirms sp^3-sp^2 transformation of the diamond tool during SPDT of all the major polytypes of SiC. Diamond also undergoes graphitization in addition to the formation of silicon carbide while machining silicon. The evolutions of the percentage wear of the cutting tools for all the cases are plotted and compared in figure 6-31.

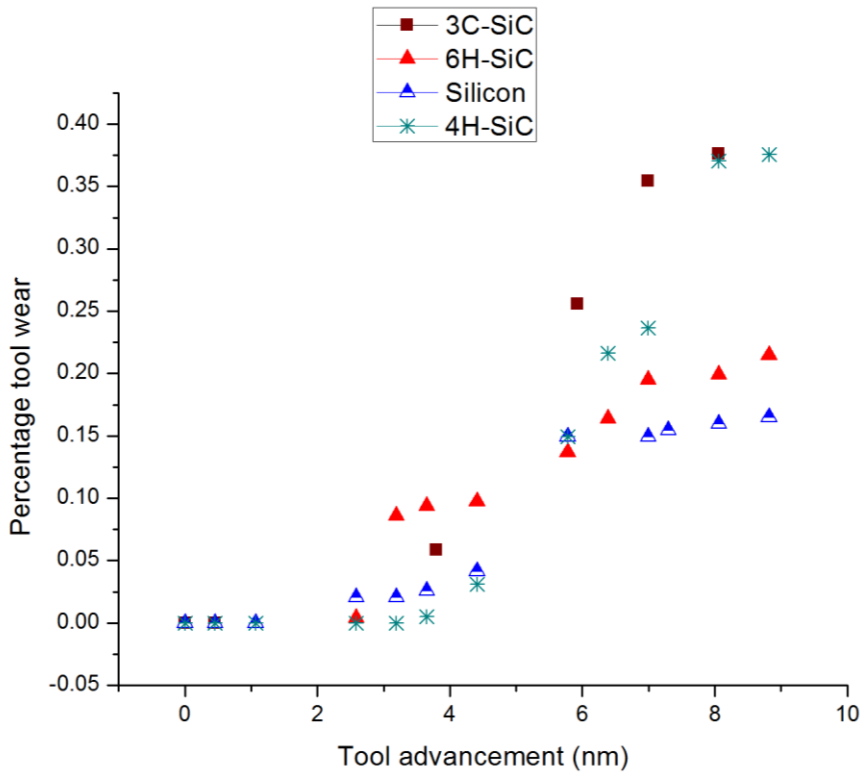

Figure 6-31: A comparison of the percentage of atoms from the diamond tool deformed during nanometric cutting of silicon and various polytypes of SiC

Figure 6-31 suggest that the most rapid wear will occur while cutting 3C-SiC and 4H-SiC. Interestingly, 6H-SiC will show the least wear among the other polytypes of SiC, approaching that of silicon. The increasing order of wear seems reasonably in line with the fact that the cutting hardness of 3C-SiC and 4H-SiC were higher than 6H-SiC, although there is a significant drop to reach with the cutting hardness of silicon. Interestingly, the mechanism by which a diamond tool wears during the SPDT of SiC is somewhat similar to how it wears during the process of polishing of diamond with another diamond as shown in figure 6-32 [163].

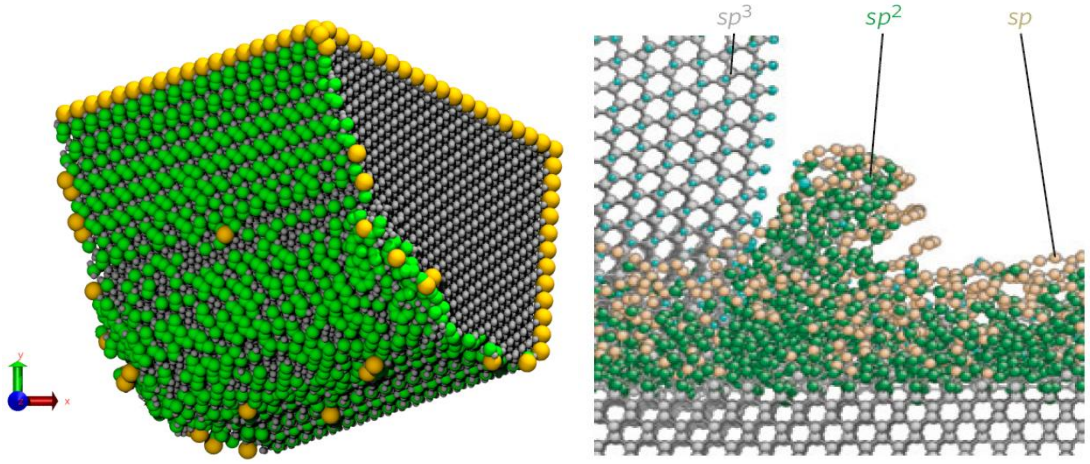

sp^3 - sp^2 transition in SPDT sp^3-sp^2 transition in polishing [163]

Figure 6-32: Wear of diamond tool [125]

6.8 Summary

This chapter presents the simulation results obtained during the nanometric cutting of silicon carbide. A comprehensive list of results for the nanometric cutting of silicon carbide can be summarized as follows:

1. sp^3-sp^2 transformation and consequent amorphization under the influence of high deviatoric stresses appears to be reason for the Herzfeld-Mott transition and consequent ductility in 3C-SiC during its ductile-regime machining. Crucially, the nature of bonding in nanocrystalline SiC can be altered by introducing non-hydrostatic stress conditions which was previously thought to require much higher hydrostatic pressures.
2. Experimentally known variations in the Young's modulus on (100), (110) and (111) plane of 3C-SiC revealed anisotropic variation of up to 43.6%. Against this experimentally known anisotropy, the simulated thrust forces showed anisotropic variation of up to 44.73% while the resultant forces showed a variation of 36.94%.
3. The material removal on (110) <001> crystal setup in 3C-SiC (soft scratching

direction of both 3C-SiC and diamond) was dominated by structural transformation without any cleavage causing the minimum sub-surface deformation comparing with other crystal setup combinations. The automated dislocation algorithm (DXA) helped to identify various dislocations and their respective Burgers vector. No sign of dislocations were observed while machining on (001) <100> and (110) <001> setups. Contrarily, multiple number of dislocations were observed on another crystal setups but were not found responsible to cause any glide or shuffle mechanism to result in ductility offered by 3C-SiC.

4. Cleavage was observed to be a dominant mechanism of material removal on the (111) crystal orientation during nanometric cutting of 3C-SiC. An occurrence of cleavage was accompanied by an instant drop in the cutting forces and tremendous release of the elastic energy in the form of heat which eventually transmits both to the workpiece and the cutting tool.
5. A reduced cutting velocity from 10 m/s to 4 m/s or an increase in the *d/r* ratio from 0.57 to 1 changed the mode of material removal mechanism from purely structural transformation to cleavage dominated during cutting on the (001)<100> crystal setup.
6. A relatively new parameter, “cutting hardness” indicates that 3C-SiC (~2.9 times that of silicon) offers the highest cutting resistance followed by 4H-SiC (~2.8 times that of silicon) and 6H-SiC (~ 2.1 times of silicon). Cutting temperatures on the tool and workpiece also indicated that 3C-SiC offered the most cutting resistance followed by 4H-SiC, 6H-SiC and silicon.
7. Deformed chips were generated in all cases which indicate that ductile regime machining is possible on all polytypes of SiC. However, there was a significant variation in the indicated quality of the machined surfaces and the sub-surface

crystal lattice deformed layer depths. The simulations indicated that 4H-SiC would produce the best sub-surface integrity followed by 3C-SiC, silicon and 6H-SiC. Thus, despite showing the lowest cutting resistance, 6H-SiC indicates the worst sub-surface integrity of all the polytypes studied.

8. An overall analysis of the machining stresses, temperature in the machining zone and cutting forces obtained from the MD simulation suggested that the amenability of 3C-SiC of being cut in particular crystal setups can be tabulated as follows:

Crystallographic planes	Least amenable cutting directions	More amenable cutting directions
Cube (001)	<-110>	<100>
Dodecahedron (110)	<-11-2>	<001>
Octahedron (111)	<-211>	<-110>

9. It has been shown that both chemically vapour deposited (CVD) SiC and reaction bonded (RB-SiC) are easier to machine than single crystal SiC. Since grain orientation changes from one crystal to another in polycrystalline SiC, the cutting tool experiences work material with different crystallographic orientations and directions of cutting. Thus, some of the grain boundaries cause the individual grains to cleave along the easy cleavage direction. This causes the build-up of stresses at the grain boundaries. Consequently, the cutting chips in RB-SiC are not deformed by plastic deformation alone rather a combination of the phase transformation at the grain boundaries and the slip of the grains both precede in tandem. Thus, RB-SiC involves a different mechanism of chip formation which is the reason why phase transformation of 6H-SiC grains was not found evident in a previous experimental study.

10. The RDF and coordination number measurement both indicated that the diamond cutting tool would graphitize due to abrasion against all the polytypes of SiC studied. While 3C-SiC and 4H-SiC indicated a high volume of wear, 6H-SiC suggests intermediate tool wear but still somewhat higher than silicon.
11. Considering all the above findings, it is reasonable to conclude that two of the polytypes may be suitable for SPDT, 4H-SiC offering the same cutting resistance as 3C-SiC but providing a better surface with less tool wear. However, 6H-SiC offered about half the cutting resistance of 4H-SiC but generated a poorer machined surface finish and sub-surface integrity. Thus, the choice between 6H-SiC and 4H-SiC would be dictated by the trade-off between machined surface quality and cost considerations.

Chapter 7 - Experimental studies on the nanometre cutting of SiC

7.1 Introduction

MD simulation has provided phenomenal information on the atomistic insights on several discrete processes of nanometric cutting of hard brittle materials. However, there are still some technical problems which were not examined in the current investigation through MD. This is because either they are too complex to be investigated through MD or it is very time-consuming and costly to cover these problems using the MD simulation. Some of these processes yet to be examined are the upper-bound of the brittle-ductile transition in silicon carbide, identification of an appropriate coolant and practical examination of the attainable machined surface roughness on SiC under the given set of practical constraints. This chapter highlights some of the mathematical parameters in an attempt to use a scientific approach to perform an experimental study of SPDT on SiC. These calculations are non-trivial as they are meant to harness the theoretical trade-off between the ductile-regime and brittle-regime. Towards the end, using the advanced state-of-the-art experimental techniques, novel insights on the influence of the coolant on nanometric cutting mechanism and brittle-ductile transition in SiC is presented. Accordingly, following experimental trials were carried out to investigate these phenomena's:

- Nano-scratching trial on single crystal 6H-SiC wafer
- Single point diamond turning trial on single crystal 6H-SiC wafer

7.2 Nanoscratching trials

From the MD simulation, interfacial abrasion between SiC and diamond was found to cause the sp^3-sp^2 transition of diamond and consequent tool wear. Reduction in friction at the tool-workpiece contact could aid to minimize the tool wear. Therefore, four coolants were identified which are demonstrated to improve the tribological properties of diamond during its frictional contact [275]. Nanoscratching tests were carried out on single crystal 6H-SiC workpiece with a Hysitron TriboIndenter [276]. A three-sided pyramidal Berkovich Probe having a negative tool rake angle of 65.35°, clearance angle of 13° and cutting edge radius of 150 nm was employed. Load control (LC) feedback system with a constant normal load of 11,000 μN was used. 6H-SiC wafer with the orientation (001) of size 5×5×0.33 mm was used. Coolants used were graphite nanoparticles, copper nanoparticles, MoS_2 nanoparticles and 3-amino propyl (diethoxyl) methyl silane [160]. Further description of the coolants used during the nano-scratching test is provided in table 7-1.

Table 7-1: Details of the coolants (APS: Average particle size)

S.No.	Coolant	Description	Source for procurement
1.	3-amino propyl (diethoxyl) methyl silane	97% pure	www.sigmaaldrich.com
2	Graphite nanoparticles	99.9% pure, APS: 400nm - 1.2 um,	US Research nanomaterials, Inc.
3.	Molybdenum disulphide (MoS_2) nanoparticles	99.5% pure, APS:1 um, powder	MTI Corporation, USA
4	Copper nanoparticles	99.9% pure, APS: 400 nm - 1.2 um,	US Research nanomaterials, Inc.

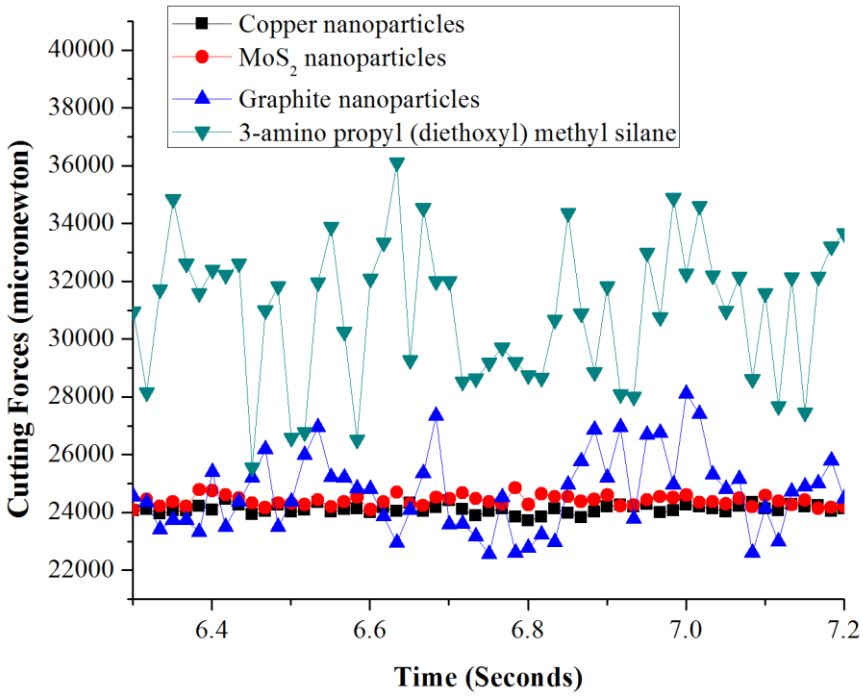

Figure 7-1: Evolution of the tangential cutting forces with respect to time in the presence of various coolants tested during nanoscratching of 6H-SiC

Since, load control feedback system was used, only tangential cutting force varied during the scratch process with respect to individual coolants. A comparison of these forces was plotted which is shown in figure 7-1. The plot indicates that the copper nanoparticles are the superior coolant on account of overall lower cutting forces and least fluctuations, which is in accordance with a recent experimental study, although carried out on RB-SiC workpiece [270].

7.3 Single point diamond turning trials

The commerical realization of SPDT of SiC is still a long way off in reality [202]. Nevertheless, attempts to demonstrate technical feasibility and to explore the possibility of execution of single point diamond turning of SiC have already been initiated. Some of these early attempts are tabulated in table 7-2.

Table 7-2: Experimental trials reported so far on nanometric cutting of SiC

S.No.	Workpiece	Reference Study	Experimental outcome	Coolant used
1.	RB-SiC	Yan *et al.* [121]	Ra : 23 nm (at high feed rate of 72 μm/rev)	Dry cutting
2.	RB-SiC	Yan *et al.* [270]	Ra: 14 nm; Rz: 300 nm	Grease of Cu nanoparticles
3.	3C-CVD SiC	Ravindra *et al.* [120]	Ra: 83 nm and Rz: 530 nm	Masterpolish 2 Final polishing suspension (contains alumina and colloidal silica with a pH~9)
4.	6H-SiC	Patten *et al.* [47, 119, 277]	Ra : Not specified	Dry cutting
5	6H-SiC	Jacob *et al.* [278]	Only a scratching test was performed to establish DBT depth which was found to be about 70 nm for 6H-SiC	
6	4H-SiC	Ravindra *et al.* [122]	Only a scratching test was performed to establish DBT depth which was found to be about 820 nm for 4H-SiC	
7	4H-SiC	Shayan *et al.*[279]	Laser assisted nano-scratching was done to observe the improvement in the machinability of SiC.	

Table 7-2 suggests that 3C-CVD-SiC was machined up to an Ra value of 83 nm while using an alumina and silica based specialized coolant. Similarly, using a coolant of the copper nanoparticles in the form of a grease, SPDT succeeded to generate a very fine machined surface roughness of Ra value 14 nm on RB-SiC. This measure of the machined surface roughness however dropped to 23 nm while dry cutting. These observation suggests that coolant plays a key role in influencing the machined surface roughness during SPDT of SiC. Surprisingly, no surface roughness data has been reported while machining a single crystal SiC despite the fact that there are significant differences in the nature of bonding, microstructure, extent of plastic deformation and the numbers of slip systems between the single crystal and the polycrystalline SiC.

Although, a polycrystalline SiC is relatively easier to machine than a single crystal SiC, but on the account of the differences highlighted above, a better machined surface finish on single crystal SiC can be anticipated. Therefore, the SPDT trial in the current work was restricted to the single crystal SiC (6H-type). The purpose of the experiment was to measure the attainable surface roughness on 6H-SiC in a single machining pass. During the trial, distilled water (pH value 7) was used as a preferred coolant as it was the one which significantly improved the tribological performance of the diamond during its abrasion with another diamond [275].

7.3.1 Experimental setup

SPDT trial was performed on an ultra precision diamond turning machine (Moore Nanotech 350 UPL). This machine tool has a liquid cooled air bearing spindle having motion error of less than 50 nm while its driving system resolution is up to 0.034 nm [197]. A major problem with SiC is its procurement. Table 7-3 provides a list of the major vendors across the globe for the procurement of the SiC wafer.

Table 7-3: Major manufacturers of SiC wafers/ films

S.No.	Manufacturer	Contact/ Website	Country
1	Cree Research Inc.	www.cree.com	USA
2	MTI Corporation	http://mtixtl.com/	USA
3	POCO Graphite	www.poco.com	USA
4	Aymant Technology Inc.	www.aymont.com	USA
5	Dow Corning	www.dowcorning.com	USA
6	Technologies and Devices International, Inc	http://www.tdii.com	USA
7	Glenn Research Centre, NASA	http://www.grc.nasa.gov/WWW/SiC/	USA
8	CoorsTek	www.coorstek.com	USA
9	Boostec	jlavenac@boostec.com	USA
10	Japan fine ceramics company limited	s_ishii@japan-fc.co.jp	Japan
11	Hoya	http://www.hoya.co.jp	Japan
12	Nipponsteel	www.nsc.co.jp	Japan
13	Semiconductor Wafer Inc.	sales.europe@semiwafer.com	Japan
14	PAM-Xiamen Power way advanced material Co. Ltd.	sales@qualitymaterial.net / http://www.powerwaywafer.com	China
15	SiCrystal AG	Peter.Sasahara@sicrystal.de	Germany
16	NOVASiC	mmarsan@novasic.com	France
17	Norstel	http://www.norstel.com	Sweden

A snapshot of the total experimental assembly is shown in figure 7-2. A three-component force dynamometer unit (Kistler 9257-B) was used for the measurement of the cutting forces. Both white light interferometer (Zygo NewView 5000) and form Talysurf surface profilometer (120L) were used to measure the machined surface roughness. Cutting tool was examined through a high magnification scanning electron microscope (SEM) (FIB- FEI Quanta 3D FEG).

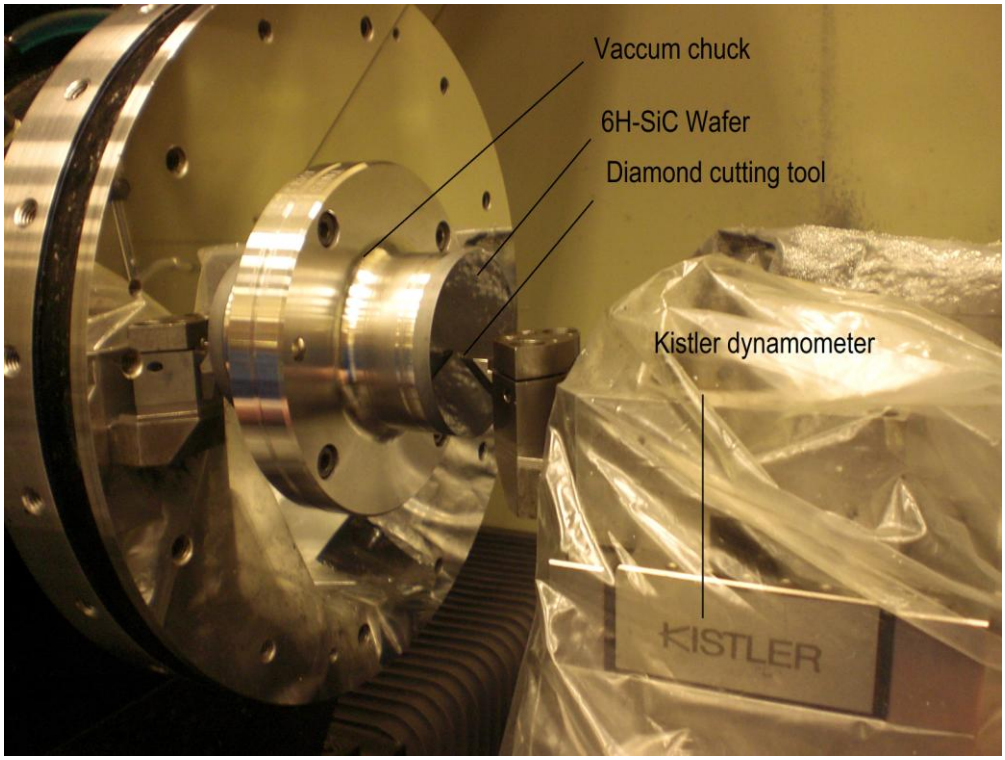

Figure 7-2: Experimental assembly for SPDT of SiC [280]

The workpiece specimen used was N type-6H-SiC wafer of diameter 50 mm and thickness 5 mm with the crystal orientation (001). Prior to the SPDT experiment, SiC workpiece was examined for its flatness and the as received surface roughness (Ra) using a form Talysurf. The polished surface of the as received workpiece showed a flatness of 1.9 μm in terms of Peak-to-valley (PV) height while Ra was measured as 4.9 nm as per the measurements shown in figure 7-3 and figure 7-4.

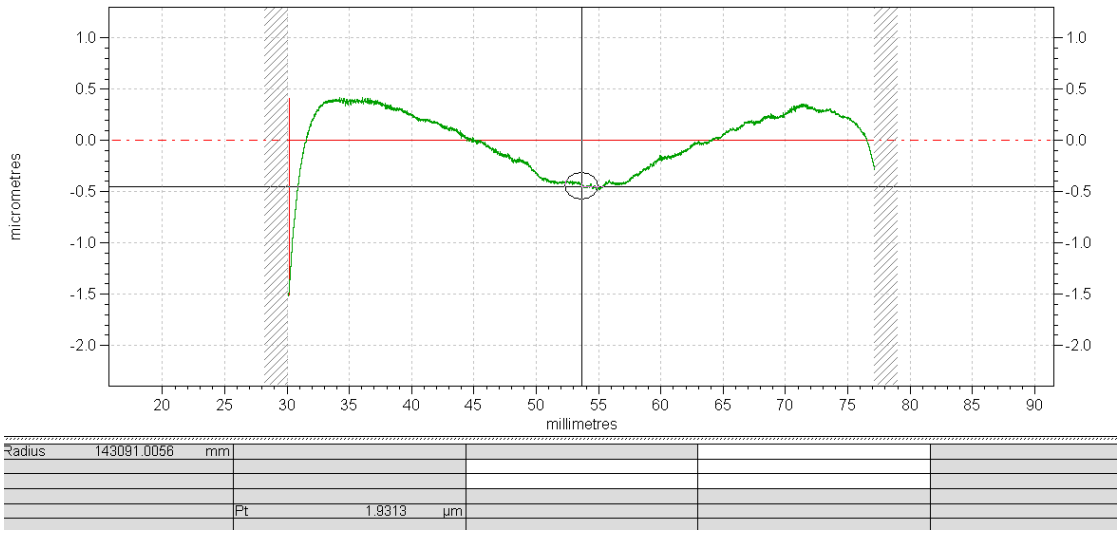

Figure 7-3: Flatness of the as received wafer (PV = 1.9 µm) through form Talysurf

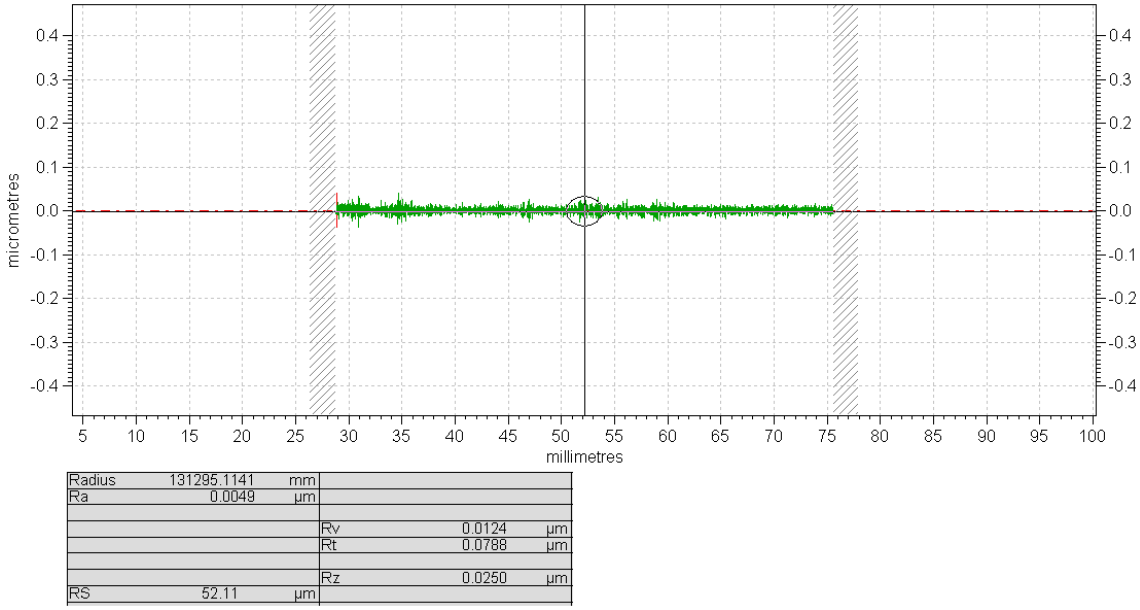

Figure 7-4: Surface roughness of the as received polished wafer (Ra = 4.9 nm) measured through form Talysurf

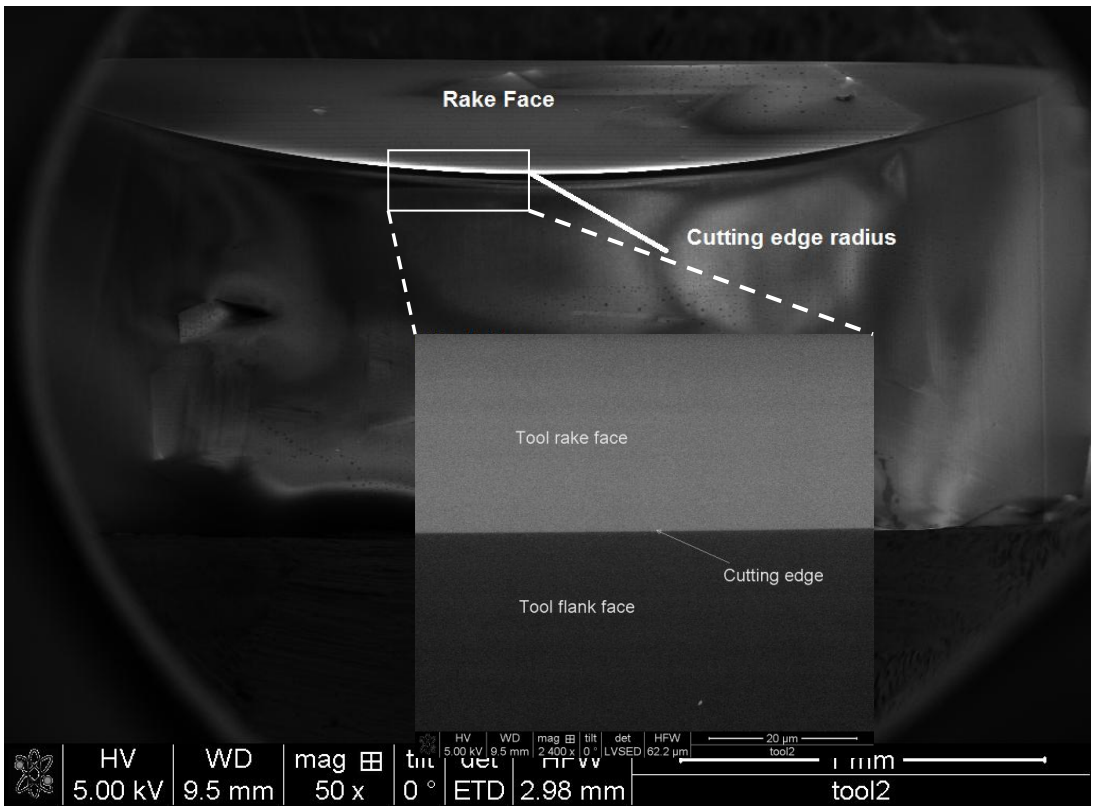

Figure 7-5: SEM image of the freshly procured diamond tool

Normally, round nose cutting tools and low feed rates are preferred while machining brittle materials in order to obtain a good machined surface. This experimental study also adapted a round nose cutting tool. Single crystal diamond cutting tool (cubic orientation) having a negative rake angle of 25°, tool nose radius of 2 mm and clearance angle of 10° was used. No wear marks either on the flank or the rake faces of the cutting tool were observed on the tool received from Contour Fine Tooling Limited, UK. This was confirmed through the SEM examination of the cutting tool before the experiment as shown in figure 7-5. The machining parameters used in this study were calculated by combining the experimental variables and empirically known relations as shown in table 7-4 and table 7-5.

Table 7-4: Critical properties of 6H-SiC

S.NO.	Material properties	Unit of measurement	Values
	Fracture Toughness (Kc)	$MPa.m^{1/2}$	1.9
	Hardness (H)	GPa	22
	Elastic Modulus (E)	GPa	347.01
1	Critical Crack Length $Y_c = 120\frac{K_c^{\ 2}}{H^2}$	µm	0.895
2	Critical Chip Thickness $d_c = 0.15 \times \frac{E}{H} \times \left(\frac{K_c}{H}\right)^2$	µm	0.01764

Table 7-5: Machining parameters

S.NO.	Parameters	Unit of measurement	Values
1	Tool nose radius of diamond tool (R)	µm	2000
2	Cutting edge radius of the diamond tool	nm	57.4
3	Diameter of workpiece (D)	mm	50
4	Cutting speed (V)	m/s	1
4	Maximum Feed Rate $f_{\max} = d_c \times \sqrt{\frac{R}{2 \times (d_c + y_c)}}$ Note: Value of d_c and y_c are taken from above table (Refer Appendices)	(µm/rev)	0.61 ~ say 0.65
5	Maximum critical depth of cut for 6H-SiC (d)	nm	70 [278]
6	Spindle speed $N = \frac{1000 \times V}{\pi D}$	RPM	382
7	Maximum critical chip thickness When $f < \sqrt{2Rd - d^2}$, where R>>f, R>>d and R is in mm. $t_{\max} = f\sqrt{\frac{2d}{R}}$	nm	5.438
8	Coolant	pH value 7	Distilled water

7.3.2 Experimental observation of brittle-ductile transition in 6H-SiC

A DXR Raman microscope developed by Thermo Scientific Limited was used to obtain an image shown in figure 7-6 taken from an uncut shoulder of 6H-SiC. Figure 7-6 clearly shows the occurrence of brittle–ductile transition. The measurement results are in accordance with the results predicted from the ductile-regime machining model (Z_{eff} ~100 μm) in 6H-SiC.

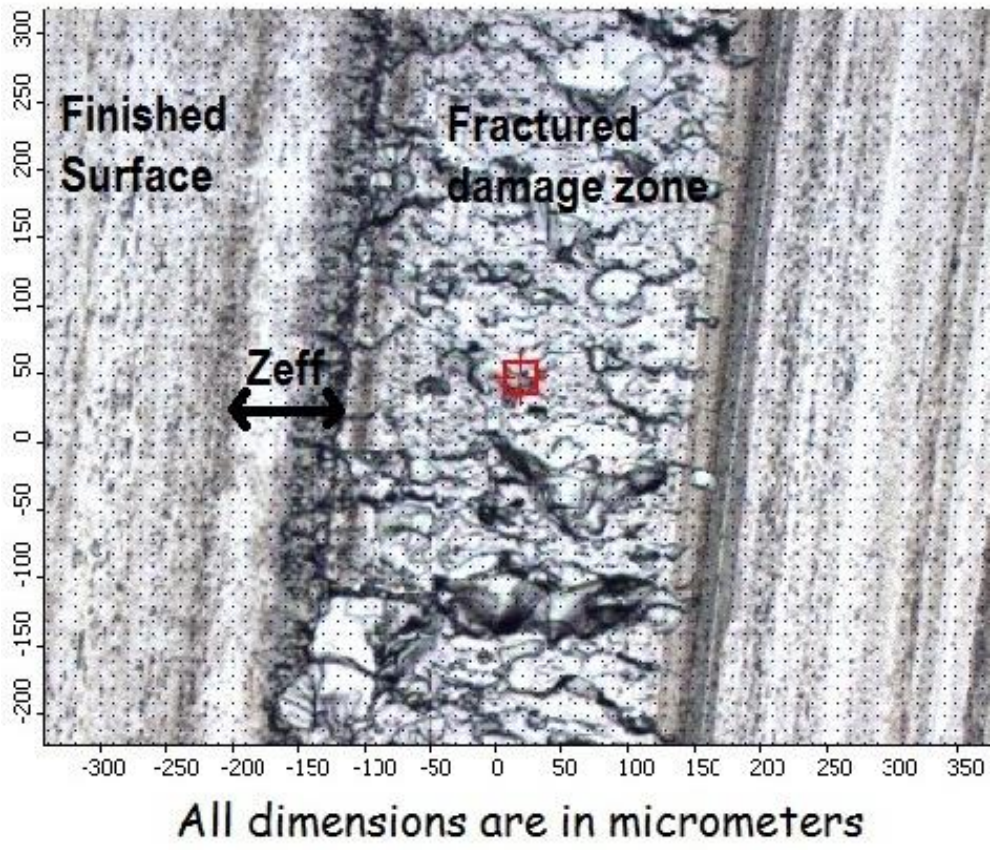

Figure 7-6: Measured uncut shoulder of diamond turned 6H-SiC using a DXR Raman microscope

Similar to other classes of brittle materials i.e. silicon and germanium, the occurrence of brittle–ductile transition was thus found to occur in 6H-SiC as well. Scattergood *et al.* [23] derived a mathematical equation to correlate the critical chip thickness with respect to the nose radius of the cutting tool and the length of the brittle-ductile transition as:

$$d_c = \frac{Zeff}{R} = \frac{50\mu m}{2000\mu m} = 25nm \qquad 7\text{-}1$$

Against, this experimental value of 25 nm, the predicted value of critical undeformed chip thickness in 6H-SiC was about 17.64 nm (obtained through the empirical equations shown in table 7-4). Both values were found to be in fairly close agreement with each other. An interesting fact to be noted here is that the critical depth of cut for 6H-SiC is only 70 nm [25] in contrast to the critical depth of cut of another polytype of SiC e.g. 4H-SiC where this depth was obtained as 820 nm [32]. This observation suggests that the material removal rate (MRR) under the same ductile-regime machining conditions would be significantly higher in 4H-SiC in comparison to 6H-SiC. However, a trade-off among the quality of the finished surface, sub-surface deformation lattice layer depth, tool wear and machining efficiency would dictate a better choice between these two polytypes of SiC.

7.3.3 Cutting forces and surface roughness measurement

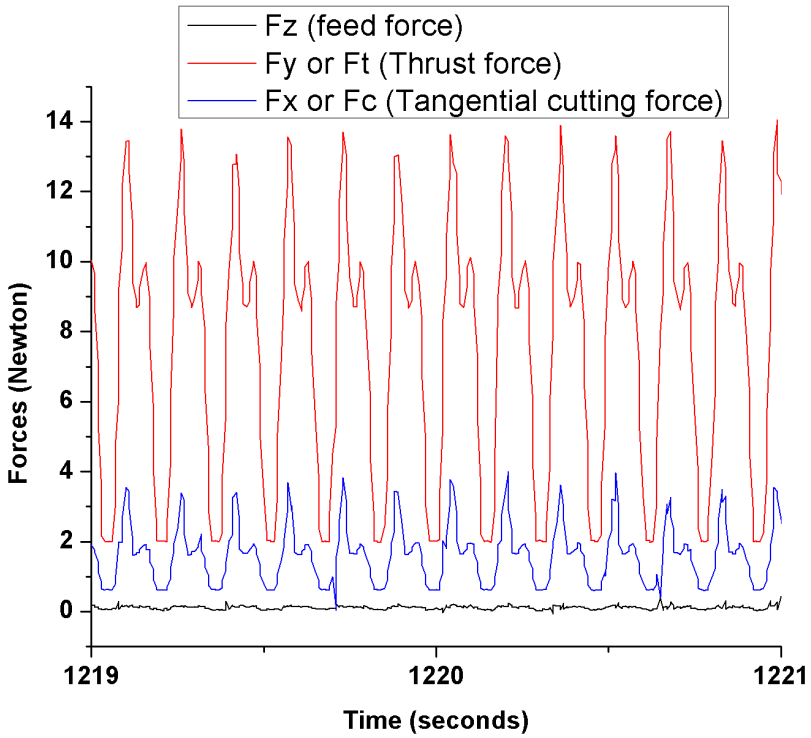

Figure 7-7: Experimental cutting forces measured during SPDT of single crystal 6H-SiC

The evolution of the cutting forces over the period of 2 seconds is presented in figure 7-7. It is evident from the figure 7-7 that the thrust forces were almost 4 times higher than the tangential cutting forces. This could be attributed to the use of high negative tool rake angle which is central to any SPDT operation of brittle materials. It is of interest to note that a MD simulation study reported that the dominance of thrust forces over the tangential cutting forces is a necessary requirement to execute ductile-regime machining on brittle materials [56]. While this looks in accordance with the current experimental trial on single crystal 6H-SiC, this is not the case observed in similar nanoscale friction based studies where the cutting forces were found dominant over the thrust forces [260, 281]. Therefore, this is an area of investigation yet to be researched. Furthermore, in contrast to machining silicon [154], both the tangential cutting forces and the thrust forces were found significantly high during SPDT of 6H-SiC. It suggests that the cutting resistance of 6H-SiC is significantly higher than silicon [260].

Figure 7-8 and figure 7-9 show measured machined surface roughness on 6H-SiC during the first kilometre of cutting length. The Ra value obtained through a Form Talysurf (120L) was found as 9.2 nm while a white light interferometer (Zygo NewView 5000) reveals a surface roughness value of 10 nm.

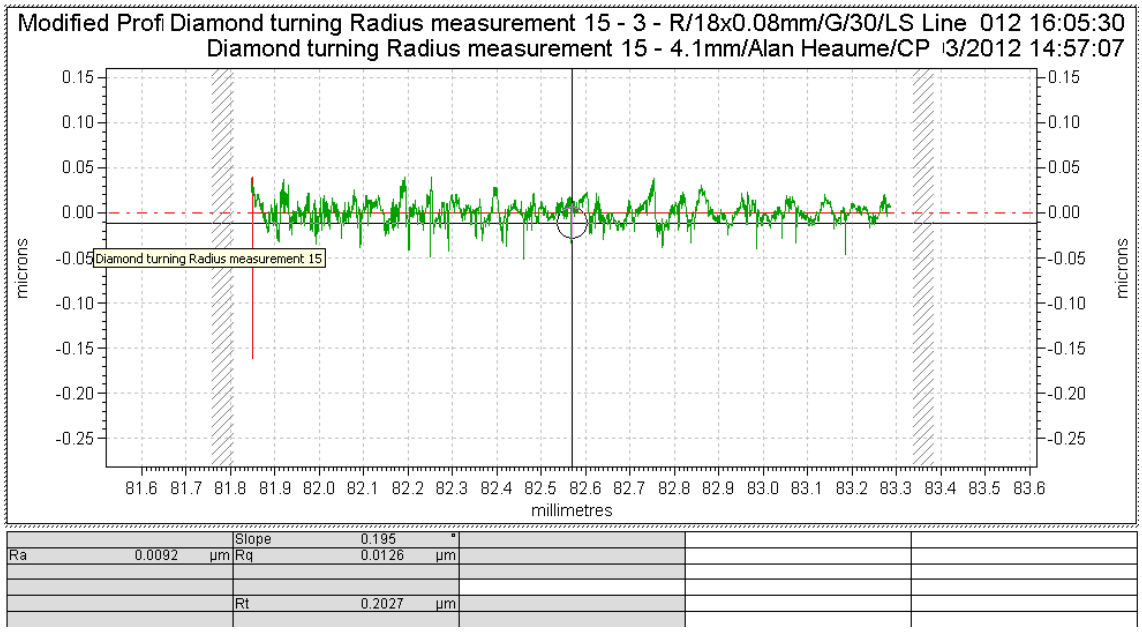

Figure 7-8: A 2D profile of the machined surface of 6H-SiC measured by a Form Talysurf (120L) profiler

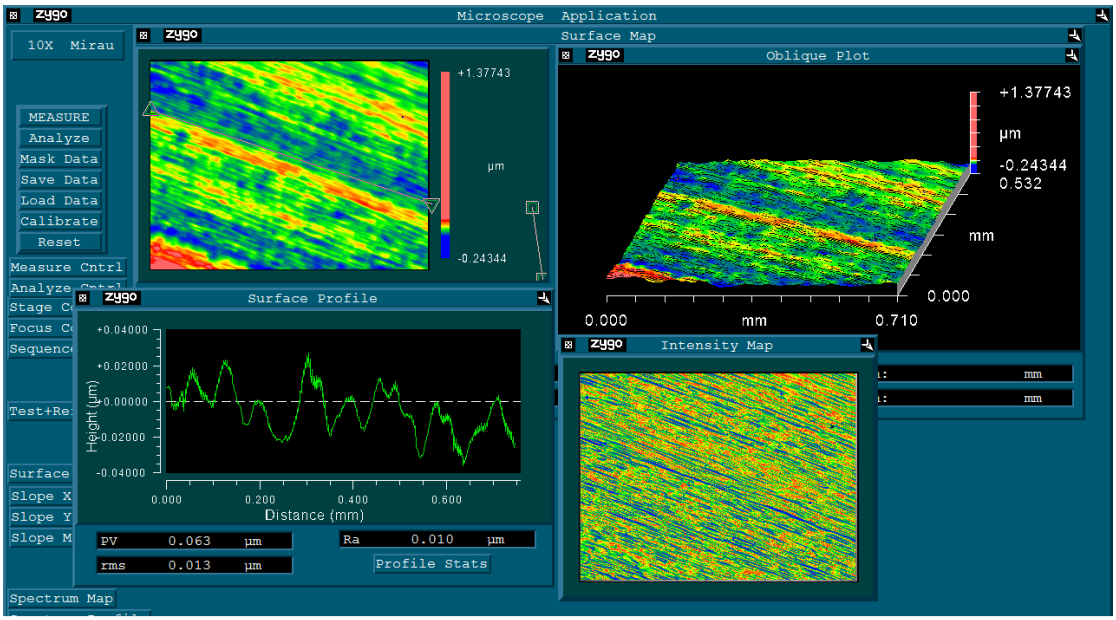

Figure 7-9: A 2D profile of the machined surface of 6H-SiC measured by a white light interferometer (Zygo Newview 5000)

Comparing the experimental value of Ra obtained in this work with the previously reported Ra values, it confirms that single crystal SiC provides a better measure of Ra value than the polycrystalline SiC. It is also now known that wavelengths in the IR spectral region are longer than those of the visible region, hence, surface roughness specifications are not very stringent for visible components [282]. The surface

roughness measurement on 6H-SiC obtained in the current work demonstrates that SPDT could be a viable option to generate nano-smooth nano-structured surfaces on SiC for the purpose of visible optics.

7.3.4 Tool wear

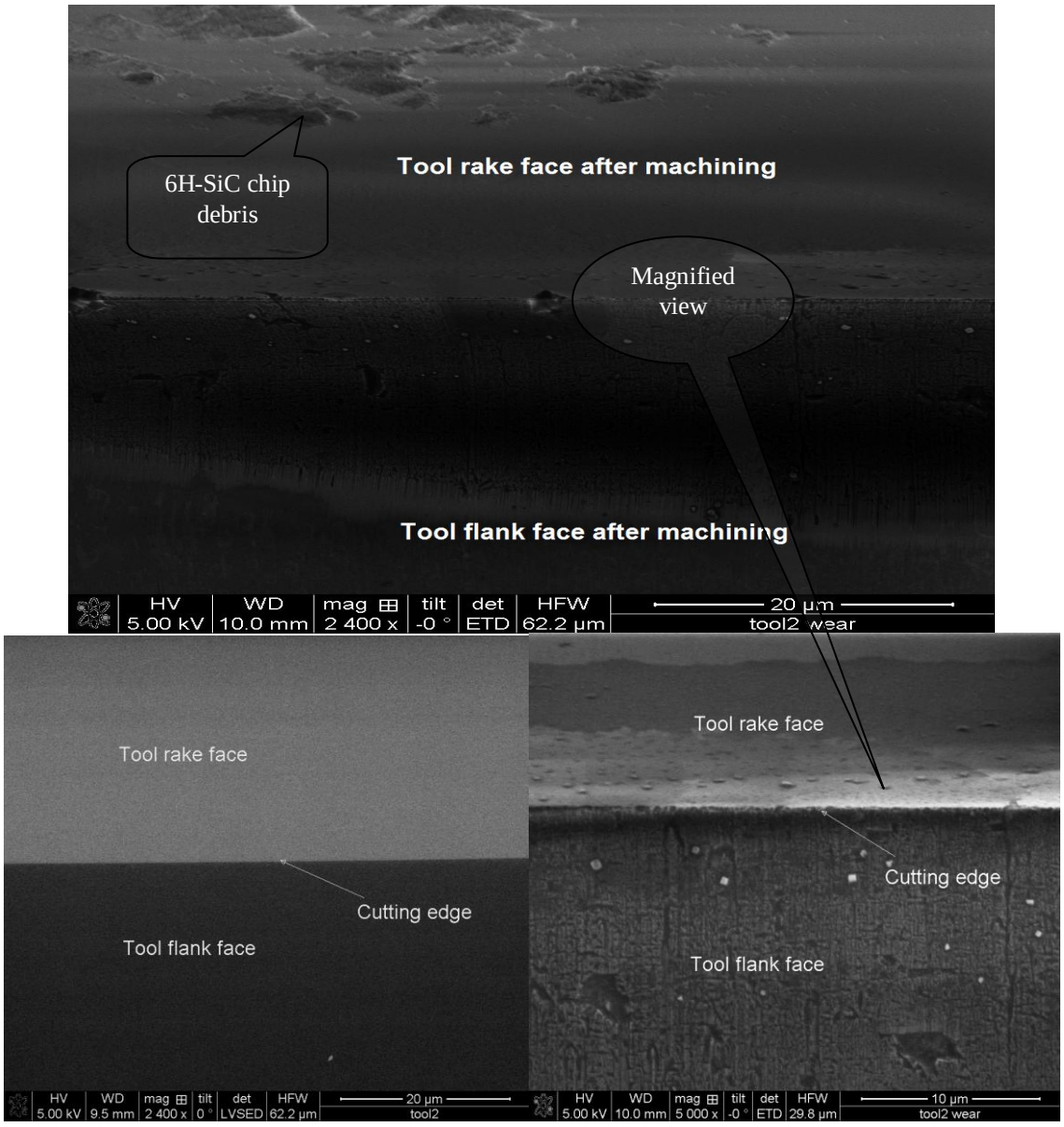

(a) magnified view of the tool before cutting (b) magnified view after cutting 1 km

Figure 7-10: SEM image of the diamond cutting tool

Unlike silicon, SiC is chemically inert and therefore the influence of tribochemistry to influence the wear of the diamond tool becomes negligible. However, abrasive wear is apt to occur during the tribological contact of diamond and SiC as seen from the MD simulation. Figure 7-10 shows the SEM image of the cutting tool after a cutting length of 1 km. In the comparison, though the SEM snapshots are taken at different scales i.e. 20 micron and 10 micron but the outcome of the result is not sensitive to these scales.

To evaluate the performance of the cutting tool on the same scale, a magnified view of the fresh tool and the used tool is compared in the bottom part of figure 7-10. It can be seen that before cutting, the cutting edge was extremely sharp and both tool flank face and tool rake face were prepared very fine without any visible marks on the edge radius of the surface of the cutting tool. After 1 km length of cutting, the tool started to show wear marks on the flank face. Consequently, the edge radius started to lose its sharpness while recession of the cutting edge is also visible in some areas. An interesting observation however was that the cutting chips were observed to cling to the tool rake face despite of using liquid coolant. The clinging of cutting chips to the rake face of the cutting tool suggests the existence of very high stress and high temperature in the cutting zone during machining of SiC confirming the observations of the MD simulation.

7.4 Summary

This chapter presents the experimental results obtained from the nanometric cutting of single crystal silicon carbide. These results can be summarized as follows:

1. Out of the four coolants i.e. graphite nanoparticles, copper nanoparticles, MoS_2 nanoparticles and 3-amino propyl (diethoxyl) methyl silane, it was found that the copper nanoparticles provide superior performance.

2. Using the proposed mathematical parameters, single crystal 6H-SiC was successfully diamond turned using a specific coolant of distilled water with pH value of 7 and an undeformed critical chip thickness of 25 nm was obtained. An average value of machined surface roughness 9.2 nm was also obtained, making SPDT as a feasible option to generate visible range optics on single crystal SiC in a single pass, albeit, for smaller cutting distances.
3. The occurrence of brittle-ductile transition was captured through a state-of-the-art DXR Raman microscope. The cutting forces during SPDT of 6H-SiC were found significantly higher than silicon i.e. they were almost two and half times in the magnitude of cutting forces while machining single crystal silicon. Also, the thrust forces were almost four times of the tangential cutting forces which are attributed to the use of high negative tool rake angle.
4. The microscopic measurement results of 6H-SiC workpiece reveals that the mechanism for material removal in single crystal 6H-SiC involves ductile deformation and brittle fracture, in accordance with the ductile-regime machining model proposed long back in 1990s.
5. Significant wear marks on the tool cutting edge and clinging of the cutting chips/debris were observed despite the usage of liquid coolant.

Chapter 8 - MD simulation study of a novel approach to machine SiC

8.1 Introduction

In this chapter a novel approach of machining named “Surface defect machining” (SDM) method is explained. Inspired by the MD simulations and experimental studies described in the previous chapters, SDM method has been successfully demonstrated on the hard turning of steel [283]. The aim of this chapter is to assess the effectiveness of the proposed SDM method in order to conduct a preliminary feasibility study to cut SiC at the atomic scale and compare this with micro-laser assisted machining (µ-LAM) of SiC at 1200 K and normal nanometric cutting at 300 K. In the subsequent sections, this chapter provides theoretical and simulation aspects of the SDM method while cutting single crystal 3C-SiC.

8.2 Description of the surface defect machining method

In the past, micro-laser assisted machining (µ-LAM) has been proposed as an efficient method to improve the machinability of SiC [279]. During µ-LAM, workpiece is preferentially heated and thermally softened at the tool-workpiece interface in order to reduce the hardness to improve the machinability of the workpiece. Similar to this method, various other methods for improved tribological response of the workpiece to make them amenable to diamond turning have been suggested over the period of time, a glance of which is shown in table 8-1. All these modifications have essentially helped in obtaining the longevity of the cutting tool and improved surface finish of the product.

Table 8-1: Modified form of measures suggested for improved machinability [284]

No.	Modification	Theoretical approach	Experimental realization
1	Process	Reduction of chemical reaction rate between diamond cutting tool and workpiece	Cryogenic turning [70]
2		Inhibit chemical reactions	Use of inert gas atmospheres [285]
3		Reduction of contact time between tool and workpiece	Vibration assisted machining [286-288]
4		Lowering of temperature rise and reducing the duration of chemical contact	Usage of appropriate coolant [270, 289]
5		Rotary Cutting	Tool swinging method [290]
6	Tool	Building a diffusion barrier on the cutting tool	Use of protective coatings [291]
7		Modification of diamond lattice	Ion implantation [15]
8		By modifying the cutting tool geometry	Straight nose cutting tools [41] Providing nanogrooves on the cutting tool [292-293]
9		Use of alternative cutting tool material	CBN [89, 294]
10	Workpiece	Surface layer modification of the workpiece	Ion implantation [295]
11		Thermal softening of the workpiece during the cutting process	Micro laser assisted machining [279]

8.2.1 Working principle of SDM method

From the manufacturing research, it has been realized that the resistance offered by the hard materials to the cutting tool can be lowered by any of the following four methods:

- varying the rake angle of the tool
- lowering the hardness of the workpiece
- increasing the hardness of the cutting tool
- decreasing the shear plane angle

The newly proposed method named surface defect machining "SDM" is aimed to decrease the shear plane angle during the machining of hard materials to realize a better machining action for the same amount of cutting energy.

The proposed SDM process harness the combined advantages of both porosity machining method [296] and the pulsed laser pre-treated machining [297] as shown in figure 8-1. It is believed that the stresses developed during the machining of the porous material pushes the particles of the cutting chips into the vacant pores which causes the formation of the layer of a quasi-continuous material on top of the machined surface [296]. Also, an increase in porosity causes a decrease in micro hardness and a subsequent reduction in the required cutting energy. On the other hand, there is also a method patented in 1982, called as pulse laser pre-treated machining [297] which uses a pulse laser drilling assisted ultra high power laser ablation method to evaporate the material to weaken the material of the uncut chip thickness.

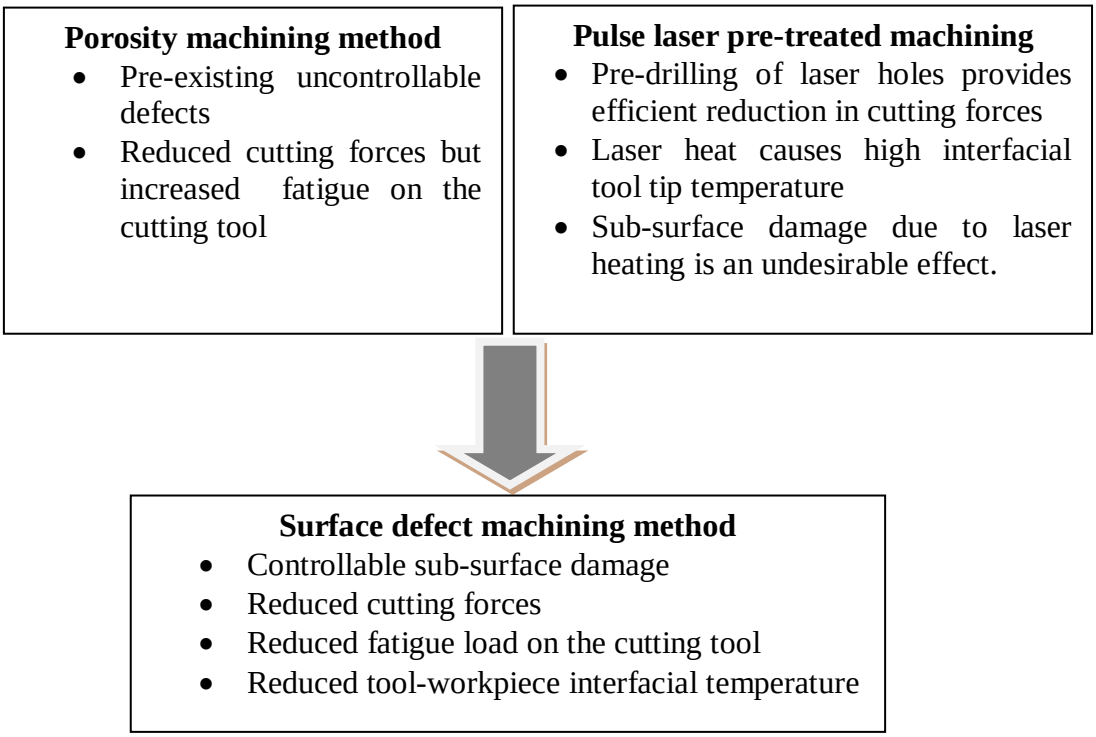

Figure 8-1: Development of the surface defect machining method

However, both these methods have their own limitations such as during porosity machining, the depth of the discontinuities below the uncut chip thickness can present a risk to the tool life due to high impact loads while poor laser power control can cause the premature degradation of the cutting tool, accelerated dissolution-diffusion and adhesion wear of the tool tip. On the other hand, SDM is developed to overcome all these problems. During SDM, a set of surface defects is firstly generated on the workpiece at depths less than the uncut chip thickness so as to mitigate the problem of high impact loads. Post-surface defect generation, a normal machining operation can be carried out. This process provides the intended porosity but in a controlled manner. The process of generating surface defects can be carried out either by mechanical means or through a focussed ion beam machining process. It is anticipated that the shape of these defects must play a significant role in governing the mechanism of deformation in the cutting zone of the workpiece. However, being a preliminary investigation, the purpose of this investigation is to only highlight the potential advantages of using SDM process. The working principle underlying the proposed SDM method is to change the removal

mechanism of cutting chips from being continuous to being discontinuous in order to minimize the problems caused by the continuous cutting chips. The cutting chips in a ductile-regime machining operation are usually continuous; therefore, they can collide either with the machined surface or with the cutting tool which could damage the surface quality of the part being machined. Moreover, surface discontinuities breaks the energy barriers associated with the critical deformation load i.e. surface defects allow easy shearing of the material as shown schematically in figure 8-2.

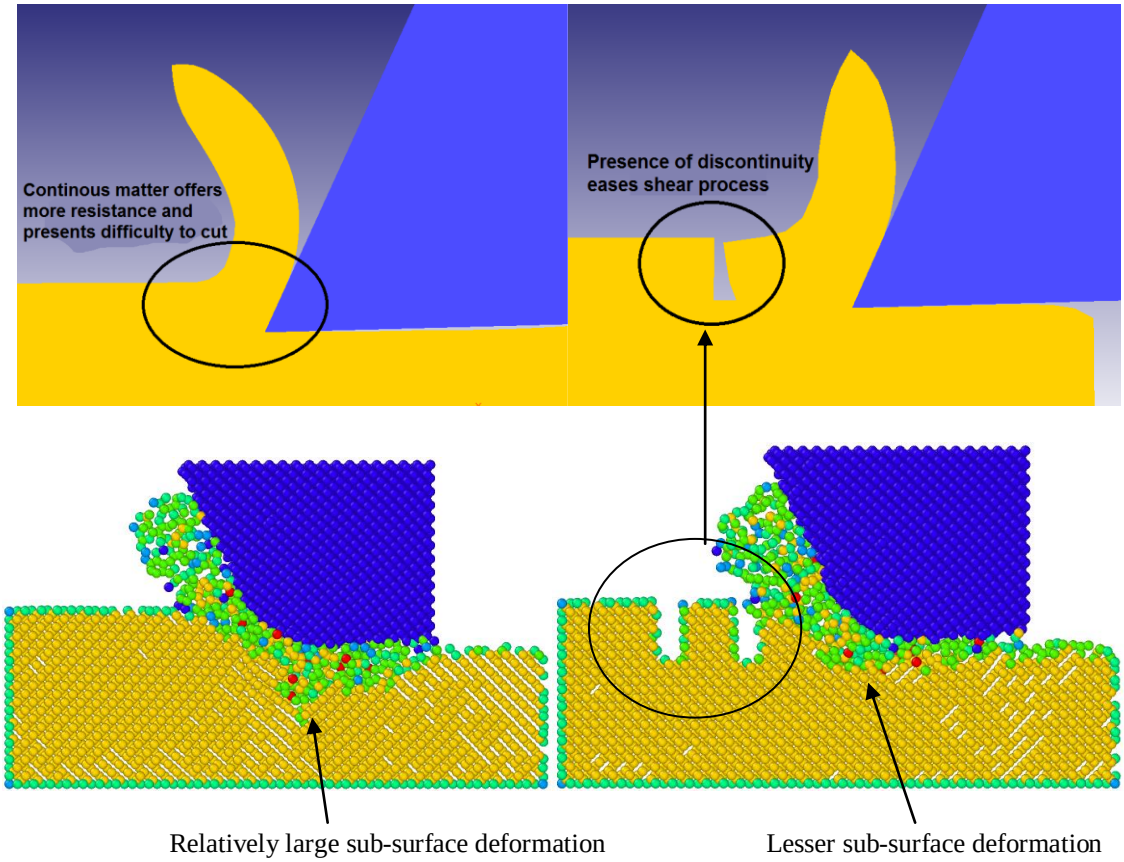

Figure 8-2: Schematic diagram indicating difference between the mode of deformation between a continuous material and a discontinuous material obtained from FEM simulation and MD simulation respectively

While it looks logical that the SDM process would be quite effective to reduce the cutting load during cutting of SiC, a theoretical can be made through a state-of-the-art MD simulation analysis. Accordingly, MD simulation of SDM process of 3C-SiC was

performed and compared with normal machining at ambient temperature of 300K and nanometric cutting at a high temperature of 1200 K, a temperature where SiC has been reported to gain significant plasticity [33]. It has remained an important precursor to MD simulation studies that they are computationally too expensive. Owing to their restrictive speed, use of high cutting speeds is frequent in MD simulation studies e.g. 500-2500 m/s cutting speed was used by Belak *et al.* [49, 253] and Komanduri *et al.* [144, 209], 150-400 m/s was used by Wang *et al.* [230] and Liang *et al.* [298], 70-100 m/s was used by Noreyan *et al.* [244-245], Rentsch *et al.* [71] and Goel *et al.* [125, 274, 299]. Although, these investigations have been successful to capture key insights of the cutting process but in the current investigation, high cutting speed could have affected the sensitivity of the results particularly when the same configuration of cutting was to be compared at 300K and 1200K. Therefore, current simulations were performed at a much realistic cutting speed of 10 m/s to suppress the effect of the cutting speed on the outcome of the results.

8.2.2 MD simulation of SDM and comparison with μ-LAM

Table 8-2 provides the computational parameters, details of the workpiece, uncut chip thickness and other relevant parameters which were used to test the performance of the SDM method. A snapshot from the MD simulation of the 3C-SiC workpiece (with and without surface defects) after the equilibration process is shown in figure 8-3 and figure 8-4 where the red and grey colours correspond to silicon and carbon atoms in the workpiece and yellow colour represents carbon atoms within the diamond cutting tool respectively.

Table 8-2: Process variables used for MD simulation

Workpiece material	Number of atoms in the workpiece	Number of atoms in the diamond cutting tool
3C-SiC without holes (14.26 nm × 4.6345 nm × 4.278 nm)	28170	21192
3C-SiC with surface defects (holes) 14.26 nm × 4.6345 nm × 4.278 nm)	27782	21192
Dimension of holes (7 number)	Diameter = 0.713 nm	Depth = 1.426 nm
Crystal orientation of the workpiece		(010)
Crystal orientation of diamond tool		Cubic
Cutting direction		<100>
Cutting edge radius (nm)		2.297
Uncut chip thickness / in-feed (nm)		1.3126
Cutting tool rake and clearance angle		-25° and 10°
Equilibration temperature		300 Kelvin
High cutting temperature		1200 Kelvin
Cutting velocity		10 m/s
Timestep		0.5 femto seconds

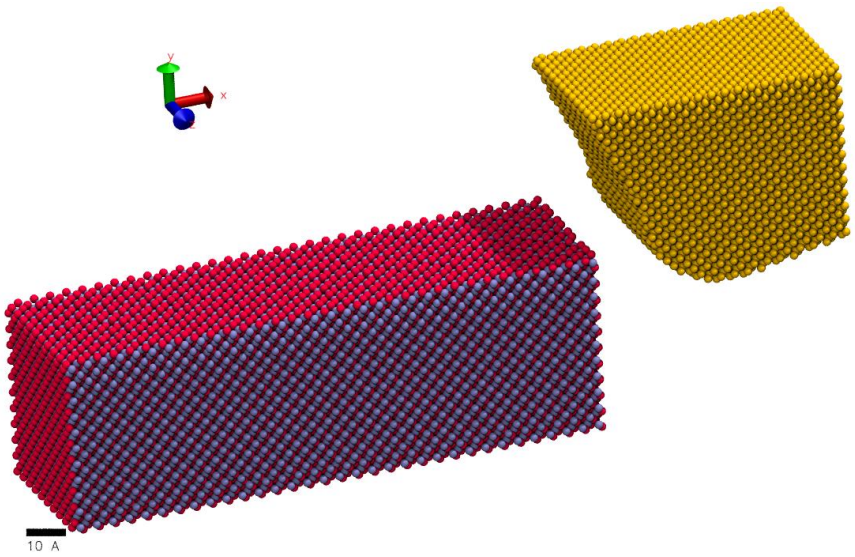

Figure 8-3: Snapshot from MD simulation for 3C-SiC specimen without surface defects

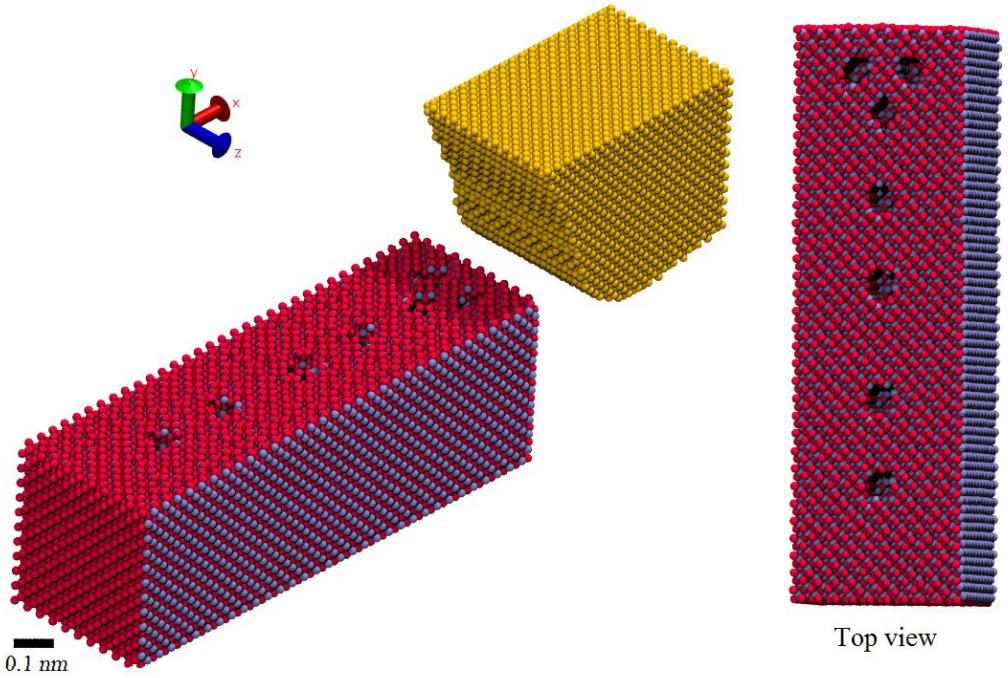

Figure 8-4: Snapshot from MD simulation for 3C-SiC specimen with defects on the top

The following sections cover the observations and discussion of the significance of the MD simulation results in terms of the cutting forces, coefficient of friction, chip morphology, cutting stresses and surface roughness. The characterization and quantification of these parameters from MD simulation testifies that SDM process is indeed effective even at the atomic scale.

8.2.3 Simulation results

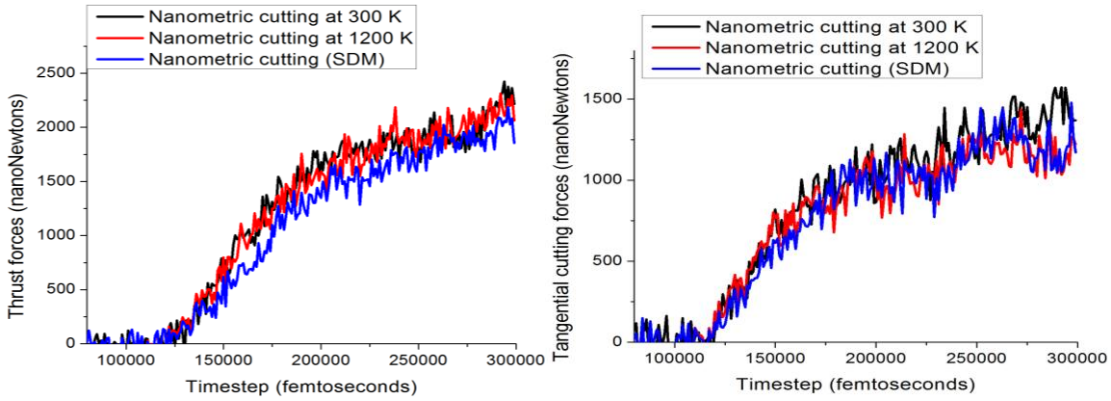

Figure 8-5: Comparison of the evolution of the cutting forces using SDM method

A comparison of the evolution of the cutting forces (F_c and F_t) for all the three cases studied is shown in figure 8-5. As evident, indeed an expected reduction in the cutting forces was observed while cutting 3C-SiC at elevated temperature of 1200K compared to the cutting of the same configuration at 300K. This reduction was however smaller than what was obtained using SDM process to cut 3C-SiC at 300K. It shall be noted here that the extent of reduction of forces will depend on various parameters such as numbers, dimension, the pitch and the shape of holes etc. However, being a preliminary simulation investigation, the results obtained here provides promising information. Since, the reduction in the cutting forces is of intermittent nature, the cutting forces and thus stresses on the cutting tool would be relieved as soon as the holes will be encountered by the cutting tool. Table 8-3 summarizes other promising results obtained from the simulation i.e. average tangential cutting forces, thrust forces, friction coefficient and resultant cutting forces.

Table 8-3: Comparison of cutting forces and friction coefficient

Machining conditions	Average tangential cutting forces (F_c)	Average thrust forces (F_t)	Average resultant forces $\sqrt{Ft^2 + Fc^2}$	Average friction coefficient (F_c / F_t)
Normal machining (300K)	835 nN	1185 nN	1449 nN	0.70
μ-LAM (1200K)	762 nN	1177 nN	1402 nN	0.65
Surface defect machining (300K)	751 nN	1038 nN	1281 nN	0.72

From table 8-3, it is ostensibly visible that compared to normal machining, μ-LAM assisted in the reduction of the resultant cutting force from a value of 1449 nN to 1402 nN, signifying a reduction in the cutting resistance of 3C-SiC by around 3.24%. However, the extent of this reduction is quite significant in SDM process i.e. the resultant forces drops to 1281 nN which implies a significant reduction of 11.59%.

It is very interesting to note here that SDM results in lowering of the cutting forces but not the coefficient of friction. During μ-LAM process, the coefficient of friction reduces by an extent of 7.14% whereas in SDM, the friction coefficient increases by 2.86%. The contradictory increase of the friction coefficient during SDM suggests that a different mechanism of chip formation is associated which has been explained further in details. At the moment, SDM has been tested on hard turning of AISI 4340 steel (hardened up to 69 HRC) and it showed promising results. Besides reduced cutting forces, an improved machined surface roughness (Ra) value of 0.227 μm was obtained through SDM in comparison to 0.452 μm from conventional machining. An experimental comparison of the cutting force is shown in figure 8-6.

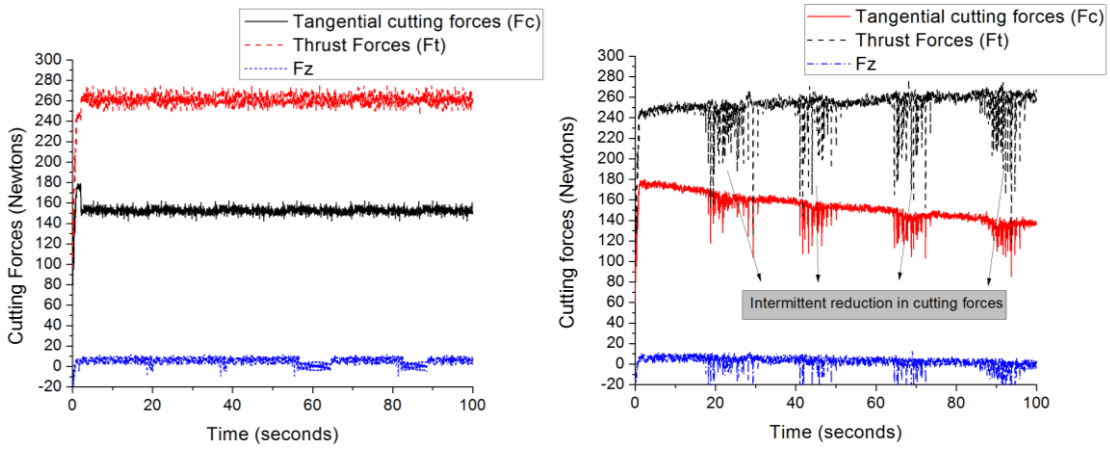

(a) normal machining process (b) SDM induced HT process

Figure 8-6: Comparison of the experimental cutting forces during hard turning of AISI 4340 steel [283]

As evident from figure 8-6, the cutting tool experiences intermittent relaxation in the cutting load during the process of cutting which causes a steep reduction in the forces while the surface defects are encountered by the cutting tool. This intermittent reduction is favourable for tool longevity as it aids to reduce the contact temperature at the tool/workpiece interface as shown in later section. This trend in the variation of the cutting load is more reminiscent to the vibration assisted machining and in this sense; a qualitative comparison between these two processes has been made and shown in table 8-4.

Table 8-4: Comparison between surface defects machining and vibration assisted machining

Surface defect machining (SDM) and vibration assisted machining (VAM)	Differences
Overall cutting load on tool	In VAM, periodic reduction in cutting load occurs at specified amplitude whereas in SDM cutting load reduces where dislocations in the form of holes are encountered.
Volume of material removal	Although, tool is periodically rotated to reduce the cutting load, the total material to be removed during VAM process remains unchanged. In SDM, due to the vacancies made in the form of holes, the total volume of the material to be removed reduces.
Tool contact with chips	During VAM, the cutting tool loses contact with the chips on specified amplitude whereas in SDM cutting chips remains in continuous contact with the tool.
Operational time	No cutting action took place while the tool is disengaged in VAM whereas in SDM continuous cutting takes place.
Requirement of machine tool	Additional device is required to execute VAM whereas with an addition of independent process, no additional device is needed for SDM process.

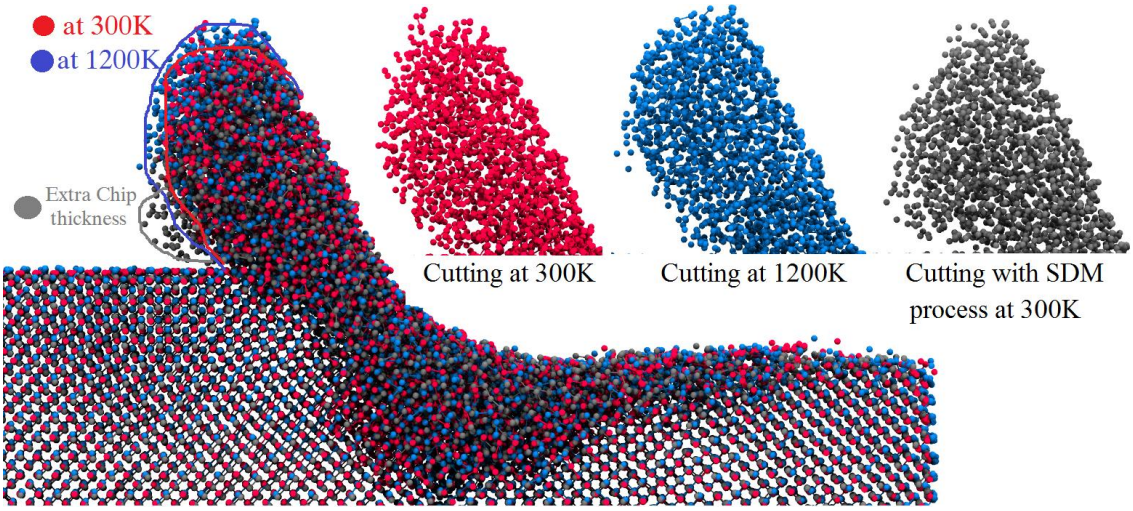

Figure 8-7: Superimposed image of the chip morphology of 3C-SiC after the cutting tool advances to 8.3 nm

Figure 8-7 shows a superimposed image to highlight the differences in the chip morphology of 3C-SiC during its ductile-regime machining in all the three cases investigated. On a comparison of high temperature cutting at 1200 K with cutting at 300K, the curliness of the chip has seemingly increased which is plausible due to the increased plasticity of SiC at high temperature. Table 8-5 shows the measurements of the ratio of uncut chip thickness to cut chip thickness and the shear plane angle measured from the MD simulation snapshots.

Table 8-5: Comparison of chip morphology and shear plane angle under different machining conditions

S.N.	Machining condition	Ratio of uncut chip thickness to cut chip thickness (r)	Shear plane angle(φ)
1	300 K	0.525	21.28°
2	μ-LAM at 1200 K	0.525	21.28°
3	SDM at 300 K	0.505	20.66°

From table 8-5, it was verified using the following classical macroscale equation [212]

(assumed to be valid at nanoscale [300]) that the shear plane angle reduces from a value of 21.28° to 20.66° while using the SDM process.

$$\tan\varphi = \frac{r\cos\alpha}{1 - r\sin\alpha} \qquad 8\text{-}1$$

where φ is the shear plane angle, α is the tool rake angle and r is the ratio of uncut chip thickness and cut chip thickness.

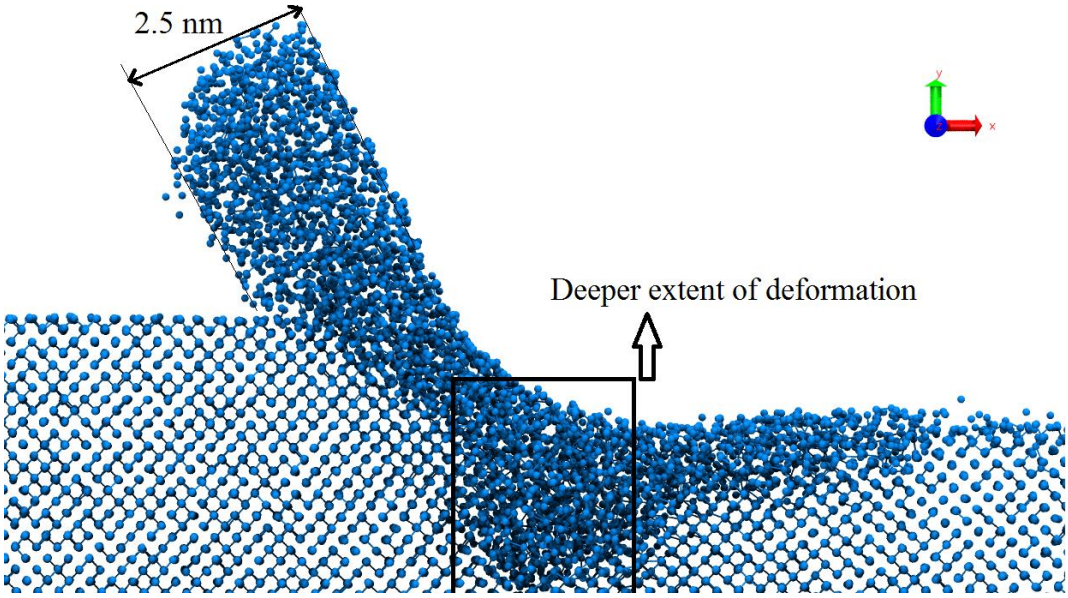

(a) normal machining process at 300 K

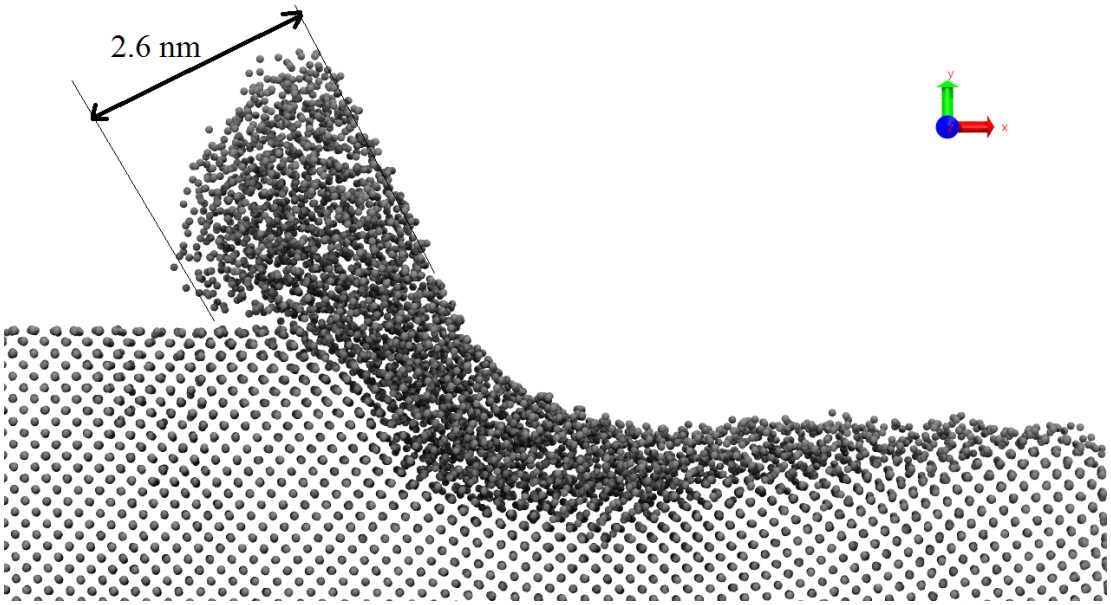

(b) SDM process at 300 K

Figure 8-8: Comparison of the lattice deformation layer depth

Figure 8-8a and figure 8-8b shows the measured cut chip thickness and highlights the variation in the sub-surface crystal deformation lattice layer depth. It is interesting to note that normal machining process shows deeper extent of sub-surface deformation in comparison to the SDM process. During SDM, it is anticipated that the pre-generated surface defects weaken the material locally which in turn reduces the bonding strength of the atoms in the area of uncut chip thickness without disturbing the sub-surface. Also, a discontinuity in the material and the consequent lack of resistance to the cutting by the material adjacent to the one being cut makes the shearing much easier. Eventually, the material removal becomes easier. Furthermore, the chips broke into smaller segmented pieces rather than the long continuous chips. This couples with the fact that tool is relieved from high cutting forces intermittently and this may be the reason of minimal sub-surface damage.

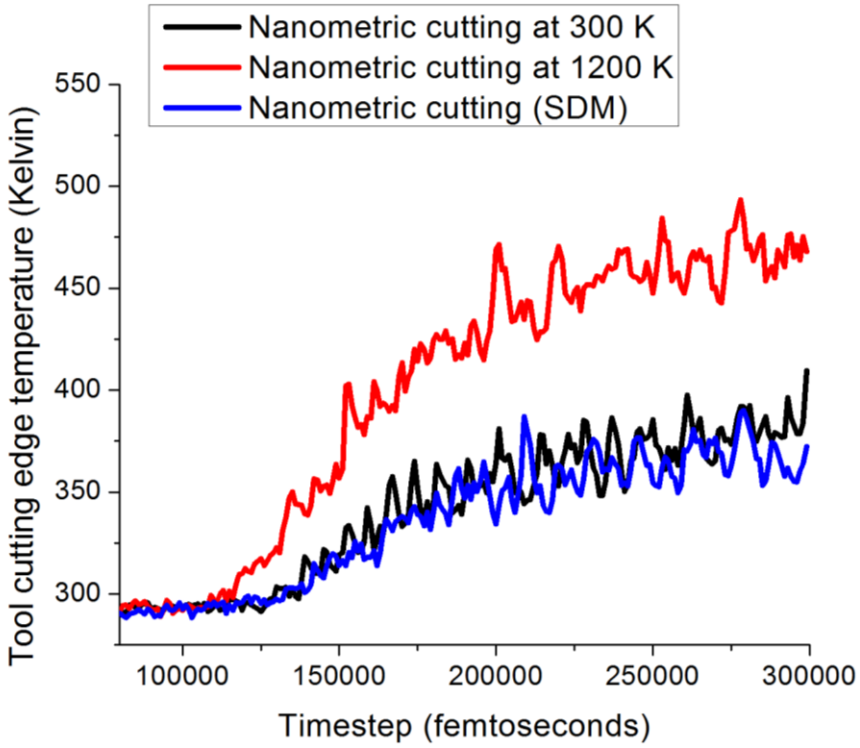

Figure 8-9: Variation in the temperature of the cutting edge of the tool

A comparison of the evolution of temperature in all the three cases over the period of 9.35 nm of tool advancement is shown in figure 8-9. A relatively higher temperature of

480 K on the tool cutting edge is evident during μ-LAM carried out at 1200 K. It is obviously for the fact that high temperature nanometric cutting causes transfer of heat from the bulk of the workpiece to the cutting tool which may compromise the life of the diamond tools. On the contrary, SDM helps to reduce the temperature at the tool cutting edge compared to the high temperature cutting and the normal nanometric cutting at 300K. Consequently, μ-LAM process presents the risk of accelerated graphitization of the diamond tools [125, 274] in contrast to the SDM process.

Of particular importance is to see the stress state of the diamond tool during nanometric cutting of SiC at 300 K and to examine the effectiveness of the SDM method. Accordingly, figure 8-10 was plotted which shows the evolution of the von Mises stress and shear stress acting on the cutting tool over the period of 9.35 nm of tool advancement.

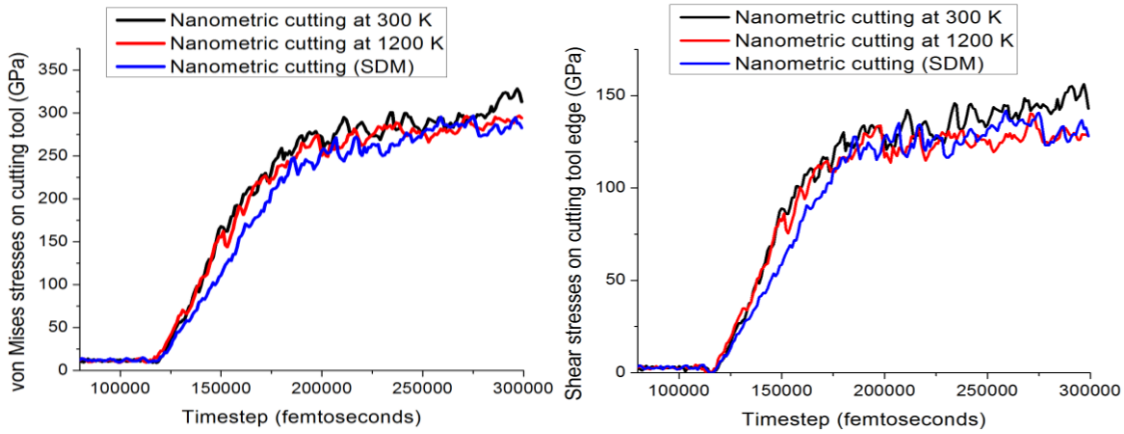

Figure 8-10: Variation in the stress acting on the cutting tool (a) von-Mises stress (b) shear stress

From figure 8-10, it appears that in all the three cases tested, a very high magnitude of von Mises stress (up to 275 GPa) and shear stresses (up to 125 GPa) was found to exert on the diamond tool cutting edge during nanometric cutting of 3C-SiC. This is attributed to the ultra high hardness of 3C-SiC which offers tremendous cutting resistance in comparison to silicon where diamond tool underwent to resist the stresses

of only upto 40 GPa (refer earlier figure 5-4). A high magnitude of von Mises stress of up to 275 GPa having a component of shear stress to the order of 125 GPa is certainly unfavourable for the life of the diamond cutting tools. The ideal strength of shear stress for diamond prior to graphitization has been reported to be around 95 GPa [218]. The stress state in all the cases suggest that graphitization of diamond tool during nanometric cutting of 3C-SiC would be inevitable owing to the high hardness of 3C-SiC. However, SDM seems to have aided to reduce the stresses on the cutting edge to some extent which would provide some relief to the cutting tool.

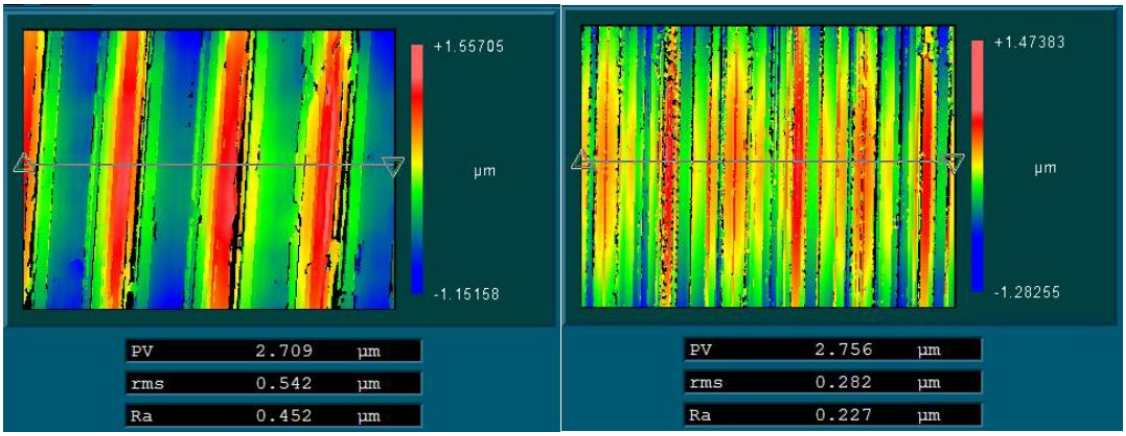

Figure 8-11: Comparison of surface roughness obtained from the hard turning of steel (69 HRC) (a) ordinary machining (b) SDM [283]

From the experimental trial on AISI 4340 steel (69 HRC), a tremendous improvement in the machined surface roughness was observed using SDM process (figure 8-11). A MD simulation was used to assess the detailed insights of this improvement. Figure 8-12 presents the MD results at different time intervals comparing the differences in the mechanism of SDM method and the normal cutting method.

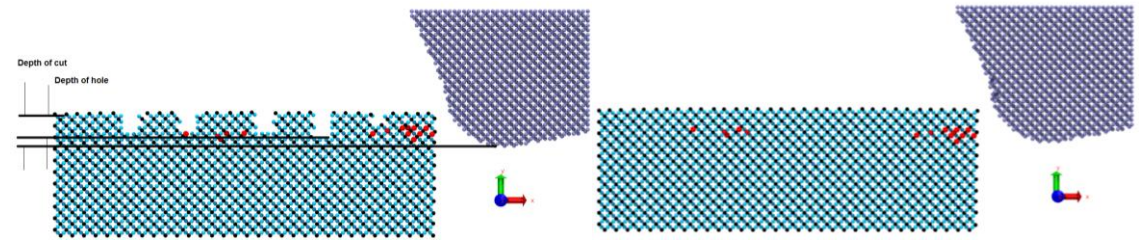

(a) Tool travel = 0 nm

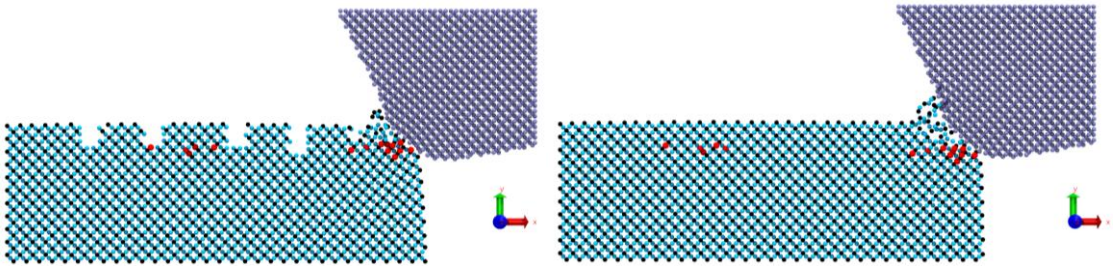

(b) Tool travel = 1.5 nm

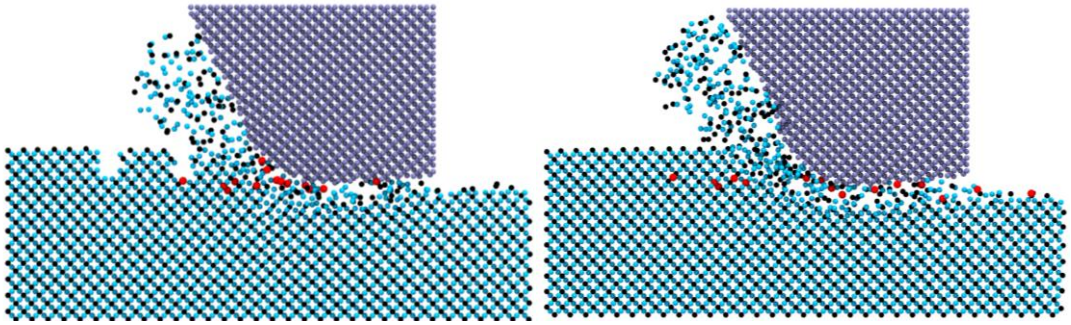

(c) Tool travel = 6.72 nm

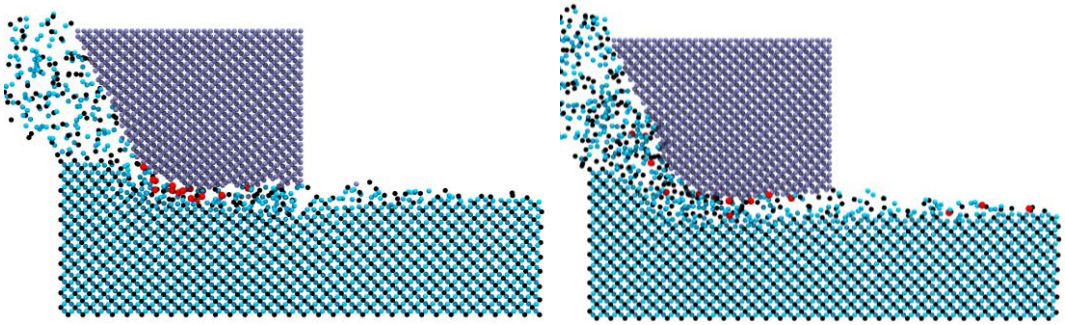

(d) Tool travel = 11.75 nm

(a) SDM method (b) Conventional machining method

Figure 8-12: MD simulation showing various stages of machining action

As shown in figure 8-12, a few atoms have been coloured red in order to provide some key insights on the differences in the cutting mechanism associated with the two cases.

In a normal cutting action, these atoms are well separated during the course of machining and they cling to the cutting tool. During normal cutting, these red atoms were found to remain on the machined surface without contributing to any cutting action on the edge radius of the tool. However, in the case of SDM the red coloured atoms are found to be concentrated underneath the cutting tool. They were observed to travel with the cutting tool rather than sticking onto the machined surface thus suggesting that during the course of machining they are serving the purpose of polishing the machined surface. Referring to the earlier discussions made on porosity machining, it is likely that the local stresses acting on the elevated portion (small) of the workpiece pushes the particles of the cutting chips into the vacant defects which causes the formation of the layer of quasi-continuous material. Particles of this material stuck right underneath the tool and continue to rub with the surface and hence destroy the remains of the feed marks left by the cutting tool. This deduction looks to be good agreement with the machined surface roughness shown in figure 8-11 where feed marks are seldom seen. Hence, it can be presumed that in addition to the cutting process occurring at the rake face, a simultaneous polishing mechanism proceed in the wake underneath the cutting tool in the case of SDM. This mechanism also suggests that feed marks or the remains of the polishing will be iterative and hence, although, an improved surface roughness is obtained, the deterministic periodic finish may be difficult to obtain using SDM.

8.3 Summary

A new machining approach named surface defect machining (SDM) to cut 3C-SiC at nanoscale has been tested using MD simulation and compared with ductile mode micro laser assisted machining at 1200 K and a normal method of cutting at 300 K. The main motivation of this newly developed method was the anticipation that the surface defects

generated on the workpiece allow easy shearing of the material and also result in the simultaneous breaking of the cutting chips into small segments. Indeed this was observed true both with the experiments and the simulation. Besides these advantages, several other favourable outcomes such as reduced cutting forces and reduced shear plane angle were also observed. A reduced shear plane angle provides a better machining action for the same amount of energy input. The extent of sub-surface crystal deformation lattice layer depth was found minimal in the case of SDM.

A relatively higher temperature on the tool cutting edge was found as an inherent characteristic with the μ-LAM process in contrast to SDM process. Consequently, μ-LAM process presents the risk of accelerated graphitization of the diamond tools. It is obviously for the fact that high temperature nanometric cutting causes transfer of heat from the bulk of the workpiece to the cutting tool which may compromise the life of the diamond tools. On the contrary, SDM helps to reduce the temperature at the tool cutting edge compared to the high temperature cutting and the normal nanometric cutting at 300K.

One of the most contrasting features of the proposed SDM method is that both combined cutting and rough polishing action proceed in tandem. These two combined actions provided an improved machined surface in comparison to the ductile mode micro laser assisted machining at 1200 K and a normal method of cutting at 300 K.

Chapter 9 - Conclusions and future work

This chapter is divided into three sections covering, respectively, an overall assessment of the contributions made in the thesis, the main conclusions of the work and, finally, the recommendations for future related work.

9.1 Assessment of research contribution

The research was aimed at investigating the atomic scale mechanisms underlying the nanometric cutting of ultra-hard, brittle materials such as silicon and silicon carbide. A molecular dynamics simulation model using a three-body potential energy function was developed for elucidating the atomic level events. Some experimental trials were performed to understand the macroscopic behaviour resulting from these atomic scale events. With this aim, this thesis has provided further insights into the current state-of-the-art developments in the field of ultra precision mechanical machining of hard, brittle materials.

The novelty and contribution arising from this research lies in:

- the development of a state-of-the-art molecular dynamics model to simulate the nanometric cutting of hard and brittle materials such as silicon and various polytypes of silicon carbide (i.e. 6H-SiC, 3C-SiC and 4H-SiC) using a potential energy function which can appropriately describe the covalent interactions of silicon and carbon.
- development of a novel approach for quantifying the tool wear from the MD simulation as well as extracting a comprehensive list of other useful measures such as cutting stresses, high pressure phase transformation, thermal effects, and cutting forces, all from a single model.

- development of a machining index (i.e. cutting hardness) which can be used to compare the nanometric cutting behaviour of silicon against various polytypes of SiC on a single scale.
- quantification and analysis of the effects of the crystal anisotropy exhibited by silicon carbide during its nanometric cutting.
- classification of the atomistic aspects of the ductile responses of silicon and silicon carbide through a novel approach using the angular distribution function.
- comprehensive investigation and clarification of the mechanism of diamond tool wear during nanometric cutting of SiC and silicon that is corroborated by the experimental results.

9.2 Conclusions of the research

The overall aim of the research was to develop a phenomenological understanding of the ductile characteristics of silicon and silicon carbide and to understand the basic mechanisms of nanometric cutting, including the mechanism by which a diamond tool wears during the process.

Using an approach of parallel molecular dynamics simulations with a many-body potential energy function combined with experimental characterization, this dissertation provides a quantitative understanding of the ductile-regime machining of silicon and SiC (polytypes: 3C, 4H and 6H SiC), and the mechanism by which a diamond tool wears during the process. The distinct MD algorithm developed in this work provides comprehensive results for thermal effects, high pressure phase transformation, tool wear (both chemical and abrasive), influence of crystal anisotropy, cutting forces and machining stresses (hydrostatic and von Mises), effects not dealt with hitherto.

Based on the simulation model developed here, a novel method has been proposed for the quantitative assessment of tool wear from the MD simulations. This model can be utilized for comparing tool wear between simulation studies on SDPT in which there is an interest in graphitization of the diamond tool.

Finally, based on the theoretical simulation results, a novel method of machining is proposed to suppress the tool wear to obtain better machined surface roughness when machining hard-to-machine materials.

The major findings resulting for the above research objectives can be summarised as follows:

I. Silicon carbide exhibits strong crystal anisotropy, with 3C-silicon carbide showing better machined surface roughness either on (111) <-110>, (110) <001> or (100) <100> setups. Further, the simulated thrust forces showed anisotropic variation of up to 44.73% while the resultant forces showed a variation of 36.94% on (100), (110) and (111) planes of 3C-SiC, based on the experimentally known anisotropic variations in Young's modulus of up to 43.6%.

II. The recently developed dislocation extraction algorithm (DXA) [264-265] was employed to detect the nucleation of dislocations in the MD simulations of varying cutting orientation and cutting direction. The analysis revealed that it is the mechanism of structural transformation of the cutting chips rather than the dislocation nucleation which brings ductility in 3C-SiC.

III. A relatively new parameter, "cutting hardness" indicates that 3C-SiC (~2.9 times that of silicon) offers the highest cutting resistance followed by 4H-SiC (~2.8 times that of silicon) and 6H-SiC (~2.1 times of silicon).

IV. There was a significant variation in the quality of machined surfaces and subsurface crystal lattice deformed layer depths between the various polytypes of SiC and Si. The simulation results indicated that 4H-SiC would produce the best sub-surface integrity followed by 3C-SiC, silicon and 6H-SiC. Thus, despite showing the lowest cutting resistance, 6H-SiC indicates the worst sub-surface integrity of the polytypes studied.

V. The radial distribution function and coordination number measurements both indicated that the diamond cutting tools would graphitize due to abrasion against all the polytypes of SiC studied. While 3C-SiC and 4H-SiC indicated a high volume of wear, 6H-SiC showed intermediate tool wear but still somewhat higher than silicon.

VI. Despite being a compound of silicon and carbon, silicon carbide was found to exhibit nanometric cutting characteristics more like diamond, e.g. irrespective of the cutting direction, 3C-SiC having cleavage as the dominant mechanism of material removal on the (111) crystal orientation during and undergoing sp^3-sp^2 transition.

VII. The stress state of the silicon in the machining zone was found to be in accordance with the reported value of pressure required to cause Herzfeld–Mott transition (metallisation) of silicon in the cutting zone. This was confirmed through the computation of change in inter-atomic distances *via* the radial distribution function and measurement of coordination number. Hence, high pressure phase transformation (HPPT) leading to the formation of Si-II metallic phase was found to be a necessary requirement for ductile-regime machining of silicon.

VIII. The chip formation mechanism in the case of single crystal SiC and polycrystalline SiC (RB-SiC) is significantly different. While it has become

apparent over the past decade that structural transformations of brittle materials are responsible for their ductile response or ductile regime machining, this is not the case with RB-SiC. Since grain orientation changes from one crystal to another in polycrystalline SiC (RB-SiC), the cutting tool encounters work material with different crystallographic orientations and directions of cutting. Thus, some of the grain boundaries cause the individual grains to slide along the easy cleavage direction. This causes the build-up of stresses at the grain boundaries. Consequently, the cutting chips in RB-SiC are not deformed by plastic deformation alone rather a combination of the phase transformation at the grain boundaries and the slip of the grains both precede in tandem. Consequently, it was found that RB-SiC, unlike single crystal SiC, involved a different mechanism of chip formation which was found to be the reason for it not exhibiting the phase transformation of 6H-SiC grains.

IX. Tribochemistry (formation of silicon carbide) through a solid state single phase reaction up to a cutting temperature of 959 K in tandem with sp^3-sp^2 disorder of diamond represents the basic wear mechanism of diamond tools against silicon during the single point diamond turning process. This finding is consistent with the experimental results obtained by others who have observed, using XPS, a mixture of SiC and carbon-like particles on a silicon wafer during the nanometric cutting process.

X. The increased frictional contact and abrasion between the tool flank face and the machined surface was found to be the main reason for higher temperatures at the flank face than the rake face. This promotes both the formation of SiC and abrasion, which explains observations of relatively high flank wear compared to rake wear during SPDT of silicon.

XI. A novel method has been proposed for quantitative assessment of tool wear from MD simulation during SPDT. This model can be used for comparing tool wear in simulation studies of SPDT where graphitization of a diamond tool is involved, e.g. SiC and ferrous alloys.

XII. Diamond turning of single crystal 6H-SiC using distilled water as coolant yielded a machined surface roughness of 9.2 nm, making SPDT a feasible option to generate visible range optics on single crystal SiC in a single pass, albeit for small cutting distances. During this operation, the undeformed critical chip thickness was measured to be 25 nm.

XIII. Based on the understanding developed from the simulation process, a generic and new methodology is proposed for machining of the hard-to-machine materials which has been named surface defect machining (SDM). An initial feasibility study to cut SiC using the SDM method using an MD simulation, which showed favourable machining outcomes. SDM involves reduced cutting forces as well as an improved machined surface roughness. The atomistic examination revealed that both cutting and polishing processes proceed in tandem with the resulting improvement in the quality of the machined surface.

9.3 Recommendations for future work

This work has opened up opportunities for a number of commercial, technological and scientific developments, some of which are outlines in the following sections.

9.3.1 Development of enhanced MD software

Currently available MD packages are not dedicated to elucidating nanoscale machining. At the moment, not only a great deal of computational power is needed but also the potential functions available to describe the materials being simulated are quite limited. This is probably the main reason why commercialization of MD tools for manufacturing of brittle materials has not been possible thus far. There is a strong need to develop a generalized formalism of potential function so that it can describe other useful brittle materials such as glass, quartz, tungsten carbide and boron carbide, and commercial software able to simulate these engineering materials could be designed and developed using the information provided in this thesis. Such a development could include the provision of much more flexibility in the size and shape of the workpiece and the cutting tool. It could be made user-friendly and also permit the simulation of other important cutting tool materials such as steel, CBN, graphene and even C_3N_4.

9.3.2 Effects of coolant and coatings

Due to the limitations of time and the lack of potential functions, the effect of coolant during nanometric cutting of silicon and silicon carbide was not studied in the current work. The presence of a coolant will certainly influence the tribo-chemistry of the diamond tool and studying its effect will help develop an understanding of the

appropriate measures for the mitigation of tool wear. For example, a cryogenic environment is already known to improve the tool life. In future work, MD simulations could be done taking account of the presence of oxygen, liquid nitrogen or water on the nanometric cutting mechanisms.

9.3.3 Comparison of single crystal and polycrystalline diamond tools

It has been demonstrated experimentally that polycrystalline (PCD) diamond tools provide more consistent tool life than single crystal diamond tools, particularly in regard to chemical wear. All the MD simulation studies carried out so far (including the current work) have considered only nanocrystalline diamond tools applied to nanometric cutting. Considering a PCD tool in the MD simulation could help to distinguish the wear traits of PCD compared with single crystal diamond. Such simulations may also help to understand if certain classes of material are more amenable to turning with PCD tools and *vice-versa*.

9.3.4 Optimization of tool geometry

It was realized from this study that the rake angle, clearance angle and the cutting edge radius of a diamond cutting tool can play an important role in influencing the process mechanics of ductile-regime machining. Not only do these variables influence the tool life and the attainable machined surface roughness but they also govern the overall cost of diamond tooling. Besides these conventional variables, it was also seen that the presence of nano-scale textures on the cutting tool can improve its tribological characteristics, e.g. textures generated on the rake face of the tool in a direction perpendicular to the chip flow direction give better performance than parallel or cross patterned textures [292]. There seems to be a complex interplay of all the variables

influencing the undeformed critical chip thickness, which has significant implications for productivity. A theoretical analysis to optimize these parameters would be too complex, but MD simulation analysis would be a convenient method of optimizing tool geometry to develop the most efficient cutting tool for a SPDT operation.

9.3.5 On-line metrology and process control

SPDT machine tools are not yet fully developed from the metrology perspective, lacking, for example, such key functions as in-process measurement of tool wear or online assessment of ductile-brittle transition.

In-process measurement of tool wear is one of the important steps in identifying ways of compensating for inconsistent tool wear. One of the usual ways of measuring tool wear is to perform a plunge cut which, for a workpiece material as hard as SiC, means the loss of a significant portion of the tool life. Furthermore, the plunge-cut workpiece needs to be dismounted and taken to a measuring device for the assessment of tool wear and re-mounting is bound to introduce measurement errors.

Thus, metrology has yet to liaise with machine tool development to enable online instrumentation not only to allow for the precise measurement of the tool wear but also to examine the cutting chips during the process itself. For example, online Raman spectroscopy could help to ascertain the HPPT state of a brittle material and hence to distinguish ductile-regime machining from brittle-regime machining. Similarly, the availability of an online infrared camera or temperature sensor could permit monitoring of the cutting temperature, which could be used to study the effectiveness of coolants to optimize the cutting process. The development of an advanced machine tool having these features is a worthwhile future challenge.

9.3.6 Optical characterization of natural diamond tools

It is well known that naturally-occurring diamonds show inconsistent wear. Even crystals selected from the same lot exhibit different properties. The normal practice for the selection of a diamond is based on the colour so, since conventional selection is time consuming and costly, an automated optical characterization technique might help to identify tools which exhibit longer life. Understanding of the chemistry of such tools and their relationship with colour and wear behaviour could help the synthesis of better tools than those currently available.

Appendices

A. Derivation of undeformed chip thickness using machining parameters of SPDT

Appendices A is meant to demonstrate the mathematical relations obtained by applying the principles of geometry to derive the critical machining parameters during nanometric cutting.

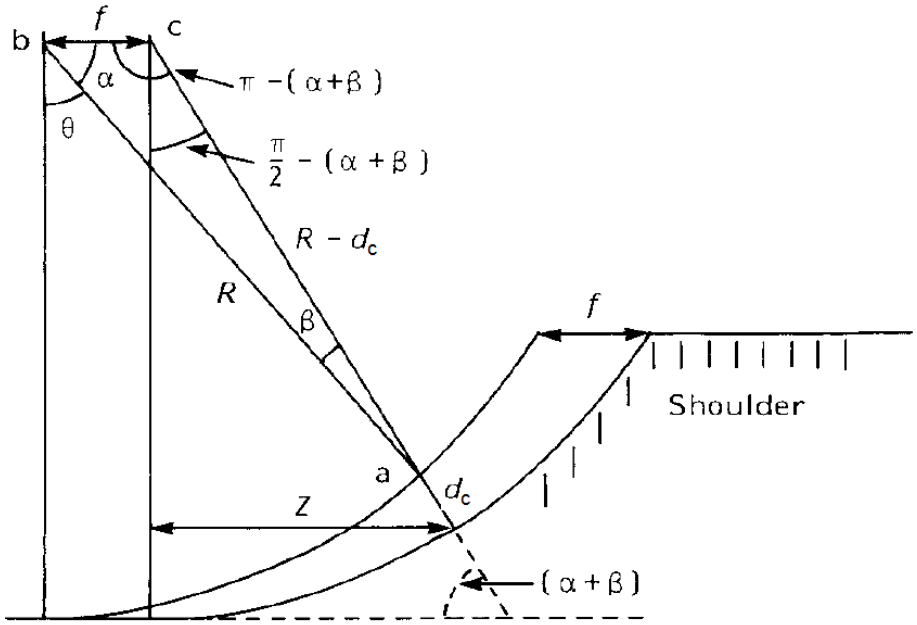

Figure A1: Tool-workpiece interface during SPDT with a round nose tool [23]

Applying sine law in Δ abc of figure A1, we can have:

$$\frac{\sin\{\pi-(\alpha+\beta)\}}{R}=\frac{\sin\beta}{f}=\frac{\sin\alpha}{R-dc}$$

$$\frac{\sin\{\pi-(\alpha+\beta)\}}{R}=\frac{\sin\beta}{f}$$

$$\frac{f\sin(\alpha+\beta)}{R}=\sin\beta$$

Expanding sin (α+β) and dividing by cos β on both sides gives the following:

$$\frac{f\sin\alpha}{R}=\tan\beta\left(1-\frac{f}{R}\cos\alpha\right)$$

$$\tan\beta=\frac{f/R(\sin\alpha)}{\left(1-\frac{f}{R}\cos\alpha\right)}$$

Since, α = 90-θ => sin α = cos θ and cos α = sin θ

$$\tan\beta = \frac{f/R(\cos\theta)}{\left(1-\frac{f}{R}\sin\theta\right)}$$

Let X = f/R

Now, f/R < < < 1 $\tan\beta = X\cos\theta$

The above equation can be presented in the form of triangle as:

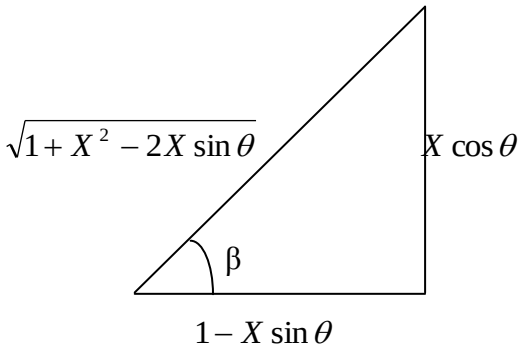

Using (1) $\frac{\sin\beta}{f} = \frac{\sin\alpha}{R-dc}$

$$dc = R - \frac{f\cos\theta}{\sin\beta}$$

Substituting value of sin β and replacing X

$$dc = R - \frac{f\cos\theta\sqrt{1+X^2-2X\sin\theta}}{X\cos\theta} = R - R\sqrt{1+f^2/R^2-2\,f/R\sin\theta}$$

Now, f/R < < < 1

$$dc = R - R\sqrt{1-2\,f/R\sin\theta}$$

Applying Taylor's expansion and by neglecting higher order terms:

since θ is extremely small

$$dc = f\sin\theta = f\theta$$

Expression for Z:

$$\frac{Z}{R} = \cos(\alpha+\beta)$$

Expanding $\cos(\alpha+\beta)=\cos\alpha\sin\beta-\cos\beta\sin\alpha$ and replacing values from Δ

$$Z=\frac{R(\sin\theta-X)}{\sqrt{1+X^2-2X\sin\theta}}$$

Now, f/R < < < 1 and θ is small

$$Z=R\left(\sin\theta-\frac{f}{R}\right)$$

$$Z=R\left(\frac{dc}{f}-\frac{f}{R}\right)=\frac{Rd_c}{f}-f$$

$$dc=\frac{f(z+f)}{R}$$

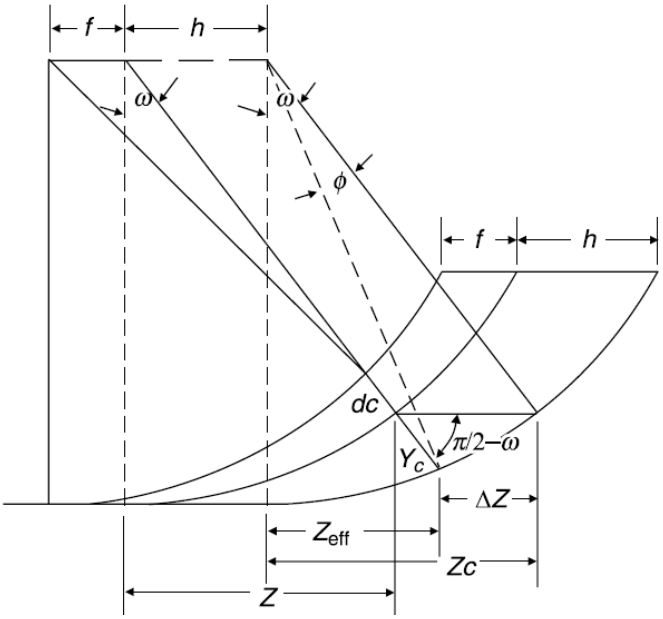

Figure A2: Geometry to derive transition point

Since, Yc is the sub-surface damage which is proportional with the feed rate which occurs at the distance Zeff where (figure A2),

$$Z_{eff}=Z_c-\Delta Z$$

$$Z_{eff}=\sqrt{Z_c^2-2RY_c}$$

$$Z_{eff}^2=Z_c^2-2RY_c$$

$$Z_{eff}^2=\left(\frac{Rd_c}{f}-f\right)^2-2RY_c$$

$$Z_{eff}^2-f^2=R^2\left(\frac{dc^2}{f^2}-\frac{2d_c}{R}-\frac{2Y_c}{R}\right)$$

$$\frac{Z_{eff}{}^2 - f^2}{R^2} = \frac{dc^2}{f^2} - \frac{2}{R}(d_c - Y_c)$$

In order to evaluate critical feed rate, the process limits would be such that Z_{eff}=0

$f_{\max} = dc\sqrt{\frac{R}{2(d_c + Y_c)}}$ by assuming that $\left(\frac{d_c}{d_c + Y_c}\right)^2$ <<<1

The maximum undeformed chip thickness, dmax, (effective depth of cut) can be calculated according to the cutting tool geometry and cutting conditions as shown in figure 3.

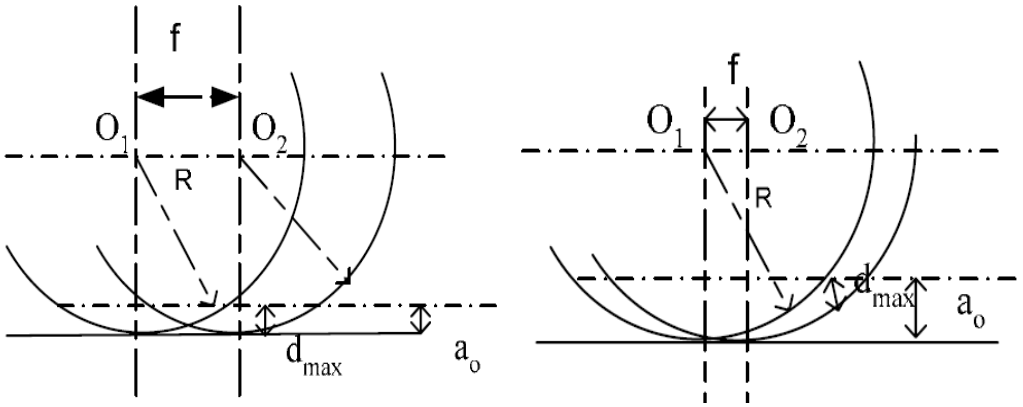

(a): Large feed rate $\sqrt{(2Ra_0 - a_0{}^2)} \le f$ (b): Small feed rate $\sqrt{(2Ra_0 - a_0{}^2)} > f$

Figure A3: Schematic for maximum undeformed chip thickness [301]

Here, a_0 is the depth of cut; R is the nose radius; O1 and O2 are the centres of two adjacent arc cutting edges, and the distance between O1 and O2 is the feed rate, f. The maximum undeformed chip thickness dmax for the two conditions as shown in figure A3 can be calculated as follows:

The maximum undeformed chip thickness for large feed rate while

$\sqrt{(2Ra_0 - a_0{}^2)} \le f$ can be expressed as:

$d_{\max} = a_0$

The maximum undeformed chip thickness for small feed rate while

$\sqrt{(2Ra_0 - a_0^{\,2})} > f$ can be expressed as:

$$d_{\max} = R - \sqrt{R^2 + f^2 - 2f\sqrt{2Ra_0 - a_0^{\,2}}}$$

When R≫f and R ≫a_0

Above equation can be finally simplified as:

$$d_{\max} \approx \frac{f}{R}\sqrt{2Ra_0 - a_0^{\,2}} \approx f\sqrt{\frac{2a_0}{R}}$$

B. Derivation of surface roughness during SPDT

Appendices B is meant to derive an expression of theoretical surface roughness attainable during nanometric cutting by applying the principles of geometry.

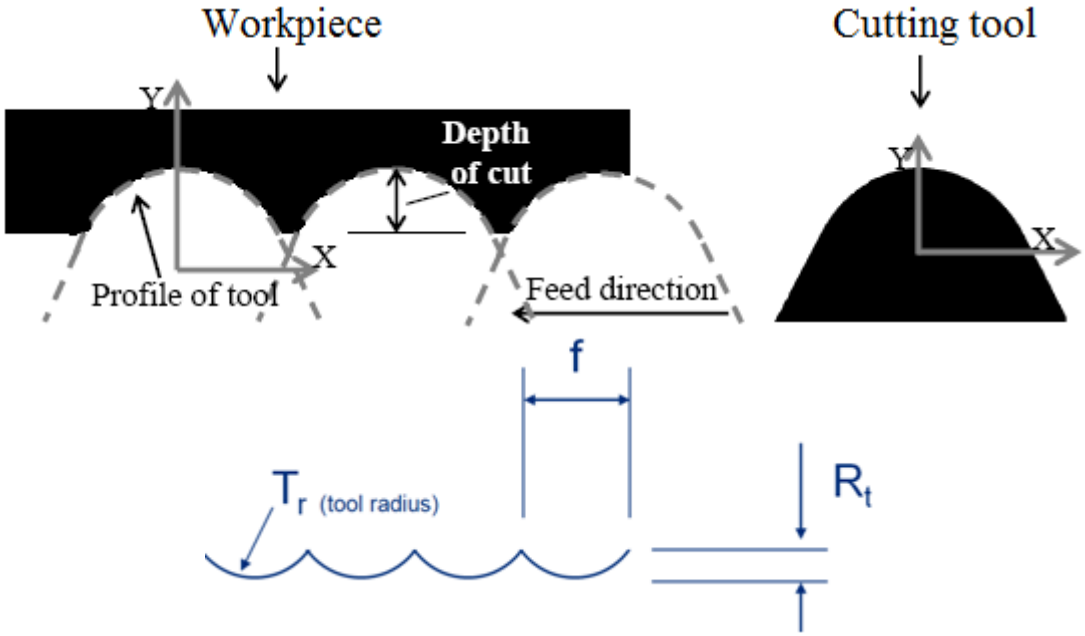

Figure B1: Schematic for model of surface roughness.

Conventionally, Scattergood *et al.* [22] gave the following empirical relation for the measurement of surface roughness (Rt) as shown in figure B1.

$$R_t \approx \frac{f^2}{8 * T_r}$$

where f = feed rate, Tr = tool radius, and R_t = maximum individual peak to valley height. However, this applies only if f/R < 1. A modification in the above equation was proposed later [302] to incorporate the asynchronous errors arising from the machine spindle as follows:

$$R_t \approx \frac{f^2}{8 * T_r} + K\{A_{asynchronous}\}$$

Author of this thesis has attempted to derive a fresh mathematical expression to deduce the mathematical expression of surface roughness for an ultra precision engineering operation such that of SPDT. Accordingly, figure B2 shows a schematic diagram to deduce a modified expression for surface roughness Rt.

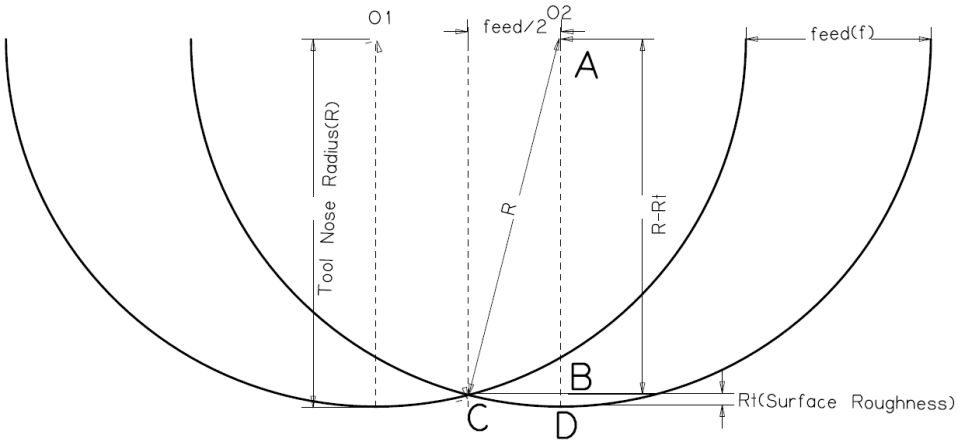

Figure B2: Proposed schematic to measure surface roughness.

In triangle ABC, using Pythagoras theorem,

$$(R-R_t)^2+\left(\frac{f}{2}\right)^2=R^2$$

Solving above equation

$$R^2+R_t^{\,2}-2RR_t+\left(\frac{f}{2}\right)^2=R^2$$

$$4R_t^{\,2}-8RR_t+f^2=0$$

This is a quadratic equation of a form $ax^2+bx+c=0$ with its root $\frac{-b\pm\sqrt{b^2-4ac}}{2a}$

In the above equation, a = 4; b = -8R; c = f^2

Therefore, $R_t=\frac{8R\pm\sqrt{64R^2-4X4f^2}}{2X4}$

$$R_t=R\pm\sqrt{R^2-\frac{f^2}{4}}$$

It shall be noted that since $R_t < f < R$ so, $R_t=R+\sqrt{R^2-\frac{f^2}{4}}$ may be neglected.

The final expression after incorporating the asynchronous errors arising from the machine spindle reduces to:

$$Rt=R-\sqrt{R^2-\frac{f^2}{4}}+K\{A_{asynchronous}\}$$

where *Rt* is the surface roughness, *R* is tool nose radius of the round tool and *f* is the feed rate.

C. Some useful experimental techniques

A list of useful state-of-the-art experimental techniques for studying chemical and physical nature of the SPDT process and other ultra precision engineering processes are shown in table C1. Table C2 shows the analytical techniques and the applications where these techniques are useful.

Table C1: Surface analysis techniques [303]

Detected radiation	**Incident radiations**				
	Electron based	**Ion based**	**X-ray photon based**	**Other photons based**	**E/M field**
Electron	TEM, SEM, STM, AES, LEED, RHEED, THEED		XPS		
Ion	MS	FIM, ISS, RBS, SIMS			
X-ray photon	EPMA		XRF, XRD, EDS		
Other photons				IR, Raman, ELL	
E/M field					NMR

TEM: Transmission electron microscope,
SEM: Scanning electron microscope,
STM: Scanning tunnelling microscope,
AES: Auger electron spectroscopy,
LEED: Low energy electron diffraction,
RHEED or RED: Reflection high energy electron diffraction
THEED or TED: Transmission high energy electron diffraction
MS: Mass spectroscopy
EPMA: Electron probe X-ray micro analyzer
FIM: Field ion microscope
ISS: Ion scattering spectroscopy
RBS: Rutherford backscattering spectroscopy
SIMS: Secondary ion mass spectroscopy
XPS: X-ray photoelectron spectroscopy
XRF: X-ray fluorescence
XRD: X-ray diffraction
EDS: Energy dispersive X-ray photo spectroscopy
IR: Infrared spectroscopy
ELL: Ellipsometry
NMR: Nuclear magnetic resonance
AFM: Atomic force microscope

Table C2: Useful analytical techniques and their applications

S.No.	Analytical technique	Applications
1.	Nanoindentation or Nano-impact test	Elastic and plastic properties
2.	SEM, AFM, profilometer or interferometer	Surface morphology
3.	Optical microscopy, SEM, TEM	Microstructure
4.	X Ray Diffraction or electron diffraction	Atomic positions/ material microstructure
5.	EDS and XPS	Chemical composition
6.	XPS, EDS, Raman spectroscopy, IR	Chemical bonding property
7.	Fluorescence confocal microscopy, HF etching, cross sectional microscopy, micro raman spectroscopy, Rutherford backscattering, photon backscattering, KOH etching, positron annihilation	Sub-surface damage
8.	While light interferometer or surface profilometer	Surface roughness
9.	DXR Raman microscope, Nomarski differential interference contrast microscopy, SEM, AFM	Brittle-ductile transition
10.	Cathodoluminescence, IR, Raman mapping analysis	Characterization of diamond tool
11.	Laue back reflection	Crystal orientation
12.	Keyence VHX-500F Digital microscope (for diamond tool 150x Zoom was found good)	Quantitative examination of Vb (tool flank wear length)

References

1. Neudeck, P.G., *SiC Technology*, in *The VLSI Handbook*, B. Raton, Editor. 2000, CRC Press and IEEE Press: Florida. p. 6.1-6.24.
2. Dzurak, A., *Quantum computing: Diamond and silicon converge.* Nature, 2011. **479**(7371): p. 47-48.
3. Shore, P., Cunningham C., et al., *Precision engineering for astronomy and gravity science.* CIRP Annals - Manufacturing Technology, 2010. **59**(2): p. 694-716.
4. Shore, P. and Morantz P., *Ultra-precision: enabling our future.* Philosophical Transactions of the Royal Society A: Mathematical, Physical and Engineering Sciences, 2012. **370**(1973): p. 3993-4014.
5. Venkatachalam, S., PhD Thesis on *Predictive modeling for ductile machining of brittle materials* in *School of Mechanical Engineering*, Georgia Institute of Technology, 2007
6. Tönshoff, H.K., C. Arendt, and R.B. Amor, *Cutting of Hardened Steel.* CIRP Annals - Manufacturing Technology, 2000. **49**(2): p. 547-566.
7. König, W., A. Berktold, and K.F. Koch, *Turning versus Grinding - A Comparison of Surface Integrity Aspects and Attainable Accuracies.* CIRP Annals - Manufacturing Technology, 1993. **42**(1): p. 39-43.
8. Davies M.A., Evans C.J., et al. *Application of precision diamond machining to the manufacture of micro-photonics components*. in *Lithographic and Micromachining Techniques for Optical Component Fabrication II*. 2003. San Diego, USA: SPIE.
9. Blynsky, G., *Closing in on Perfection*, in *Fortune*. 23/06/2003. p. 112[F]-112[L].
10. Corbett, J., Mckeown P.A., et al., *Nanotechnology: International Developments and Emerging Products.* CIRP Annals - Manufacturing Technology, 2000. **49**(2): p. 523-545.
11. Taniguchi, N., *Current Status in, and Future Trends of, Ultraprecision Machining and Ultrafine Materials Processing.* CIRP Annals - Manufacturing Technology, 1983. **32**(2): p. 573-582.
12. McKeown, P.A., *The Role of Precision Engineering in Manufacturing of the Future.* CIRP Annals - Manufacturing Technology, 1987. **36**(2): p. 495-501.
13. Taniguchi, N. *On the basic concept of 'nano-technology'*. in *Proceedings of Production Engineering, Part -II, Japan Society of Precision Engineering*. 1974. Tokyo, Japan.
14. Liu, X., DeVor R.E., et al., *The Mechanics of Machining at the Microscale: Assessment of the Current State of the Science*. Journal of Manufacturing Science and Engineering, 2004. **126**(4): p. 666-678.
15. Brinksmeier, E. and Preuss W., *Micro-machining.* Philosophical Transactions of the Royal Society A: Mathematical, Physical and Engineering Sciences, 2012. **370**(1973): p. 3973-3992.
16. Jain, V.K., *Magnetic field assisted abrasive based micro-/nano-finishing.* Journal of Materials Processing Technology, 2009. **209**(20): p. 6022-6038.
17. Subbiah, S. and Melkote S.N., *Evaluation of Atkins' model of ductile machining including the material separation component.* Journal of Materials Processing Technology, 2007. **182**(1–3): p. 398-404.
18. Gutowski, T.G., Branham M.S., et al., *Thermodynamic Analysis of Resources Used in Manufacturing Processes.* Environmental Science & Technology, 2009. **43**(5): p. 1584-1590.
19. John, B.P., *Scaling down of manufacturing systems: meso and nano level machining – an analysis*, in *Industrial and manufacturing engineering*. 2003, The Pennsylvania State University: Pennsylvania.
20. Blake, P.N., *PhD Thesis on Ductile-regime diamond turning of germanium and silicon*, North Carolina State University, USA, 1988.
21. Bifano, Dow and Scattergood, *Ductile-Regime Grinding: A New Technology for Machining Brittle Materials.* Journal of Engineering for Industry, 1991. **113**(184).
22. Scattergood R.O., Blake, N., *Ductile-regime machining of germanium and silicon.* Journal of the American ceramic society, 1990. **73**(4): p. 949-957.
23. Blackley, W.S. and Scattergood R.O., *Ductile-regime machining model for diamond turning of brittle materials.* Precision Engineering, 1991. **13**(2): p. 95-103.
24. Patten, J.A., PhD thesis on *High Pressure Phase Transformation Analysis and Molecular Dynamics Simulations of Single Point Diamond Turning of Germanium,*, in North Carolina State University: Raleigh N.C, USA, 1996.
25. Morris, J.C., Callahan D.L., et al., *Origins of the Ductile Regime in Single-Point Diamond Turning of Semiconductors.* Journal of the American Ceramic Society, 1995. **78**(8): p. 2015-2020.

26. Ravindra, D., PhD Thesis on *Ductile mode material removal of ceramics and semiconductors*, in *Department of Mechanical and Aeronautical Engineering*, Western Michigan University: Michigan. p. 312, 2011.
27. Cai, M.B., Li X.P., et al., *Crack initiation in relation to the tool edge radius and cutting conditions in nanoscale cutting of silicon.* International Journal of Machine Tools and Manufacture, 2007. **47**(3-4): p. 562-569.
28. Weck M., Hartel R., and Bispink T., *Limits of workpiece accuracy caused by the geometrical and dynamical behaviour of ultraprecision diamond turning machines, ISBN: 3540192417*. 1988, Berlin; Newyork; Springer-Verlag c1988: Berlin. p. 153-169.
29. King, R.F. and Tabor D., *The Strength Properties and Frictional Behavior of Brittle Solids*, in *Series A: Mathematical and Physical Science*. 1954, Proceedings of the Royal Society of London. p. 225-238.
30. Bridgman, P.W. and Simon I., *Effects of Very High Pressures on Glass.* Journal of Applied Physics, 1953. **24**(4): p. 405-413.
31. Lawn, B. and Wilshaw R., *Indentation fracture: principles and applications.* Journal of Materials Science, 1975. **10**(6): p. 1049-1081.
32. Venkatesh V.C. and Sudin Izman, *Precision Engineering, DOI: 10.1036/0071548270*. 2007, New Delhi, India: Tata Macgraw Hill.
33. Niihara, K., *Slip systems and plastic deformation of silicon carbide single crystals at high temperatures.* Journal of the Less Common Metals, 1979. **65**(1): p. 155-166.
34. Lawn, B.R. and Marshall D.B., *Hardness, Toughness, and Brittleness: An Indentation Analysis.* Journal of the American Ceramic Society, 1979. **62**(7-8): p. 347-350.
35. Wang, M.,Wang W., and Z. Lu, *Anisotropy of machined surfaces involved in the ultra-precision turning of single-crystal silicon—a simulation and experimental study.* The International Journal of Advanced Manufacturing Technology, 2012. **60**(5): p. 473-485.
36. Marshall, D.B. and L. B.R., *Indentation of Brittle Materials*. Microindentation Technology in Materials Science and Engineering. Vol. 889. 1986: ASTM STP,.
37. Jasinevicius, R.G., Duduch J.G., et al., *Dependence of brittle-to-ductile transition on crystallographic direction in diamond turning of single-crystal silicon.* Proceedings of the Institution of Mechanical Engineers, Part B: Journal of Engineering Manufacture, 2011.
38. Arif, M., Zhang X., et al., *A predictive model of the critical undeformed chip thickness for ductile–brittle transition in nano-machining of brittle materials.* International Journal of Machine Tools and Manufacture, 2013. **64**(0): p. 114-122.
39. Nakasuji, T., Kodera S., et al., *Diamond Turning of Brittle Materials for Optical Components.* CIRP Annals - Manufacturing Technology, 1990. **39**(1): p. 89-92.
40. Inamura, T., Nobuhiro T., et al., *On a Possible Mechanism of Shear Deformation in Nanoscale Cutting.* CIRP Annals - Manufacturing Technology, 1994. **43**(1): p. 47-50.
41. Yan, J., Syoji, Katsuo, Kuriyagawa, Tsunemoto, Suzuki, Hirofumi, *Ductile regime turning at large tool feed.* Journal of Materials Processing Technology, 2002. **121**(2-3): p. 363-372.
42. Gilman, J.J., *Insulator-metal transitions at microindentations.* Journal of Materials Research, 1992. **7**: p. 535-538.
43. Gilman, J.J. *Metallization at Microindentations*. in *MRS Spring Meeting*. 1992: Cambridge University Press.
44. Gilman, J.J., *Mechanism of shear-induced metallization.* Czechoslovak Journal of Physics, 1995. **45**(11): p. 913-919.
45. Bouwelen Van, F.M., L.M. Brown, and J.E. Field, *A new view on the mechanism of diamond polishing.* Industrial diamond review, 1997. **57**(1): p. 21-25.
46. Jiwang, Y., Hongwei Z., and K. Tsunemoto, *Effects of tool edge radius on ductile machining of silicon: an investigation by FEM.* Semiconductor Science and Technology, 2009. **24**(7): p. 075018.
47. Patten, J. and Jacob J., *Comparison between numerical simulations and experiments for single-point diamond turning of single-crystal silicon carbide.* Journal of Manufacturing Processes, 2008. **10**: p. 28-33.
48. Alder, B.J. and T.E. Wainwright, J. Chem. Phys., 1957. **1208**(27).
49. Belak J.F. and Stowers I.F., *A Molecular Dynamics model of Orthogonal Cutting process.* Proceedings of American Society Precision Engineering Annual conference, 1990: p. 76-79.
50. Ikawa, Shimada, et al., *Minimum thickness of cut in micromachining.* Nanotechnology, 1992. **1**(3): p. 6-9.
51. Voter, A.F. and Kress J.D., *Atomistic Simulation of Diamond-Tip Machining of Nanoscale Features*. in *Principles of Cutting Mechanics: Applications of Ultra-Precision Machining and Grinding, 1993 Spring Topical Meeting* 1993. Tucson, AZ, USA: ASPE Proceedings.

52. Inamura, T., Soichi S., et al., *Brittle/Ductile Transition Phenomena Observed in Computer Simulations of Machining Defect-Free Monocrystalline Silicon.* CIRP Annals - Manufacturing Technology, 1997. **46**(1): p. 31-34.
53. Rentsch, R. *Influence of Crystal Orientation on the Nanomeric Cutting Process*. in *Proceedings of the First International Euspen Conference*. 1999. Bremen, Germany,.
54. Komanduri, R., N. Chandrasekaran, and L.M. Raff, *Effect of tool geometry in nanometric cutting: a molecular dynamics simulation approach.* Wear, 1998. **219**(1): p. 84-97.
55. Cheng, K., Luo X., et al., *Modeling and simulation of the tool wear in nanometric cutting.* Wear, 2003. **255**: p. 1427-1432.
56. Cai, M.B., X.P. Li, and M. Rahman, *Study of the mechanism of nanoscale ductile mode cutting of silicon using molecular dynamics simulation.* International Journal of Machine Tools and Manufacture, 2007. **47**(1): p. 75-80.
57. Belak J.F., Stowers I.F, Boercker D.B., *Simulation of Diamond turning of silicon surfaces.* Proceedings of 7th American Society Precision Engineering Annual conference, 1992: p. 76-79.
58. Maekawa, K. and A. Itoh, *Friction and tool wear in nano-scale machining--a molecular dynamics approach.* Wear, 1995. **188**(1-2): p. 115-122.
59. Nozaki, T., Masao D., et al., *Micromachining of pure silicon by molecular dynamics.* Thin Solid Films, 1998. **334**(1–2): p. 221-224.
60. Shimada, S., Naoya I., et al., *Brittle-Ductile Transition Phenomena in Microindentation and Micromachining.* CIRP Annals - Manufacturing Technology, 1995. **44**(1): p. 523-526.
61. Komanduri, R., N. Chandrasekaran, and L.M. Raff, *Molecular dynamics simulation of the nanometric cutting of silicon.* Philosophical Magazine Part B, 2001. **81**(12): p. 1989 - 2019.
62. Arefin, S., Li X.P., et al., *The Effect of the Cutting Edge Radius on a Machined Surface in the Nanoscale Ductile Mode Cutting of Silicon Wafer.* Proceedings of the Institution of Mechanical Engineers, Part B: Journal of Engineering Manufacture, 2007. **221**(2): p. 213-220.
63. Lucca, D.A., Y.W. Seo, and R.L. Rhorer, *Energy Dissipation and Tool-Workpiece Contact in Ultra-Precision Machining.* Tribology Transactions, 1994. **37**(3): p. 651-655.
64. Patten, J.A., Jacob J., et al., *Chapter 2: Numerical simulations and cutting experiments on single point diamond machining of semiconductors and ceramics*, in *Semiconductor Machining at the Micro-Nano Scale, ISBN : 978-81-7895-301-4*, J. Yan and J.A. Patten, Editors. 2007, Transworld Research Network: Trivandrum-695 023, Kerala, India.
65. Ravindra, D. and Patten J.A., *Determining the Ductile to Brittle Transition (DBT) of a Single-Crystal 4H-SiC Wafer by Performing Nanometric Cutting*, in *ISAAT 2007 Precision Grinding and Abrasive Technology at SME International Grinding Conference*. 2007.
66. Bhattacharya, B., J.A. Patten, and J. Jacob, *Single Point Diamond Turning of CVD Coated Silicon Carbide.* ASME Conference Proceedings, 2006. **2006**(47624): p. 1153-1158.
67. Young, H.T., Liao H.T., and H.-Y. Huang, *Novel method to investigate the critical depth of cut of ground silicon wafer.* Journal of Materials Processing Technology, 2007. **182**(1–3): p. 157-162.
68. Leung, T.P., W.B. Lee, and X.M. Lu, *Diamond turning of silicon substrates in ductile-regime.* Journal of Materials Processing Technology, 1998. **73**(1-3): p. 42-48.
69. Durazo-Cardenas, I., Shore P., Jacklier T, Luo X., and C.A. Impey et al., *3D characterisation of tool wear whilst diamond turning silicon.* Wear, 2007. **262**(3-4): p. 340-349.
70. Evans, C. and J.B. Bryan, *Cryogenic Diamond Turning of Stainless Steel.* CIRP Annals - Manufacturing Technology, 1991. **40**(1): p. 571-575.
71. Rentsch, R. and I. Inasaki, *Effects of fluids on the surface generation in material removal processes - Molecular dynamics simulation.* Cirp Annals-Manufacturing Technology, 2006. **55**(1): p. 601-604.
72. Paul, E., Evans C., et al., *Chemical aspects of tool wear in single point diamond turning.* Precision Engineering, 1996. **18**(1): p. 4-19.
73. Jackson, M. and J. Morrell, *Machining Brittle Materials Using Nanostructured Diamond Tools*, in *Machining with Nanomaterials*. 2009, Springer US. p. 1-30.
74. Wong, C.J., *Fracture and Wear of Diamond Cutting Tools.* Journal of Engineering Materials and Technology, 1981. **103**(4): p. 341-345.
75. Jasinevicius, R.G., J.G. Duduch, and A.J.V. Porto, *Investigation on diamond turning of silicon crystal - generation mechanism of surface cut with worn tool.* Journal of the Brazilian Society of Mechanical Sciences, 2001. **23**: p. 241-252.
76. Li, X.P., T. He, and M. Rahman, *Tool wear characteristics and their effects on nanoscale ductile mode cutting of silicon wafer.* Wear, 2005. **259**(7-12): p. 1207-1214.
77. Cai, M.B., X.P. Li, and M. Rahman, *Characteristics of "dynamic hard particles" in nanoscale ductile mode cutting of monocrystalline silicon with diamond tools in relation to tool groove wear.* Wear, 2007. **263**(7-12): p. 1459-1466.

78. Khurshudov, A.G., K. Kato, and H. Koide, *Wear of the AFM diamond tip sliding against silicon.* Wear, 1997. **203-204**: p. 22-27.
79. Yan, J., Syoji, Katsuo, Tamaki, Jun'ichi, *Some observations on the wear of diamond tools in ultra-precision cutting of single-crystal silicon.* Wear, 2003. **255**(7-12): p. 1380-1387.
80. O'Connor, B.P., Marsh, E. R. and Couey, J. A., *On the effect of crystallographic orientation on ductile material removal in silicon.* Precision Engineering, 2005. **29**: p. 124-132.
81. Wilks, J., *Performance of diamonds as cutting tools for precision machining.* Precision Engineering, 1980. **2**(2): p. 57-70.
82. Oomen, J.M. and J. Eisses, *Wear of monocrystalline diamond tools during ultraprecision machining of nonferrous metals.* Precision Engineering, 1992. **14**(4): p. 206-218.
83. Puttick, K.E., Whitmore L.C., et al., *Energy scaling transitions in machining of silicon by diamond.* Tribology International, 1995. **28**(6): p. 349-355.
84. Goel, S., Stukowski A., et al., *Nanotribology at high temperatures.* Beilstein Journal of Nanotechnology, 2012. **3**: p. 586-588.
85. Seagal, M., *Learning from silicon.* Nature, 2012. **483**: p. S43-S44.
86. Narulkar, R., Komanduri R., et al., *Graphitization as a precursor to wear of diamond in machining pure iron: A molecular dynamics investigation.* Computational Materials Science, 2009. **45**(2): p. 358-366.
87. Gilman, J.J., *Why silicon is hard.* Science, 1993. **261**: p. 1436-1439.
88. Melinon, P., Mesenelli P., et al., *Playing with carbon and silicon at the nanoscale.* Nature Materials, 2007. **6**(7): p. 479-490.
89. Goel, S., Luo X., et al., *Replacing diamond cutting tools with CBN for efficient nanometric cutting of silicon.* Materials Letters, 2012. **68**(0): p. 507-509.
90. Jardret, V., Zahouani H., et al., *Understanding and quantification of elastic and plastic deformation during a scratch test.* Wear, 1998. **218**(1): p. 8-14.
91. Leyland, A. and A. Matthews, *On the significance of the H/E ratio in wear control: a nanocomposite coating approach to optimised tribological behaviour*. Wear, 2000. **246**(1–2): p. 1-11.
92. Gogotsi, Y., Sascha W., et al., *Conversion of silicon carbide to crystalline diamond-structured carbon at ambient pressure*. Nature, 2001. **411**(6835): p. 283-287.
93. Puttick, K.E., Rudman M.R., et al., *Single-Point Diamond Machining of Glasses.* Proceedings of the Royal Society of London. A. Mathematical and Physical Sciences, 1989. **426**(1870): p. 19-30.
94. Tsurimoto, S. and T. Moriwaki. *Machining of carbides for dies and moulds - P 6.24.* in *12th International EUSPEN conference*. 2012. Stockholm: EUSPEN, Cranfield.
95. Komanduri, R. and L. Raff, *A review on the molecular dynamics simulation of machining at the atomic scale*. Proceedings of the Institution of Mechanical Engineers, Part B: Journal of Engineering Manufacture, 2001. **215**(12): p. 1639-1672.
96. http://onlineheavytheory.net/silicon.html, *Crystal Structure of Silicon accessed on 10/3/2011.*
97. http://invsee.asu.edu/nmodules/carbonmod/crystalline.html, *Crystal Structure of Diamond accessed on 10/3/2011*.
98. Domnich, V. and Gogotsi Y., *Phase transformations in silicon under contact loading.* Reviews on advanced materials science, 2001. **3**(1).
99. Hinkle, K.H., R. Drake, and A.E.Timothy. *Cryogenic single-crystal silicon optics*. in *Proceedings of SPIE - Instrumentation in Astronomy VIII, Volume 2198*. pp 516-524, 1994.
100. Field, J.E., *The mechanical and strength properties of diamond.* Reports on Progress in Physics, 2012. **75**(12): p. 126505.
101. Perrone, D., *PhD Thesis on Process and characterisation techniques on 4H - Silicon Carbide*, in *Micronanotechnology*, Politecnico di Torino, 2007.
102. Wilks J. and Wilks E., *Properties and applications of diamond*, ed. British Library. 1991, Oxford, London: Butterworth Heinemann.
103. Taylor, A. and Laidler D.S., *The Formation and Crystal Structure of Silicon Carbide.* British Journal of Applied Physics, 1950. **1**(7): p. 174.
104. Tao, H., Thesis on *Atomistic model for nanoscale ductile mode cutting of silicon wafers*, in *Mechanical Engineering*, National University of Singapore, 2004.
105. Shimojo, F., Ebbsjo I., et al., *Molecular Dynamics Simulation of Structural Transformation in Silicon Carbide under Pressure.* Physical Review Letters, 2000. **84**(15): p. 3338.
106. Tse, J.S., D.D. Klug, and F. Gao, *Hardness of nanocrystalline diamonds.* Physical Review B, 2006. **73**(14): p. 140102.
107. *http://www.memsnet.org/material/siliconsibulk/*. accessed on 27/12/2011.
108. Vashishta, P., Kalia R.K., et al., *Interaction potential for silicon carbide: A molecular dynamics study of elastic constants and vibrational density of states for crystalline and amorphous silicon carbide.* Journal of Applied Physics, 2007. **101**(10): p. 103515-12.

109. *CREE Material datasheet* 2011.
110. Qian, J., Daemen L.L., and Y. Zhao, *Hardness and fracture toughness of moissanite.* Diamond and Related Materials, 2005. **14**(10): p. 1669-1672.
111. Pharr M., Katoh Yutai, and Bei Hongben *Dependence of Fracture toughness on crystallographic orientation in single crystalline cubic (β) silicon carbide*. www.imechanica.org accessed on 08.02.2012.
112. Pirouz, P., Zhang M., et al., *Transition from brittleness to ductility in SiC.* Journal of Physics: Condensed Matter, 2002. **14**(48): p. 12929.
113. Brede, M. and Haasen P., *The brittle-to-ductile transition in doped silicon as a model substance.* Acta Metallurgica, 1988. **36**(8): p. 2003-2018.
114. Codreanu, C., Avram M., et al., *Comparison of 3C–SiC, 6H–SiC and 4H–SiC MESFETs performances.* Materials Science in Semiconductor Processing, 2000. **3**(1-2): p. 137-142.
115. Bhatnagar, M. and Baliga B.J., *Comparison of 6H-SiC, 3C-SiC, and Si for power devices.* Electron Devices, IEEE Transactions on, 1993. **40**(3): p. 645-655.
116. Ko, G., Kim H.Y., et al., *Electrical characterizations of Neutron-irradiated SiC Schottky diodes.* Korean Journal of Chemical Engineering, 2009. **26**(1): p. 285-287.
117. Carlo, *PhD Thesis on Process and characterisation techniques on 3C - Silicon Carbide*, in *Micronanotechnology*, Politecnico di Torino, 2007.
118. Yu, M., C.S. Jayanthi, and S.Y. Wu, *Geometric and electronic structures of graphitic-like and tubular silicon carbides: Ab-initio studies.* Physical Review B, 2010. **82**(7): p. 075407.
119. Patten, J., W. Gao, and K. Yasuto, *Ductile Regime Nanomachining of Single-Crystal Silicon Carbide.* Journal of Manufacturing Science and Engineering, 2005. **127**(3): p. 522-532.
120. Ravindra, D. and J. Patten, *Improving the Surface Roughness of a CVD Coated Silicon Carbide Disk by Performing Ductile Regime Single Point Diamond Turning.* ASME Conference Proceedings, 2008. **2008**(48517): p. 155-161.
121. Yan, J., Z. Zhang, and T. Kuriyagawa, *Mechanism for material removal in diamond turning of reaction-bonded silicon carbide.* International Journal of Machine Tools and Manufacture, 2009. **49**(5): p. 366-374.
122. Ravindra, D. and J.A. Patten, *Chapter 4: Ductile regime material removal of silicon carbide(SiC)*, in *Silicon Carbide: New Materials, Production methods and application*, S.H. Vanger, Editor. 2011, Nova Publishers: Trivandrum, India. p. 141-167.
123. Madar, R., *Materials science: Silicon carbide in contention.* Nature, 2004. **430**(7003): p. 974-975.
124. http://www.grc.nasa.gov/WWW/SiC/, *Silicon Carbide electronics*. accessed on 01/05/2011.
125. Goel, S., Luo X., et al., *Atomistic aspects of ductile responses of cubic silicon carbide during nanometric cutting.* Nanoscale Research Letters, 2011. **6**(1): p. 589.
126. Vogler, M.P., DeVor R.E., and S.G. Kapoor, *On the Modeling and Analysis of Machining Performance in Micro-Endmilling, Part I: Surface Generation.* Journal of Manufacturing Science and Engineering, 2004. **126**(4): p. 685-694.
127. Lee, D.-E., Min S., et al., *Variation in Machinability of Single Crystal Materials in Micromechanical Machining (http://escholarship.org/uc/item/6991f42f).* Precision Manufacturing Group, Laboratory for Manufacturing and Sustainability, UC Berkeley, 2006. Precision Manufacturing Group.
128. Marsh, E.R., Sommer E.J., et al., *Detection of orientation-dependent, single-crystal diamond tool edge wear using cutting force sensors, while spin-turning silicon.* Precision Engineering, 2010. **34**(2): p. 253-258.
129. Shibata Y., F.S., Makino E. and Ikeda M., *Ductile-regime turning mechanism of single-crystal silicon.* Precision Engineering, 1996. **18**: p. 129-137.
130. Born, D.K. and W.A. Goodman, *An empirical survey on the influence of machining parameters on tool wear in diamond turning of large single-crystal silicon optics.* Precision Engineering, 2001. **25**(4): p. 247-257.
131. Ichida Y. *Ductile Mode Maching of Single Crystal Silicon Using a Single Point Diamond Tool*. in *Proceedings of the first International Conference and General Meeting of the European Society for Precision Engineering and Nanotechnology (EUSPEN)*. 1999. Bremen, Germany.
132. Zhang, J., Sun T., et al., *Molecular dynamics study of groove fabrication process using AFM-based nanometric cutting technique.* Applied Physics A: Materials Science & Processing, 2009. **94**(3): p. 593-600.
133. Mohammad, S., Thesis on *Effect of crystallographic orientation on wear of diamond tools in nanoscale ductile cutting of silicon*, in *Mechanical*, National University of Singapore, 2004.
134. Zong, W.J., Cheng K., et al., *The ultimate sharpness of single-crystal diamond cutting tools—Part I: Theoretical analyses and predictions.* International Journal of Machine Tools and Manufacture, 2007. **47**(5): p. 852-863.

135. Zong, W.J., Cheng K., et al., *The ultimate sharpness of single-crystal diamond cutting tools—Part II: A novel efficient lapping process.* International Journal of Machine Tools and Manufacture, 2007. **47**(5): p. 864-871.
136. Buzio, R., Boragno C., et al., *The contact mechanics of fractal surfaces.* Nature Materials, 2003. **2**(4): p. 233-236.
137. Bex, P.A., *Diamond Turning Tools*, in *Industrial Diamond Review*. 1975. p. 11-18.
138. Casey, M. and J. Wilks, *Some experiments to study turning tools using the scanning electron microscope.* International Journal of Machine Tool Design and Research, 1976. **16**(1): p. 13-22.
139. Hurt H.H. and Decker D.L., *Tribological considerations of the diamond single-point tool.* Proceedings of SPIE, Production Aspects of Single-point Machined Optics, 1986. **508**, p. 126–131.
140. Ikawa, N., S. S., and M. H., *Technology of Diamond Tool for Ultraprecision Metal Cutting*, in *Bulletin: Japan Society of Precision Engineering*. 1987. p. 233-238.
141. Yuan, Z.J., J.C. He, and Y.X. Yao, *The Optimum Crystal Plane of Natural Diamond Tool for Precision Machining.* CIRP Annals - Manufacturing Technology, 1992. **41**(1): p. 605-608.
142. Ikawa, N., S. Shimada, and H. Tsuwa, *Microfracture of Diamond as Fine Tool Material.* CIRP Annals - Manufacturing Technology, 1982. **31**(1): p. 71-74.
143. Astakhov, V.P. and J.P. Davim, *Tools (geometry and material) and tool wear.* Machining. Fundamentals and Recent Advances, 2008: p. 37-52.
144. Komanduri, R., N. Chandrasekaran, and L.M. Raff, *Molecular dynamics simulation of atomic-scale friction.* Physical Review B, 2000. **61**(20): p. 14007-14019.
145. Lucca, D.A., Y.W. Seo, and R. Komanduri, *Effect of Tool Edge Geometry on Energy Dissipation in Ultraprecision Machining.* CIRP Annals - Manufacturing Technology, 1993. **42**(1): p. 83-86.
146. Komanduri, R., *Some aspects of machining with negative rake tools simulating grinding.* International Journal of Machine Tool Design and Research, 1971. **11**(3): p. 223-233.
147. Astakhov, V.P., *Fundamentals of the Selection of Cutting Tool Geometry Parameters Geometry of Single-point Turning Tools and Drills*. 2010, Springer London. p. 127-204.
148. Komanduri, R. and W.R. Reed Jr, *Evaluation of carbide grades and a new cutting geometry for machining titanium alloys.* Wear, 1983. **92**(1): p. 113-123.
149. Biddut A.Q., Rahman M., et al., *Performance of single crystal diamond tools with different rake angles during micro-grooving on electroless nickel plated die materials.* International Journal of Advanced Manufacturing Technology, 2007. **33**(0): p. 891-899.
150. Samuels L. E., *The Mechanisms of Abrasive Machining.* Scientific American, 1978. **239**(5): p. 132.
151. Krulewich D., Syn C., et al., *An empirical survey on the influence of machining parameters on tool wear in diamond turning of large single crystal silicon optics - Paper prepared for submission to ASPE 14th Annual meeting at Monterey, CA.* 1999, Lawrence Livermore National Laboratory: Livermore, USA.
152. Lai, M., X.D. Zhang, and F.Z. Fang, *Study on critical rake angle in nanometric cutting*. Applied Physics A, 2012. **108**(4): p. 809-818.
153. Patten, J.A. and W. Gao, *Extreme negative rake angle technique for single point diamond nano-cutting of silicon.* Precision Engineering, 2001. **25**(2): p. 165-167.
154. Durazo-Cardenas, I., Luo X., et al., *3D characterisation of tool wear whilst diamond turning silicon*. Wear, 2007. **262**(3-4): p. 340-349.
155. Fang, F.Z. and Venkatesh V.C., *Diamond Cutting of Silicon with Nanometric Finish.* CIRP Annals - Manufacturing Technology, 1998. **47**(1): p. 45-49.
156. Yan, J., Asami T., et al., *Crystallographic effect on subsurface damage formation in silicon microcutting.* CIRP Annals - Manufacturing Technology, 2012. **61**(1): p. 131-134.
157. Komanduri, R., Chandrasekaran M., et al., *Molecular dynamics simulation of the nanometric cutting of silicon.* Philosophical Magazine Part B, 2001. **81**(12): p. 1989 - 2019.
158. Promyoo, R., H. El-Mounayri, and X. Yang, *Molecular dynamics simulation of nanometric cutting.* Machining Science and Technology, 2010. **14**(4): p. 423-439.
159. Rapaport, D., *The Art of Molecular Dynamics Simulation.* 2004: Cambridge University Press.
160. Bhushan, B., J.N. Israelachvili, and U. Landman, *Nanotribology - Friction, Wear and Lubrication at the Atomic-Scale*. Nature, 1995. **374**(6523): p. 607-616.
161. Luan, B. and M.O. Robbins, *The breakdown of continuum models for mechanical contacts.* Nature, 2005. **435**(7044): p. 929-932.
162. Cai, W., J. Li, and S. Yip, *1.09 - Molecular Dynamics*, in *Comprehensive Nuclear Materials*, J.M.K. Editor-in-Chief: Rudy, Editor. 2012, Elsevier: Oxford. p. 249-265.
163. Pastewka, L., Moseler M., et al., *Anisotropic mechanical amorphization drives wear in diamond.* Nature Materials, 2011. **10**(1): p. 34-38.
164. Sen, D., Thaulow C., et al., *Atomistic Study of Crack-Tip Cleavage to Dislocation Emission Transition in Silicon Single Crystals.* Physical Review Letters, 2010. **104**(23): p. 235502.

165. Notman, R. and J. Anwar, *Breaching the skin barrier — Insights from molecular simulation of model membranes.* Advanced Drug Delivery Reviews, 2012(0).
166. Balamane, H., T. Halicioglu, and W.A. Tiller, *Comparative study of silicon empirical interatomic potentials.* Physical Review B, 1992. **46**(4): p. 2250-2279.
167. Daw, M.S. and M.I. Baskes, *Embedded-atom method: Derivation and application to impurities, surfaces, and other defects in metals.* Physical Review B, 1984. **29**(12): p. 6443-6453.
168. Stillinger, F.H. and T.A. Weber, *Computer simulation of local order in condensed phases of silicon.* Physical Review B, 1985. **31**(8): p. 5262-5271.
169. Stillinger, F.H. and T.A. Weber, *Erratum: Computer simulation of local order in condensed phases of silicon [Phys. Rev. B 31, 5262 (1985)].* Physical Review B, 1986. **33**(2): p. 1451-1451.
170. Berendsen, H.J.C., J.R. Grigera, and T.P. Straatsma, *The missing term in effective pair potentials.* The Journal of Physical Chemistry, 1987. **91**(24): p. 6269-6271.
171. Tersoff, J., *New empirical approach for the structure and energy of covalent systems.* Physical Review B, 1988. **37**(12): p. 6991.
172. Tersoff, J., *Empirical interatomic potential for silicon with improved elastic properties.* Physical Review B, 1988. **38**(14): p. 9902.
173. Tersoff, J., *Modeling solid-state chemistry: Interatomic potentials for multicomponent systems.* Physical Review B, 1989. **39**(8): p. 5566.
174. Tersoff, J., *Erratum: Modeling solid-state chemistry: Interatomic potentials for multicomponent systems.* Physical Review B, 1990. **41**(5): p. 3248.
175. Tersoff, J., *Carbon defects and defect reactions in silicon.* Physical Review Letters, 1990. **64**(15): p. 1757.
176. Tersoff, J., *Chemical order in amorphous silicon carbide.* Physical Review B, 1994. **49**(23): p. 16349.
177. Agrawal, P.M., L.M. Raff, and R. Komanduri, *Monte Carlo simulations of void-nucleated melting of silicon via modification in the Tersoff potential parameters.* Physical Review B, 2005. **72**(12): p. 125206.
178. Devanathan, R., T. Diaz de la Rubia, and W.J. Weber, *Displacement threshold energies in β-SiC.* Journal of Nuclear Materials, 1998. **253**(1–3): p. 47-52.
179. Baskes, M.I., J.S. Nelson, and A.F. Wright, *Semiempirical modified embedded-atom potentials for silicon and germanium.* Physical Review B, 1989. **40**(9): p. 6085-6100.
180. Brenner, D.W., *Empirical potential for hydrocarbons for use in simulating the chemical vapor deposition of diamond films.* Physical Review B, 1990. **42**(15): p. 9458-9471.
181. Stuart, S.J., A.B. Tutein, and J.A. Harrison, *A reactive potential for hydrocarbons with intermolecular interactions.* The Journal of Chemical Physics, 2000. **112**(14): p. 6472-6486.
182. van Duin A, et al., *ReaxFF: A Reactive Force Field for Hydrocarbons.* The Journal of Physical Chemistry A, 2001. **105**(41): p. 9396-9409.
183. Erhart, P. and K. Albe, *Analytical potential for atomistic simulations of silicon, carbon, and silicon carbide.* Physical Review B, 2005. **71**(3): p. 035211.
184. Yu, J., S.B. Sinnott, and S.R. Phillpot, *Charge optimized many-body potential for the Si/SiO2 system.* Physical Review B, 2007. **75**(8): p. 085311.
185. Zhou, X.W. and F.P. Doty, *Embedded-ion method: An analytical energy-conserving charge-transfer interatomic potential and its application to the La-Br system.* Physical Review B, 2008. **78**(22): p. 224307.
186. Bartók, A.P., Payne M.C., et al., *Gaussian Approximation Potentials: The Accuracy of Quantum Mechanics, without the Electrons.* Physical Review Letters, 2010. **104**(13): p. 136403.
187. de Brito Mota, F., J.F. Justo, and A. Fazzio, *Structural properties of amorphous silicon nitride.* Physical Review B, 1998. **58**(13): p. 8323.
188. Matsunaga, K. and Y. Iwamoto, *Molecular Dynamics Study of Atomic Structure and Diffusion Behavior in Amorphous Silicon Nitride Containing Boron.* Journal of the American Ceramic Society, 2001. **84**(10): p. 2213-2219.
189. Matsunaga, K., C. Fisher, and H. Matsubara, *Tersoff Potential Parameters for Simulating Cubic Boron Carbonitrides.* Japenese Journal of Applied physics, 2000. **39**: p. L48-L51.
190. Plimpton, S.J. and A.P. Thompson, *Computational aspects of many-body potentials (DOI:10.1557/mrs.2012.96).* MRS Bulletin, 2012. **37**: p. 513-521.
191. Ikawa, N., Donaldson R., et al., *An Atomistic Analysis of Nanometric Chip Removal as Affected by Tool-Work Interaction in Diamond Turning.* CIRP Annals - Manufacturing Technology, 1991. **40**(1): p. 551-554.
192. Nordlund, K., J. Keinonen, and T. Mattila, *Formation of Ion Irradiation Induced Small-Scale Defects on Graphite Surfaces.* Physical Review Letters, 1996. **77**(4): p. 699.
193. Erhart, P. and K. Albe, *Analytical potential for atomistic simulations of silicon, carbon, and silicon carbide.* Physical Review B, 2005. **71**(3): p. -.

194. Pastewka, L., Moseler M., et al., *Bond order potentials for fracture, wear, and plasticity.* MRS Bulletin-Three decades of many-body potentials in materials research, 2012. **37**(5): p. 493-503.
195. http://www.siliconfareast.com/lattice_constants.htm, *Lattice Constants accessed on 9/4/2011.*
196. Zhang, Z.G., Sun T., et al., *Molecular dynamics study on various nanometric cutting boundary conditions.* Journal of Vacuum Science & Technology B, 2009. **27**(3): p. 1355-1360.
197. Luo, X., PhD Thesis on *High Precision Surfaces Generation: Modelling, Simulation and Machining Verification*, in *Mechanical Engineering*, Leeds Metropolitan University, 2003.
198. Plimpton, S., *Fast Parallel Algorithms for Short-Range Molecular Dynamics.* Journal of Computational Physics, 1995. **117**: p. 1-19.
199. Humphrey, W., Dalke, A. and Schulten, K., *VMD - Visual Molecular Dynamics.* J. Molec. Graphics, 1996. **14**: p. 33-38.
200. Stukowski, A., *Visualization and analysis of atomistic simulation data with OVITO–the Open Visualization Tool.* Modelling and Simulation in Materials Science and Engineering, 2010. **18**(1).
201. Pizani, P.S., Jasinevicius R., et al., *Ductile and brittle modes in single-point-diamond-turning of silicon probed by Raman scattering.* Journal of Materials Science Letters, 1999. **18**(14): p. 1185-1187.
202. Patten J.A., Cherukuri H., and J. Yan, *Ductile Regime Machining of Semiconductors and Ceramics*, in *High Pressure Surface Science and Engineering*, Y.G. Gogotsi and V. Domnich, Editors. 2003, Taylor and Francis, CRC Press: Philadelphia, Pennsylvania, USA. p. 639.
203. Stukowski, A., *Structure identification methods for atomistic simulations of crystalline materials.* Modelling and Simulation in Materials Science and Engineering, 2012. **20**(4): p. 045021.
204. Cheong, W.C.D. and L.C. Zhang, *Molecular dynamics simulation of phase transformations in silicon monocrystals due to nano-indentation.* Nanotechnology, 2000. **11**(3): p. 173.
205. http://isaacs.sourceforge.net/phys/rdfs.html, *g(r) RDF Explanation accessed on 10/3/2011.*
206. Ackland, G.J. and A.P. Jones, *Applications of local crystal structure measures in experiment and simulation.* Physical Review B, 2006. **73**(5): p. 054104.
207. Pei, Q.X., C. Lu, and H.P. Lee, *Large scale molecular dynamics study of nanometric machining of copper.* Computational Materials Science, 2007. **41**(2): p. 177-185.
208. Kelchner, C.L., Plimpton S.J., and J.C. Hamilton, *Dislocation nucleation and defect structure during surface indentation.* Physical Review B, 1998. **58**(17): p. 11085.
209. Komanduri, R., Chandrasekaran N., and L.M. Raff, *M.D. Simulation of nanometric cutting of single crystal aluminum–effect of crystal orientation and direction of cutting.* Wear, 2000. **242**(1–2): p. 60-88.
210. Uddin, M.S., Seah K.H. W., et al., *Effect of crystallographic orientation on wear of diamond tools for nano-scale ductile cutting of silicon.* Wear, 2004. **257**(7-8): p. 751-759.
211. Chen, H.P., Kalia R.K., et al., *Multimillion-atom nanoindentation simulation of crystalline silicon carbide: Orientation dependence and anisotropic pileup.* Journal of Applied Physics, 2007. **102**(6).
212. Shaw, M.C., *Metal Cutting Principles.* Oxford Series on Advanced Manufacturing, ed. J.R. Crookall, M.C. Shaw, and N.P. Suh. 2004, New York: Oxford University Press.
213. Schuh, C.A. and A.C. Lund, *Atomistic basis for the plastic yield criterion of metallic glass.* Nature Materials, 2003. **2**(7): p. 449-452.
214. Jasinevicius, R.G., J.G. Duduch, and P.S. Pizani, *The influence of crystallographic orientation on the generation of multiple structural phases generation in Silicon by cyclic microindentation.* Materials Letters, 2008. **62**(6–7): p. 812-815.
215. Gupta, M.C. and A.L. Ruoff, *Static compression of silicon in the [100] and in the [111] directions.* Journal of Applied Physics, 1980. **51**(2): p. 1072-1075.
216. Goel, S., X. Luo, and R.L. Reuben, *Wear mechanism of diamond tools against single crystal silicon in single point diamond turning process.* Tribology International, 2013. **57**(0): p. 272-281.
217. Gogotsi, Y.G., A. Kailer, and K.G. Nickel, *Pressure-induced phase transformations in diamond.* Journal of Applied Physics, 1998. **84**(3): p. 1299-1304.
218. Roundy, D. and M.L. Cohen, *Ideal strength of diamond, Si, and Ge.* Physical Review B, 2001. **64**(21): p. 212103.
219. Chacham, H. and L. Kleinman, *Instabilities in Diamond under High Shear Stress.* Physical Review Letters, 2000. **85**(23): p. 4904-4907.
220. Domnich, V., Y. Gogotsi, and M. Trenary, *Identification of Pressure-Induced Phase Transformations Using Nanoindentation.* MRS Online Proceedings Library, 2000. **649**: p. null-null.

221. Hisham A. Abdel-Al and S.T. Smith. *Thermal modeling of silicon machining - issues and challenges*. in *ASPE Spring topical meeting:Silicon machining, Carmel-by-the-sea*. 1998. California.
222. Kovalchenko, A., et al., *Phase Transformations in Silicon Under Dry and Lubricated Sliding.* Tribology Transactions, 2002. **45**(3): p. 372-380.
223. Jasinevicius, R.G., J.G. Duduch, and P.S. Pizani, *Structure evaluation of submicrometre silicon chips removed by diamond turning.* Semiconductor Science and Technology, 2007. **22**(5): p. 561.
224. Cahn, R.W., *Metallic solid silicon.* Nature, 1992. **357**(6380): p. 645-646.
225. Yury, G., Guohui Z., et al., *Raman microspectroscopy analysis of pressure-induced metallization in scratching of silicon.* Semiconductor Science and Technology, 2001. **16**(5): p. 345.
226. Ge, D., V. Domnich, and Y. Gogotsi, *High-resolution transmission electron microscopy study of metastable silicon phases produced by nanoindentation.* Journal of Applied Physics, 2003. **93**(5): p. 2418-2423.
227. Chrobak, D., Tymiak N., et al., *Deconfinement leads to changes in the nanoscale plasticity of silicon.* Nat Nano, 2011. **6**(8): p. 480-484.
228. Cross, G.L.W., *Silicon nanoparticles: Isolation leads to change.* Nat Nano, 2011. **6**(8): p. 467-468.
229. Cai, M.B., X.P. Li, and M. Rahman, *Study of the Mechanism of Groove Wear of the Diamond Tool in Nanoscale Ductile Mode Cutting of Monocrystalline Silicon.* Journal of Manufacturing Science and Engineering, 2007. **129**(2): p. 281-286.
230. Zhiguo Wang, Y.L., Mingjun Chen, Zhen Tong, Jiaxuan Chen. *Analysis about diamond tool wear in nano-metric cutting of single crystal silicon using molecular dynamics method.* 2010: SPIE.
231. Beyers, R., *Thermodynamic considerations in refractory metal-silicon-oxygen systems.* Journal of Applied Physics, 1984. **56**(1): p. 147-152.
232. Cheng, Z., Thesis on *Reaction kinetics and structural evolution for the formation on nanocrystalline silicon carbide via carbothermal reduction*- Materials Science & Engineering, Georgia Institute of Technology, 2004.
233. Viscomi, F.a.H., L, *"Kinetic and Mechanistic Study on the Formation of Silicon Carbide from Silica Flour and Coke Breeze,*. Journal of Metals, 1978(6): p. 21-24.
234. Weimer, A.W., Nilsen, K. J., Cochran, G. A., and Roach, R. P., *Kinetics of Carbothermal Reduction Synthesis of Beta Silicon Carbide.* AIChE Journal, 1993. **39**(3): p. 493-502.
235. Goel, S., Luo X., et al., *Influence of temperature and crystal orientation on tool wear during single point diamond turning of silicon.* Wear, 2012. **284–285**(0): p. 65-72.
236. Fineberg, J., *Diamonds are forever - or are they?* Nature Materials, 2011. **10**.
237. Rigney, D. and S. Karthikeyan, *The Evolution of Tribomaterial During Sliding: A Brief Introduction.* Tribology Letters, 2010. **39**(1): p. 3-7.
238. Zhang, Z., Yan J., and T. Kuriyagawa, *Study on tool wear characteristics in diamond turning of reaction-bonded silicon carbide*. The International Journal of Advanced Manufacturing Technology, 2011. **57**(1): p. 117-125.
239. Albrecht, P., *New Developments in the Theory of the Metal-Cutting Process: Part I. The Ploughing Process in Metal Cutting.* Journal of Engineering for Industry, 1960. **82**(4): p. 348-357.
240. Zong, W.J., Sun T., et al., *XPS analysis of the groove wearing marks on flank face of diamond tool in nanometric cutting of silicon wafer.* International Journal of Machine Tools and Manufacture, 2008. **48**(15): p. 1678-1687.
241. Aourag, H., Merad G., et al., *The high pressure behaviour of InSb and β-SiC.* Computational Materials Science, 1992. **1**(1): p. 78-86.
242. Tang, M., *Elastic Instabilities and Structural responses of Beta-SiC under stress*, in *Nuclear Engineering*. 1995, Massachusetts Institute of Technology: Cambridge, Massachusetts, USA.
243. Szlufarska, I., Kalia R.K., et al., *Atomistic mechanisms of amorphization during nanoindentation of SiC: A molecular dynamics study.* Physical Review B, 2005. **71**(17).
244. Noreyan, A., J.G. Amar, and I. Marinescu, *Molecular dynamics simulations of nanoindentation of beta-SiC with diamond indenter.* Materials Science and Engineering B-Solid State Materials for Advanced Technology, 2005. **117**(3): p. 235-240.
245. Noreyan, A. and J.G. Amar, *Molecular dynamics simulations of nanoscratching of 3C SiC.* Wear, 2008. **265**(7-8): p. 956-962.
246. Yan, J., X. Gai, and H. Harada, *Subsurface Damage of Single Crystalline Silicon Carbide in Nanoindentation Tests.* Journal of Nanoscience and Nanotechnology, 2010. **10**(11): p. 7808-7811.

247. Yoshida, M., Onodera A., et al., *Pressure-induced phase transition in SiC.* Physical Review B, 1993. **48**(14): p. 10587-10590.
248. Mishra, M. and I. Szlufarska, *Possibility of high-pressure transformation during nanoindentation of SiC.* Acta Materialia, 2009. **57**(20): p. 6156-6165.
249. Mishra, M. and I. Szlufarska, *Dislocation controlled wear in single crystal silicon carbide.* Journal of Materials Science (2012): p. 1-11.
250. Chang, K.J. and M.L. Cohen, *Ab initio pseudopotential study of structural and high-pressure properties of SiC.* Physical Review B, 1987. **35**(15): p. 8196-8201.
251. Karch, K., Pavone P., et al., *Ab initio calculation of structural and lattice-dynamical properties of silicon carbide.* Physical Review B, 1994. **50**(23): p. 17054-17063.
252. Gogotsi, Y.G., A. Kailer, and K.G. Nickel, *Materials: Transformation of diamond to graphite.* Nature, 1999. **401**(6754): p. 663-664.
253. Belak, J., *Nanotribology: Modelling Atoms When Surfaces Collide*, in *Energy and Technology Review*. 1994, Lawrence Livermore Laboratory.
254. Allred, A.L. and E.G. Rochow, *Electronegativities of carbon, silicon, germanium, tin and lead.* Journal of Inorganic and Nuclear Chemistry, 1958. **5**(4): p. 269-288.
255. Menon, M., Richter E., et al., *Structure and stability of SiC nanotubes.* Physical Review B, 2004. **69**(11).
256. Sun, X.-H., Li C.P., et al., *Formation of Silicon Carbide Nanotubes and Nanowires via Reaction of Silicon (from Disproportionation of Silicon Monoxide) with Carbon Nanotubes.* Journal of the American Chemical Society, 2002. **124**(48): p. 14464-14471.
257. Goel, S., Luo X., and R.L. Reuben, *Shear instability of nanocrystalline silicon carbide during nanometric cutting.* Applied Physics Letters, 2012. **100**(23): p. 231902.
258. Patten, J.A., R.O. Scattergood, and R. Nemanich, *http://www.micro.physics.ncsu.edu/ accessed on 22/10/2012*. 2012.
259. Levitas, V.I., Ma Y., et al., *High-density amorphous phase of silicon carbide obtained under large plastic shear and high pressure.* Physical Review B, 2012. **85**(5): p. 054114.
260. Luo, X., Goel S., and R.L. Reuben, *A quantitative assessment of nanometric machinability of major polytypes of single crystal silicon carbide.* Journal of the European Ceramic Society, 2012. **32**(12): p. 3423-3434.
261. To, S., W.B. Lee, and C.Y. Chan, *Ultraprecision diamond turning of aluminium single crystals.* Journal of Materials Processing Technology, 1997. **63**(1–3): p. 157-162.
262. Jonathan A. Salem, Zhuang Li, and Richard C. Bradt, *Thermal expansion and elastic anisotropy in single crystal Al2O3 and SiC Reinforcements, NASA Technical Memorandum 106516 prepared for ASME Symposium on advances in composite materials and structure sponsored by American society of Mechanical Engineers*. December 10-12, 1986: Anaheim, California.
263. Pastewka, L., PhD Thesis on *Multi-scale simulations of carbon nanomaterials for supercapacitors, actuators and low-friction coatings*, in *Mathematics and Physics Department*. 2010, Fruanhofer IWM, Albert-Ludwigs-Universität, Germany.
264. Stukowski, A. and K. Albe, *Extracting dislocations and non-dislocation crystal defects from atomistic simulation data.* Modelling and Simulation in Materials Science and Engineering, 2010. **18**(8): p. 085001.
265. Stukowski, A., V.V. Bulatov, and A. Arsenlis, *Automated identification and indexing of dislocations in crystal interfaces.* Modelling and Simulation in Materials Science and Engineering, 2012. **20**(8): p. 085007.
266. Cai, M.B., X.P. Li, and M. Rahman, *High-pressure phase transformation as the mechanism of ductile chip formation in nanoscale cutting of silicon wafer.* Proceedings of the Institution of Mechanical Engineers, Part B: Journal of Engineering Manufacture, 2007. **221**(10): p. 1511-1519.
267. Mishra, M. and I. Szlufarska, *Dislocation controlled wear in single crystal silicon carbide.* Journal of Materials Science, 2012: p. 1-11.
268. Inasaki, I., *Grinding of Hard and Brittle Materials.* CIRP Annals - Manufacturing Technology, 1987. **36**(2): p. 463-471.
269. Cai, M.B., X.P. Li, and M. Rahman, *Study of the temperature and stress in nanoscale ductile mode cutting of silicon using molecular dynamics simulation.* Journal of Materials Processing Technology, 2007. **192-193**: p. 607-612.
270. Yan, J., Z. Zhang, and T. Kuriyagawa, *Effect of Nanoparticle Lubrication in Diamond Turning of Reaction-Bonded SiC.* International Journal of Automation Technology, 2011. **5**(3): p. 307-312.
271. Goel S., Luo X., *Influence of nanoparticle coolant and crystal structure of the workpiece during nanometric cutting of silicon carbide*. in *proceedings of the 12th EUSPEN International Conference*. 2012. Stockholm: EUSPEN.

272. Monnoye, S., D. Turover, and P. Vicente, *Surface Preparation Techniques for SiC Wafers Silicon Carbide*, W.J. Choyke, H. Matsunami, and G. Pensl, Editors. 2004, Springer Berlin Heidelberg. p. 699-710.
273. Lucca, D.A., Seo Y.W., et al., *Aspects of Surface Generation in Orthogonal Ultraprecision Machining.* CIRP Annals - Manufacturing Technology, 1994. **43**(1): p. 43-46.
274. Goel, S., Luo X., and R.L. Reuben, *Molecular dynamics simulation model for the quantitative assessment of tool wear during single point diamond turning of cubic silicon carbide.* Computational Materials Science, 2012. **51**(1): p. 402-408.
275. Grillo, S.E. and J.E. Field, *The friction of natural and CVD diamond.* Wear, 2003. **254**(10): p. 945-949.
276. *Probe Selection Guide - Hysitron Triboindenter Manual*, H. Incorporated, Editor. 2007: Minneapolis, USA.
277. Patten J.A., Jacob J., et al., *Chapter 2: Numerical simulations and cutting experiments on single point diamond machining of semiconductors and ceramics*, in *Semiconductor Machining at the Micro-Nano Scale*, J. Yan and J.A. Patten, Editors. 2007, Transworld Research Network: Trivandrum-695 023, Kerala, India.
278. Jacob, J., Patten J., et al., *Determination of the ductile to brittle transition and critical depth of cut in 6h-silicon carbide through fly cutting*, ed. P. NO.1748. 2005: ASPE.
279. Shayan, A.R., Patten J., et al., *Force Analysis, Mechanical Energy and Laser Heating Evaluation of Scratch Tests on Silicon Carbide (4H-SiC) in Micro-Laser Assisted Machining ([micro sign]-LAM) Process.* ASME Conference Proceedings, 2009. **2009**(43611): p. 827-832.
280. Goel, S., Luo X., et al., *Brittle–ductile transition during diamond turning of single crystal silicon carbide.* International Journal of Machine Tools and Manufacture, 2013. **65**(February): p. 15-21.
281. Zykova-Timan, T., D. Ceresoli, and E. Tosatti, *Peak effect versus skating in high-temperature nanofriction.* Nature Materials, 2007. **6**(3): p. 230-234.
282. Riedl, M., *Advances in single-point diamond turning provide improved performance for visible as well as IR optics.*, SPIE Magazine by Precitech (July 2004). p. 26-29.
283. Waleed, B.R., Goel S., et al., *An experimental investigation for the improvement of attainable surface roughness during hard turning process in* Proceedings of IMechE Part B: Journal of Engineering Manufacture, 2013.
284. Brinksmeier, E. and R. Gläbe, *Advances in Precision Machining of Steel.* CIRP Annals - Manufacturing Technology, 2001. **50**(1): p. 385-388.
285. Casstevens, J.M., *Diamond turning of steel in carbon-saturated atmospheres.* Precision Engineering, 1983. **5**(1): p. 9-15.
286. Brehl, D.E. and T.A. Dow, *Review of vibration-assisted machining.* Precision Engineering, 2008. **32**(3): p. 153-172.
287. Shamoto, E. and T. Moriwaki, *Ultaprecision Diamond Cutting of Hardened Steel by Applying Elliptical Vibration Cutting.* CIRP Annals - Manufacturing Technology, 1999. **48**(1): p. 441-444.
288. Moriwaki, T. and E. Shamoto, *Ultraprecision Diamond Turning of Stainless Steel by Applying Ultrasonic Vibration.* CIRP Annals - Manufacturing Technology, 1991. **40**(1): p. 559-562.
289. Inada, A., S. Min, and H. Ohmori, *Micro cutting of ferrous materials using diamond tool under ionized coolant with carbon particles.* CIRP Annals - Manufacturing Technology, 2011. **60**(1): p. 97-100.
290. Yan, J., Z. Zhang, and T. Kuriyagawa, *Tool wear control in diamond turning of high-strength mold materials by means of tool swinging.* CIRP Annals - Manufacturing Technology, 2010. **59**(1): p. 109-112.
291. Zareena, A.R. and S.C. Veldhuis, *Tool wear mechanisms and tool life enhancement in ultra-precision machining of titanium.* Journal of Materials Processing Technology, 2012. **212**(3): p. 560-570.
292. Kawasegi, N., Sugimori H., et al., *Development of cutting tools with microscale and nanoscale textures to improve frictional behavior.* Precision Engineering, 2009. **33**(3): p. 248-254.
293. Chang, W., Sun J., et al., *Investigation of microstructured milling tool for deferring tool wear.* Wear, 2011. **271**(9–10): p. 2433-2437.
294. Fujisaki, K., Yokota H., et al., *Development of ultra-fine-grain binderless cBN tool for precision cutting of ferrous materials.* Journal of Materials Processing Technology, 2009. **209**(15-16): p. 5646-5652.
295. Fang, F.Z., Venkatesh V.C., et al., *Nanometric cutting of single crystal silicon surfaces modified by ion implantation.* CIRP Annals - Manufacturing Technology, 2011. **60**(1): p. 527-530.
296. Tutunea-Fatan, O.R., M.A. Fakhri, and E.V. Bordatchev, *Porosity and cutting forces: from macroscale to microscale machining correlations.* Proceedings of the Institution of Mechanical Engineers, Part B: Journal of Engineering Manufacture, 2011. **225**(5): p. 619-630.

297. Komanduri, R., Lee M., et al., *Pulse Laser Pretreated Machining, US Patent No. 4356376 against application no. 263235* 26th October 1982, Assignee: General Electric Company, N.Y.: United States of America.
298. Liang, Y.C., Guo W.B., et al. *Molecular dynamics simulation of heat distribution during nanometric cutting process*. in *Nanoelectronics Conference, 2008. INEC 2008. 2nd IEEE International*. 2008.
299. Goel, S., Luo X., et al., *Single Point Diamond Turning of Single Crystal Silicon Carbide: Molecular Dynamic Simulation Study*, in *Key Engineering Materials*. 2012, Key Engineering Materials: Liverpool. p. 150-155.
300. Robinson, G., M. Jackson, and M. Whitfield, *A review of machining theory and tool wear with a view to developing micro and nano machining processes.* Journal of Materials Science, 2007. **42**(6): p. 2002-2015.
301. Javvaji, R., Thesis on *Nanoscale ductile mode ultraprecision cutting of potassium dihydrogen phosphate*, in *Mechanical Engineering*, National University of singapore, Singapore, 2008.
302. Shore P., PhD thesis on *Machining of Optical Surfaces in Brittle Materials using an Ultra Precision Machine Tool*, Cranfield University,UK, 1995.
303. Bharat, B., *Tribology and mechanics of magnetic storage devices, ISBN:0387946276*. 2nd ed. Vol. 1. 1996, Ohio, USA: Springer-verlag NewYork Inc.